Structural and mechanical properties of metallic nanowires: in the border between crystallinity and weird configurations

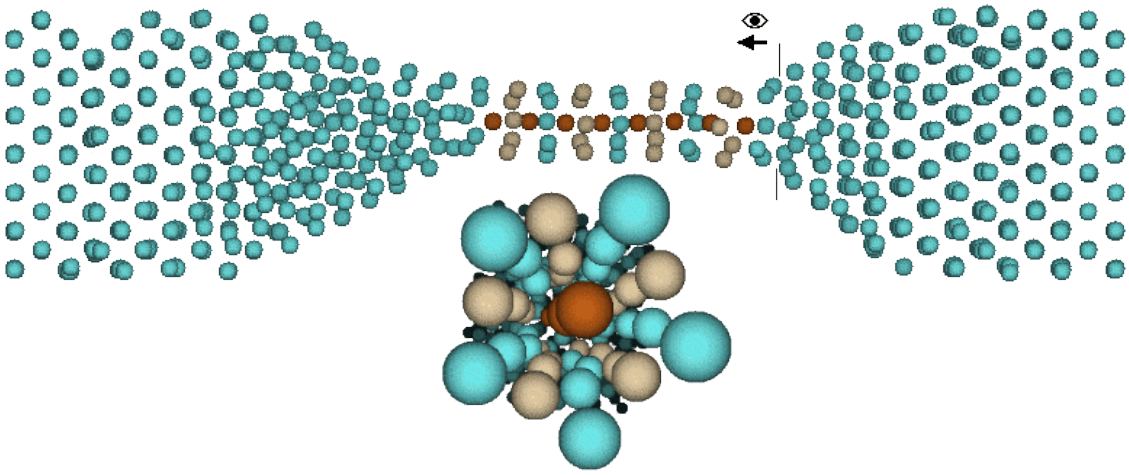

Samuel Peláez Machado

Dpto. de Física de la Materia Condensada

Universidad Autónoma de Madrid

Structural and mechanical properties of metallic nanowires: in the border between crystallinity and weird configurations

by

Samuel Peláez Machado

Dpto. de Física de la Materia Condensada

Universidad Autónoma de Madrid

Dissertation submitted for the degree of

PhD. in Physics

Advisors: Pedro A. Serena Domingo
and Pedro García-Mochales Caro

Madrid, January 2012

Samuel Peláez Machado
Instituto de Ciencia de Materiales de Madrid (ICMM)
Consejo Superior de Investigaciones Científicas (CSIC)
C/Sor Juana Inés de la Cruz 3, Cantoblanco, Madrid - 28049
http://www.icmm.csic.es/

Abstract

In this thesis we have studied structural and mechanical properties of Al, Ni and Cu ultra-thin nanowires by computer simulations. Due to their large surface/volume ratio, ultra-thin metallic nanowires exhibit a number of properties that differ from wires in the micrometer and larger scales. Among these properties it can be mentioned, for instance, that in some cases these nanowires abandon their bulk FCC structure in favor of helical or disordered arrangements. Also, in some cases their mechanical response to external applied stress becomes even stronger than a bulk structure.

The use of computer simulations is a valuable tool to get a deeper insight in the behaviour of these systems. It provides the ability to control the exact coordinates and velocities of atoms, as well as their time evolution under a wide variety of possible "computer experiments". The accuracy of such experiments, however, is limited by the available computer resources. A balance must be done between system sizes and simulation times in order to perform accurate enough (reliable) calculations within reasonable times. For these reasons in this thesis we have decided to use semi-classical potentials to describe the interatomic interactions. In particular, we have used the Embedded Atom Method (EAM), analyzing its reliability when simulating nanoscale systems compared to other calculation methodologies.

In this thesis we use the Molecular Dynamics (MD) method to obtain the equilibrium structure of nanowires of different thicknesses, shapes and crystallographic orientations, as well as studying their elastic response to induced axial stress. We have developed an Equation of State (EOS) that models the cohesive energy of FCC nanowires as a function of the number of surface and edge atoms and the type of exposed facets. This concept of an EOS allows a determination of the *edge energy* μ, a quantity that has not been estimated in the literature and that has certain influence in the total cohesive energy of small systems like ultra-thin nanowires or small clusters.

Furthermore, we have studied the elastic response of these nanowires upon externally applied stress. Our results confirm the non-linear stress-strain behaviour of these systems reported by other authors. We have also studied the Young's modulus of these nanowires, which is strongly influenced by the non-linear stress-strain response.

Another part of this thesis is devoted to study the dynamics of the breaking processes of nanowires, mimicking several experimental techniques that produce metallic nanocontacts. Among other results, we have observed that under certain conditions

these nanocontacts adopt the form of a long pentagonal chains. We have carried out a statistical study on the probability of formation of such chains, and propose experimental setups that could allow to observe their appearence.

Resumen

En esta tesis se estudian propiedades estructurales y mecánicas de nanohilos ultra-finos de Al, Cu y Ni mediante simulaciones computacionales. Debido a su alto ratio de superficie/volumen, los nanohilos metálicos ultra-finos muestran ciertas propiedades que difieren de las de hilos metálicos de tamaños micrométricos o mayores. Entre esas propiedades pueden mencionarse, por ejemplo, que en algunos casos estos nanohilos abandonan su estructura de volumen FCC en favor de arreglos helicoidales o desordenados. También, en algunos casos su respuesta mecánica ante presiones externas es incluso más fuerte que la de la estructura FCC de volumen.

El uso de simulaciones computacionales es una herramienta valiosa para alcanzar un conocimiento más profundo del comportamiento de estos sistemas. Permite controlar las coordenadas y velocidades atómicas con precisión, así como su evolución en diferentes "experimentos computacionales". La precisión de estos experimentos, no obstante, se encuentra limitada por los recursos computacionales disponibles. Es necesario hacer un balance entre el tamaño de los sistemas a estudiar y los tiempos a simular con el fin de realizar cálculos suficientemente precisos (confiables) en intervalos de tiempo razonables. Por estas razones en esta tesis se ha decidido usar potenciales semi-clásicos para describir las interacciones interatómicas. En particular, se ha usado el Método del Átomo Embebido (EAM), analizando su fiabilidad cuando se trata de simular sistemas en la nanoescala comparada con la de otras metodologías computacionales.

En esta tesis se hace uso del método de Dinámica Molecular (MD) para obtener la estructura de equilibrio de nanohilos de differentes grosores, formas y orientaciones cristalográficas, así como para estudiar su respuesta elástica ante estrés externo. Se ha desarrollado una Ecuación de Estado (EOS) que modela la energía de cohesión de un nanohilo FCC en función del número de átomos en sus superficies y aristas y del tipo de facetas que muestra al exterior. Este concepto de EOS permite determinar la *energía de arista* μ, una cantidad que no ha sido estimada en la literatura y que tiene cierta influencia en la energía de cohesión total de sistemas pequeños, como nanohilos ultra-finos o pequeños clusters.

Adicionalmente, en esta tesis se ha estudiado la respuesta elástica de estos nanohilos ante estrés externo. Los resultados aquí obtenidos confirman la no-linealidad en la relación estress-estiramiento que ha sido reportada por otros autores. También se ha estudiado el módulo de Young de estos nanohilos, el cual está fuertemente influenciado por la respuesta no-lineal de estrés-estiramiento.

Otra parte de esta tesis está dedicada al estudio de la dinámica de los procesos de ruptura de nanohilos, simulando algunas técnicas experimentales que producen nanocontactos metálicos. Entre otros resultados, se ha observado que bajo ciertas condiciones estos nanocontactos adoptan la forma de cadenas pentagonales largas. Se ha llevado a cabo un estudio estadístico de la probabilidad de formación de estas cadenas y se proponen montajes experimentales que podrían permitir observar su formación.

Contents

List of Figures

Chapter 1

Introduction

1.1 Nanotechnology

In his famous speech "There is plenty of room at the bottom" in 1959, Richard Feynman discussed how to manipulate and control things on a small scale in order to achieve electronic and mechanical systems with atomic sized components [Feynman1960]. He concluded that the development of technologies to construct such small systems would be interdisciplinary, combining fields such as physics, chemistry and biology, and would offer a new world of possibilities that could radically change the technology around us. Today, Feynman's vision is generally known as *Nanotechnology*: a useful cross disciplinary technology aiming at control at the atomic scale [Taniguch1974, Drexler1981]. This technology has the potential to create a new Industrial Revolution that will have profound impact on society and everyday life, comparable to electricity or information technology [Ramsden2009]. Nanotechnology is very diverse, it ranges from extensions of conventional device physics to completely new approaches based upon molecular self-assembly. From developing new materials with dimensions on the nanoscale to investigating whether we can directly control matter on the atomic scale. It entails the application of fields of science as diverse as surface science, organic chemistry, molecular biology, semiconductor physics, microfabrication, and a long etc. Nanotechnology may be able to create many new materials and devices with a vast range of applications, such as in medicine, electronics, biomaterials and energy production [Schaefer2010, Serena2010, Joachim2009].

1.1.1 Size effects

It has long been understood that significantly reducing the size of a structure can have dramatic implications for its properties, behaviour and potential applications.

For instance, the reduction in size of crystalline structures will ultimately mean that physical principles important to atoms, but normally negligible in bulk, begin to increase in importance [Goddard 2007]. The size reduction of mechanical components and particularly electronic components, occurring over the past few decades, has generated intense interest in understanding the unusual behaviour of very small structures.

Size effects become important when at least one dimension of a solid is reduced to the order of hundreds of atoms -the length scale of nanometers. The unique properties of nanostructures can be roughly separated into two primary categories: surface-related effects and quantum confinement effects. Surface effects arise because atoms at the surface of a crystalline solid experience a different chemical environment than other atoms, changing their behaviour. In bulk materials the proportion of surface atoms to bulk atoms is entirely negligible, and processes that take place at the surface of a material are usually of little consequence to the behaviour of the material as a whole. However, the surface-to-volume ratio of a structure on the nanoscale is considerably higher. High enough that surface effects often cannot be ignored. The increased reactivity of the surface compared to the rest of the material reduces the inertness of materials with high surface area. As well, the structure of the solid state can change somewhat to accommodate the high proportion of surface atoms, ultimately decreasing the stability of the crystal [Shchukin2004].

Quantum effects occur when the wavelength of an electron in a sample material is of the same order as a dimension of the sample. This limits the motion of the electron in the sample, which becomes quantized in that confining dimension. The density of states of the electrons is then determined by the number of dimensions in which electrons are quantized [Weisbuch1991].

As the understanding of the unique properties of nanostructures increases, so does the interest in and potential of practical applications that take advantage of these properties. To date, device components have been fabricated in laboratory settings that demonstrate the possibilities available. However, the transition from promising science to practical technology requires an even greater understanding and control of the function and effects of nanoscale structures. Since the properties and functions at the nanoscale depend so strongly on the structure, reliable, reproducible and controlled means of fabricating such structures are necessary.

1.1.2 Nanoelectronics

The branch of nanotechnology that develops electronic components in the nanoscale is usually refered to as *nanoelectronics*. Specifically, by electronics we mean the handling of complicated electrical wave forms for communicating information (as in cellular phones), probing (as in radar) and data processing (as in computers). Semiconductor electronics has seen a sustained exponential decrease in size and cost and a similar increase in performance and level of integration over the last forty years. This trend was predicted by Gordon E. Moore in 1965 [Moore1998]. The silicon roadmap is laid out for the next ten years [Arden2010]. After that, either economical or physical barriers will pose a huge challenge. The former is related to the difficulty of making a profit in view of the exorbitant costs of building the necessary manufacturing capabilities if present day technologies are extrapolated. The latter is a direct consequence of the shrinking device size, leading to physical phenomena impeding the operation of current devices. Quantum and coherence effects, high electric fields creating avalanche dielectric breakdowns, heat dissipation problems in closely packed structures as well as the non-uniformity of dopant atoms and the relevance of single atom defects are all obstacles along the current road of miniaturization [Peercy2000]. These phenomena are characteristic for structures a few nanometers in size. However, instead of being viewed as an obstacle to future progress, they might form the basis of post-silicon information processing technologies. Actually it is not even clear wheter electrons will be the method of choice for signal processing or computation in the long term. Quantum computing, spin electronics, optics, DNA biocomputing, or even computing based on (nano-) mechanics are actively being discussed. Nanoelectronics thus needs to be understood as a general field of research aimed at developing an understanding of the phenomena characteristic of nanometer sized objects with the aim of exploiting them for information processing purposes [Landauer1968].

Currently the most active field of research in nanoelectronics is the fabrication and characterization of individual components that could replace the macroscopic silicon components with nanoscale systems [Iniewski2010]. Examples are molecular diodes, single atom switches or the increasingly better control and understanding of the transport of electrons in quantum dot structures. A second field with substantial activity is the investigation of potential interconnects. Here, mostly carbon nanotubes, graphene, and metallic or self-assembled organic structures are being investigated. Among them, metallic nanowires are also subject of an increasing interest.

1.2 Nanowires

Nanowires are usually defined as structures that have a lateral size constrained to tens of nanometers or less and an unconstrained longitudinal size. Actual realizations of nanowires show aspect ratios of the order of 10-100 (length/diameter). At these scales, both surface and quantum mechanical size effects are important. Hence such wires are also known as *quantum wires*. Nanowires with a variety of physical properties may be constructed. Depending on their atomic species, they may have the properties of an insulator (e.g., SiO2, TiO2), a semiconductor (e.g., InP, Si, GaN, etc.) or a metal (e.g., Ni, Pt, Au) [Hashim2011].

For instance, semiconductor nanowires have unique electrical and optical properties that make them candidates to be used as building blocks in nanoscale devices. Because of their low dimensionality they exhibit quantum confinement effects: Narrowing the wire's diameter increases its band gap, compared to the bulk material. Today semiconductor nanowires are increasingly used in electronic devices including field-effect transistors, sensors, detectors and light-emitting diodes. More complicated devices are expected soon, requiring new and improved ways of growing such wires in a reproducible way at industrial scales.

Another interesting property is that some nanowires present *ballistic* conduction [Fazio2003]. In normal conductors, electrons collide with the atomic nuclei. This slows down the electrons as they travel and creates heat as a byproduct. However, when nanowires are of a length comparable with the electronic *mean free path*, the electrons can travel through the conductor without collisions. These nanowires could conduct electricity efficiently without the byproduct of intense heat. For the particular case of metallic nanowires, at room temperature, they present a typical mean free path value of few tens of nanometers, and as consequence, nanowires with sizes below this values are expected to show ballistic effects.

1.2.1 Experimental techniques of fabrication

Before we go further in the discussion of the physical properties of nanowires, here we briefly describe the experimental methodologies used in their fabrication. There are two basic approaches to obtain nanowires: top-down and bottom-up approach. In a top-down approach a large piece of material is cut down to small pieces through different means such as lithography and electrophoresis. Whereas in a bottom-up approach the nanowire is synthesized by the combination of constituent ad-atoms.

1.2.1.1 Top-down approach

In a top-down process ion-beam, scanning-probe or electron-beam lithography are used to shape a nanowire from a bulk sample of material. This is the most flexible method with regard to wire shape. Nanowires formed in this manner typically are small and often undergo various reorganizations once removed from the bulk in response to their high surface-to-volume ratio. This high surface-to-volume ratios, and the resulting high surface energies, have been shown to drive the reorientation of gold thin films from (100) to (111) when film thicknesses were less than eight atomic layers [Diao2003]. In gold nanobridges, cut from (100) thin films with [001] orientation axes and thicknesses smaller than 2 nm, reconstruction occurs in hexagonal prism shapes with [110] axes and (111) lateral surfaces [Diao2003]. This feature was investigated using atomistic simulations showing that gold nanowires with similar configurations and cross-sectional areas less than 1.83nm×1.83nm spontaneously reorganized into body-centered-tetragonal (BCT) structures [Diao2003]. Nanowires with larger sections did not exhibit any transformation.

Suspended nanowires: The top-down approach produces so-called *suspended nanowires*. This term applies to nanowires produced in a high-vacuum chamber and that are attached to two atomic reservoirs at their ends. To produce these type of nanowires, a larger wire is held at its longitudinal extremities. Then a thinner wire is "sculpted" from it either by chemical etching or by bombardment with highly energetic ions [Kondo1997]. The Mechanically Controllable Break Junction (MCBJ) method allows a precise control of this stretching process [Krans1995]. In MCBJ, the supporting ends of a sculpted nanowire are attached to a flexible substrate as seen in figure 1.1. By bending this substrate, a slight elongation of the nanowire happens, which allows a precise controlled way to stretch it. Sucessive cycles of breaking and formation of nanocontacts are performed just by bending and un-bending of the substrate. Another way to produce suspended nanowires is by indenting the tip of a Scanning Tunneling Microscope (STM) in the surface of a metal near its melting point and then retracting it, as schematically depicted in figure 1.2 [Yanson1998].

1.2.1.2 The bottom-up approach

The bottom-up fabrication of nanowires can produce numerous nearly single-crystal nanowires with high aspect ratios (length to width). Here we briefly mention some of the most used techniques.

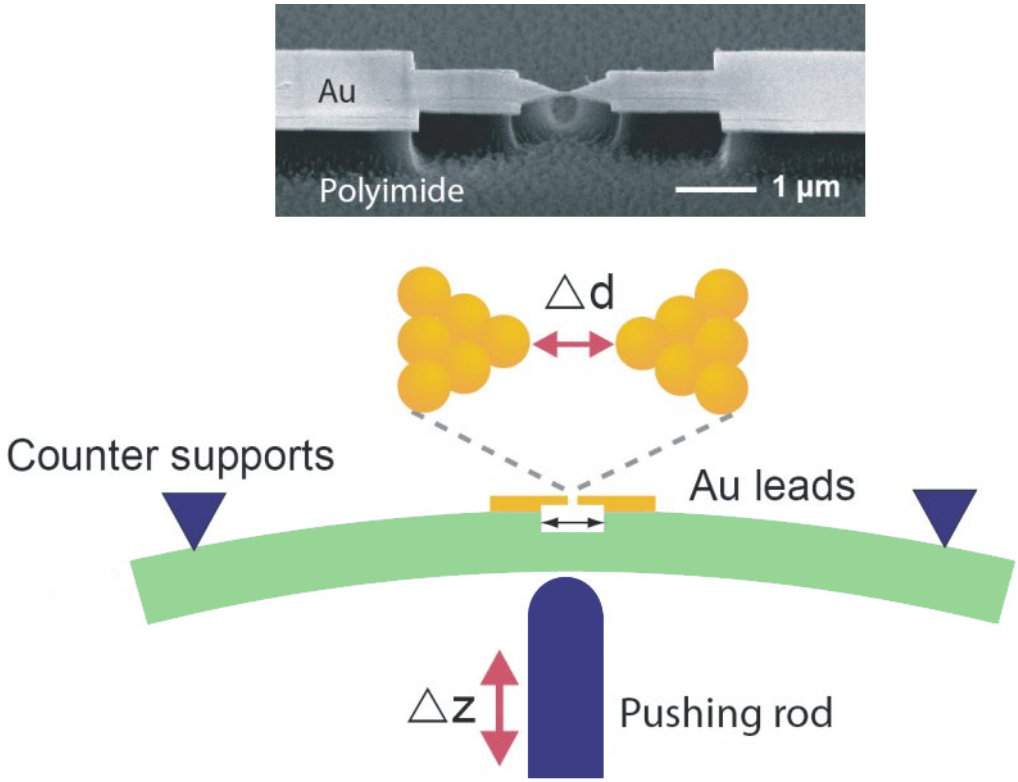

Figure 1.1: Scheme of the Mechanically Controllable Break Junction (MCBJ) technique. While bending the flexible substrate using a push-rod, a metallic constriction can be broken up to even form a pair of atomic sized contacts. The top SEM picture shows a free-standing Au constriction on top of a polyimide-coated stainless steel flexible substrate. (Image based on the original picture at http://www.nanoelectronics.ch/research/molecular.php)

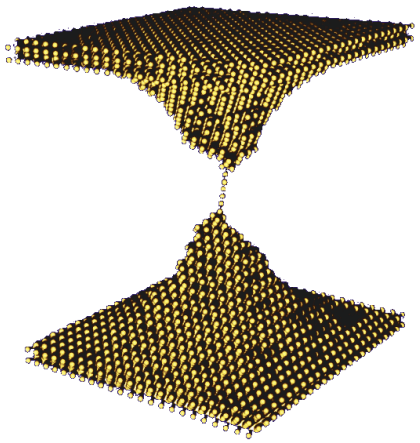

Figure 1.2: Simulation of the formation of a one atom Au chain from a STM indentation-retraction cycle. (Image based on the original illustration at http://www.physics.leidenuniv.nl/sections/cm/amc/goldchains/article_main.htm).

VLS: A common technique for creating nanowires is the Vapor-Liquid-Solid (VLS) synthesis method [Steiner2004]. This technique uses as source material either laser ablated particles or a feed gas (such as silane). The source is then exposed to a catalyst. For nanowires, the best catalysts are liquid metal (such as gold) nanoclusters, which can either be purchased in colloidal form and deposited on a substrate or self-assembled from a thin film by dewetting. This process can often produce crystalline nanowires in the case of semiconductor materials. The source enters these nanoclusters and begins to saturate it. Once supersaturation is reached, the source solidifies and grows outward from the nanocluster. The final nanowire's length can be adjusted by simply turning off the source. Even compound nanowires with super-lattices of alternating materials can be created by switching sources while still in the growth phase.

Solution-phase synthesis: Nanowires of many types of materials can be grown in solution. Solution-phase synthesis has the advantage that it can be scaled-up to produce very large quantities of nanowires as compared to methods that produce nanowires on a surface. The polyol synthesis, in which ethylene glycol is both solvent and reducing agent, has proven particularly versatile at producing nanowires of Pb, Pt, and Ag [Sun2003, Coskun2011].

Template synthetic method: Long metallic nanorods may be produced by utilizing electrochemical replication of cylindrical pores in nonconductive porous mem-

branes, a technique also known as the template synthetic method [Hurst2006]. Using this method, single-crystal gold wires have been found to grow epitaxially primarily along the [111] direction with fewer than 10% showing [110], [100] and [112] orientations [Tian2003]. Primarily, these wires exhibit characteristic defects such as stacking faults, twin boundaries, and surface defects or surface steps. Given the current difficulties with manipulating nanowires on the dimensional scale of a few to tens of nanometers, there has been only limited experimental mechanical testing of these nanostructures [Kline2006].

To this point, most simulations have been performed to investigate the unique, smallest structures created by top-down processing, including nanocontacts, single atom chains and helical or shell-like nanowires. The simulations reported in the literature have been mostly for nanowires aligned along the [100], [110] and [111] crystallographic directions with rectangular cross-sectional shapes in order to investigate the effect of low index surfaces. These wires are generally defect free and always maintain simplified rectangular or rhombohedral geometries.

1.2.2 Welding

One of the biggest steps towards incorporation of nanowire technology into industrial applications is the capability of welding nanowires together. This has been achieved in the past few years by placing a sacrificial metal nanowire adjacent to the ends of the pieces to be joined (using manipulators of a scanning electron microscope). Then an electric current is applied, which fuses the wire ends. This technique has been applied to nanowires as small as 10 nm [Peng2009]. Another recent work shows that single-crystalline ultrathin gold nanowires with diameters $\sim 3-10$ nm can be "cold-welded" together within seconds by mechanical contact alone, and under remarkably low applied pressures (unlike macro- and micro-scale cold welding process) [Lu2010]. High-resolution transmission electron microscopy and in situ measurements reveal that the welds are nearly perfect, with the same crystal orientation, strength and electrical conductivity as the rest of the nanowire. The high quality of the welds is attributed to the nanoscale sample dimensions, oriented-attachment mechanisms and mechanically assisted fast surface diffusion. Nanowire welds were also demonstrated between gold and silver, and silver and silver nanowires (with diameters $\sim 5-15$ nm) at near room temperature, indicating that this technique may be generally applicable for ultrathin metallic nanowires. Combined with other nano- and microfabrication technologies [Zhong2003, Huo2008], cold welding is anticipated to have

potential applications in the future bottom-up assembly of metallic one-dimensional nanostructures.

1.3 Metallic nanowires

During the last two decades, the study of the properties of metallic nanowires has been one of the keystones for the development of nanotechnology [Serena1996, Agraït2003]. This is due to the relevance of their electrical and mechanical properties in fundamental knowledge as well as for the future development of technological applications. Many experimental studies have addressed the creation, stabilization and deformation of metallic nanowires in order to understand their mechanical, structural and electron transport properties [Untiedt1997, Huang2008, Serena1997].

These experimental studies have shown that electron transport through metallic nanowires is in the ballistic regime [Muller1992, Muller1996]. On the other hand, due to their reduced traversal dimensions, quantum effects arise. As a result, the conductance through these nanowires is quantized [CK1997]. STM experiments have allowed to measure the transition from tunnel to contact at room temperature and atmospheric pressure. The current between tip (gold) and sample (gold) shows quantization just before the contact breaks [Pascual1993, Pascual1995]. Other interesting features of metallic nanowires have to do with their structural properties. It has also been observed that ultra-thin nanowires abandon their bulk-like crystal structure and prefer to adopt hellical or disordered structures in order to minimize their surface energy [Gülser1998, Kondo2000].

Most of these experimental works have been carried out in suspended metallic nanowires, as those formed in MCBJ or STM setups. However, with the advent of powerful computational resources and the achievement of realistic descriptions of the atomic interactions, it has been possible to reproduce *in silico*[1] many of the properties of metallic nanowires. An important example are computer simulations on the breaking process of metallic nanowires. These simulations have provided a better understanding of the time evolution of the conductance as the nanowire breaks, through cross-section histograms $H(S_m)$ analogous to the conductance histograms $H(G)$ obtained in experiments [Medina2003, GM2008b]. An important part of these simulation studies has been done using Molecular Dynamics (MD) algorithms, which

[1] *In silico* is an expression used to mean "performed on computer or via computer simulation." The phrase is analogous to the Latin phrases *in vivo* and *in vitro* which are commonly used in biology and refer to experiments done in living organisms and outside of living organisms, respectively.

allow to elucidate how this formation-elongation-breakage occurs. Furthermore, MD simulations allow the accurate determination of the different structures that appear during the final stages of the breaking process. Getting insight of such structures is a crucial matter since they control the electron transport through the nanowire, allowing a comparison with the experimental data.

However, the comparison between experimental results and MD computational simulations usually requires an extra ingredient: the use of statistics. In general, the study of nanoscale systems demands a statistical approach. This becomes more evident in electron transport studies, since little modifications of the atomic positions results in large conductance variations. It is necessary to statistically address the study of many nanowire breaking events, mimicking the experimental indentation-retraction cycles. In these cases, semiclassical approximations based in accurate interatomic potential are usually used since they are much less demanding of computational resources than sophisticated but time consuming ab initio methods [Jaffe2000, GM2008a].

MD simulations have not only proved successful in accounting for complex properties of many nanowires during the breaking process, allowing to detect the presence of ultranarrow structures as monomers, dimers and long atomic chains [Bahn2001] that govern the electrical properties of the nanowire just before its breaking. MD techniques have also been used to demonstrate the formation of new non-crystalline structures, as helical or weird structures [Gülser1998], not corresponding to the initial FCC or BCC crystallographic disposition of the metal under study. This is also the case of the icosahedral or pentagonal nanowires formed by subsequent staggered parallel pentagonal rings (with a relative rotation of $\pi/5$) connected with single atoms [Mehrez1997, GM2008c, Peláez2009], showing a characteristic $-5-1-5-1$ ordering that have been confirmed experimentally for some metallic species [Gonzál2004].

1.4 Importance of simulations in the nanoscale

Computer simulations have a valuable role to play in providing essentially exact results for problems in statistical mechanics which would otherwise only be soluble by approximate methods, or might be quite intractable. In this sense, computer simulation may be regarded as a benchmark of theories. The results of computer simulations may also be compared with those of real experiments. In the first place, this is a test of the underlying model used in a computer simulation. Eventually, if the model is a good one, the scientist running the simulations hopes to offer insights to the experimentalist, and assist in the interpretation of new results. This dual role

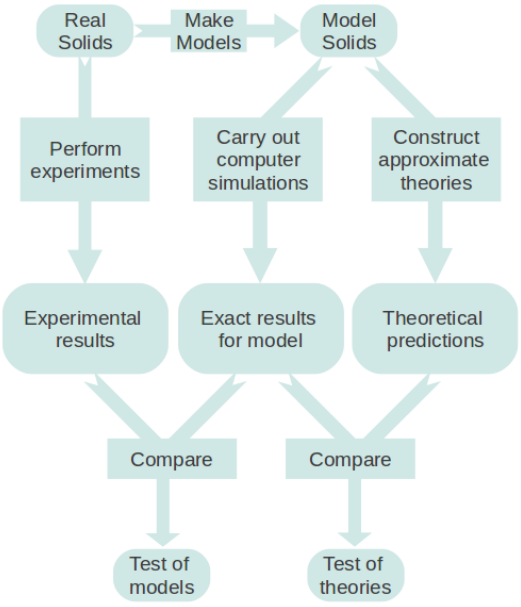

Figure 1.3: Connection between experiments, theory and computer simulation. (Based on figure 1.2 of [Allen1999]).

of simulation, as a bridge between models and theoretical predictions on the one hand and between models and experimental results on the other, is illustrated in figure 1.3. Because of this connecting role, and the way in which simulations are conducted and analysed, these techniques are often termed "computer experiments" [Allen1999].

Computer simulation provides a direct route from the microscopic details of a system (the masses of the atoms, the interactions between them, molecular geometry, etc.) to macroscopic properties of experimental interest (equations of state, transport coefficients, structural order parameters, and so on). As well as being of academic interest, this type of information is technologically useful. It may be difficult or impossible to carry out experiments under extreme values of temperature, pressure, radiation, etc., while a computer simulation of the material in, say, a shock wave, a high-temperature plasma, a nuclear reactor, or a planetary core, would be perfectly feasible. Quite subtle details of molecular motion and structure, for example in heterogeneous catalysis, fast ion conduction, or enzyme action, are difficult to probe experimentally, but can be extracted readily from a computer simulation. Finally, while the speed of molecular events is itself an experimental difficulty, it presents no hindrance to simulations. A wide range of physical phenomena, from the molecular scale to the galactic, may be studied using some form of computer simulation.

1.5 About this thesis

In the last decade our research group at the Instituto de Ciencia de Materiales de Madrid (ICMM-CSIC) has actively participated in leading research in the field of structural and electronic properties of metallic nanocontacts [Serena1997, Hasmy2001, FP2002, Medina2003, Hasmy2005, Díaz2006]. A recent PhD thesis in our group by Guerrero [Guerrero2010] has addressed the breaking process of metallic nanocontacts, focusing on the appearence of "magic" configurations in the nanocontact narrowest cross section. As a natural continuation of these works, in the present thesis we have carried out computer simulations in order to study other aspects of metallic nanowires, including their structural stability, elastic properties and the appearence of non-crystalline structures during their breaking process [GM2005a, Peláez2006, Peláez2007, GM2008a, GM2008b, GM2008c, GM2008d, Peláez2009, Peláez2010].

We have focused on nanowires of three metallic species: Al, Cu and Ni. The choice of these materials is based on their great technological importance because of their potential applications in nanoscale electronics, photonics, biological and chemical sensors, resonators, etc. Besides, there are interatomic many-body semi-empirical potentials available in the literature to describe properly the dynamics of these atomic species in the nanoscale. Moreover, our choice comprehends materials with different electronic valences (electronic structures for Al, Ni and Cu are [Ne]$3s^2 3p^1$, [Ar]$3d^8 4s^2$ and [Ar]$3d^{10} 4s^1$, respectively) including one with magnetic properties (Ni).

Chapter 2 describes the methodological aspects of the work reported in the remainder of this thesis. In particular we address the role of interatomic potentials in the modelling of solid state systems by computer simulations. Then the Molecular Dynamics (MD) and Conjugate Gradients (CG) techniques are detailed. These two methodologies are among the most used in the literature when it comes to describing the time evolution or equilibrium structures (respectively) of atomic and molecular structures. Also other methodologies not used in this thesis are shortly described for the sake of completeness.

As above mentioned, there are available many-body semi-empirical interatomic potentials to describe properly the energetics and dynamics of Al, Ni and Cu in the nanoscale [Mishin1999, Mishin2001]. These potentials belong to the family of so-called Embedded Atom Method (EAM) potentials. A detailed description of these potentials is presented in chapter 3. This chapter also includes a comparison between the most used EAM potentials along with ab initio results to decide which of these approaches is more suitable to be used in our simulations.

In chapter 4 we present results on the equilibrium configuration of FCC nanowires. By MD simulations at 4 K, the optimal structures of nanowires with different crystalline orientations, shapes and thicknesses are obtained. This comprehensive study allows to evaluate dependence of the nanowire's cohesive energy with its thickness. From these results we calculate the energetic cost associated to the presence of sharp edges in this nanowires.

Starting from the obtained equilibrium configurations of FCC nanowires, in chapter 5 we address the nanowires' stress response to strain in the elastic regime. This study comprehends the calculation of the Young's modulus E and its dependence with the nanowire crystalline orientation, cross-section shape and thickness. The appearence of non-linearities in the stress-strain response is also discused.

Chapter 6 addresses the study of the breaking process of these nanowires. By means of MD simulations at different temperatures, we monitor the time evolution of the minimum nanowire cross section S_m during the elongation. We have carried out a statistical study by accumulating hundreds of such curves and constructed minimum cross section histograms $H(S_m)$ in analogy with the conductance histograms obtained experimentally. This statistical analysis also included nanowires with different sizes and crystallographic orientations, providing more insight on the influence of these parameters on the breaking dynamics.

We have observed that in the breaking process of Al, Ni and Cu nanowires some conditions favor the spontaneous formation of long pentagonal (a.k.a. icosahedral) chains. In chapter 7 we examine this process, as well as determine the temperature, crystalline orientation and nanowire size conditions that statistically exhibit higher probabilities of producing such chains.

Two appendices are at the end of this thesis. In the first one we present a brief summary of the topics that we believe should be addressed in future works by our group. In the second appendix a short CV of the candidate is presented. It contains a list of the scientific publications derived from this thesis, as well as the conferences in which its main results have been presented, either as oral or as poster presentations.

Part I

Methodology

Chapter 2

Simulation tools

This chapter aims at providing a comprehensive account of the methodologies used through this thesis. The main ingredient of a simulation is to define a model for the physical system. In general, this amounts to choosing the *interatomic potential*. This issue is addressed in the first section. Then we show in detail the two most used computational methodologies in this thesis: Molecular Dynamics and structural optimization via Conjugate Gradients. Later, whithin "other tools" we present a brief overview of some other relevant computational techniques, like Monte Carlo, or optimization via Simulated Annealing, which although used frequently in other works, we do not use in this thesis, and we mention here just for completeness.

2.1 Interatomic potentials

In computer simulation, forces are derived from a potential energy function V, which depends on the particles' coordinates $\mathbf{r}_i$:

$$\mathbf{F}_i = -\nabla V(\mathbf{r}_1, ..., \mathbf{r}_N) \tag{2.1}$$

The problem of modelling a material relies on our capability to describe an accurate potential function $V(\mathbf{r}_1, ..., \mathbf{r}_N)$ for that material. However, to find such a function we must keep in mind that the actual material is controlled by the laws of quantum mechanics rather than classical mechanics, and that electrons play the major role in determining the bonding properties of the system. So, the problem of finding an appropriate potential energy function is one of the key issues in computer simulations.

2.1.1 The Born-Oppenheimer approximation

A system of interacting atoms is really made up of nuclei and electrons which interact with each other. The true non-relativistic Hamiltonian for this sytem may be written

as:

$$H = \sum_i \frac{P_i^2}{2M_i} + \sum_n \frac{p_n^2}{2m} + \frac{1}{2}\sum_{ij} \frac{Z_i Z_j e^2}{|\mathbf{R}_i - \mathbf{R}_j|} + \frac{1}{2}\sum_{nn'} \frac{e^2}{|\mathbf{r}_i - \mathbf{r}_j|} - \sum_{in} \frac{Z_i e^2}{|\mathbf{R}_i - \mathbf{r}_n|} \quad (2.2)$$

where indexes i,j run on nuclei, n and n' on electrons, $\mathbf{R}_i$ and $\mathbf{P}_i$ are, respectively, positions and momenta of the nuclei, $\mathbf{r}_n$ and $\mathbf{p}_n$ are positions and momenta of the electrons, Z_i is the atomic number of nucleus i, M_i its mass and m the electron mass. The first two terms can be easily recognized as the kinetic energies of nuclei and electrons. The remainder three terms correspond to the coulombic interaction between pairs of nuclei, pairs of electrons and nucleus-electron pairs respectively. In principle one should solve the Schrödinger equation for the total wave function $\Psi(\mathbf{R}_i, \mathbf{r}_i)$ and then everything about the system is known, since all the electronic and mechanical properties depend on the electronic structure of the system.

However, this is impossible to be solved in practice, and approximation schemes have to be employed. In 1927 Born and Oppenheimer [Born1927] noted that nuclei are much heavier than electrons, and move on a time scale which is about two orders of magnitude larger than that of the electrons:

$$\frac{\omega_{el}}{\omega_{nuc}} \sim \sqrt{\frac{M}{m}} \sim 100 \quad (2.3)$$

It is therefore possible to decouple the nuclear movement from the electronic movement, and factorize the total wavefunction as

$$\Psi(\mathbf{R}_i, \mathbf{r}_n) = \chi(\mathbf{R}_i)\Phi(\mathbf{r}_n; \mathbf{R}_i) \quad (2.4)$$

where $\chi(\mathbf{R}_i)$ is the wavefunction that describes the nuclei, and $\Phi(\mathbf{r}_n; \mathbf{R}_i)$ is the wavefunction that describes the electrons (depending parametrically on the positions of the nuclei).

With these assumptions, the Born-Oppenheimer approximation reformulates the problem in terms of two steps. In the first step the nuclear kinetic energy is neglected, that is, the nuclear kinetic energy operator $T_n = \sum_i {}^{P_i^2}/_{2M_i}$ is subtracted from the total Hamiltonian (2.2). In the remaining electronic Hamiltonian H_{el} the nuclear positions enter as parameters

$$H_{el} = \sum_n \frac{p_n^2}{2m} + \frac{1}{2}\sum_{ij} \frac{Z_i Z_j e^2}{|\mathbf{R}_i - \mathbf{R}_j|} + \frac{1}{2}\sum_{nn'} \frac{e^2}{|\mathbf{r}_n - \mathbf{r}_{n'}|} - \sum_{in} \frac{Z_i e^2}{|\mathbf{R}_i - \mathbf{r}_n|}. \quad (2.5)$$

The electron–nuclei interactions are not removed and the electrons still "feel" the Coulomb potential of the nuclei clamped at certain positions in space. The following

electronic Shrödinger equation is solved:

$$H_{el}(\mathbf{r}_n;\mathbf{R}_i)\Phi(\mathbf{r}_n;\mathbf{R}_i) = E_{el}\Phi(\mathbf{r}_n;\mathbf{R}_i) \tag{2.6}$$

where the electronic energy eigenvalues E_{el} depend on the chosen positions $\mathbf{R}_i$ of the nuclei.

In the second step of the Born-Oppenheimer approximation the nuclear kinetic energy T_n (containing partial derivatives with respect to the components of $\mathbf{R}_i$) is reintroduced and the Schrödinger equation for the nuclear motion

$$\left[\sum_i \frac{P_i^2}{2M_i} + E_{el}(\mathbf{R}_i)\right]\chi(\mathbf{R}_i) = E\chi(\mathbf{R}_i). \tag{2.7}$$

is solved. The eigenvalue E is the total energy of the system, including contributions from electrons and nuclear motion (vibrations and overall rotation and translation of the system).

The electronic energy eigenvalue $E_{el}(\mathbf{R}_i)$ will depend parametrically on the coordinates of the nuclei; we call this quantity the *interatomic potential* $V(\mathbf{R}_i)$. Once found, this quantity enters equation 2.7, which will give the forces felt by the nuclei. Note that in this equation there are no electronic degrees of freedom: all the electronic effects are incorporated in $V(\mathbf{R}_i)$. It is customary to replace this Schrödinger equation with a Newton equation, that is, to move the nuclei classically.

2.1.2 Using the classical regime in atomistic simulations

This classical treatment of the atoms is valid when the system's de Broglie thermal wavelength

$$\Lambda = \sqrt{\frac{2\pi\hbar^2}{Mk_BT}} \tag{2.8}$$

is considerably smaller than the mean nearest neighbor separation ($\Lambda \ll d_{nn}$) of the system [Hansen2006]. Here M is the atomic mass and T is the temperature. For instance, in a simulation of Al at 100K, $\Lambda = 0.336$ Å and the nearest neighbor distance is an order of magnitude larger ($d_{nn} = 2.86$ Å). So, when lighter elements such as Li or Ar are considered, or when the system temperature is lowered, the computer simulation results should be interpreted with caution.

If we are to describe the properties of the system with some degree of accuracy, one should use some approximations to solve equation 2.6. This is what *ab initio* methods do. However, solving the electronic Schrödinger equation requires massive

computer resources, and quite sets limits on the maximum size of the system and on the simulation time.

Due to these practical limitations of *ab initio* methods (which we shall explore in detail later), in this thesis we focus on the *classical* approach, where we get rid completely of electronic degrees of freedom and move nuclei (atoms) according to some potential function $V(\mathbf{R}_i)$ whose analytical form we specify in advance. This way we must select functional forms which mimic the behavior of the "true" potential in realistic ways for specific materials. This process of constructing a potential involves two steps: 1) Selecting an analytical form for the potential, and 2) Finding an appropriate parameterization for these functions.

A variety of techniques have been used over the years to this end. In any case, potentials must be designed with a "range of applicability" in mind. Due to the vast differences in the electronic structure, it would probably be too ambitious to try modelling a bulk metal and a diatomic molecule of the same element with the same potential: the environment is dramatically different. However, it could be feasible to model simultaneously a bulk and a surface environment, where the environment differs (due to the reduced coordination of the atoms at the surface) but not as dramatically as in the previous example. The ability of a potential to work properly in different environments is called *transferability*. When using a potential, care must be taken on its transferability properties. Simulation results should be critically interpreted when obtained in unusual conditions (like very low coordinations, very high temperature o very high pressure).

2.1.3 Pair potentials vs. many-body potentials

One of the most commonly used interatomic potentials is the one proposed by Lennard-Jones (LJ) [LJ1924]. In this approximation, the potential energy associated to a pair of atoms separated a distance r is

$$\phi_{LJ}(r) = 4\epsilon \left[\left(\frac{\sigma}{r}\right)^{12} - \left(\frac{\sigma}{r}\right)^{6} \right]. \tag{2.9}$$

This potential has an attractive tail at large r, reaching a minimum around 1.122σ and it is strongly repulsive at shorter distances, passing through 0 at $r = \sigma$ and increasing steeply as r is decreased further. This potential function is depicted in figure 2.1.

In the LJ approximation, the term $\sim 1/r^{12}$, dominating at short distance, models the repulsion between atoms when they are brought very close to each other. Its

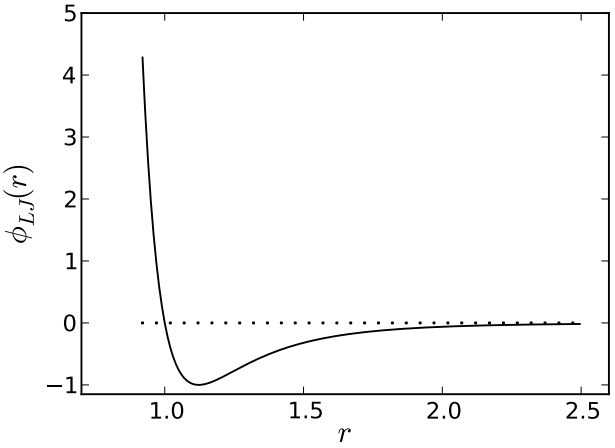

Figure 2.1: Functional form of the Lennard-Jones potential. This function has been normalized so that $\epsilon = 1$ and $\sigma = 1$.

physical origin is related to the Pauli principle: when the electronic clouds surrounding the atoms start to overlap, the energy of the system increases abruptly. The exponent 12 was chosen exclusively on a practical basis: equation (2.9) is particularly easy to compute. In fact, on physical grounds an exponential behaviour would be more appropriate.

The term $\sim 1/r^6$, dominating at large distance, constitutes the attractive part. This is the term which provides cohesion to the system. A $1/r^6$ attraction is originated by van der Waals dispersion forces, originated by dipole-dipole interactions, in turn due to fluctuating dipoles. These are rather weak interactions, which however, dominate the bonding character of closed-shell systems, that is, rare gases such as Ar or Kr. Therefore, these are the materials that a LJ potential could mimic fairly well. The parameters ϵ and σ are chosen to fit some of the physical properties of the material.

Obviously a LJ potential is not at all adequate to model situations with open shells, where strong localized bonds may form (as in covalent systems), or where there is a delocalized "electron sea" surrounding the ions (as in metals). In these systems the two-body interactions scheme fails dramatically.

Considering for instance noble metals, one can easily identify a few indicators of many-atom effects, which we summarize in table 2.1 (extracted from [Ercoless1997]), where experimental data for a few metals are compared with Lennard-Jones data (but other pair potentials yield similar results).

$E_c/k_B T_m$ is the ratio between the cohesive energy and the melting temperature. This ratio is about 30 in metals, and about 10 in two-body systems. This result

Property	Cu	Ag	Pt	Au	LJ
E_c/k_BT_m	30	28	33	33	13
E_v/E_c	0.33	0.36	0.26	0.25	~ 1
C_{12}/C_{44}	1.5	1.9	3.3	3.7	1

Table 2.1: Comparison of the experimental values and results from Lennard-Jones simulations at describing three physical observables in metals (see text for definitions of these observables).

indicates that metals exhibit some extra cohesion with respect to pairwise systems, which is less effective than two-body forces in keeping the system in the crystalline state.

E_v/E_c is the ratio between the vacancy formation energy and the cohesive energy. This number is between 1/4 and 1/3 in metals, but about 1 in two-body systems. When forming a vacancy in a crystal structure with coordination number Z, one has to pay the energy E_v to decrease coordination from Z to $Z-1$ for Z atoms. In contrast, E_c is the energy to pay to decrease the coordination of a single atom from Z to 0. In a two-body model, where a fixed energy contribution is attached to bonds bewteen pairs of atoms, these two energies are the same as they are both associated to the breaking of Z bonds. But this is not what happens in real metals.

C_{12}/C_{44} is the ratio between two elastic constants of a cubic crystal (all the systems in the table are FCC). This ratio is exactly 1 in two body systems: this is the so-called *Cauchy relation* which can be demonstrated analytically [Daw1984]. But deviations in metals are very common. The high value in Au is to be related to its well-known high ductility and malleability.

If one consider semiconductors, deviations from a two-body behavior are even worse. For instance, silicon undergoes a series of structural phase transitions (from tetrahedral to β-tin to simple cubic to FCC) under pressure. This indicates that the energy difference between this structures is not too large. In other words, the cohesive energy is nearly independent upon coordination, while a two-body model should favor the more packed structures, which have more bonds.

Due to these and other shortcomings [Ercoless1988], since the mid '80s researchers started to figure out how to improve the two body approach by incorporating realistic many-atom effects in potentials. As result, a significant progress was made by the develpment of many-atom potentials for metals based on the concept of *density*, or *coordination*, as the key variable to consider. The main physical point to model is that bonds become weaker when the local environment becomes more crowded: another consequence of the Pauli principle. So, a plot of the cohesive energy as a function

of coordination should not be decreasing linearly as in two-body systems, but should exhibit a positive curvature: decreasing faster when coordination is low, and more slowly as coordination increases.

A possible form for the attractive part of the potential (the repulsive one being still conveniently treated by a pairwise law) can be qualitatively obtained by working out a connection with the tight-binding formalism [Ashcroft1976]. The result of this argument suggests a form for the energy of an atom i

$$E_i \propto \sqrt{\sum_j h^2(r_{ij})} \propto \sqrt{Z_i} \tag{2.10}$$

where $h(r_{ij}) = \langle i|H|i\rangle$ are the overlap integrals between wave functions of atom i and its neighbors. In the tight-binding formalism the orbitals are localized and these functions vanish beyond a certain cutoff distance.

The key result contained in 2.10 is that the energy is proportional to *the square root* of the coordination, rather than to the coordination itself as in two-body models. One can easily verify that such a scheme goes in the right direction in solving the problems associated with pairwise potentials in metals. For instance,

$$\frac{E_v}{E_c} \sim \frac{Z[\sqrt{Z} - \sqrt{Z-1}]}{\sqrt{Z}} \sim \frac{1}{2}, \tag{2.11}$$

and one can also verify that the Cauchy relation $C_{12} = C_{44}$ no longer holds.

Following this and other considerations, several schemes to construct many-atom potentials for metals were developed, all essentially based on an analytical form with the following general scheme:

$$V = \frac{1}{2} \sum_{\substack{i,j=1 \\ (j \neq i)}}^{N} \phi(r_{ij}) + \sum_{i=1}^{N} U(n_i) \tag{2.12}$$

where $\phi(r)$ is a two-body repulsive part, and $U(n)$ is a function giving the energy of an atom as a function of a "generalized coordination" n. This coordination n for a given atom is in turn constructed as a superposition of the contributions from neighboring atoms:

$$n_i = \sum_{\substack{j=1 \\ (j \neq i)}}^{N} \rho(r_{ij}) \tag{2.13}$$

where $\rho(r)$ is a short-ranged, decreasing function of the interatomic distance. Belonging to this scheme are the "glue" model [Ercoless1988], the Embedded Atom Method [Daw1993] (which we use in this thesis and will describe in detail in the next chapter)

and the Finnis-Sinclair (FS) potentials [Finnis1984]. Also a similar spirit is followed within the effective medium theory [Tinga1973]. Even if sharing the analytical form, these schemes differ vastly in the procedure used to build the three functions ($\phi(r)$, $\rho(r)$ and $U(n)$) constituting the model, often resulting in rather different parameterizations for the same material. Fitting is in fact the true key of the matter of building potentials.

To implement these potentials in a simulation program, one has to evaluate the forces

$$\mathbf{F}_i = -\sum_{j \neq i} \left(\phi'(r_{ij}) + \left[U'(n_i) + U'(n_j) \right] \rho'(r_{ij}) \right) \frac{\mathbf{r}_{ij}}{r_{ij}} \tag{2.14}$$

where $\phi'(r_{ij})$ and $\rho'(r_{ij})$ are derivatives of ϕ and ρ with respect to r evaluated at r_{ij}. $U'(n_i)$ is the derivative with respect to n evaluated at the coordination n_i. This calculation is only slightly more complex than that required for a two-body system. Energy and forces can still be obtained by using pair distances as the only input. No angular term or other 3-or-4-body terms are present. This allows to write very fast simulation programs. On the other hand, the lack of true angular forces makes it difficult to use these schemes to model metals where covalent effects in the bonding are important, for instance transition metals.

Semiconductors are even more challenging than metals. Consider for instance silicon. Its most stable phase is the diamond structure, which is very open and has a coordination number $N_c = 4$. However it changes rapidly to other structures when pressure is applied, which means that these are not too far in energy. Besides its liquid structure is a metal, and is more dense than the solid. These properties make finding potential functions that describe semiconductors an even more complex task. Some approaches are the Stillinger-Weber potential [Stilling1985], (in which the potential functions have angular terms that favor some preferable angles) and the Tersoff potential [Tersoff1988] (based on the concept of bond order).

2.1.4 Periodic boundary conditions

Computer simulations are usually performed on a small number of particles $10 \leq N \leq 10000$. The size of the system is limited by the available storage and, more crucially, by the processors performance and the design of the computational code. The time taken for a double loop used to evaluate the forces or potential energy is proportional to N^2. Special techniques may reduce this dependence to $\mathcal{O}(N)$ for very large systems. But the force/energy loop dictates inevitably the overall speed. So, smaller systems will always be less expensive. If we are interested in the properties

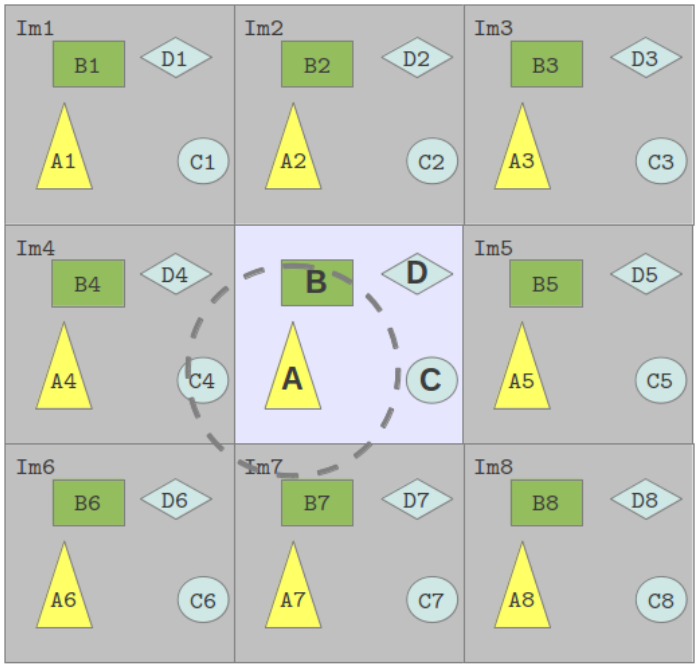

Figure 2.2: A bidimensional representation of a simulation box with its 8 image boxes.

of a very small cluster, or a microcrystal, the cohesive forces between the atoms may be sufficient to hold the system together unaided during the course of a simulation. However, there is an obstacle to simulate a bulk system due to the large fraction of molecules which lie on the surface of any small sample. For instance, for 1000 atoms arranged in a $10 \times 10 \times 10$ cube, 488 atoms are located on the cube faces. Whether or not the cube is surrounded by a containing wall, atoms on the surface will experience quite different forces than those atoms in the bulk. These finite size effects must be overcome when using cells for representing infinite systems.

The problem of surface effects can be overcome by implementing *periodic boundary conditions* [Born1912]. The cubic box is replicated throughout space to form an infinite lattice. In the course of the simulation, as a molecule moves in the original box, its periodic image in each of the neighbouring boxes moves in exactly the same way. Thus, as an atom leaves the central box through a given face, one of its images will enter through the opposite face. There are no walls at the boundary of the central box, and no surface atoms. This box simply forms a convenient axis system for measuring the coordinates of the N atoms. A two-dimensional version of such a periodic system is shown in figure 2.2. The duplicate boxes are labelled $Im1$, $Im2$, etc. As particle A moves through a boundary, its images, $A1$, $A2$, etc. (where the subscript specifies in which box the image lies) move across their corresponding boundaries. The number density in the central box (and hence in the entire system)

is conserved. It is not necessary to store the coordinates of all the images in a simulation. Just the atoms in the central box. When an atom leaves the box by crossing a boundary, attention may be switched to the image just entering into the simulation box through the opposite boundary.

It is important to consider if the properties of a small, infinitely periodic, system, and the macroscopic system which it represents, are the same. This will depend both on the range of the intermolecular potential and the phenomenon under investigation. If the potential is long ranged (i.e. $V(r) \sim r^{-\nu}$ where ν is less than the dimensionality of the system) there will be a substantial interaction between a particle and its own images in neighbouring boxes, and consequently the symmetry of the cell structure is imposed on a system which is actually isotropic.

The use of periodic boundary conditions inhibits the occurrence of long-wavelength fluctuations. For a cube of side L, the periodicity will suppress any density waves with a wavelength greater than L. Thus, it would not be possible to simulate a liquid close to the gas-liquid critical point, where the range of critical fluctations is macroscopic. Furthermore, transitions which are known to be first order often exhibit the characteristics of higher order transitions when modelled in a small box because of the suppression of fluctuations. The same limitations apply to the simulation of long-wavelength phonons in model solids, where, in addition, the cell periodicity picks out a discrete set of available wave-vectors (i.e. $\mathbf{k} = (k_x, k_y, k_z)2\pi/L$, where k_x, k_y, k_z are integers) in the first Brillouin zone.

Despite the above remarks, the common experience in simulation work is that PBC have little effect on the equilibrium thermodynamic properties and structures of fluids away from phase transitions and where interactions are short-ranged. However, it is always important to check that this holds for each model studied. It should be checked that increasing the number of particles (and box size, so as to maintain constant density) does not influence the results.

2.1.5 Potential truncation

Now let us consider the question of calculating properties of systems subject to periodic boundary conditions. The core of any simulation program is the calculation of the potential energy (and/or force) of a particular configuration. To this end, we must include interactions between particle i and every other particle j in the simulation box. There are $N - 1$ terms in this sum. However, we must also include all interactions between particle i and image particles lying in the surrounding boxes.

This is an infinite number of terms, and of course is impossible to calculate in practice. For a short-ranged potential energy function, we may restrict this summation by making an approximation. The largest contribution to the potential and forces comes from neighbours close to the particle of interest, and is a standard practice to apply a *spherical cutoff*. This means setting the pair potential $V(r)$ to zero for $r \geq r_c$, where r_c is the cutoff distance. The dashed circle in figure 2.2 represents a cutoff region, and in this case particles B and $C4$ contribute to the force on A, since their centres lie inside such region. In a cubic simulation box of side L, the number of neighbours explicitly considered is reduced by a factor of approximately $4\pi r_c^3/3L^3$, and this may be a substantial saving. The introduction of a spherical cutoff should be a small perturbation, as the cutoff distance should be sufficiently large to ensure this. As an example, in the simulation of atoms interacting through Lennard-Jones potentials, the value of the pair potential at the boundary of a cutoff sphere of typical radius $r_c = 2.5\sigma$ is just 1.6 percent of the well depth.

2.2 Molecular Dynamics (MD)

Molecular Dynamics (MD) is a specialized discipline of computational simulation and modelling. This technique provides a way to predict the dynamic evolution of a set of particles given their initial coordinates and velocities at a given time. The MD method was first introduced by Alder and Wainwright in the late 1950's [Alder1957, Alder1959] to study the interactions of hard spheres. Many important insights concerning the behavior of simple liquids emerged from their studies. The next major advance in the development of MD was in 1964, when Rahman carried out the first simulation using a simple potential (Lennard-Jones) for liquid argon [Rahman1964]. The first MD simulation of a realistic system was done by Rahman and Stillinger in their simulation of liquid water in 1974 [Rahman1974].

Although having its origin in theoretical physics of fluids, the MD method gained popularity in materials science and since the 1970s also in biochemistry and biophysics. In chemistry, MD serves as an important tool in protein structure determination and refinement using experimental tools such as X-ray crystallography and NMR. It has also been applied with limited success as a method of refining protein structure predictions. In physics, MD is used to examine the dynamics of atomic-level phenomena that cannot be observed directly. It is also used to examine the physical properties of nanotechnological devices that have not or cannot yet be created.

MD is a quite powerfull technique, but has (of course) limitations. Let us consider, for instance, how realistic is a MD simulation. The essential ingredient in a simulation of the dynamics of atoms and/or molecules is the calculation of the forces that atoms feel. A simulation is realistic (i.e., it mimics the behavior of the real system) only to the extent that interatomic forces are similar to those that real atoms (or, more exactly, nuclei) would experience when arranged in the same configuration. Now, forces are usually obtained as the gradient of the *potential energy function*, which depends on the positions of the particles. The realism of the simulation therefore depends on the ability of the potential chosen to reproduce the behavior of the material under the conditions at which the simulation is run. The problem of selecting -or constructing- "realistic" potentials will bet addressed in more detail in the next chapter.

Another limitation has to do with the simulation time and size. Typical MD simulations can be performed on systems containing thousands (or even millions) of atoms, and for simulation times ranging from a few picoseconds to hundreds of nanoseconds. However, a simulation is *safe* from the point of view of its duration when the simulation time is much longer than the relaxation time of the quantities we are interested in. Of course, different properties have different relaxation times. In particular, systems tend to become slow in the proximity of phase transitions, and it is not uncommon fo find cases where the relaxation time of a physical property is orders of magnitude larger than the time scales achievable by simulation.

2.2.1 The basic MD algorithm

MD can be thought of as the way Newton would have simulated the movement of planets in a solar system ...if he had a computer. The method is simple in principle [Rapaport1997]:

1. **Initial conditions.** Let's assume that we know the positions $\mathbf{r}_i$ and velocities $\mathbf{v}_i$ of all the particles of a system at a time t.

2. **Force computation.** And let's assume that we know the laws that govern the interaction between these particles, so we can compute the force $\mathbf{F}_i$ excerted on every particle i.

3. **Integration.** One may then solve Newton's equations of motion for every one of the particles in order to get their position and velocity at a time Δt later:

$$\mathbf{r}_i(t + \Delta t) = \mathbf{r}_i(t) + \mathbf{v}_i(t)\Delta t + \frac{1}{2}\frac{\mathbf{F}_i}{m_i}\Delta t^2 \tag{2.15}$$

$$\mathbf{v}_i(t + \Delta t) = \mathbf{v}_i(t) + \frac{\mathbf{F}_i}{m_i}\Delta t \tag{2.16}$$

4. **Loop back.** You go back to step 1 with the newly computed positions and velocities.

2.2.2 Integration algorithms

The engine of a molecular dynamics program is its time integration algorithm, required to integrate the equations of motion of the interacting particles and follow their trajectory.

Time integration algorithms are based on *finite difference methods*, where time is discretized on a finite grid, the *time step* Δt being the distance between consecutive points on the grid. Knowing the positions and some of their time derivatives at time t (the exact details depend on the type of algorithm), the integration scheme gives the same quantities at a later time $t + \Delta t$. By iterating the procedure, the time evolution of the system can be followed for long times.

Of course, these schemes are approximated, giving rise to some intrinsic errors. In particular, one can distinguish between

- *Truncation errors*, related to the accuracy of the finite difference method with respect to the true solution. Finite difference methods are usually based on a Taylor expansion truncated at some term, hence the name. These errors do not depend on the implementation: they are intrinsic to the algorithm.

- *Round-off erros*, related to errors associated to a particular implementation of the algorithm. For instance, to the finite number of digits used in computer arithmetics.

Both errors can be reduced by decreasing Δt. For large Δt, truncation errors dominate, but they decrease quickly as Δt is increased. For instance, the Verlet algorithm (to be discussed below) has a truncation error proportional to Δt^4 for each integration time step. Round-off errors decrease more slowly with decreasing Δt, and dominate in the small Δt limit. Using 64-bit precision in computer codes and hardware architectures helps to decrease round-off errors, making them negligible.

The two most popular integration methods for MD calculations are the Verlet algorithm and predictor-corrector algorithms, which we shall introduce next.

2.2.2.1 Verlet

In Molecular Dynamics, the most commonly used time integration algorithm is probably the so-called Verlet algorithm [Verlet1967, Verlet1968]. The basic idea is to write two third-order Taylor expansions for the positions $\mathbf{r}(t)$, one forward and one backward in time. Calling $\mathbf{v}$ the velocities, $\mathbf{a}$ the accelerations, and $\mathbf{b}$ the third derivatives of $\mathbf{r}$ with respect to t, one has

$$\begin{aligned} \mathbf{r}(t+\Delta t) &= \mathbf{r}(t) + \mathbf{v}(t)\Delta t + (1/2)\mathbf{a}(t)\Delta t^2 + (1/6)\mathbf{b}(t)\Delta t^3 + O(\Delta t^4) \quad (2.17) \\ \mathbf{r}(t-\Delta t) &= \mathbf{r}(t) - \mathbf{v}(t)\Delta t + (1/2)\mathbf{a}(t)\Delta t^2 - (1/6)\mathbf{b}(t)\Delta t^3 + O(\Delta t^4). \quad (2.18) \end{aligned}$$

Adding the two expressions gives

$$\mathbf{r}(t+\Delta t) = 2\mathbf{r}(t) - \mathbf{r}(t-\Delta t) + \mathbf{a}(t)\Delta t^2 + O(\Delta t^4). \quad (2.19)$$

This is the basic form of the Verlet algorithm. Since we are integrating Newton's equations, $\mathbf{a}(t)$ is just the force divided by the mass, and the force is in turn a function of the positions $\mathbf{r}(t)$:

$$\mathbf{a}(t) = -(1/m)\nabla V(\mathbf{r}(t)). \quad (2.20)$$

As one can inmediatly see, the truncation error of the algorithm when evolving the system by Δt is of the order of Δt^4, even if third derivatives do not appear explicitly. This algorithm is at the same time simple to implement, accurate and stable, explaining its large popularity among MD code developers.

A problem with this version of the Verlet algoritm is that velocities are not directly generated. While they are not needed for the time evolution, their knowledge is sometimes necessary. Actually, they are required to compute the kinetic energy K, whose evaluation is necessary to test the conservation of the total energy $E = K + V$. To overcome this difficulty, some variants of the Verlet algorithm have been developed. They give rise to exactly the same trajectory, and differ in what variables are stored in memory and at what times.

The best implementation of the same basic algorithm is the so-called *velocity Verlet* scheme, where positions, velocities and accelerations at time $t+\Delta t$ are obtained from the same quantities at time t in the following way:

$$\begin{aligned} \mathbf{r}(t+\Delta t) &= \mathbf{r}(t) + \mathbf{v}(t)\Delta t + (1/2)\mathbf{a}(t)\Delta t^2 \quad (2.21) \\ \mathbf{v}(t+\Delta t/2) &= \mathbf{v}(t) + (1/2)\mathbf{a}(t)\Delta t \quad (2.22) \\ \mathbf{a}(t+\Delta t) &= -(1/m)\nabla V(\mathbf{r}(t+\Delta t)) \quad (2.23) \\ \mathbf{v}(t+\Delta t) &= \mathbf{v}(t+\Delta t/2) + (1/2)\mathbf{a}(t+\Delta t)\Delta t. \quad (2.24) \end{aligned}$$

Note that we need $9N$ memory locations to save the $3N$ positions, velocities and accelerations, but we never need to have simultaneously stored the values at two different times for any of these quantities.

2.2.2.2 Predictor-corrector algorithm

Predictor-corrector algorithms constitute another commonly used class of methods to integrate the equations of motion. Those more often used in MD consist of three steps:

1. *Predictor.* From the positions and their time derivatives up to a certain order q, all known at time t, one "predicts" the same quantities at time $t + \Delta t$ by means of a Taylor expansion. Among these quantities are, of course, accelerations $\mathbf{a}$.

2. *Force evaluation.* The force is computed taking the gradient of the potential at the predicted positions. The resulting acceleration will be, in general, different from the "predicted acceleration". The difference between the two constitutes an "error signal".

3. *Corrector.* This error signal is used to "correct" positions and their derivatives. All the corrections are proportional to the error signal, the coefficient of proportionality being a "magic number" determined to maximize the stability of the algorithm.

Predictor-corrector methods offer great flexibility in that many choices are possible for both the prediction and correction steps. They may be either one-step, in which case they are self-starting, or multistep methods, requiring specific approaches to start the calculation. With the judicious combinations of predictor and corrector they offer good stability because the corrector step amounts to a feedback mechanism that can dampen instabilities that might be introduced by the predictor.

Any given predictor-corrector algorithm can be made more elaborate and of higher order by repeating the evaluation and correction steps. Let P be the prediction, E be evaluation, and C be correction. Then the procedure described above can be represented as PEC. If the corrected positions and velocities are used as second predictions, we obtain the algorithm $PEC(EC) = P(EC)^2$. Obviously, the E and C steps can be repeated as many times as desired, $P(EC)^n$. This strategy, while simple to implement is rarely done in MD because each $E-$step requires force calculations; a $P(EC)^n$ simulation will execute nearly n times slower than the PEC simulation.

Predictor-corrector algorithms were first introduced into MD by Rahman [Rahman1974, Brooks1988]. Those commonly used in MD are often taken from the collection of methods devised by Gear [Gear1966, Gear1971].

2.2.3 Statistical ensembles

The above equations generate trajectories with constant energy (within computer accuracy). That way MD utilizes the microcanonical (NVE) ensemble. However, it is often more interesting to perform simulations in other ensembles, commonly the canonical (constant temperature NVT) ensemble or the isothermal-isobaric (constant pressure NPT) ensemble. In order to sample these ensembles, some modifications to the standard equations of motion must be introduced.

2.2.3.1 Canonical ensemble (NVT)

Simulations at constant temperature are important for studying the behaviour of systems at different temperatures. There have been a number of different approaches for performing constant temperature (NVT) MD. As the temperature of a system is related to the average kinetic energy of the particles, the temperature can be controlled by scaling the velocities, i.e. at each time step the velocities are scaled according to $\mathbf{v}' = \chi\mathbf{v}$. One such thermostat in this spirit is the Berensden thermostat [Berendse1984]. Here the velocity rescaling parameter, χ, is given by

$$\chi = \left[1 + \frac{\delta t}{\tau}\left(\frac{T}{T_0} - 1\right)\right] \tag{2.25}$$

where δt is the time step, T is the current temperature, T_0 is the desired temperature, and τ is a time constant.

Another method, similar to velocity rescaling is to constrain the velocities by a Gaussian constraint method [Evans1983]. Alternatively, the temperature can be held constant by a heat bath. In this method, originally due to Andersen [Andersen1980], the velocity of a randomly selected particle is replaced by one chosen from the Maxwell-Boltzmann distribution. This is equivalent to a collision with a particle in an imaginary heat bath.

A final possibility is the extended system method. Similarly to the Andersen thermostat, the system is assumed to be in contact with a heat bath. However, in this case the interaction between the simulated system and the heat bath is modelled by an exchange of energy between them. In the original formulation of this method due to Nosé [Nosé1984], this was handled by an extended Hamiltonian, with an extra

degree of freedom , which acts as a time scaling parameter. Hoover then reformulated the method without that extra degree of freedom [Hoover1985]. The equations of motion for this thermostat are

$$\dot{\mathbf{r}} = \frac{\mathbf{p}}{m} \tag{2.26}$$

$$\dot{\mathbf{p}} = \mathbf{F} - \zeta \mathbf{p} \tag{2.27}$$

$$\dot{\zeta} = \frac{N_f k_B T_0}{Q} \left(\frac{T}{T_0} - 1 \right), \tag{2.28}$$

where ζ is a friction coefficient, N_f is the number of degrees of freedom, Q is the thermal inertia coefficient, which describes the rate of energy exchange between the system and the heat bath, and T and T_0 are the current and desired temperatures respectively.

2.2.3.2 Isothermal-isobaric ensemble (NPT)

Many experiments are performed at constant temperature and pressure, so the isothermal-isobaric (NPT) ensemble is commonly used for MD simulations. Many of the methods used for controlling the temperature of a simulation can be adapted to control the pressure, with the pressure being controlled by changing the size of the simulation cell. The change in the simulation cell can be isotropic where the cell shape remains unchanged or anisotropic where the cell shape changes. One simple method due to Berensden and co-workers [Berendse1984] involves coupling the system to a pressure bath. At each step the volume of the box is scaled by a factor of a parameter η and so the centre of mass coordinates are scaled by a factor of $\eta^{1/3}$, i.e. $\mathbf{r}' = \eta^{1/3}\mathbf{r}$. The system obeys the equation

$$\dot{P} = \frac{P_0 - P}{\tau_P} \tag{2.29}$$

where P is the current pressure, P_0 is the desired pressure, and τ_P is a time constant. Barostats in the spirit of Nosé-Hoover thermostat have also been proposed. One such barostat that generates the proper NPT ensemble averages has been proposed by Melchionna *et al.* [Melchion1993]. Here the equations of motion are given by

$$\dot{\mathbf{r}} = \frac{\mathbf{p}}{m} + \eta(\mathbf{r} - \mathbf{r}_{com}) \tag{2.30}$$

$$\dot{\mathbf{p}} = \mathbf{F} - (\eta + \zeta)\mathbf{p} \tag{2.31}$$

$$\dot{\zeta} = \frac{1}{\tau_T^2} \left(\frac{T}{T_0} - 1 \right) \tag{2.32}$$

$$\dot{\eta} = \frac{1}{N k_B T_0 \tau_P^2} V(P - P_0) \tag{2.33}$$

$$\dot{V} = 3\eta V \tag{2.34}$$

where $\mathbf{r}_{com}$ is the system center of mass position, and τ_T and τ_P are the thermostat and barostat time constants. These constants are typically set to $\tau_T \sim 1$ ps and $\tau_P \sim 0.1$ ps [Melchion1993, Stern2004]. In this set of equations of motion, η is the volume scaling factor and ζ is the friction coefficient, which regulates the system's temperature.

2.2.4 *Ab initio* Molecular Dynamics

About 20 years ago, Car and Parrinello [Car1985] developed a powerful method allowing to perform MD simulations where the ions are still moved classically, but under the action of forces obtained by solving the electronic structure problem, thus eliminating the need for empirical potentials at the expense of much larger computational requirements. This important development spawned one of the most important research lines in today's condensed matter physics, known as *first principles* or *ab initio molecular dynamics* (AIMD), or simply as Car-Parrinello method [Kohanoff2006].

Anyway, it is safe to say that the existence of the more accurate AIMD technique does not imply the death of classical molecular dynamics based on empirical potentials. While at present classical MD simulation is being run on systems containing millions of particles, or for simulation times of the order of nanoseconds, the current limit for AIMD is of the order of a thousand atoms, and its typical simulation times are measured in picoseconds. This means that several problems requiring large sizes and/or large times can be approached only by classical methods. Even if the speed of computers keeps increasing at a breathtaking pace, so does the size of problems of interest, and it is very likely that all the MD techniques that we know today will remain in use for quite some time from now, and new ones may appear.

2.3 Conjugate Gradients (CG)

In computer simulations at the nanoscale we are quite often interested in finding the *optimal* or *minimum energy* configuration of a given system. In classical simulations, this accounts to finding the atomic coordinates that minimize the total energy of the system. There exist several mathematical methodologies that, given an initial system configuration, iterate until atomic coordinates are pushed down to the system's minimum energy positions. Non-linear Conjugate Gradients (CG) is one of the most reliable of such methodologies.

The problem of finding the optimal configuration of a N-atoms system can be restated as that of finding the value of $\mathbf{x} = (x_0, x_1, ..., x_{3N-1})$ that minimizes the

function $f(\mathbf{x})$, where $f(\mathbf{x})$ is the system's total energy when atomic coordinates of atom n ($0 \leq n < N$) are: $(x_{3n}, x_{3n+1}, x_{3n+2})$. At this minimum point $\mathbf{x}_{min}$ the gradient $\nabla f(\mathbf{x})$ is equal to zero. This minimum is found by the CG method iteratively the following way:

1. Start at any point $\mathbf{x}_0$ (given by the initial choice of the atomic coordinates).
2. Find the direction of maximum increase of the function. This is given by the vector $\mathbf{\Delta x}_0 = -\nabla f(\mathbf{x}_0)$.
3. Perform a *line search* of the minimum of $f(\mathbf{x})$ in that direction. The result is the step length α_0 that minimizes $f(\mathbf{x}_0 + \alpha \mathbf{\Delta x}_0)$.
4. Compute the next starting point as $\mathbf{x}_1 = \mathbf{x}_0 + \alpha_0 \mathbf{\Delta x}_0$.

After this first iteration, in which the line search is done along the gradient direction ($\mathbf{\Delta x}_0 = -\nabla f(\mathbf{x}_0)$), the second step is replaced by $\mathbf{\Delta x}_i = -\nabla f(\mathbf{x}_i) + \beta_i \mathbf{\Delta x}_{i-1}$. Here the scalar β_i is obtained from any of the several proposed forms:

- Fletcher-Reeves [Fletcher1964]:

$$\beta_i^{FR} = \frac{\mathbf{\Delta x}_i^T \mathbf{\Delta x}_i}{\mathbf{\Delta x}_{i-1}^T \mathbf{\Delta x}_{i-1}} \tag{2.35}$$

- Polak-Ribière [Polak1969]:

$$\beta_i^{PR} = \frac{\mathbf{\Delta x}_i^T (\mathbf{\Delta x}_i - \mathbf{\Delta x}_{i-1})}{\mathbf{\Delta x}_{i-1}^T \mathbf{\Delta x}_{i-1}} \tag{2.36}$$

- Hestenes-Stiefel [Hestenes1952]:

$$\beta_i^{HS} = \frac{\mathbf{\Delta x}_i^T (\mathbf{\Delta x}_i - \mathbf{\Delta x}_{i-1})}{\mathbf{\Delta x}_{i-1}^T (\mathbf{\Delta x}_i - \mathbf{\Delta x}_{i-1})}, \tag{2.37}$$

where $\mathbf{\Delta x}^T$ is the transposed of vector $\mathbf{\Delta x}$. A value of $\beta = 0$ can also be used. This is exactly the same as using the so-called *steepest descent* method.

With a pure quadratic function the minimum is reached within $3N$ iterations (excepting roundoff error), but a non-quadratic function will make slower progress. Subsequent search directions lose conjugacy, requiring the search direction to be reset to the steepest descent (i.e., gradient) direction at least every $3N$ iterations, or sooner if progress stops. However resetting every iteration turns the method into steepest descent. The algorithm stops when it finds the minimum, determined when

no progress is made after a direction reset (i.e. in the steepest descent direction), or when some tolerance criterion is reached.

Newton based methods (like the Newton-Raphson Algorithm, or the so-called Quasi-Newton methods [Press2007]) tend to converge in fewer iterations, although each iteration typically requires more computation than a conjugate gradient iteration as Newton-like methods require computing the Hessian (matrix of second derivatives) in addition to the gradient. Quasi-Newton methods also require more computer memory to operate.

One of the problems with CG and the other iterative optimization methods mentioned above is the fact that typically the function to be minimized (the system's energy) has many local minima into which the conjugate gradient minimizer may become trapped because it takes exclusively downhill steps. An improvement of this situation could be expected from other structure optimization algorithms that have the possibility to "escape" from unfavorable local minima. In the following section we describe two methodologies (Monte Carlo and Simulated Annealing) that provide this possibility.

2.4 Other simulation tools

2.4.1 Monte Carlo

Monte Carlo simulations aim at exploring the conformation space of a system in order to determine the equilibrium average of some property A [Robert2004]. This could, in principle, be achieved by evaluating the integral

$$\langle A \rangle = \int A(\mathbf{r}) P(\mathbf{r}) d\mathbf{r}, \tag{2.38}$$

where the probability distribution function $P(\mathbf{r})$ is given by

$$P(\mathbf{r}) = \frac{e^{-\frac{E(\mathbf{r})}{k_B T}}}{\int e^{-\frac{E(\mathbf{r})}{k_B T}} d\mathbf{r}}, \tag{2.39}$$

where $E(\mathbf{r})$ is the energy of the system characterized by the set $\mathbf{r}$ of atomic coordinates. The denominator in equation 2.39 is the partition function of the system. While the above equations cannot be evaluated analytically, they could in principle be calculated using a numerical integration procedure. However, for all but the very smallest system this would involve an unfeasible number of calculations. Alternatively the integrals could be evaluated by sampling different configurations of the system

to provide a representative sample of all the states. In its crudest form this would consist of making random changes to the coordinates of the system. From the energies calculated at each move, $A(\mathbf{r})P(\mathbf{r})$ can then be estimated and $\langle A \rangle$ can be found. This approach is flawed as each different configuration would contribute equally to the integral. Since $P(\mathbf{r})$ is proportional to the Boltzmann factor, only low energy configurations make a significant contribution to the integrals. However, a large number of configurations have a small Boltzmann factor due to high energy overlaps between molecules. Thus only a small proportion of configuration space corresponds to low energy configurations where there are no overlaps and which correspond to physically observed states. Therefore many of the generated configurations would have little or no influence and so proper sampling would not have been achieved. The sampling problem above can be solved by employing importance sampling, which is the essence of the *Metropolis Monte Carlo* method. This method is so wide spread that it is usually referred to simply as the *Monte Carlo* (MC) method [Robert2004]. The crucial feature is that it biases the generation of configurations to those that make a significant contribution to equation 2.39. Specifically it generates a series of states with a Boltzmann distribution and counts them equally. This differs from the crude method outlined above which generates states with equal probability and then assigns them a Boltzmann weight. The simulation must have a procedure for generating new configurations so that at the end of the simulation the appropriate probability distribution has occurred. This is achieved by setting up what is known as a Markov chain [Allen1999], which satisfies the following conditions

- The outcome of each trial belongs to a finite set of possible outcomes.
- Each trial depends only on the outcome of the trial that precedes it.

These conditions are required to produce the correct limiting distribution, i.e. to produce the correct ensemble averages.

Although MC method is often used in the optimization of solid state systems, in this thesis we have not used it. We include its description here just for completeness. Instead, we have decided to use conjugate gradients for zero temperature structure optimization and the simulated annealing technique (see below) for low temperature optimization. This choice is due to the need to monitor physical observables (like stress components) that depend on the velocity of particles, which cannot be obtained from MC simulations.

2.4.2 Simulated annealing

MD may also have a role as an optimization tool. Let us suppose that a set of N particles has many possible equilibrium configurations. The energy of these configurations is in general different, and one of them will be the optimal one. All of them, however, correspond to *local minima* in the energy, and are each other separated by energy barriers. Such a situation occurs very commonly, for instance, in cluster physics [Alonso2005].

Finding the optimal structure within an approach based on traditional minimization techniques (like steepest descent, or conjugate gradients methods) is tricky, as these methods do not normally overcome energy barriers and tend to fall into the nearest local minimum. One therefore would have to try out several different starting points, corresponding to different "attraction basins" in the energy landscape, and relax each of them to the bottom of the basin. The optimal structure would then be the one with the lowest energy, provided that we were sage enough to select it in the list of initial trial configurations.

Temperature in a molecular dynamics (or Monte Carlo) calculation provides a way to "fly over the barriers": states with energy E are visited with a probability $exp(-E/k_BT)$. If T is sufficiently large, the system can "see" the simultaneous existence of many different minima, spending more time in the deeper ones. By decreasing slowly T to 0, there is a good chance that the system will be able to pick up the best minimum and land into it. This consideration is the base of *simulated annealing* methods, where the system is equilibrated at a certain temperature and then is slowly cooled down to $T = 0$. While this procedure does not guarantee that the true minimum will be reached, it often brings the system into a good minimum and, as no a priori assumptions are made about the optimal structure, it often brings about structures which were difficult to foresee by intuition alone.

This method is often used to optimize atomic structures, but its validity is more general: given an objective function $Z(\alpha_1, ..., \alpha_2)$ depending on N parameters, one can regard each of these parameters as a degree of freedom, assign a "virtual mass" to them, and move the system with a molecular dynamics or Monte Carlo algorithm to perform simulated annealing. One of the early application of this method can be found in a famous paper discussing an application to the "traveling salesman" problem [Kirkpatr1983].

Chapter 3

Embedded Atom Method (EAM)

As we have mentioned in chapter 2, *ab initio* methods impose practical limitations for studying systems containing a large number of atoms (let us say, above ~ 1000 atoms). For this reason, in this thesis we have relied on a *classical* approach to treat the interactions among nuclei. By doing so we completely discard the electronic degrees of freedom and move nuclei (atoms) according to some potential function $V(\mathbf{R}_i)$ whose analytical form we specify in advance. In chapter 2 we have also discussed the advantages of using a many-body formalism rather than pair potentials.

In this chapter we present a general description of the Embedded Atom Method (EAM) approach. EAM is perhaps the most frequently used classical many-body method to describe the atomic interactions in metallic systems [Daw1993]. In practice, EAM potentials are stated in terms of a set of parameters whose values are determined by least-squares fitting to a suite of experimental data and (often) *ab initio* results for specific stuctures of the material under consideration. These data usually includes bulk cohesive energy E_c, nearest neighbors distance d_{nn}, surface energies γ, vacancy energies E_v, some phonon frequencies, elastic constants and stacking fault energies for several crystalline geometries (FCC, BCC, etc.). The predictive power of EAM potentials has been studied for several atomic species [Daw1983, Daw1984, Daw1993, Sutton1990, Ercoless1994, Mishin1999, Jaffe2000], however, their effectiveness for describing structures with a low atomic coordination number N_c has not been extensively considered.

There exist several parameterizations of the EAM functions. However, the ones proposed by Mishin *et al.* [Mishin1999, Mishin2001] and Sutton and Chen [Sutton1990] (hereafter named MFMP and SC respectively) are the most used in the literature. In this chapter we perform a comparative study between these two EAM parameterizations in a range of systems with high and low atomic coordination in one (1D), two (2D) and three (3D) dimensions. In particular we are interested in analyzing the

transferability of these potentials. It is not obvious that a given interatomic potential (optimised for bulk) will be able to describe the energetics and forces of such atomic configurations in which low atomic coordination N_c situations naturally appear, as clusters, nanowires, adsorbed species, etc. This possible lack of transferability, from high to low coordination situations, represents a serious concern when predicting stable atomic configurations and their dynamical behaviour at the nanoscale.

The aim of this chapter is to study the transferability of EAM potentials in Al, Ni and Cu. It is organized as follows. In the following section we describe the EAM method and two of its most implemented parameterizations: MFMP and SC. In the next section we present a comprehensive comparison of these two parameterizations with Density Functional Theory (DFT) *ab initio* calculations in a wide variety of systems from high to low coordinations. We also compute the surface energies and surface relaxations in these systems for the (100), (110) and (111) facets. In the final section we show a summary of the most relevant results of this comparative study and decide which of these two EAM parameterizations is best suited to our simulations of metallic nanowires in the following chapters.

3.1 General description of the EAM method/model

The EAM method is a semi-empirical, many-atom potential for computing the total energy of a metallic system. It was first proposed by Daw and Baskes in 1983 [Daw1983, Daw1984] as a model to approximate the many-atom interactions neglected by pair-potential schemes. The advent of the EAM allowed simulation of a very large set of interesting problems: point defects, melting, alloying, grain boundary structure and energy, dislocations, segregation, fracture and surface structure. A comprehensive review on the history and applications of EAM was written by Daw *et al.* [Daw1993].

A particularly appealing aspect of the EAM is its physical picture of metallic bonding. Each atom is embedded in a host electron gas created by its neighboring atoms. The atom-host interaction is described in a way that is inherently more complex than the simple pair-bond model. In this way, the embedding function incorporates some important many-atom interactions. It is possible to describe and understand interatomic interactions at defects in terms of either the embedding function or the effective many-atom interactions that arise from it. In particular, it is simple to demonstrate how bonding is affected by coordination. This naturally leads to an understanding of the difference between bulk and surface bonds, for example.

EAM combines the computational simplicity needed for larger systems with a physical picture that includes many-atom effects and avoids some of the problems of the pair-potential scheme.

The EAM approach describes the potential energy V of a metallic system through the two terms expression:

$$V = \frac{1}{2}\sum_{i,j}^{N}\phi(r_{ij}) + \sum_{i=1}^{N}F(\rho_i) \tag{3.1}$$

where $\phi(r_{ij})$ is a pair repulsive term that depends on the interatomic distance between atoms i and j. The function $F(\rho_i)$ corresponds to the required energy to embed an atom into the background electron density ρ_i at site i. $F(\rho_i)$ represents the cornerstone of the EAM methodology and is known as the "embedding function". The electron density background acting on atom i is due to the electronic clouds associated to the neighboring atoms. This "atomic density" is expressed as $\rho_i = \sum_j \rho(r_{ij})$, where the function $\rho(r_{ij})$ provides the contribution from atom j to the electron density of the atom i depending on their relative distance r_{ij}.

The specific shapes of these EAM functions ($\phi(r_{ij})$, $F(\rho_i)$ and $\rho(r_{ij})$) are chosen in a convenient way in order to reproduce several properties of a given system. Different functional forms (refered to as "parameterizations") of these EAM functions have been proposed in the literature that model different properties (like cohesive energy, lattice constant, etc) of a given material. In the following sub-sections we describe two of the most used EAM parameterizations for the simulations of metallic systems.

3.1.1 EAM parameterization by Sutton and Chen (SC)

The Sutton-Chen (SC) parameterization of EAM was proposed in 1990 [Sutton1990]. It belongs to the subclass of Finnis-Sinclair potentials [Finnis1984]. It was designed with the idea of fitting van der Waals interactions between neighbor clusters and this is the reason it has a long range tail. Under the SC parameterization the potential energy of the system is

$$V = \epsilon\left[\sum_{i\neq j}\left(\frac{a}{r_{ij}}\right)^{n} - c\sum_{i}\sqrt{\sum_{j\neq i}\left(\frac{a}{r_{ij}}\right)^{m}}\right], \tag{3.2}$$

where a is the bulk lattice constant and the parameters ϵ, c, n and m are optimized to best fit the bulk cohesive energy E_c, bulk modulus K and the elastic constants C_{11}, C_{12} and C_{44} (only E_c and a are fitted exactly). Table 3.1 shows the values of

	Z	m	n	$\epsilon(eV)$	c	E_C	a
Al	13	6	7	3.3147×10^{-2}	16.399	3.34	4.05
Ni	28	6	9	1.5707×10^{-2}	39.432	4.44	3.52
Cu	29	6	9	1.2382×10^{-2}	39.432	3.50	3.61
Rh	45	6	12	4.9371×10^{-3}	144.41	5.75	3.80
Pd	46	7	12	4.1790×10^{-3}	108.27	3.94	3.89
Ag	47	6	12	2.5415×10^{-3}	144.41	2.96	4.09
Ir	77	6	14	2.4489×10^{-3}	334.94	6.93	3.84
Pt	78	8	10	1.9833×10^{-2}	34.408	5.86	3.92
Au	79	8	10	1.2793×10^{-2}	38.408	3.78	4.08
Pb	82	7	10	5.5765×10^{-3}	45.778	2.04	4.95

Table 3.1: SC parameters for several atomic species (extracted from [Sutton1990]).

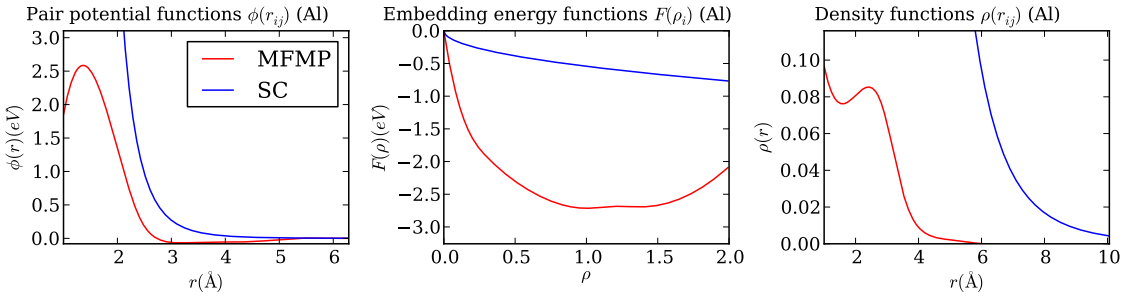

Figure 3.1: Comparison of SC and MFMP EAM pair potential $\phi(r)$, embedding energy $F(\rho)$ and electron density $\rho(r)$ functions for Al.

m, n, ϵ, and c optimized for several metallic species. Notice that m is always ≥ 6, to prevent the potential to have an even larger tail.

3.1.2 EAM parameterization using numerical functions: MFMP

The MFMP parameterization [Mishin1999, Mishin2001] has been designed with a different approach to the fitting of physical observables. Instead of using analytical forms, the three EAM functions are given as numerical sets of discrete points. In order to get continuous functions, these points must be interpolated by cubic splines. A clear advantage of this approach is that it provides a much larger set of parameters (actually, as many parameters as points are used). This allows a flexible way to fit more physical properties. A disadvantage of this method is that evaluation of the EAM energy is a bit slower than in SC since an interpolation procedure is required every time one of the EAM functions must be evaluated.

In figures 3.1, 3.2 and 3.3 we show the shape of the MFMP and SC EAM functions for Al, Cu and Ni respectively. These graphs show how different are the shapes of

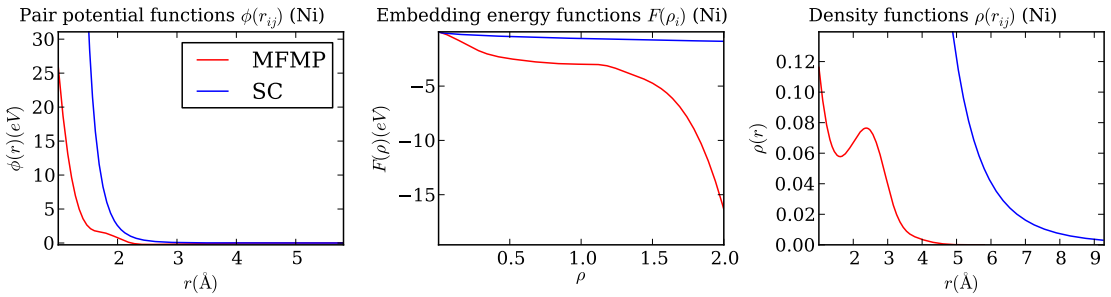

Figure 3.2: Comparison of SC and MFMP EAM pair potential $\phi(r)$, embedding energy $F(\rho)$ and electron density $\rho(r)$ functions for Ni.

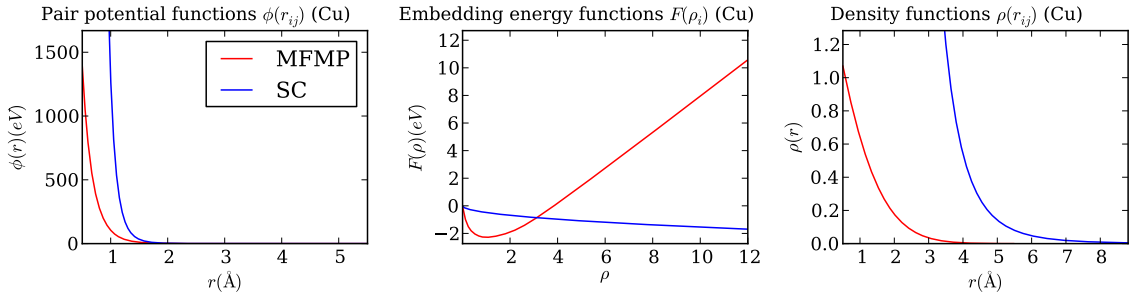

Figure 3.3: Comparison of SC and MFMP EAM pair potential $\phi(r)$, embedding energy $F(\rho)$ and electron density $\rho(r)$ functions for Cu.

the discrete MFMP functions versus the analytical SC ones. Also it is important to notice the longer range of SC potential. This is particularly clear in the embedding energy function of any of the three materials presented here. At a first glance it is clear that large differences are expected when computing several observables between using MFMP or SC EAM functions.

3.2 Comparison of MFMP and SC with *ab initio* calculations in low coordinated systems

As we have already mentioned, the ability of the EAM potentials to properly describe the behaviour of the bulk FCC structured materials does not at all guarantee that systems with other structures (specially those with lower coordination) can be reliably described. For this reason, we have performed a systematic study to test the performance of both MFMP and SC parameterizations of EAM in a variety of crystalline structures. Part of the results detailed in this chapter have been published in reference [Peláez2006] for Al and Ni. However, they are presented here in more detail.

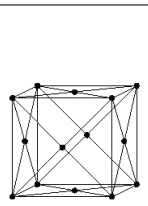	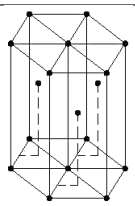	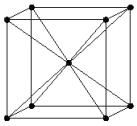	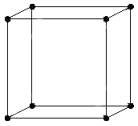				
FCC	HCP	BCC	SC	2D-hex	2D-squ	chain	dimer
N_c : 12	12	8	6	6	4	2	1

Table 3.2: Lattice structures used in this study to compare MFMP and SC parameterizations. Coordination number N_c of the every structure is shown in the bottom row.

Table 3.2 shows the different structures used in this study. The systems here considered are: face centered cubic (FCC), hexagonal closed packing (HCP), body centered cubic (BCC) and simple cubic (SC) bulk lattices. Additionally to these 3-dimensional structures, we have also tested EAM potentials in 2-dimensional lattices: a hexagonal (hereafter called 2D-hex) and a square one (further referred to as 2D-squ). Furthermore, we have tested EAM in a linear atomic chain and a two-atoms configuration (dimer). The choice of this variety of structures includes values of the atomic coordination N_c from 12 (in FCC and HCP structures) to $N_c = 1$ (in the dimer).

In order to compare the performance of these EAM parameterizations in this variety of systems we have focused on three physical quantities: the cohesive energy per atom E_c, the nearest neighbors distance d_{nn} and the second derivative of E_c with respect to d_{nn}. To obtain these values for each of the structures under consideration implies that we have to run an optimization process of the atomic coordinates and unit cell size. This optimization was carried out using the conjugate gradients (CG) method (described in section 2.3) to minimize the total cohesive energy of the system as a function of both atomic positions and unit cell length.

In parallel to the estimation of the EAM values of E_c, d_{nn} and $\frac{\partial^2 E_c}{\partial d_{nn}^2}$, we have calculated the same quantities using an *ab initio* methodology. We have chosen to use the SIESTA package [SP1997, Soler2002], which allows electronic structure and total energy calculations within the density functional theory (DFT) formalism. In SIESTA's implementation of DFT, core electrons are described by effective pseudopotential functions and valence electronic states as a combination of numerical atomic orbitals [Artacho1999, Junquera2001]. The exchange-correlation energy is computed self-consistently using both the local density (LDA) or the generalized gradient approximation (GGA).

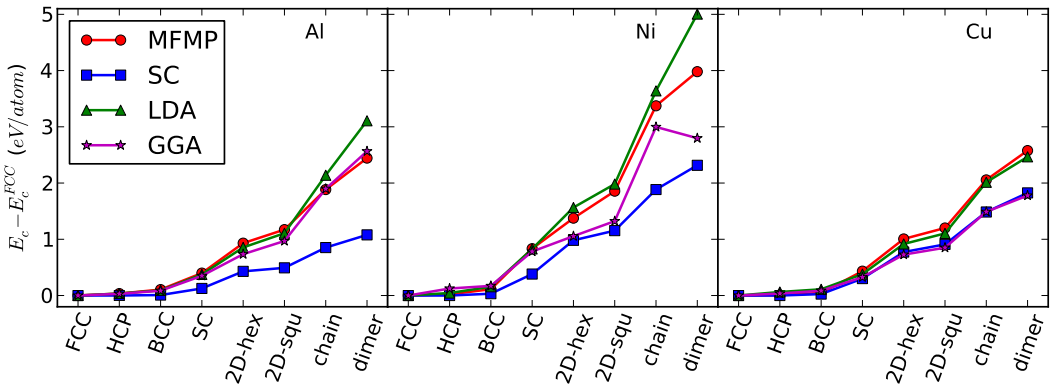

Figure 3.4: Comparison betwen MFMP and SC EAM parameterizations with LDA and GGA DFT calculations of the optimum cohesive energy E_c of several structures compared to that of the FCC structure. Notice that lines are just guides to the eyes.

In this work, we have run structure optimizations with the SIESTA package in order to find the minimum energy structures for all the systems under study. In all cases we have performed the optimization using both the LDA and GGA approaches to the exchange-correlation energy.

3.2.1 Cohesive energy E_c

Figure 3.4 shows the values of E_c obtained with the two EAM parameterizations under consideration (MFMP and SC) and the two DFT approaches (LDA and GGA). E_c values are depicted with respect to the cohesive energy of the FCC structure, which is the lowest energy structure for the three metallic species studied here (Al, Ni and Cu).

As expected, figure 3.4 shows that all structures show higher energy than the FCC one. It can be seen that both EAM parameterizations perform well for the FCC, HCP and BCC structures (the ones with the highest coordination N_c). However, as N_c decreases, the values of E_c obtained from the SC potential begin to deviate from the DFT and MFMP values. This is particularly noticeable for Al and Ni, in which the difference in cohesive energy between SC and DFT estimations grows up to 2 and 3 $eV/atom$ respectively for the dimer structure.

The MFMP parameterization, on the other hand, gives a reasonably good set of E_c values for all the structures, compared to the LDA results. Actually, the difference between MFMP and LDA is always below 0.2 $eV/atom$. An exception to this is the

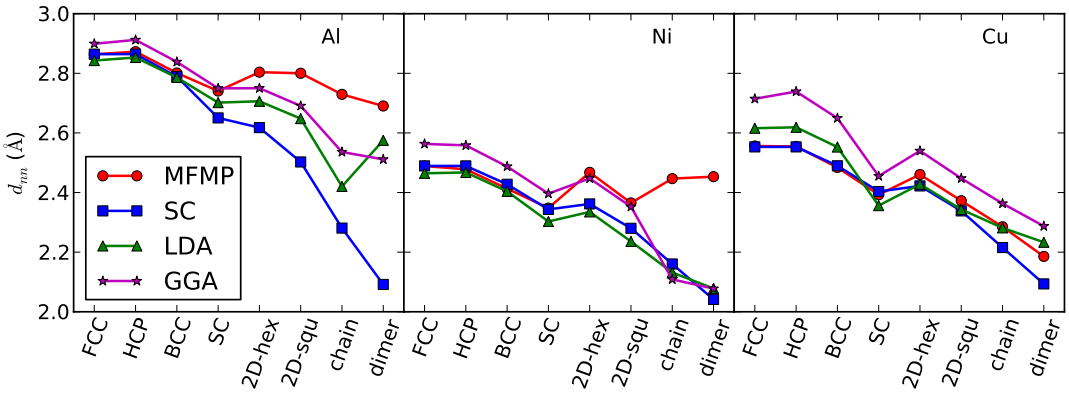

Figure 3.5: Comparison betwen MFMP and SC EAM parameterizations with LDA and GGA DFT calculations of the optimum nearest neighbor distance d_{nn} in several configurations.

dimer structure in which this difference goes to $\sim 1\,eV/atom$ for Ni. Notice that even GGA and LDA are about $2\,eV/atom$ away in the E_c estimation for the Ni dimer.

The case of Cu is curious, since while MFMP values of E_c are almost identical to those obtained from the LDA DFT approximation, SC EAM values are also quite similar to those from the GGA approximation. In this case we can only conclude that both EAM parameterization perform as good as DFT approximations in the estimation of the cohesive energy E_c of Cu systems even at the lowest coordination.

3.2.2 Nearest neighbors distance d_{nn}

The second physical observable that we have monitored in this work is the nearest neighbors distance. This quantity is plotted in figure 3.5 for the three metallic species and all the structures under study. In this figure we can see that, in general, as the coordination decreases, d_{nn} also decreases. This is, of course, an expected trend, since metallic atoms tend to be closer to each other as a way to compensate for fewer neighbors situations.

Regarding the comparison between EAM and DFT estimations of d_{nn} we can see in figure 3.5 that both EAM parameterizations give nearly identical values for the 3-dimensional structures (FCC, HCP, BCC and SC). These values are fairly close (within cents of Å) to those obtained with the LDA approximation. However, for 2- and 1-dimensional systems MFMP and SC values exhibit different values. In all of these cases, d_{nn} values obtained from the MFMP parameterization are larger than those from the SC one. The difference is more noticeable for Al, in which MFMP values of d_{nn} are up to 0.2 Å above the DFT values and SC values are also far

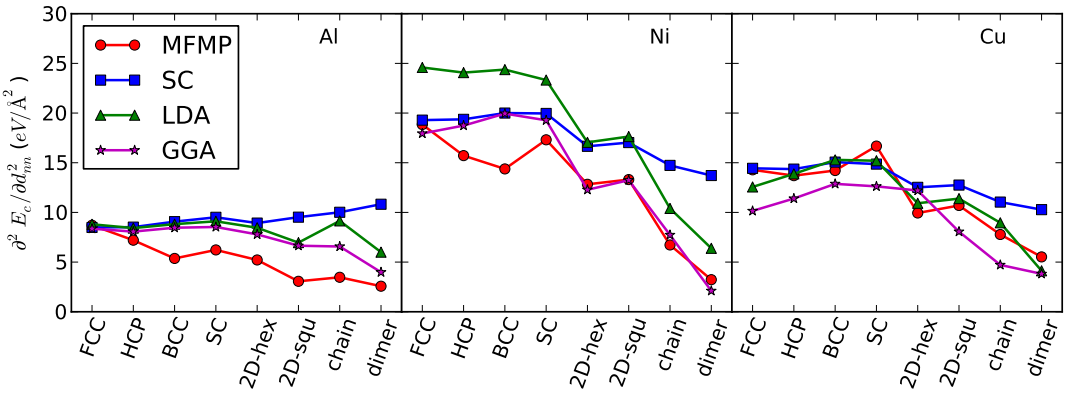

Figure 3.6: Comparison betwen MFMP and SC EAM parameterizations with LDA and GGA DFT calculations of the second derivative of the cohesive energy with respect to the nearest neighbors distance $\frac{\partial^2 E_c}{\partial d_{nn}^2}$ in several configurations.

below DFT ones. In the Ni calculations only the chain and the dimer structures give MFMP values of d_{nn} too far above the DFT and SC values (more than 0.3 Å). Copper exhibits a better agreement between EAM and DFT estimations of d_{nn}. Even for low N_c structures, the maximum difference between EAM and DFT values is ~ 0.1 Å.

It should be noticed that the values of d_{nn} obtained from both EAM parameterizations for the FCC structure are exactly equal to the experimental values . However, this is an expected result, since these parameterizations have been designed to fit the lattice constant of the equilibrium FCC structure exactly. On the other hand, both DFT approximations are slightly deviated from the experimental d_{nn} value. Here the typical over-(under-)estimation of the lattice constant in the GGA (LDA) approximation is observed.

3.2.3 Second derivative of E_c with respect to d_{nn}

In bulk systems, the *compressibility modulus* $K = -V\frac{\partial P}{\partial V}$ (a.k.a. *bulk modulus*, where V is the system's volume and P is the pressure) is a measurement of a structure's resistance to uniform compression [Kittel1995]. This quantity is a relevant property of solid systems. In this work, however, we are dealing with bidimensional and one-dimensional structures, in which the concept of volume does not apply any more. In order to provide a measurement of the system's resistance to compression that was applicable to all the structures of interest in this study, we have decided to compute the second derivative of the energy as a function of the nearest neighbors distance $\frac{\partial^2 E_c}{\partial d_{nn}^2}$.

Figure 3.6 shows the values of $\frac{\partial^2 E_c}{\partial d_{nn}^2}$ for all the systems under study. In this figure we can see that MFMP and SC parameterizations provide the same value only for the FCC structure. For all of the other systems, SC values are above those of MFMP. It can be seen that, for the case of Al, MFMP values are, in average, ∼30% below those of DFT for all non-FCC structures. In Ni, such a difference is only observed in the HCP and BCC structures. For the rest of Ni structures, MFMP values are within a 10% error with respect to the DFT GGA values. In the case of Cu, both EAM parameterizations give values of $\frac{\partial^2 E_c}{\partial d_{nn}^2}$ similar to the DFT results. MFMP values are very similar (with differences of less than 10%) to the LDA values. SC parameterization also yields similar results to the LDA values, but only for 3D systems. Actually, for the three materials considered, in the case of monomer and dimer structures, the SC parameterization always overestimates $\frac{\partial^2 E_c}{\partial d_{nn}^2}$ when compared to the MFMP or DFT values.

3.3 EAM description of free surfaces

3.3.1 Surface energy γ

Surfaces represent an exigent benchmark to test the accuracy of the two chosen EAM parameterizations, since surface atomic coordination naturally differs from that of bulk. It is well-known that free surfaces have properties which make them differ from the underlying bulk material. In the case of solids, it has long been known that different crystallographic surfaces have different surface energies (γ) and that this can decide which surfaces 'survive' during crystal growth, and govern how small solid particles respond to (for instance) prolonged annealing.

Surface energy γ is defined as the energetic cost per unit area of forming a given surface with respect to the cohesive energy of the infinite bulk. In computer simulations, one way to determine it is by defining a slab that shows two parallel surfaces of the desired surface type (ijk). Then γ can be calculated as:

$$\gamma = \frac{E_c - N_{atoms} E_c^{bulk/atm}}{2A}, \tag{3.3}$$

where E_c is the total cohesive energy of the slab of N_{atoms} atoms, A is the area of the bidimensional unit cell and $E_c^{bulk/atm}$ is the bulk value of the cohesive energy per atom. In order to avoid size effects due to the presence of two surfaces, the number of atomic layers of the slab must be long enough so both surfaces do not "see" each

		MFMP	SC	DFT	Avg. exp.
Al	100	0.943	0.611	1.347	
	110	1.006	0.647	1.271	0.980
	111	0.870	0.571	1.199	
Ni	100	1.878	1.655	2.426	
	110	2.049	1.756	2.368	2.280
	111	1.629	1.551	2.011	
Cu	100	1.345	1.237	2.166	
	110	1.475	1.313	2.237	1.790
	111	1.239	1.160	1.952	

Table 3.3: Surface energies γ (J/m^2) computed with different theoretical approaches. DFT data was obtained by Vitos *et al* [Vitos1998] using a GGA approximation. Experimental values correspond to averages over random orientations [Murr1975, Tyson1977].

other. In this work we have defined thick metallic slabs with up to 50 atomic layers, which is enough to avoid these size effects.

In table 3.3 we summarize the surface energies γ for Al, Ni and Cu (100), (110) and (111) surfaces, obtained using both MFMP and SC approaches. We also include results from DFT calculations (extracted from [Vitos1998]) using the GGA approximation. The experimental data shown in this table was obtained as an average over random crystallographic orientations.

From data in table 3.3 we can see that in all the cases the MFMP approach provides a better description of surface energies than the SC parameterization. In fact, we have estimated the surface energy average error (with respect to experimental data) to be larger than $\sim 30\%$ for the SC approach, and of the order of $\sim 15\%$ for the MFMP and $\sim 17\%$ for the GGA one.

The values of γ reported with the DFT-GGA method show that for the three materials, the (111) surface has the lowest surface energy. This result is expected, because the (111) surface has the most packed atomic structure. Both EAM parameterizations agree in the (111) surface being the lowest energy facet. However discrepancies arise for the other two facets. On one hand, the calculations by Vitos [Vitos1998] indicate that the (100) surface has the highest γ value for Al and Ni, whereas for Cu the (110) facet has the highest energetic cost. On the other hand, both EAM parameterizations suggest that the (110) surface is the one with the highest value of surface energy.

The low values of E_c observed in figure 3.4 may explain why surface energies obtained with the Sutton-Chen potential are much lower than MFMP or DFT results.

Al		MFMP	SC	Exp.
100	$\Delta_{12}(\%)$	0.28	-7.52	
	$\Delta_{23}(\%)$	-0.22	-0.22	
	$\Delta_{34}(\%)$	0.05	-0.02	
110	$\Delta_{12}(\%)$	-0.15	-8.97	-8.6
	$\Delta_{23}(\%)$	-0.07	-4.89	5.0
	$\Delta_{34}(\%)$	0.11	-0.29	-1.6
111	$\Delta_{12}(\%)$	-0.32	-5.08	
	$\Delta_{23}(\%)$	0.10	-0.05	
	$\Delta_{34}(\%)$	0.05	-0.01	

Table 3.4: Layer relaxations on different Al surfaces. Available experimental data from [Monnier1978].

Ni		MFMP	SC	Exp.
100	$\Delta_{12}(\%)$	-0.93	-2.78	
	$\Delta_{23}(\%)$	0.22	-0.0	
	$\Delta_{34}(\%)$	0.56	0.00	
110	$\Delta_{12}(\%)$	-1.85	-4.35	-8.7
	$\Delta_{23}(\%)$	0.77	-2.29	3.0
	$\Delta_{34}(\%)$	0.26	-0.03	-0.5
111	$\Delta_{12}(\%)$	-1.38	-2.00	
	$\Delta_{23}(\%)$	0.83	0.023	
	$\Delta_{34}(\%)$	-0.10	0.00	

Table 3.5: Layer relaxations on different Ni surfaces. Available experimental data from [Adams1985].

In SC calculations the lack of atomic coordination does not produce a large energetic cost.

3.3.2 Surface relaxations

We have also monitored the relaxations of the outermost layers of free surfaces with both EAM parameterizations. Surface relaxations are usually described in terms of the interplanar distances d_{ij} between sucessive layers of the surfaces. The relaxation Δ_{ij} is defined as the change (in percent) of d_{ij} from the bulk interplanar distance d^{bulk}:

$$\Delta_{ij} = \frac{d_{ij} - d^{bulk}}{d^{bulk}} \times 100. \tag{3.4}$$

Negative (positive) values of Δ_{ij} correspond to inwards (outwards) relaxations.

Results from the surface relaxations of the low index facets of Al, Ni and Cu are shown in tables 3.4, 3.5 and 3.6 respectively. A first inspection at these tables shows

Cu		MFMP	SC	Exp.
100	$\Delta_{12}(\%)$	-0.69	-2.77	-1.2
	$\Delta_{23}(\%)$	-0.24	-0.01	0.9
	$\Delta_{34}(\%)$	0.39	0.00	
110	$\Delta_{12}(\%)$	-4.14	-4.34	-8.5
	$\Delta_{23}(\%)$	0.02	-2.29	2.3
	$\Delta_{34}(\%)$	1.36	-0.02	
111	$\Delta_{12}(\%)$	-0.84	-1.99	-0.7
	$\Delta_{23}(\%)$	-0.01	0.00	
	$\Delta_{34}(\%)$	0.27	0.00	

Table 3.6: Layer relaxations on different Cu surfaces. Available experimental data from [Lind1987] and [Adams1983].

that, in general, no correspondence is found between values of Δ_{ij} predicted by the MFMP and the SC parameterizations. Furthermore, these values do not correspond to the experimental data when available.

Surfaces modelled with MFMP exhibit much less relaxations than those simulated with SC. This can be related to the tendency of the SC parameterization to induce large atomic compresions in low coordination situations compared to MFMP, as seen in figure 3.5.

We have observed that SC estimations of the interlayer relaxations are in all of the cases (except for Δ_{23} in the (111) surface of Ni) inwards (negative) relaxations. This trend does not correspond to real surfaces, where oscillatory values of Δ_{ij} have been predicted for some surfaces, like the (110) surfaces of Al [Monnier1978] and Ni [Adams1983] shown in tables 3.4 and 3.5.

One must keep in mind that Δ_{ij} measures atomic displacements of a few percents with respect to bulk. And as seen in figure 3.5 and discussed in subsection 3.2.2, both EAM potentials show errors of tenths of angstroms with respect to DFT calculated values. Considering this it is understandable that both EAM parameterizations give bad estimations of such a sensitive quantity as the surface relaxations.

3.4 Conclusions

In this chapter we have carried out a comprehensive test of the MFMP and SC EAM potential parameterizations. We have compared the performance of these potentials in estimating the equilibrium cohesive energy, geometry and compressibility of a variety of structures in three, two and one dimensions. Our results show that, in general, both EAM approaches provide fairly good estimations of these observables. Some

differences appear, though, in low coordination systems. However, these discrepancies are expected from this type of models which are optimized to model only bulk equilibrium structures. Some discrepancies also appear between the LDA and GGA approximations in the DFT calculations we performed. For instance, GGA estimations of the nearest neighbor distances d_{nn} are always higher than that of LDA. Values obtained with both methods follow the same trend as the coordination decreases, but keeping always a difference in d_{nn} of about 0.05 Å.

We have observed that the MFMP parameterization gives better estimations of E_c. This is specially true in Al and Ni, where as lower N_c systems are considered, a stronger deviation of E_c values from SC compared to the DFT values are observed. We have proposed that these too low values of $E_c - E_c^{FCC}$ given by the SC parameterization even for low N_c structures may be an explanation to the low values of the surface energies γ obtained with this potential parameterization.

Regarding the nearest neighbors distance d_{nn} we have observed that both EAM parameterizations provide nearly the same results for the high N_c systems. However, they tend to perform bad for $N_c \leq 6$ more noticeably for Al and Ni.

MFMP estimations of the compressibility $\frac{\partial^2 E_c}{\partial d_{nn}^2}$ are in all cases below those of the SC parameterization. This means that with the SC potential the structures present more resistance to deformation than with the MFMP parameterization. Actually, in the case of Al, MFMP values are even$\sim 30\%$ below the DFT estimations for all of the structures (except for the FCC). Values of $\frac{\partial^2 E_c}{\partial d_{nn}^2}$ for the chain and the dimer structure calculated with the SC parameterization are always overestimated if compared to the DFT or MFMP values.

We have also computed the surface energies γ for the (100), (110) and (111) facets using the two EAM parameterizations. As a general trend, we observed that (111) surfaces show the lowest value of γ for the three materials under study. Our results show that γ values computed using the MFMP potential are much closer to the experimental average estimations than those of the SC method. Actually, MFMP values of γ are in some cases even better than those calculated with the DFT method by Vitos *et al* [Vitos1998]. However it must be noticed that none of the EAM parameterizations gives reasonable values of the surface relaxations Δ_{ij}. This result could be expected, since atomic displacements in surface relaxations are small compared to the observed errors in the nearest neighbors estimations for low coordination systems.

In the remainder of this thesis we rely on the MFMP potential parameterization for the simulations and calculations of different properties of metallic nanowires. The

reasons for this choice of MFMP over SC are the following. First of all, MFMP has been parameterized to fit more properties in bulk FCC than SC. Furthermore, as we have shown in this chapter, it gives better estimations of E_c at low coordinations and also better estimations of the surface energies γ. Its ability to describe low N_c systems better than SC makes it a more reliable parameterization to model the physical properties of metallic nanowires, which exhibt a large surface/volume ratio.

Part II

Metallic nanowires with FCC structure

Chapter 4

Structural properties of FCC metallic nanowires

4.1 Introduction

Micro-electro-mechanical systems (MEMS) have been extensively studied and developed in recent decades [Ghodssi2011, Franssil2010]. Now, as nano-electro-mechanical systems (NEMS) emerge, an understanding of the role of geometric size restrictions in the structures is needed for their design and development [Lyshevsk2002]. Size-mediated plasticity has become an important field of study within the mechanics community. As characteristic dimensions of NEMS structures approach the smaller size scales in at least one characteristic dimension, physical properties can no longer be induced from larger sizes [Sutrakar2009]. In particular, an understanding of the equilibrium structural and mechanical properties of nano-scale structures such as metallic nanowires and nanocontacts is needed for their incorporation into novel architectures of future nanoelectronic devices.

4.1.1 Ground state of FCC nanowires

In the most basic form, the ground state, total energy of a metallic face-centered-cubic (FCC) nanowire may be considered as the sum of core, surface, and edge components. In the ideal case, atoms in the core of the nanowire are fully coordinated and possess a cohesive energy approximately equivalent to the bulk value. This energy is essentially isotropic; the electron gas surrounding a central atom is equally dispersed among its twelve nearest neighbor atoms. In contrast, atoms comprising the free surfaces and edges are under-coordinated with respect to bulk atoms, and thus increase the total energy of the nanowire, since in metallic bonding the density of the electron gas is tightly coupled with the atomic coordination. For a particular element, there exists an

ideal electron density that minimizes the energy of an individual atom. Any variation in the electron density from the ideal value results in an increase in the energy of the atom. Under-coordination of an atom causes an increase in energy due to increased electrostatic attraction, whereas over-coordination results in excessive repulsive energy on the central atom. The degree of under-coordination of an atom on a surface or edge relative to an atom in the nanowire core is dependent on the crystallographic orientation of the free surface, which is defined by the vector normal to the surface plane. For this reason, the surface and edge energies are anisotropic. In order to approach the ideal, energy minimizing electron density, surface atoms contract towards the nanowire core thus imposing a compressive surface stress on the core of the nanowire. As we consider nanowires with smaller cross-sectional dimensions, the surface area to volume ratio is amplified, and the relative contribution of the surface and edge energies to the total energy of the nanowire increases accordingly.

At a critical length in the nanometer scale regime, there exists a crossover where the total energy of the material is more strongly affected by the excess energy from the free surfaces than by the core energy. The magnitude of surface energy is dependent on the crystallographic orientation of the surface. For FCC metals, the close packed (111) surfaces exhibit the lowest surface energy, followed by (100) surfaces and then (110) type surfaces. Thus, the total energy of a material depends not only on the surface-area-to-volume ratio, but also on the particular crystallographic orientation of the exposed surfaces/facets. Moreover, the intersecting regions between these facets define different kinds of edges with their corresponding edge energies.

4.1.2 Non-crystalline nanowires

However, the regular crystalline packing of metallic atoms, which usually minimizes energy in a bulk solid, is known not to last indefinitely as physical size is decreased. For very small elemental clusters, for example, one expects a structural switch from bulklike to some new arrangement at some critical radius [Garzón1998, Wang2002]. The driving force causing this morphological change at small size can generally be traced back to two very distinct sources: (i) electronic magic sizes, stabilized by filling of shells, as in atoms and nuclei; (ii) competition between optimal internal packing and minimal surface energy, the latter dominating for sufficiently small size.

Using MD simulations on Al and Pb, Gülseren *et al.* first suggested the formation of non-crystalline structures in ultrathin nanowires [Gülser1998]. In this work authors reported several amorphous and helical structures of diameters below 10.6 and 19.6 Å for Al and Pb respectively. Further works by Takayanagi *et al*

[Kondo1997, Kondo2000, Oshima2006] and Ugarte's group [Rodrigue2000] confirmed experimentally the appearance of Au nanowires with helical structures using high resolution transmission electron microscopy (HRTEM).

The study of non-crystalline, helical or amorphous nanowires is out of the scope of this thesis. Notwithstanding, we should briefly mention some simulations we carried out aiming to study the stability of a helical nanowire formed by 3 strands [Peláez2006]. In that work we compared the stability of the helical *versus* the 3-staggered nanowire structure. We found that the staggered structure was energetically more favourable. However, some interesting aspects concerning the use of periodic boundary conditions in our simulations showed up. The matching of the two ends of the unit cell imposed a strong restriction over the helicity of the nanowire. Thus, an infinitely long unit cell should be implemented in order to find the optimal nanowire helicity. However, we did not continue studies in this direction, and in this thesis we focus on the properties of FCC nanowires.

4.1.3 About this chapter

In this chapter we show results of our MD simulations aiming to understand structural properties of metallic nanowires. In particular, we are interested in nanowires that do not experience phase transformations, but in those that keep their FCC structure. In the following section we address the methodological aspects of this work: describing the types of nanowires we have considered and our simulation approach to find their equilibrium structure and cohesive energy. In section 4.3 we present results on the cohesive energy E_c of the nanowires under study. In particular we study the thickness dependence of E_c. The following sections show how the structure of these optimized nanowires is different from their unrelaxed bulk-like structures. We show results on the axial compression as well as surface relaxations these nanowires suffer. The next sections propose an equation of state (EOS) that relates the nanowire cohesive energy with the nanowire thickness. This equation of state is based on the concept of surface and edge energies and extends previous works [Gülser1998] where some approaches were not very accurate, leading to large errors in estimating edge energies. Finally, we use our corrected EOS to estimate the value of the edge energies in these nanowires.

4.2 Methodology

4.2.1 Nanowire families under study

In this chapter we address the structural properties of aluminum, copper and nickel nanowires. We have restricted ourselves to study nanowires with their main axis parallel to the [100], [110] and [111] directions of the FCC structure. For each axial orientation we have considered nanowires with three different cross sectional shapes: rectangular, hexagonal and octagonal. We define a nanowire *family* as a set of nanowires with the same axial orientation and similar cross-section shape. Through this work we will denote these nanowire *families* using the label $xxx-ijk$ where xxx corresponds to the keys *rec*, *hex* or *oct* for rectangular, hexagonal or octagonal, respectively, and $[ijk]$ describes the nanowire axial orientation (using the Miller index notation).

The combination of three different nanowire shapes with three crystalographic orientations gives rise to nine different families. Those nanowires that form a given family present a similar cross-section shape only differing in their effective diameter. Figures 4.1, 4.2 and 4.3 show schematic views of the nanowires under study. These figures also show the Miller index of the exposed facets. Notice that some kinds of exposed facets appear in different families. For instance, in figure 4.3, the $(11\bar{2})$ facet is exposed in $rec-111$ and $oct-111$ nanowires.

4.2.2 Optimizing the nanowire structure

As stated above, we are interested in finding the equilibrium configuration of infinite FCC nanowires. To do this we have run MD simulations at 4K. Temperature is kept constant by a Nosé-Hoover thermostat, generating a NVT ensemble as described in section 2.2.3.1 [Nosé1984]. Equations of motion are solved using a velocity-Verlet [Verlet1967] integration algorithm (see section 2.2.2.1) with a time step Δt between 5×10^{-2} ps and 1×10^{-1} ps for Al, Cu and Ni. Infinite nanowires are modeled by implementing periodic boundary conditions (PBC) along the z-direction, which corresponds to the nanowire axis orientation. We denote as L_z the simulation cell length along the z-direction. For nanowires oriented along an $[ijk]$ direction, the initial L_z is chosen to be an integer multiple of the interplanar distance d_{ijk} in the corresponding FCC orientation. In particular, for [100]-, [110]- and [111]-oriented nanowires, we have used $L_z = 4d_{100}$, $4d_{110}$ and $6d_{111}$ respectively. These nanowire lengths are larger than the EAM potential cutoff radius. Howerver, for some particular nanowires we have also performed simulations with two and three times the original

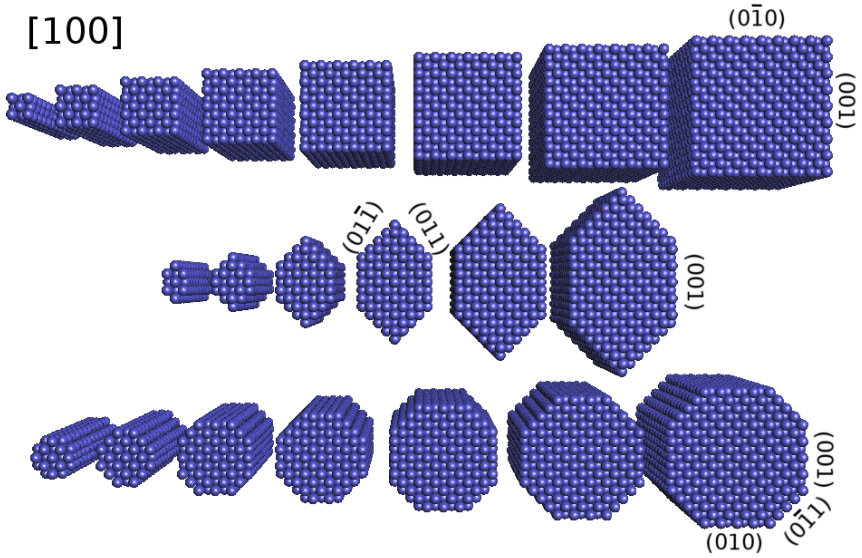

Figure 4.1: Schematic cross sectional view (in perspective) of nanowires under study. This figure depicts nanowires whose main axis is oriented along the [100] crystallographic direction. Three different cross section geometries have been considered: rectangular (top), hexagonal (middle) and octogonal (bottom), which define three *nanowire families*. The exposed surface types are labeled for some representative nanowire facets.

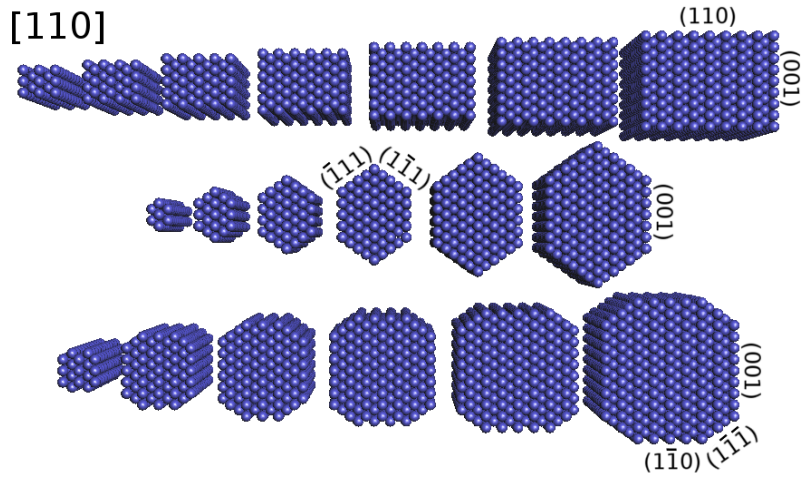

Figure 4.2: Schematic cross sectional view (in perspective) of nanowires under study. This figure depicts nanowires whose main axis is oriented along the [110] crystallographic direction. Three different cross section geometries have been considered: rectangular (top), hexagonal (middle) and octogonal (bottom), which define three *nanowire families*. The exposed surface types are labeled for some representative nanowire facets.

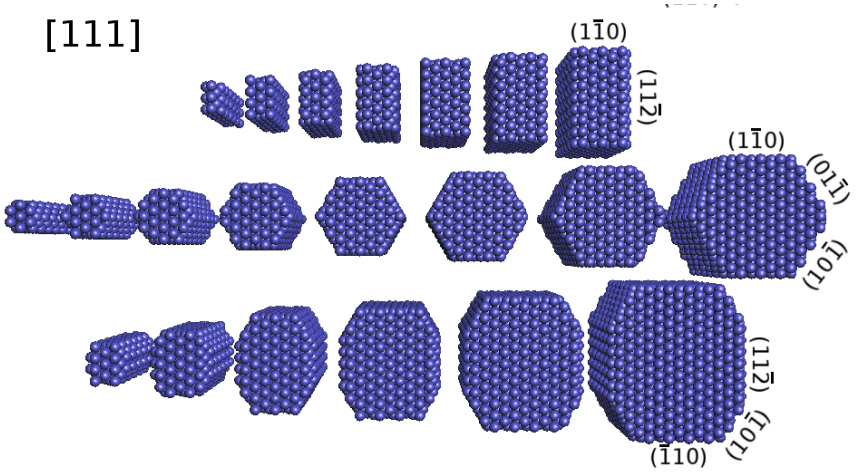

Figure 4.3: Schematic cross sectional view (in perspective) of nanowires under study. This figure depicts nanowires whose main axis is oriented along the [111] crystallographic direction. Three different cross section geometries have been considered: rectangular (top), hexagonal (middle) and octogonal (bottom), which define three *nanowire families*. The exposed surface types are labeled for some representative nanowire facets.

L_z, guaranteeing that results were independent on the choice of unit cell length and that the use of PBC did not cause inconsistencies.

In order to find the equilibrium configuration of the infinite nanowires we have systematically varied the unit cell length L_z. For every value of L_z we monitor the cohesive energy per atom E_c of the system during $6{\times}10^4$ simulation steps and extract the average E_c. Then the atomic coordinates are expanded/contracted and a new L_z is fixed. This procedure is run up to an 8% expansion/contraction. As a result we accumulate E_c *vs* L_z curves for every nanowire under study. Figure 4.4 shows one of these curves. This one corresponds to an Ni nanowire of the $rec-111$ family. In this curve we can see some common features with all the rest of simulations: there is an elastic region with a parabolic-like behavior. At some given strain value of the expansion/contraction the nanowire undergoes an inelastic deformation, in which strong atomic reorganizations take place and the nanowire looses its original structure. From the elastic region we can determine the optimal nanowire length L_z^{opt} at which the cohesive energy E_c is minimal. This structure corresponds to the equilibrium configuration of the crystalline phase of the nanowire.

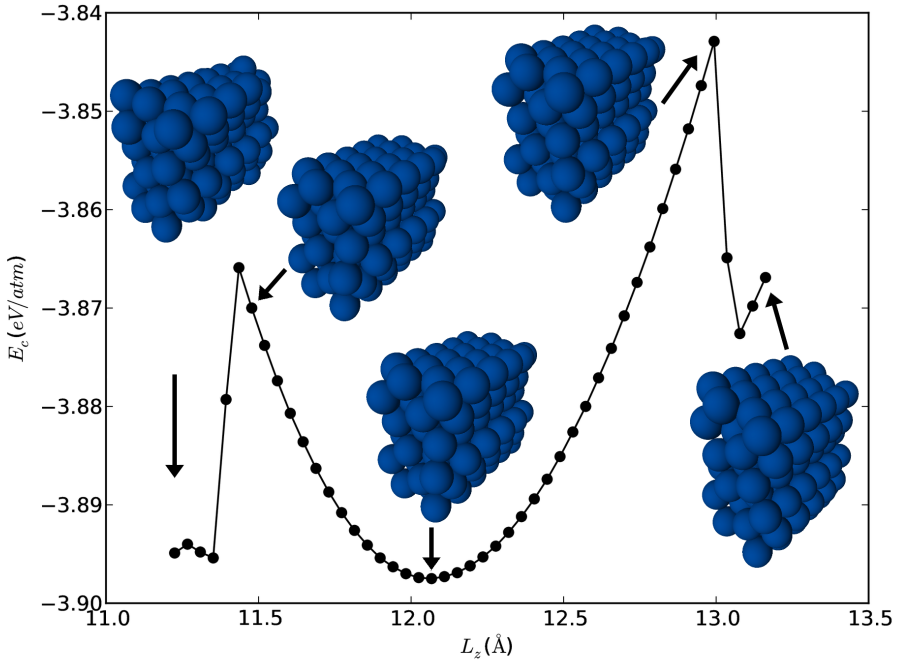

Figure 4.4: Cohesive energy per atom for one of the $rec-111$ Ni nanowires. Here we can see the parabolic-like region which corresponds to an elastic regime. However, when the nanowire is compressed below 11.4 Å or elongated above 13 Å its structure is irreversibly deformed (plastic phase). This particular nanowire shows its most favourable configuration at $L_z = 12.07$ Å.

4.2.3 Critical sizes for maintaining FCC structures

It must be noticed that some of the thinnest nanowires in figures 4.1, 4.2 and 4.3 do not hold their FCC structure even at this low temperature. Immediately after the simulation starts, they suffer a structural transformation to a non-FCC or disordered nanowire. This transformation from a crystalline to a non-crystalline structure has been reported for suspended ultra-thin Al and Pb nanowires [Gülser1998]. This behaviour is easily understood in terms of the huge surface/volume and edge/surface ratios in these ultra-thin nanowires. Due to the low atomic coordination of most of their atoms, the FCC structure is no longer favourable, and even a temperature as low as 4 K allows the system to explore more favourable configurations.

Howerver, the aim of this chapter is restricted to studying structural and mechanical properties of nanowires with FCC structure. Moreover, nanowires with non-FCC configurations lack of well defined surfaces and edges, which renders the study of their surface and edge energies unfeasible. For this reasons, these ultra-thin nanowires that abandon their original FCC structure have been discarded in the remainder of this and the next chapter. So, only nanowires that hold their structures upon at least small variations of L_z are included in the present results.

4.3 Cohesive energy E_c of nanowires

For each nanowire shown in figures 4.1, 4.2 and 4.3, we have performed MD simulations following the above described process of axial compression and expansion by variating the nanowire unit cell length L_z. During this process the system's cohesive energy E_c is monitored and the minimum energy L_z^{opt} value is calculated. We have thus obtained a full set of *optimized* nanowires. In this section we show some of the features we have observed and studied as a result of these simulations.

First of all, we have observed that the cohesive energy E_c^{nw} of the nanowires is always higher (less negative) than the bulk cohesive energy E_c^{bulk}. The thinner the nanowire, the larger the difference between E_c^{bulk} and E_c^{nw}. This is actually an expected result, since it is well known that the surface/volume ratio increases for thinner nanowires and the cohesive energy of surface atoms is lower that that of bulk atoms. The balance between small bulk-like core and large proportion of surface atoms gives an overall less cohesive nanowire.

Figure 4.5 illustrates this behaviour. In the abscissas, the nanowire radius R is used to denote its thickness. Since this radius R shall be used hereafter to denote nanowires thickness, it is important to state the way this quantity is estimated.

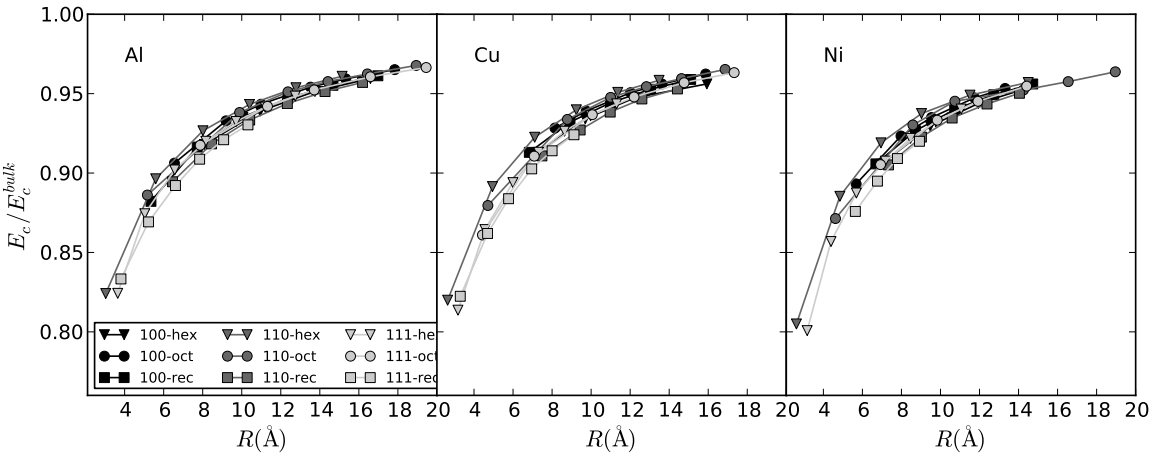

Figure 4.5: Measured cohesive energy E_c and unit cell length along the nanowire axis L_z for all the nanowires under study. Values shown correspond to the optimal L_z value (minimal E_c). The cohesive energy is normalized to the bulk E_c^{bulk} for the three studied materials. Similarly, the length of the nanowire is normalized to the bulk length corresponding to every orientation.

Following a previously proposed procedure [Gülser1998], the nanowire radius is calculated as that of a cylinder with the same cross sectional area A_{cs} as the nanowire.

$$R = \sqrt{\frac{A_{cs}}{\pi}} \tag{4.1}$$

This area is estimated as follows: We project the atomic coordinates onto the xy-plane. A line joining the coordinates of surface and edge atoms shapes the nanowire's perimeter. This perimeter is enhanced by a half of the interplanar distance of its exposed facets. The area of this "extended perimeter" is our estimated nanowire area A_{cs}. This procedure for estimating A_{cs} ensures aditivity: The total area of two nanowires joined together one aside the other must be equal to the sum of their separate areas.

4.4 Axial compression

We have also observed that, as a general trend, nanowires prefer a constrained situation with respect to the original (bulk-like) structure. This means that the length of the simulation cell L_z of thicker nanowires tends to the bulk value L_z^{bulk} of the initial nanowire. Thinner ones have $L_z < L_z^{bulk}$. This is due to the fact that most of the atoms are in surface or edge positions. In order to compensate for their very low atomic coordination, these atoms tend to come closer to each other. This implies a

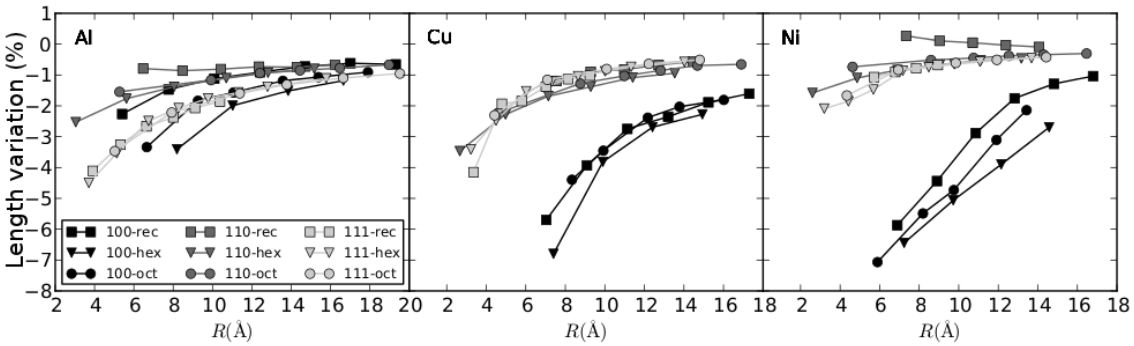

Figure 4.6: Percentage of axial length variation of the nanowires under study with respect to the corresponding bulk system as a function of the effective nanowire radius R.

reduction of the L_z length in most of the cases. An exception to this behaviour are Ni nanowires of the $100 - rec$ family, which seem to prefer a strong x-y contraction which makes L_z be slightly larger than L_z^{bulk} by up to a 0.26%). As the amount of core (bulk) atoms increases (thicker nanowires) these effects are weaker.

Figure 4.6 shows the axial length variation of all nanowires under study as a function of the nanowire effective radius R. This length variation is calculated as $(L_z^{opt} - L_z^{bulk})/L_z^{bulk} \times 100$. The first general trend to notice in this figure is that thinner nanowires exhibit larger values of axial compression. Also it can be seen that [100]-oriented nanowires exhibit the strongest contraction. This is particularly notorious in Cu and Ni nanowires. On the other hand axial compression in [111]-oriented nanowires is generally weaker (specially in those nanowires with rectangular cross section) than in the other orientations. Ni nanowires in the [110] direction with rectangular cross section are the only nanowires that are not compressed, but a little bit expanded (up to a 0.27%). Another feature to notice is that the nanowire cross sectional shape does not seem to influence too much the compression. Nanowire families of the same orientation have similar compression trends regardless of their cross sectional shape.

These results compare well with those reported by Wen *et al.* [Wen2007] for Ni nanowires. In that work nanowires oriented along the [100] direction exhibit the strongest compression, which goes up to a 3.7% for the thinnest nanowire they simulated ($R \simeq 10$ Å). On the other hand, nanowires oriented along the [110] and [111] directions show a weaker compression (up to $\sim 1.4\%$ for nanowires of similar thickness). In our simulations thinner nanowires are studied, but similar trends are observed. Nanowires oriented along the [100] direction also exhibit the strongest compression (of about 4% at $R = 10$) and both [110]- and [111]-oriented nanowires

show about 1% compression at this nanowire thickness. Nevertheless it should be noticed that in the work by Wen *et al.* [111]-oriented nanowires are slightly less compressed than [110] ones, whereas in our work both orientations exhibit almost the same compression.

These subtle differences are most likely due to the different type or EAM potential used in their simulations [Wen2007]. They have used the so-called Quantum Sutton-Chen (QSC) method [Kimura1998], which is a variant of the Sutton-Chen (SC) method described in section 3.1.1. However, QSC suffers from the same limitations as the SC method. Actually the functional forms defining its repulsive and embedding energy, as well as atomic density are just the same as those in the SC method (equation 3.2). The only difference are the values of the 4 parameters that define the parameterization (c, ϵ, m and n; table I of Kimura's work [Kimura1998]), which were optimized to fit 7 observables (lattice constant, cohesive energy, bulk modulus, elastic constants, phonon dispersion, vacancy formation energy and surface energy). As we have already discussed (see section 3.2), in spite of their more easy implementation, SC-like potentials lack the reliability of the potentials we have used (MFMP) because of the difficulty in fitting as many physical properties with only 4 parameters. The use of numerical functions in MFMP method (as described in section 3.1.2) allows a better fitting of more physical properties, making our results more reliable than those obtained using the QSC method.

4.5 Surface and edge relaxations

Another interesting feature we have observed in the structure of optimized nanowires is the atomic relaxations of the outermost surfaces and edges. As we have already discussed in section 3.3, it is well known that atoms at crystal surfaces behave differently from bulk atoms, due to the change in their atomic coordination [Lüth2001]. For instance, in many cases, the loose of neighbors of surface atoms is compensated by a uniform displacement of the outermost layers. This is known as surface relaxation. However, in some cases even the atomic structure of these outer layers changes. In these cases we talk about surface reconstruction [Oura2010, Hermann2011]. The relaxation and reconstruction of crystal surfaces has been thoroughtly studied over the last decades [Fisher2009].

It is not a specific goal of this work to describe in detail the characteristics of surface reconstructions in metallic nanowires. Nevertheless, should we breafly mention the general features of the atomic relaxations that we have observed in surface and

edge positions of our simulated nanowires. Figure 4.7 shows, for a few example cases, the unrelaxed (bulk-like) and relaxed atomic coordinates. Here it can be seen that for some nanowire families strong atomic relaxations occur in their surface and even more at their edge atoms. We have observed, as a general rule, that for a given nanowire orientation, less coordinated atoms show stronger relaxations. This is the case of atoms located at the edges of rectangular nanowires or those in the acute angle edge of hexagonal nanowires. The strongest change in the interatomic distances with respect to the bulk value was observed for the edge atoms of nanowires of the 111-rec family (shown in figure 4.7 for Al). For this edge atoms, we have seen a change of up to 30% in the distance to its nearest neighbors.

However, there does not seem to be a straightforward relation between the type of exposed facets and the magnitude of the relaxation of edge atoms. As suggested above, the angle ϕ between the free surfaces defining an edge is the relevant parameter that seems to influence the magnitude of this relaxation: Strongest edge relaxations happen in the edges of rectangular nanowires ($\phi = 90^o$) or in the acute angle edges of some hexgonal nanowires (when $\phi < 90^o$).

Regarding the relaxation of free surfaces (away from edges), we have observed that, surprisingly, outermost surface layers do not always exhibit the same relaxation as reported in section 3.3 for pure surfaces. For instance, a detailed look at the Ni 110-rec nanowire depicted in figure 4.7 shows that whereas the (100) surfaces (left and right sides) are compressed towards the center of the nanowire, the (110) surfaces (top and bottom sides) are expanded outwards. This is in contrast with the expected contraction towards the bulk reported in section 3.3 for Ni (110) surfaces.

We believe that these discrepancies point towards a different mechanism of surface relaxation in nanowires compared to free surfaces. Although a detailed study is out of the scope of this thesis, we can guess that the presence of other surfaces and edges strongly influences the way surface atoms try to compensate for their low atomic coordination with respect to bulk atoms.

4.6 E_c *vs* R: Equation Of State (EOS)

We may consider the cohesive energy E_c of a given nanowire to be the result of the contribution of the bulk-like coordinated core atoms plus the contribution of the less coordinated surface and edge atoms. In other words, we might regard E_c to be the sum over all atoms assuming they have the bulk cohesive energy E_c^{bulk} minus the surface and edge energies, which account for the energy cost of having exposed

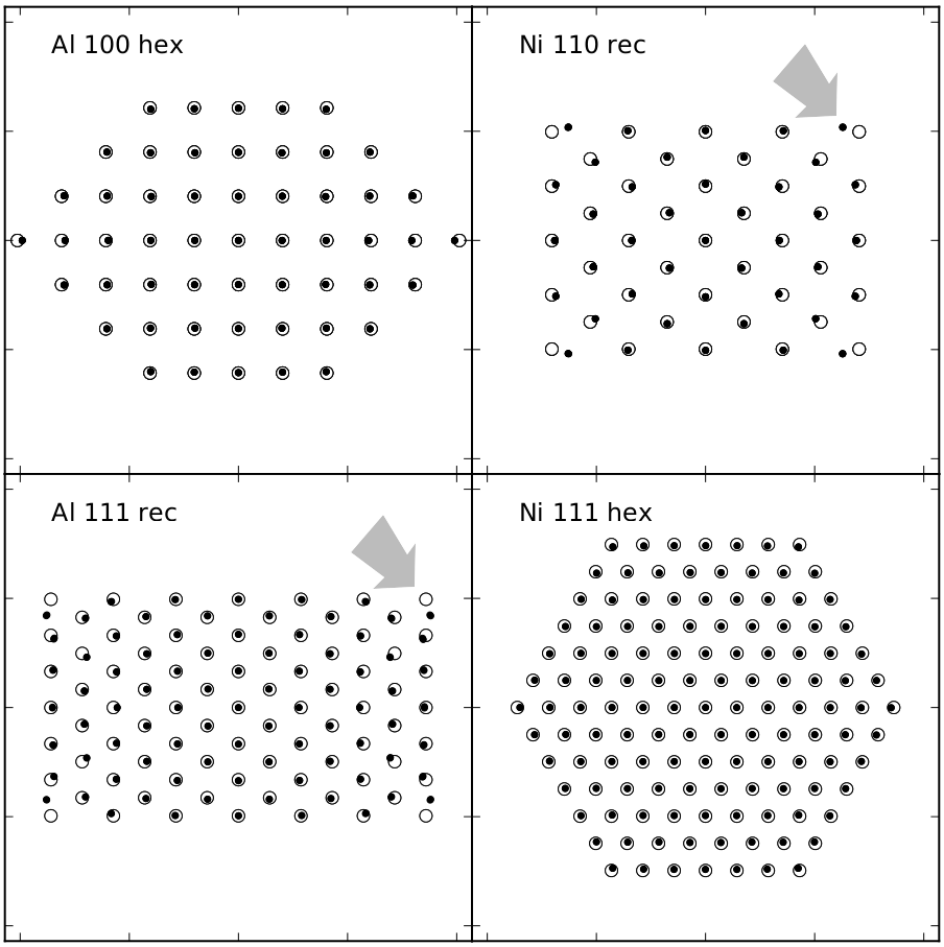

Figure 4.7: Atomic relaxations for some nanowires under study. Open circles correspond to the atomic coordinates of the unrelaxed nanowires. Black dots show the position of atoms in their optimal configuration (minimum value of E_c). Notice the strong relaxation of those atoms at the edges of the rectangular nanowires, which are pointed by the gray arrows.

surfaces and edges. This approach has been typically used, for instance, in estimations of the cohesive energy of solid clusters [Yu2007]. In the case of nanowires, this can be expressed in terms of the following equation of state (EOS)

$$E_c = N_{tot}E_c^{bulk} - \Delta E^{surf} - \Delta E^{edges} \tag{4.2}$$

where N_{tot} is the total number of atoms in the nanowire and $\Delta E^{surf/edge}$ represents the energy cost associated to the formation of surfaces/edges. For a crystalline nanowire with well defined facets and edges this can be put as follows:

$$E_c = N_{tot}E_c^{bulk} - \sum_{all\ facets} A_{facet}\gamma^{facet} - \sum_{all\ edges} L_{edge}\mu^{edge}. \tag{4.3}$$

Here A_{facet} is the surface area of a given exposed facet and γ^{facet} is the corresponding surface energy associated to that type of facet. Notice that for every type of exposed surface (ijk) in this study the value of its corresponding surface energy γ^{ijk} was calculated and reported in section 3.3. For each of the edges in a nanowire, L_{edge} represents its length and μ^{edge} its energetic cost, i.e., its edge energy.

Unlike surface energy, whose influence is quite relevant in the total cohesive energy of metal clusters, the edge energy term on 4.2 is usually neglected in the literature. Actually, when it comes to nanowires, the value of μ has been only approximately estimated in the work by Gülseren *et al.* [Gülser1998]. However, when we are dealing with ultra-thin nanowires, the importance of μ increases proportionally as the edge/surface ratio does.

Let us consider the EOS proposed in the work by Gülseren *et al.* [Gülser1998]. In that work, the ΔE^{surf} term of (4.2) is approximated as $\Delta E^{surf} = P_{cyl}L_z\bar{\gamma}$, where $\bar{\gamma}$ is the average surface energy of the different exposed facets of the nanowire. P_{cyl} $(= 2\pi R)$ stands for the perimeter of a cylinder with the same radius R as the nanowire (where this radius is estimated from the cross-section area A_{cs} of the nanowire as $R = \sqrt{A_{cs}/\pi}$). This approximation induces two errors: on one hand it assumes the exposed area of the nanowire to be equal to that of a cylinder, neglecting the polygonal shape of the nanowire cross section; on the other hand, this approximation considers all the exposed atoms of the nanowire to be surface atoms. This is not accurate, because some of the exposed atoms are really in edge positions and then should not contribute to ΔE^{surf}. These two inaccuracies assumed for constructing the nanowire EOS (a wrong estimation of the nanowire surface and a double-counting of edge atoms) are two critical factors when this EOS is used to determine the values of the average edge energies.

We have done a more accurate implementation of the EOS based on an exact counting of the surface and edge atoms. Let N_{surf}^{ijk} be the number of atoms in exposed facets of (ijk) surface type and let σ^{ijk} be the corresponding surface atomic density (which can be known from simple crystal analysis). Then the actual area associated to (ijk) surfaces is

$$A_{ijk} = N_{surf}^{ijk}/\sigma^{ijk} \tag{4.4}$$

In a similar way, for each type of edge present in a nanowire, the total edge length can be determined as

$$L_{ijk-lmn}^{uvw} = N_{ijk-lmn}^{uvw}/\lambda^{uvw}, \tag{4.5}$$

where a specific type of edge $E_{ijk-lmn}^{uvw}$ is defined by the two types of intersecting surfaces (ijk)-(lmn) that form the edge and its crystalline orientation $[uvw]$. So $N_{ijk-lmn}^{uvw}$ is the number of atoms in a given edge situation and λ^{uvw} is the linear atomic density along the $[uvw]$ crystalline direction.

Using this approach, the more accurate EOS takes the form:

$$E_c = N_{tot}E_c^{bulk} - \sum_{ijk} N_{surf}^{ijk}/\sigma^{ijk}\gamma^{ijk} - \sum_{\alpha} N_\alpha/\lambda^\alpha\mu^\alpha \tag{4.6}$$

Where α runs over all the edges $E_{ijk-lmn}^{uvw}$ in the nanowire.

4.7 Determining the edge energies μ

Notice that almost all of the quantities of equation (4.6) are known. E_c is obtained for every nanowire as the cohesive energy at the optimal L_z. Both E_c^{bulk} and γ^{ijk} for any surface of interest are known from the literature and from the calculations we have run in section 3.3. Also surface and linear atomic densities are all easily derivable from simple crystal analysis. Now, all the edges α of a nanowire have the same length ($\lambda^{uvw} = L_z$). Then the last sum of the right hand side of Eq(4.6) can be rewritten as $n_e L_z \bar{\mu}$, where n_e is the number of edges of the nanowire (4 for square, 6 for hexagonal and 8 for octagonal nanowires) and $\bar{\mu}$ is the average edge energy from the different types of edges in the nanowire. This average edge energy $\bar{\mu}$ can be solved from the equation (4.6):

$$\bar{\mu} = \frac{1}{n_e L_z}\left(E_c - N_{tot}E_c^{bulk} - \sum_{ijk} N_{surf}^{ijk}/\sigma^{ijk}\gamma^{ijk}\right) \tag{4.7}$$

Using this equation we are able to determine the average edge energy of the nanowires under study. More important, as we shall discuss later, our procedure allows an

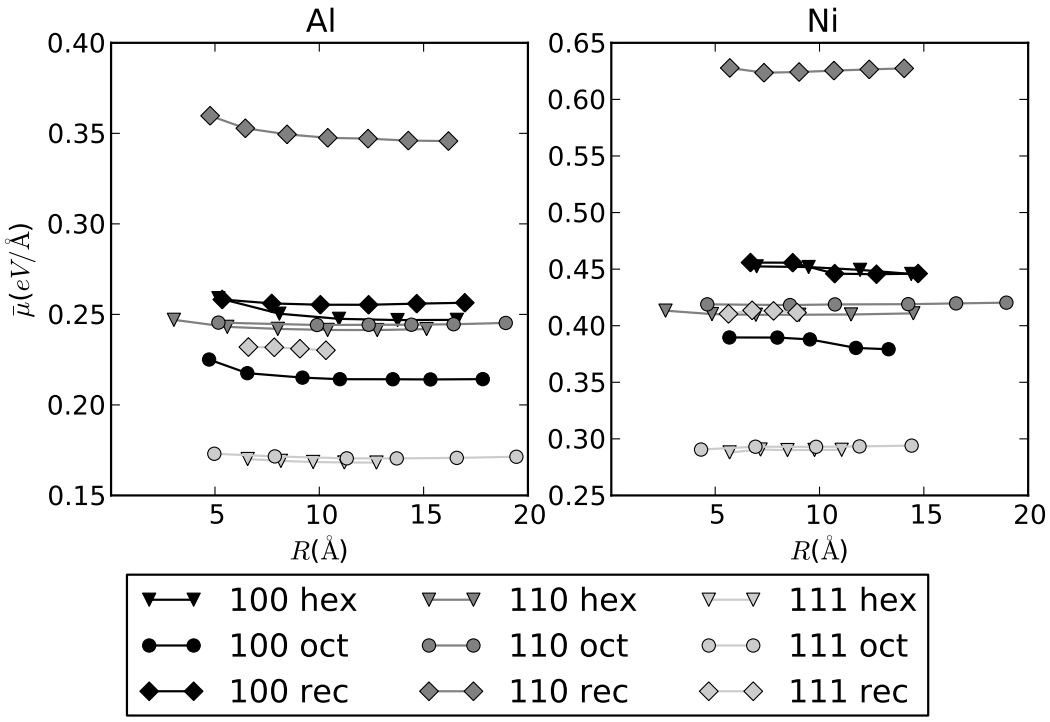

Figure 4.8: Average edge energy $\bar{\mu}$ of all nanowires under study.

accurate calculation of the specific value of the edge energy μ associated to a given kind of nanowire edge.

In the following we present results of edge energies calculations from the Al and Ni simulations. We have not estimated values of μ for Cu nanowires. This has been due to the lack of a reliable value for the surface energy γ of the (211) facet of Cu. This quantity is necesary for the estimation of μ in some nanowires, so we omit the calculation of μ for Cu.

4.7.1 Average edge energies $\bar{\mu}$

By filling in equation 4.7 with the appropriate values, we have calculated the average edge energy $\bar{\mu}$ for all the nanowires that show an elastic response keeping their original structure. The result of this calculation is presented in figure 4.8. Here we can see that $\bar{\mu}$ is nearly constant, particularly for thick nanowires. From this data the average edge energy can be extrapolated for the $R \to \infty$ nanowires. The resulting values are shown in table 4.1. From these values we can see that Al edge energies are lower than Ni ones. However this ratio is 0.6, which is not far from the ratio between

		[100]	[110]	[111]
Al	rec	0.2562	0.3498	0.2244
	hex	0.2501	0.2428	0.1688
	oct	0.2163	0.2447	0.1713
Ni	rec	0.4498	0.6258	0.4122
	hex	0.4498	0.4106	0.2898
	oct	0.3853	0.4192	0.2914

Table 4.1: Extrapolated values of $\bar{\mu}$ (in eV/Å) as $R \to \infty$ for all the nanowire families under study.

bulk cohesive energies of Al and Ni (≈ 0.75). A further inspection shows that, for every axial orientation rectangular nanowires exhibit the highest value of $\bar{\mu}$ for a given orientation. This is related to the low atomic coordination of atoms located in their edges (all edges are in a 90^o surface intersection) compared to hexagonal or octogonal cross sectional shapes, in which most of the edge atoms (or even all of them) have a higher atomic coordination (their edges are mostly in $> 90^o$ surface intersections).

It is important to notice that these values of $\bar{\mu}$ are about an order of magnitude larger than that reported by Gülseren *et al.* in Ref. [Gülser1998] for Al (35 meV/Å). This difference is due to two major differences in the way $\bar{\mu}$ is calculated in that work. On one hand, the total exposed surface of a nanowire is calculated as that of a cylinder of the same cross sectional area A; this introduces an error in the second term in Eq. 4.3, since the perimeter of a polygon is always greater than that of a circle (for instance, the perimeter of a polygon, divided by that of a circle of the same area is ${}^{P_{polygon}}/_{P_{square}}$ =1.128, 1.05 and 1.027 for squares, hexagons and octagons). On the other hand, the cylinder approach assumes that all exposed atoms are in a surface position, neglecting edge atoms, which are in a much lower coordinated situation. These two error contributions to the second order term in Eq. 4.3 induce a huge error on $\bar{\mu}$, which is a third order remainder.

4.7.2 Single edge energies

We have observed that in some particular cases a certain type of edge appears in different nanowire families. For instance, by looking at figure 4.1 we can see that the edge $E^{[100]}_{(001)-(0\bar{1}1)}$ (formed by the intersection of facets (001) and $(0\bar{1}1)$ in nanowires along the [100] direction) is present in both hexagonal and octogonal nanowires. Furthermore, we have decomposed the average edge energies $\bar{\mu}$ in the contributions

of individual edges, as follows:

$$[100]\ direction:$$

$$4\bar{\mu}_{\infty,rec-100} = 4\mu^{[100]}_{(010)-(001)} \tag{4.8}$$

$$6\bar{\mu}_{\infty,hex-100} = 4\mu^{[100]}_{(011)-(001)} + 2\mu^{[100]}_{(01\bar{1})-(110)} \tag{4.9}$$

$$8\bar{\mu}_{\infty,oct-100} = 8\mu^{[100]}_{(011)-(001)} \tag{4.10}$$

$$[110]\ direction:$$

$$4\bar{\mu}_{\infty,rec-110} = 4\mu^{[110]}_{(001)-(1\bar{1}0)} \tag{4.11}$$

$$6\bar{\mu}_{\infty,hex-110} = 4\mu^{[110]}_{(001)-(1\bar{1}1)} + 2\mu^{[110]}_{(\bar{1}11)-(1\bar{1}1)} \tag{4.12}$$

$$8\bar{\mu}_{\infty,oct-110} = 4\mu^{[110]}_{(001)-(1\bar{1}1)} + 4\mu^{[110]}_{(1\bar{1}0)-(1\bar{1}\bar{1})} \tag{4.13}$$

$$[111]\ direction:$$

$$4\bar{\mu}_{\infty,rec-111} = 4\mu^{[111]}_{(1\bar{1}0)-(11\bar{2})} \tag{4.14}$$

$$6\bar{\mu}_{\infty,hex-111} = 6\mu^{[111]}_{(1\bar{1}0)-(01\bar{1})} \tag{4.15}$$

$$8\bar{\mu}_{\infty oct-111} = 4\mu^{[111]}_{(1\bar{1}0)-(01\bar{1})} + 4\mu^{[111]}_{(01\bar{1})-(11\bar{2})} \tag{4.16}$$

where $\mu^{[uvw]}_{(ijk)-(lmn)}$ is the edge energy associated to the intersection of (ijk)- and (lmn)-type surfaces along the $[uvw]$ crystallographic direction. This decomposition shows that in some cases it is possible to determine the edge energy μ corresponding to a single type of edge by a suitable combination of equations 4.8 to 4.16 (between nanowires of the same orientation).

Some edge energies are straightforward to extract. That is the case of rectangular nanowires. For instance, from equation 4.11 it is obvious that $\mu^{[110]}_{(1\bar{1}0)-(001)} = \bar{\mu}_{\infty,rec-110}$. In other cases systems of two equations must be solved. From these particular relations some single edge values of μ have been obtained. These values are shown in table 4.2. Notice that for the [110] direction we have only calculated the edge energy corresponding to the $(E^{[110]}_{(1\bar{1}0)-(001)})$ edge, since equations (4.12) and (4.13) cannot be used to extract more information about other single edge situations because they involve three unknown edge energy values. Table 4.2 also shows some parameters that allow the characterization of every edge type: the coordination number N_c, the angle ϕ between the two planes defining the edge and the atomic linear density λ along the edge.

From results shown in table 4.2 it is possible to draw some trends: *i*) Ni edge energies are larger than those obtained from Al. *ii*) Edges with large angles present

			Al			Ni		
$\mu^{[\alpha\beta\delta]}_{(ijk)-(lmn)}$	N_c	ϕ	λ	μ	σ_{zz}	λ	μ	σ_{zz}
$\mu^{[100]}_{(010)-(001)}$	5	90^o		0.2562	39.6		0.4498	99.1
$\mu^{[100]}_{(011)-(001)}$	6	135^o	0.249	0.2163	69.7	0.287	0.3853	128.7
$\mu^{[100]}_{(01\bar{1})-(110)}$	4	90^o		0.3177	108.6		0.5788	206.2
$\mu^{[110]}_{(001)-(1\bar{1}0)}$	7	90^o	0.352	0.3498	-2.5	0.403	0.6298	14.4
$\mu^{[111]}_{(1\bar{1}0)-(11\bar{2})}$	4	90^o		0.2244	23.1		0.4122	18.5
$\mu^{[111]}_{(01\bar{1})-(11\bar{2})}$	6	150^o	0.144	0.1738	57.6	0.165	0.2930	43.5
$\mu^{[111]}_{(1\bar{1}0)-(01\bar{1})}$	5	120^o		0.1688	60.7		0.2898	66.7

Table 4.2: Properties of specific edges. Second and third columns show the coordination number N_c of edge atoms and the angle ϕ between the two facets defining the edge. The linear density λ (in $1/\text{Å}$) along the edge atoms is shown for every nanowire orientation. The single edge energy $\mu^{[\alpha\beta\delta]}_{(ijk)-(lmn)}$ (in eV/Å) is calculated (for some specific edge configurations) using the set of equations 4.8-4.16 and the average edge energies shown in Table 4.1. Also shown is the atomic stress σ_{zz} of edge atoms, computed according to equation 5.2. Notice the low stress of edge atoms in $E^{[1\bar{1}0]}_{(1\bar{1}0)-(001)}$ and $E^{[111]}_{(1\bar{1}0)-(11\bar{2})}$, due to their strong relaxation, as seen in figure 4.7.

lower edge energies *iii*) There is no clear relation between edge energy and the stress of edge atoms. Therefore, there is a complex interplay involving several quantities (λ, N_c, ϕ), and edge energies cannot be easily predicted from these values.

4.8 Conclusions

In this chapter we have shown results of our MD simulations on metallic nanowires. We have found the equilibrium configurations of Al, Cu and Ni nanowires with FCC crystalline structure. We have analysed the influence of crystallographic axial orientaion and cross sectional shape of nanowires on several properties. In particular, we have studied the thickness dependence of nanowire cohesive energy, axial compression and average edge energy.

We have observed that optimized nanowires tend to exhibit axial compression with respect to their unrelaxed bulk structure. As we have discussed, this behaviour is a way of maximize cohesion and compensate for the high surface to volume ratio. For this reason, the axial compression is stronger in thinner nanowires.

As expected in systems with low atomic coordination, we have observed that atoms located at the edges of nanowires exhibit strong reconstructions. Also, as we

pointed out, in these ultra-thin nanowires the edge to surface ratio is still high enough to alter the surface relaxations of the exposed facets.

We have used the concept of an Equation of State (EOS) to relate the cohesive energy of nanowires with their thickness. The use of this EOS allowed a estimation of the average edge energies of the nanowires under study. As expected, the values of $\bar{\mu}$ that we obtained converge as nanowire thickness R increases. The values of these edge energies are larger than those proposed by Gülseren *et al.* [Gülser1998] for Al. However, we believe this discrepancy is due to some artifacts in the way $\bar{\mu}$ is calculated in the work by Gülseren *et al.*

For the first time in the literature (as far as we know) values of the edge energy μ for specific edges have been proposed. However we have not been able to fully correlate these values with geometrical aspects or atomic coordination of edges.

Chapter 5

Mechanical properties of FCC nanowires

5.1 Introduction

When subjected to an applied stress, bulk and nanometer scale materials exhibit fundamentally different mechanical responses. Figure 5.1 illustrates this. In bulk materials, mechanical response is typified by a linear-elastic deformation followed by yield and subsequent plastic flow, generally not exceeding the MPa range. However, at nanometer scales, strengths in the GPa range are attainable and the overall response is characterized by a series of discrete yielding events leading to fracture [Agraït1995, Stalder1996]. The quantized nature of deformation at the nanometer scale reveals a disparity in the loading method. If the applied tensile stress is incrementally increased during deformation, the mechanical response exhibits instabilities in strain corresponding to 'instantaneous' changes in specimen length due to the motion of internal defects. Conversely, applying an incrementally increasing strain reveals yielding in increments of force (stress) instability attributable to dissipation of stored strain energy through the nucleation and motion of internal defects.

The complexities associated with experimental measurements of the mechanical properties of nanometer scale materials preclude conventional or nanoscale (like SPM) testing methods and lend towards computational tools to simulate their mechanical behavior. The vast majority of this computational work is carried out by using atomistic simulations, specially, Molecular Dynamics (MD). MD simulations using the Embedded Atom Method (EAM) have provided a fundamental understanding of the mechanical behavior of nanowires. In particular, FCC metallic nanowires have been studied extensively [Qiao2008, Ao2008, Jiang2009, Wen2010, Liu2011]. Simulations of gold nanowires [Diao2003] have shown that surface-stress resulting from

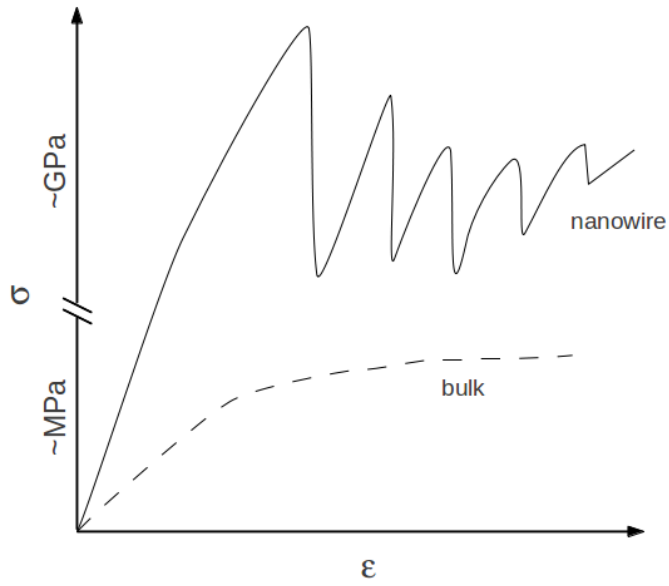

Figure 5.1: Illustration scheme of the elastic behaviour of metallic nanowires compared to bulk systems. σ represents the stress and ϵ the strain.

excess energy at free surfaces can be sufficient to induce a phase transformation from FCC to BCT if the wire cross-section is reduced to a critical dimension. Recently it has been demonstrated that surface stresses may also facilitate reversible lattice reorientations in some FCC nanowires, leading to shape-memory and pseudoelastic behavior [Liang2006, Liang2005b, Park2005a, Park2006b, Cao2010]. Upon external applied stress, in general, single crystal metallic nanowires deform by two deformation mechanisms: twinning and slip by partial dislocation motion [Park2006a]. Crystal twinning occurs when domains are formed with different orientations within the nanowire, as seen in fig 5.2a. In slip, nanowire slices displace along well defined parallel crystal planes, as seen in fig 5.2b. It has been shown that the initial deformation mechanism is dependent not only on the nanowire axial and free surface orientations (in relation to the loading direction), but also on the predictive capacity of the atomistic model with respect to the unstable and intrinsic stacking-fault energies [Park2005b, Zimmerma2000]. In this sense, the MFMP EAM parameterization provides a reliable approach to study the deformation and breaking of metallic nanowires, since it has been designed to fit vacancy, interstitial and planar defects energies.

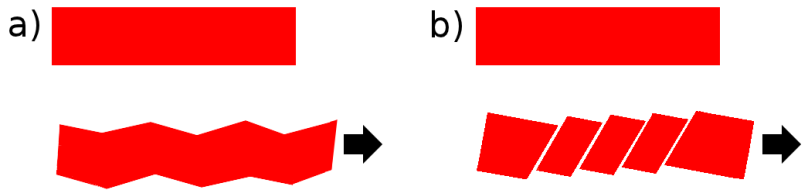

Figure 5.2: Schematic illustration of a) twinning and b) slip deformation mechanisms in single crystal metallic nanowires.

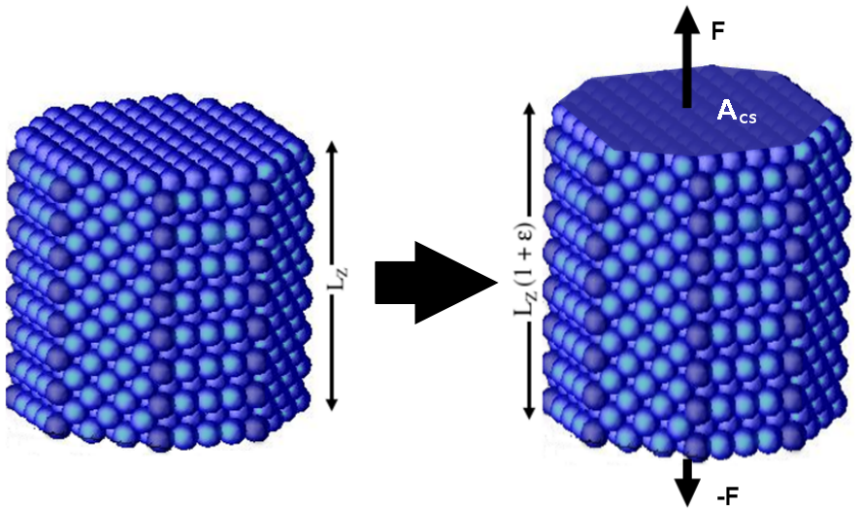

Figure 5.3: Scheme of the axial elongation of an octogonal nanowire.

5.1.1 About this chapter

In this chapter we have studied the response of FCC metallic nanowires to uniaxial strain. In particular, we focus on the elastic phase of this deformation process. To this end we have calculated their Young's modulus E (also known as *tensile modulus*). This quantity is a measure of the stiffness of an elastic material. It is defined as the ratio of the uniaxial stress σ_{zz} over uniaxial strain ϵ within the range of elastic deformation. Consider the octogonal nanowire depicted in figure 5.3. In this figure a force F is exerted along the nanowire axis. This force produces a linear deformation of the nanowire, changing its length L_z into $L_z + \Delta L_z$. From the definition of uniaxial strain $\epsilon = \Delta L_z / L_z$, the Young's modulus can be calculated as:

$$E \equiv \frac{\sigma_{zz}}{\epsilon} = \frac{F/A_{cs}}{\Delta L_z / L_z} \tag{5.1}$$

where A_{cs} is the cross-sectional area of the nanowire, calculated as explained in section 4.3.

In order to compute the Young's modulus of nanowires, we have used the same families of nanowires used in the previous chapter. These consist of nanowires of Al, Ni and Cu with three different cross-sectional shapes (rectangular, hexagonal and octogonal), with their axis aligned with three crystallographic directions ([100], [110] and [111]), and with different thicknesses. Like in the previous chapter, the choice of these families of nanowires allows a comprehensive analysis of the influence of shape and orientation on the thickness dependence of elastic behaviour of these nanowires.

As explained in the previous chapter (section 4.2.2), we have run MD simulations of the dynamics of nanowires at a constant temperature of 4 K. In our simulations, the length of the simulation unit cell is expanded/contracted along the z-axis. By monitoring the zz-component of the stress tensor we have accumulated stress *vs.* strain curves. The slope of these curves at the equilibrium configuration (minimum cohesive energy and zero stress) is a measure of the Young's modulus.

The stress tensor is computed the standard virial procedure [Basinski1971, Chen2005], in which the $\alpha\beta$-component of the tensor on particle i is

$$\sigma^i_{\alpha\beta} = \frac{1}{V_i}\left[\frac{1}{2}m_i v_i^\alpha v_i^\beta - \frac{1}{2}\sum_j \frac{\partial U}{\partial r_{ij}}\frac{r_{ij}^\alpha r_{ij}^\beta}{r_{ij}}\right] \tag{5.2}$$

and the total stress of the system is just a sum over all the atoms:

$$\sigma_{\alpha\beta} = \frac{1}{V}\sum_i V_i \sigma^i_{\alpha\beta}. \tag{5.3}$$

where U is the potential energy V_i is the volume of atom i, v_i^α and r_{ij}^α are the α-component of its velocity and its distance to atom j respectively.

In this chapter, in section 5.2 we present the results obtained for the thickness dependence of the Young's modulus E of nanowires of all of the families we have considered. We compare these values of E with the corresponding value of the Young's modulus of a bulk sample E_{bulk}. However in monocrystals the value of E_{bulk} depends on the strain direction. For a strain direction given by the (unitary) vector $\mathbf{n}$, the value of E_{bulk} can be obtained from the elastic constants of the crystal [Chen2005] as:

$$\frac{1}{E_{bulk}} = \frac{C_{11}+C_{12}}{(C_{11}+2C_{12})(C_{11}-C_{12})} + \left(\frac{1}{C_{44}} - \frac{2}{C_{11}-C_{12}}\right)(n_x^2 n_y^2 + n_y^2 n_z^2 + n_z^2 n_x^2) \tag{5.4}$$

where C_{11}, C_{12} and C_{22} are three independent elastic constants [Ashcroft1976]. Using this equation we have calculated the values of E_{bulk} for the three crystal orientations of our families of nanowires ([100], [110] and [111]) and the three metallic species under

	Al	Ni	Cu
C_{11}	114	247	138
C_{12}	62	147	170
C_{44}	32	125	76

Table 5.1: Experimental values of the elastic constants C_{ij} (in GPa) for Al, Ni and Cu FCC crystals. Values extracted from [Simmons1971].

E_{bulk}	Al	Ni	Cu
[100]	70.4	137.3	88.89
[110]	79.9	233.5	154.17
[111]	83.7	304.6	204.15

Table 5.2: Young's moduli E_{bulk} (in GPa) for Al, Ni and Cu and for three crystallographic orientations. These values have been obtained from equation 5.4 and data from table 5.1.

consideration. The values of the elastic constants were extracted from [Simmons1971] and are shown in table 5.1. The resulting values of E_{bulk} are shown in table 5.2.

Following the calculation of the Young's moduli of nanowires, in section 5.3 we show the form of the stress *vs.* strain curves. This allows a better understanding of the Young's moduli shown in section 5.2. We have observed remarkable non-linear elastic behaviour in some of the nanowires under study and propose an explanation to this unexpected features.

5.2 Young's moduli

From the MD simulations detailed in section 4.2.2, we have accumulated the stress *vs.* strain curves for all the nanowires depicted in figures 4.1 to 4.3. By calculating the slope of these curves within the elastic range around the equilibrium (zero stress) nanowire configuration, we have calculated the Young's modulus E of every nanowire.

Figure 5.4 shows the Young's modulus E of all nanowires simulated. For every nanowire family $ijk - xxx$ and metallic species, E is shown normalized by the bulk value of Young's modulus along the $[ijk]$ direction. A first look at this figure shows that the axial orientation of nanowires plays the most relevant role in the size dependence of the Young's modulus. For every axial orientation, nanowires of different shapes exhibit approximately the same behaviour of E *vs* R.

In the case of Al it can be seen that, for every family of nanowires, E tends to the bulk value as R increases. The deviation from E_{bulk} is clearly orientation-dependent: thinner nanowires along the [100] orientation have a decreasing E, whereas [110] and

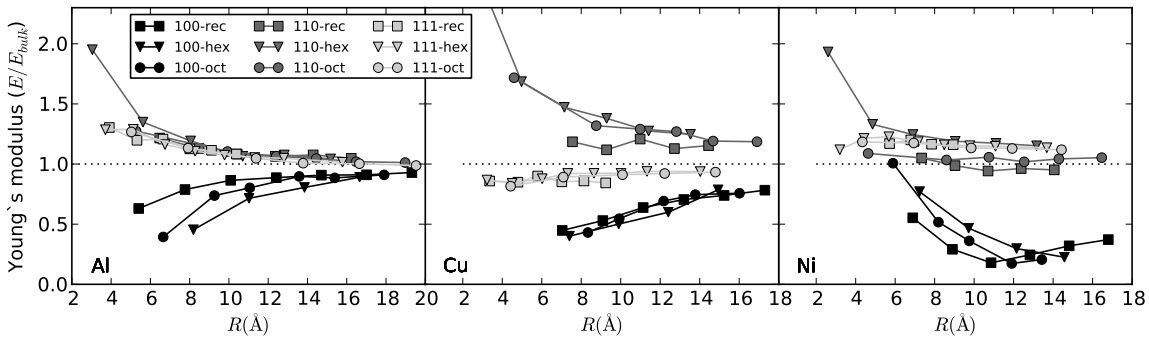

Figure 5.4: Young's modulus E of the nanowires under study as a function of their radius R. For every nanowire family and metallic species, E is normalized by the bulk value E_{bulk} along the corresponding orientation.

[111] oriented nanowires have $E > E_{bulk}$ for thinner nanowires. On the other hand, Cu nanowires along the [111] orientation exhibit a small deviation from E_{bulk}. But unlike Al [111] nanowires, Cu ones have $E < E_{bulk}$. Nanowires along the [100] orientation show small values of E ($\sim E_{bulk}/2$) which increase slowly with R. Narrowest nanowires in the [110] orientation exhibit larger values of E. These results for Cu are in agreement with those reported by Liang *et al.* [Liang2005a]. They studied the size dependence of the Young's modulus of nanowires with different orientations. In their work they also found that [111]-oriented nanowires had values of E slightly smaller than E_{bulk}, whereas nanowires along the [100] and [110] orientation exhibit a larger deviation from E_{bulk} towards lower and higher values of E respectively as R decreases.

The case of Ni is particularly striking. Young's modulus of Ni nanowires oriented along the [110] and [111] increases slowly as R decreases. The deviation from E_{bulk} is small for most of the families in these orientations. Only the thinnest nanowire of the $110 - hex$ family has $E > 1.5E_{bulk}$. However, [100] oriented nanowires exhibit an unexpected dependence of E *vs* R: For the three families under study (*rec*, *hex* and *oct*) E presents a minimum value at $R \sim 11 - 15$ Å. In order to understand this behaviour of E *vs* R we have studied in detail all of the stress-strain cycles, as discused in the following section.

5.3 Stress-Strain response

The stress response to axial deformation in metallic nanowires has been already analyzed by other authors [Liang2005a, Wen2007]. In these works the second derivative of stress with respect to axial deformation ($d^2\sigma_{zz}/d\epsilon^2$) is different from zero. That is,

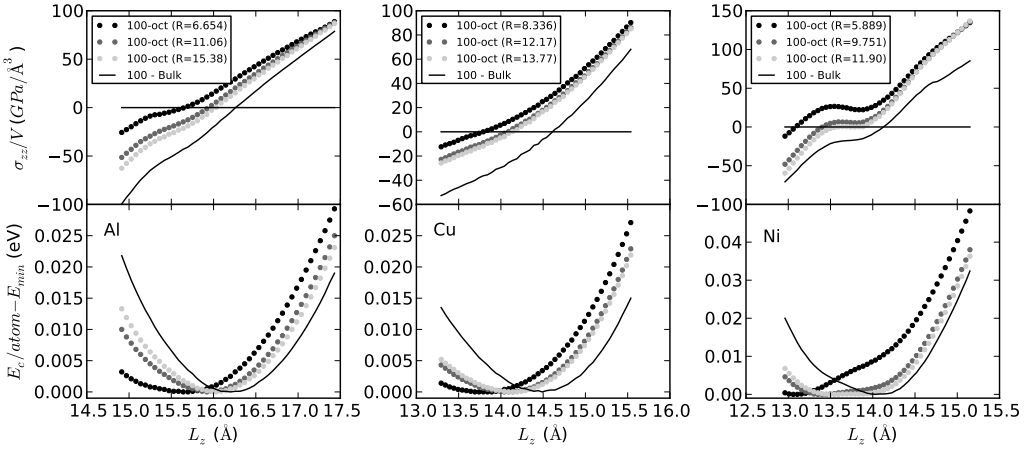

Figure 5.5: Stress (top) and cohesive energy (bottom) response to axial deformation in a few $100 - oct$ nanowires (dots) for Al (left), Cu (middle) and Ni (right). Solid lines show the σ_{zz} and E_c behaviour of the corresponding bulk monocrystals.

stress response is non-linear. Furthermore, a work by Wen *et al.* [Wen2008] shows that even bulk Ni monocrystals exhibit this non-linear behaviour. In the present work we have analyzed the σ_{zz} *vs* ϵ dependence for all families of nanowires, as well as for the corresponding bulk monocrystals.

Figure 5.5 shows these curves for a few sample nanowires of the $100 - oct$ family of the three metallic species under study. The upper graphs show σ_{zz} normalized by the system's volume, whereas the bottom graphs depict the cohesive energy per atom shifted so as to have all curves with the same minimum value $E_c = 0\,eV$. In all these plots the darker dots correspond to thinner nanowires, and the continuous line corresponds to the bulk behaviour for that orientation.

The first thing to notice in Figure 5.5 is that the stress response is not linear in any of the cases, even in bulk. However one must keep in mind that these simulations correspond to a $\pm 8\%$ strain. If we restricted ourselves to a, say, $\pm 1\%$, the linear approximation seems reasonable for Cu and even for Al nanowires. Another thing to notice is that the equilibrium configuration (*i.e.*, the point of minimum E_c and $\sigma_{zz} = 0$) of the thinner nanowires is found at smaller values of L_z. This produces the axial compression of nanowires discused above and shown in Figure 4.6.

The stress-strain behaviour observed in Figure 5.5 also helps to understand the thickness dependence of Young's modulus reported and discused in section 5.2. The deviation from E_{bulk} observed in thinner nanowires is a consequence of two factors: 1) non-linear stress-strain response in crystalline systems (even in bulk) and 2) nanowire contraction, which makes the equilibrium configuration be a L_z value corresponding

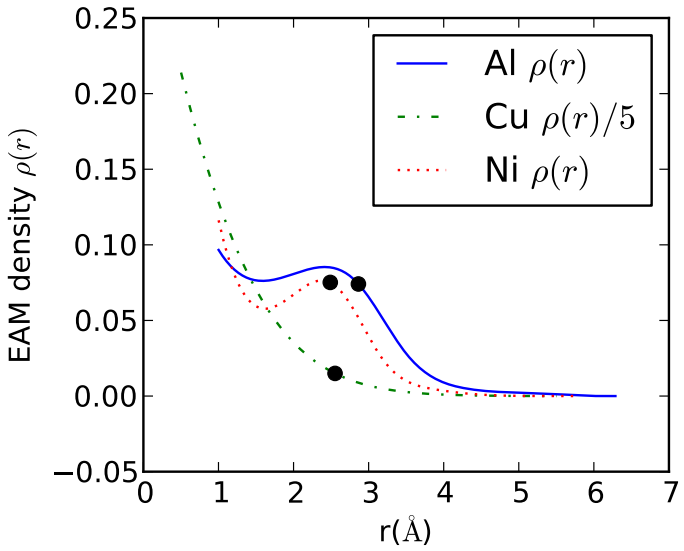

Figure 5.6: Density function of MFMP EAM potentials for Al, Cu and Ni [Mishin1999, Mishin2001].

to a point of higher (or lower) slope of the stress-strain curve than the bulk L_z.

By looking at the Ni nanowires in Figure 5.5 the unexpected behaviour of Young's modulus E of figure 5.4 can be understood. Bulk Ni exhibits a strong non-linear stress response curve along the [100] direction. It is evident from this curve that when compression is applied to a [100]-oriented crystal, there is a region of near zero stress slope (*i.e.*, near zero E). Since Ni nanowires oriented along the [100] orientation exhibit a strong axial compression (as discussed in section 4.4), there is expected to be a range of nanowire thickness' whose axial compression falls in the near zero E regime, producing the effect observed in Ni $100 - xxx$ nanowires in Figure 5.4.

In order to understand this striking behaviour of the Ni $100 - xxx$ family, we have looked into the structural changes that take place during the strain process. By inspecting the evolution of the radial and angular distribution functions we have observed no structural changes in the nanowire (appart from the obvious axial contraction or expansion).

5.4 Understanding the non-linear elastic response

A clue on the origin of this behaviour can be found by inspection of the potential energy function that we have used to describe the interatomic interactions. As explained above, the EAM potential that we have used has an energy contribution that depends on the local density of the system. Figure 5.6 shows the density function

$\rho(r)$ used to determine the atomic density. In the Al and Ni curves, there is a local maximum at ~ 2.5 Å and a local minimum at ~ 1.5 Å respectively. This contrasts with the monotonically decreasing curve for Cu. This may explain the oscilation in the stress-strain curve observed for Al and Ni in Figure 5.5 even for bulk systems.

This raises several questions: Is this non-linear behaviour a consequence of an erroneous estimation of the electronic density in the EAM parameterization we used? Or is it a real physical property of these systems? If the latter, then why do Al and Ni exhibit this property and does not Cu?

In favor of the EAM parameterization used in this work, it shoud be noticed that these EAM parameterizations (by Mishin *et al.*) do fit the elastic constants C_{11}, C_{12} and C_{44} [Mishin1999, Mishin2001] of the bulk FCC structure. This agreement suggests that they are reliable enough regarding the elastic properties of materials. Furthermore, compared with other semi-empirical potentials that usually have a few parameters, the Mishin EAM parameterizations are expected to provide a better fit to other physical properties it has not been originally designed to fit.

Nevertheless, there is no guarantee that its agreement on the elastic properties of the bulk equilibrium structure will hold under variation of the lattice constants. A deeper insight on this subject may be obtained by implementing *ab initio* simulations that deal with the elastic response of bulk and nanoscale objects upon deformation. However, attempting MD simulations such as those we carried out is currently unfeasible using *ab initio* methods. A first approach could be to compute the stress-strain response for bulk systems to check if the non-linear effects observed in figure 5.5 are also observed. This kind of calculations would be an exigent benchmark for the ability of EAM potentials to describe the elastic properties of materials. We plan to attempt to carry on these calculations in the near future.

An important aspect of these results is the tunneability of the Young's modulus of a given material by controlling the diamter of the nanowire (with little dependence on the chosen cross section shape). This property could be of interest for developing NEMS with well controlled mechanical properties.

Part III

Breaking metallic nanowires

Chapter 6

The breaking process of Ni nanowires

6.1 Introduction: Interest in the breaking process of metallic nanowires

The interest in metallic nanowires and nanocontacts arises from their very rich phenomenology. In particular, electron transport through metallic nanowires presents ballistic features at and below room temperature (RT) since, in general, the electron mean free path (l) is larger than the characteristic nanowire dimensions (in Cu, for instance l is about 30 nm at RT and up to ~ 3 mm at 4 K [Kittel1995]). Furthermore, well-defined electron transport modes appear, associated to the transversal confinement of electrons, as illustrated in figure 6.1. In these systems the conductance G (inverse of the nanowire resistance, $G = 1/R$) can be described in terms of the Landauer formula [Landauer1970]

$$G = \frac{2e^2}{h} \sum T_i \tag{6.1}$$

which relates the conductance with the transmission probabilities T_i associated with electron scattering processes taking place at the nanocontact region. Here e is the electron charge and h is Plank's constant. The factor $2e^2/h$ is known as the *conductance quantum* G_0.

As explained in chapter 1, metallic nanowires are fabricated using a variety of techniques. Some of these methods, like those based on Scanning Tunneling Microscopy (STM) and Mechanically Controllable Break Junctions (MCBJs), allow one to monitor the so-called conductance trace, $G(t)$, *i.e.* the time evolution of conductance during the nanowire breaking. Each conductance trace shows its own features since it is impossible to accurately control the nanowire geometry during its mechanical deformation. Figure 6.2 shows a few typical $G(t)$ curves obtained from Au nanocontacts breaking, illustrating the independent character of every breaking event.

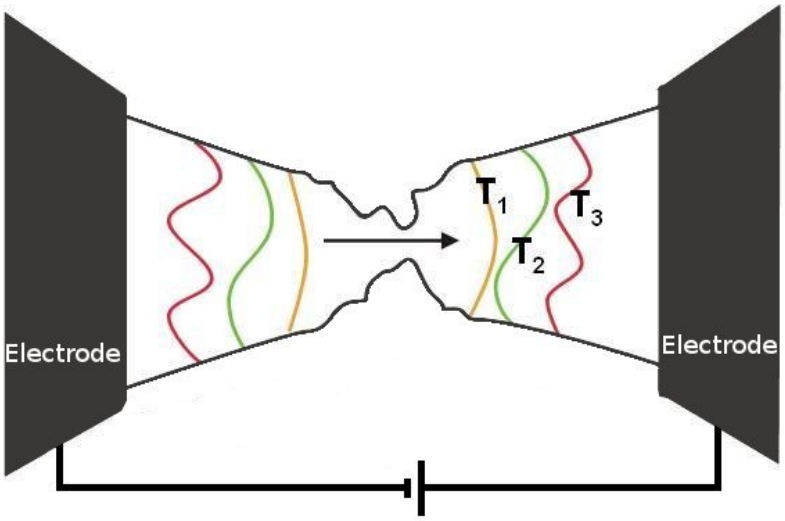

Figure 6.1: Scheme of the electronic transport through a nanosized conductor. The lateral confinement induces a quantization of the available electronic channels. Based on an illustration by Makk Peter (http://doktori.bme.hu/).

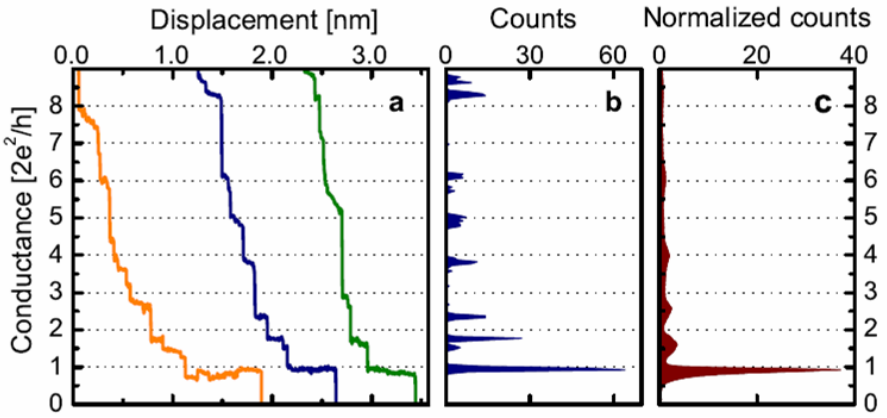

Figure 6.2: Left graph: typical curves for the time evolution of conductance G (normalized by the conductance quantum G_0) during the breaking of Au nanowires at room temperature. Middle graph: conductance histogram extracted from these three conductance traces. Right graph: conductance histogram obtained from a larger sample of (not shown) $G(t)$ curves. Based on an illustration by Makk Peter (http://doktori.bme.hu/).

The fact that $G(t)$ curves from sucessive breaking events are always different even under the same conditions makes it necesary to perform a statistical analysis in order to extract relevant information from them. Conductance histograms $H(G)$ are constructed by accumulating hundreds of $G(t)$ curves obtained under the same experimental conditions (see figure 6.2). These histograms reveal the most probable conductance values, observed as peaks in the histogram. This provides valuable statistical information on the transport and structural nanocontacts properties. In many cases, conductance histograms present well-defined peaked structures close to integer multiples of the conductance quantum G_0. Such preferred conductance values have been interpreted in terms of conductance quantization [Yanson1999] or favourable atomic arrangements [Yanson1997, Hasmy2001]. Actually the interpretation of $H(G)$ is a complex issue due to this merging of mechanical and electrical information. Moreover, both properties are strongly correlated [RB1996]. These interpretation problems are more intricate for polyvalent metals, where several channels per atom are available [Scheer1997].

The situation worsens for magnetic species where the electron spin must be considered as well as the presence of additional scattering sources (such as magnetic domain walls, for instance). However, the simultaneous control of charge and spin transport opens new opportunities for future applications in spintronics. For this reason, electronic transport in atomic sized magnetic nanowires has been profusely studied. The first study in which a conductance histogram was shown [Olesen1995] also reported the existence, at RT, of a $H(G)$ with a peaked structure for Ni nanocontacts. However, further experiments at RT (without external magnetic field) obtained featureless $H(G)$ adding unselected $G(t)$ curves [CK1997, Ott1998]. In contrast, $H(G)$ obtained in ultrahigh vacuum (UHV) at room and higher temperatures showed peaks on fractional values of G_0 [Oshima1998]. Similar results were obtained in Ni experiments carried out at RT using a few selected conductance traces [Ono1999, Ooka2001, Shimizu2002, Sekiguch2005], using Ni nanowires prepared with electrochemical methods [Elhoussi2002], as well as for other magnetic metallic species [Rodrigue2003] and for nanowires made of bulk non-magnetic metals [Rodrigue2003, Gillingh2002]. Nevertheless, it has been demonstrated that conductance histograms formed with not enough conductance traces must be cautiously considered [Díaz2006].

The situation is different at low temperatures (4K and UHV conditions), where experiments showed Ni $H(G)$ with two well-defined peaks, one around $\sim 1.6\,G_0$ and another at $\sim 3.1\,G_0$ [Bakker2002, Untiedt2004] (not modified by the presence of strong

magnetic fields [Untiedt2004]), the lower peak being consistent with pioneering jump-to-tunnel results [Sirvent1996]. More recent experiments [Jacob2006] show that this peak is formed by the superposition of two sub-peaks located at $G \sim 1.2\,G_0$ and $G \sim 1.5\,G_0$.

Summarizing, we can describe two opposite results for Ni: on one hand the low temperature $H(G)$ showing a well-defined and reproducible peaked structure, and, on the other hand, RT results showing a bunch of different $H(G)$'s. These differences between low and room temperature results are not well understood since, in both cases, the system is below its bulk Curie temperature ($T_c = 903$ K) as well as its melting temperature ($T_m = 1728$ K), and consequently similar magnetic and mechanical behaviours are expected.

Theoretical studies on Ni nanocontacts provide a more defined situation. G takes values in the range 1.35–1.6 G_0 for a Ni nanowire formed by three atoms attached to two (100) leads [Smogunov2006]. The conductance takes values in the range 1–2.5 G_0 for different trial monomer and dimer configurations used to describe the nanocontact region [Sirvent1996]. Recent calculations on dimer-like Ni nanocontacts have demonstrated that $G \sim 1.8\,G_0$ for a full ferromagnetic situation [Jacob2005]. Therefore there are several theoretical results on structures with a single atom contact that could explain the origin of the first experimental peak found in Ni histograms at low temperature. However, the behaviour of $H(G)$ at RT as well as its differences with the low temperature situation remain unexplained.

The diversity of experimental results has encouraged us to study the behaviour of nanowires during their breaking process at low and room temperatures by means of Molecular Dynamics (MD) computer simulations. We have followed a statistical approach, just like in the experimental setups, where breaking-joining cycles are sucessively repeated, thus accumulating a great amount of $G(t)$ traces. However, the nature of these experimental procedure does not allow a control of the crystallographic orientation of the sample after serveral breaking cycles. For this reason, in our simulations we have considered nanowires with different crystallographic orientations. Furthermore, we have restricted ourserves to only breaking the nanowires, avoiding the time consuming joining part of the cycles.

In general, previous computational simulations focused on the description of single nanowire breaking events, neglecting the study of statistical effects due to their high computational cost [Olesen1994, Landman1990, Bratkovs1995, Sorensen1998, Ikeda1999, Braníc2000]. More recently, several MD studies have statistically established a correlation between preferred atomic configurations and experimental con-

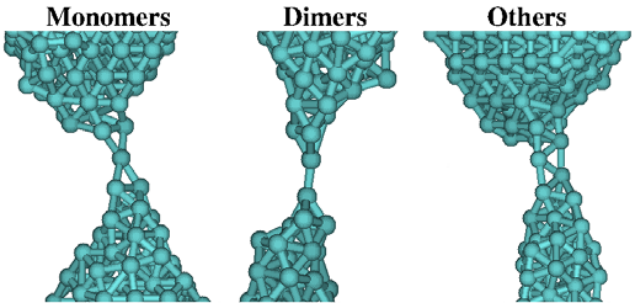

Figure 6.3: Three examples illustrating different types of Ni nanowire configurations just before breakage (from the [110] orientation at $T = 4$ K; other orientations and temperatures present similar structures).

ductance histograms at different temperatures [Hasmy2001, Hasmy2005, Jacob2006, Medina2003, GM2005a].

We have developed a methodology [Hasmy2005, Medina2003, GM2005a] to analyse the different types of structures appearing at the last stages of the breaking processes. In previous studies, our group has studied the breaking process of Ni[111] nanowires with large initial thickness [GM2005a]. In these studies, well-defined peaked structures were found in the computational histograms identifying the geometric shape of the narrowest part of the nanoneck for sections with less than 16 atoms [GM2005a]. However, these results were very different from those obtained for small initial thickness Ni[100] nanowires by other authors [Jacob2006, Pauly2006]. Therefore, these discrepancies must be understood to validate the construction of computational histograms as a useful methodology. Furthermore, it is mandatory to know their dependence on the nanowire crystallographic direction as well as the nanowire initial size.

It is worth saying that the lowest conductance peaks observed in conductance histograms are associated with those configurations appearing during the last stages of the breaking process (as those examples shown in figure 6.3). It is also known that for polyvalent metallic species (like Al or Ni) the electron transport is very different if the nanocontact is formed by one atom (monomer) or two atoms (dimer) [Sirvent1996, Dreher2005, Hasmy2005]. To complete the information depicted in the computational histograms, the MD computational tools we have developed allow the analysis of the types of structures appearing when the nanocontact has one atom cross-section size. This allows us to determine the relative abundance of monomer-like and dimer-like structures. Furthermore, our MD approach provides information about the surrounding environment of atoms in these configurations.

As part of the work of our group in this topic, a PhD. thesis was presented recently [Guerrero2010], focusing mainly on the appearence of magic numbers in the minimum cross sections of nanowires during their breaking process. In the present thesis we extend that work by performing an exhaustive study of the breaking of nanowires paying special attention to the formation of one atom contacts (monomers or dimers), as well as long pentagonal chain structures (next chapter) in the last stages of the breaking process.

6.1.1 About this chapter

This chapter is organized as follows. In the following section we detail the particular aspects of the methodology used in our simulations of nanowire breaking. This includes a detailed description of the MD procedure used to simulate the breaking of metallic nanowires. In order to get output from the simulations that can be compared to the experimental data, we have implemented a methodology able to average histograms of the nanowire minimum cross section obtained from different crystallographic orientations. These procedures are explained in section 6.2. In section 6.3 we show the results obtained from our simulations. These include the production of histograms of the minimum cross section, identification of the atomic configurations of the narrowest section of the nanowire just before its breaking, and measurements on the amount of disorder along the nanowire.

6.2 Methodology

6.2.1 MD simulations of breaking nanowires

Our approach is based on the statistical study of the structural evolution of many nanowires under stretching, using standard Molecular Dynamics (MD) simulations (see section 2.2). Each breaking event, even starting from identical initial conditions, evolves showing its own features. This is due to thermal fluctuations, that provide randomness and unpredictibility to the atomic motion (just as in actual experiments, where different $G(t)$ traces are observed under identical experimental conditions). Therefore, the only possibility to carry out an accurate study of the mechanical and electrical properties of the breakage process is performing a statistical analysis. We follow a similar strategy to the experimental one, simulating hundreds of independent breaking events, in order to determine the presence of preferred configurations. In particular, we have developed a methodology [Hasmy2001, Medina2003, Hasmy2005,

GM2005b] able to generate hundreds of computational breaking events and analyse them statistically to determine the different structures appearing in the breaking processes. We describe this methodology in the following.

The dynamics of the nanowires has been studied at constant temperature T using a standard velocities scaling algorithm [Rapaport1997] at every MD step (see section 2.2.3.1). The time interval used for the integration of atomic trajectories (MD time step) is $\Delta t = 10^{-2}$ps. Atomic trajectories and velocities were determined using conventional Verlet velocity integration algorithms [Verlet1968]. We have checked that results obtained using this value of Δt are equivalent to those obtained with shorter time intervals, ensuring the quality of the results with the smallest computational cost.

The simulation of a single nanowire breaking event consists of three stages. The first stage corresponds to the definition of the initial unrelaxed structure. We consider as initial nanowire a bulk super-cell with parallelepiped shape, containing hundreds of atoms ordered according to a FCC structure with bulk lattice dimensions. Notice that we have considered only a rectangular (or square) cross section for the initial nanowire, discarding the use of hexagonal or octagonal shapes. However, we believe that these geometry constrictions do not change the general breaking picture, specially the last stages when the nanowire is about to break. The initial parallelepiped height coincides with the stretching direction and is larger than the base edges. We define the z axis as the stretching (pulling) direction. In these studies we have considered three different stretching directions corresponding to the [100], [110] and [111] crystalline directions of the FCC structure and two different parallelepiped sizes (large and small) with similar aspect ratio for each direction. Figure 6.4a shows the initial configuration corresponding to a [111] Ni nanowire. At the beginning of the simulation, each atom's velocity is assigned randomly according to a Maxwellian distribution corresponding to the desired simulation temperature [Rapaport1997].

The second stage corresponds to the relaxation of the bulk-like initial structure. Firstly, we define two supporting bilayers at the top and bottom of the supercell. Atomic x and y coordinates within these bilayers will be kept frozen during the simulation. The nanowire will remain attached to these two bulk-like supporting bilayers during the relaxation stage. This stage lasts for 3000 MD steps in order to optimize the geometry of the isolated parallelepiped-like nanowire. However, in some partiular cases (for large nanowires) we have used larger relaxation times in order to get a well optimized structure as starting point of the stretching process. In our simulations scheme periodic boundary conditions are not used at all. Instead, the

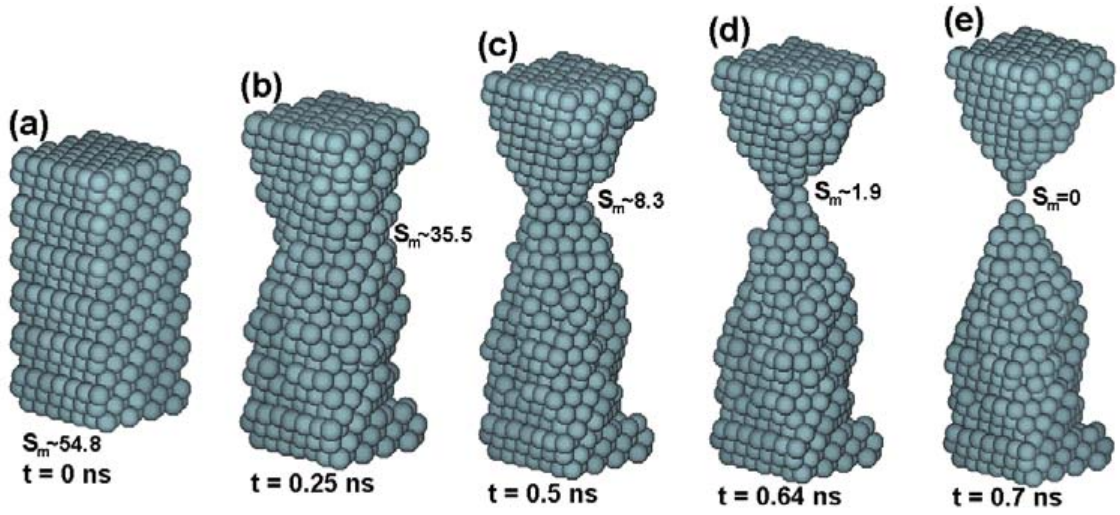

Figure 6.4: Five different snapshots of a [111] Ni nanowire during stretching at $T =$ 300K from its initial parallelepiped shape. Each snapshot includes information on the simulation time and the minimum cross-section S_m at that time.

"frozen" bilayers represent the connection with the bulk-like electrodes of a suspended nanowire.

The third stage is the stretching process. The z coordinate of those atoms forming the top (down) frozen bilayer is forced to increase (decrease) a quantity $\Delta z = 10^{-4}$Å after every MD step. This incremental process simulates the separation of the supporting bilayers in opposite directions at constant velocity of 2 m/s, which ultimately gives rise to the nanowire fracture. Those atoms located between the frozen regions move following the forces derived from their EAM-like interaction with the surrounding atoms. Finally, we consider that the nanowire has completely broken when its minimum cross-section is zero (the determination of this magnitude shall be explained in the following subsection). It must be noticed that our choice of the stretching velocity is much larger than that used in experiments [Agraït2003]. However, it is smaller than the sound velocity in the solid metals we are working with (Al, Cu and Ni) [Landman1996], which allows for atomic relaxation between successive instabilities.

In figure 6.4 we depict five snapshots corresponding to different stages of a representative nanowire breaking process (a Ni nanowire stretched along the [111] orientation at 300K), starting with the initial (unrelaxed) configuration and finishing with the configuration just after the breakage. During stretching the nanowire shape develops through typical slip processes leading to inelastic deformations. Notice that during the last stages of the breaking process the nanowire structure evolves, forming

a bipyramidal structure, each pyramid formed by three energetically favourable (111) facets.

6.2.2 Minimum cross section during a nanowire breakage

During the stretching stage, the accurate knowledge of the atomic coordinates and velocities allows the full determination of the minimum cross-section S_m of the nanowire. This quantity provides relevant information on the favourable configurations appearing at the narrowest part of the nanowire during its evolution under stretching. Furthermore, S_m provides a first-order approximation of the conductance, since in ballistic conductors the electronic transport can be related to the cross sectional area by the Sharvin's fourmula [Sharvin1965]:

$$G_S = \frac{2e^2}{h}\left(\frac{k_F R}{2}\right)^2$$

where R stands for the nanocontact radius and k_F for the Fermi wave vector of the electrons passing through the nanocontact. The minimum cross-section S_m (in units of atoms) is calculated following standard procedures that have been successfully used in previous studies [Bratkovs1995, Sorensen1998].

In order to calculate the cross-section S_i at a given z_i position, we firstly compute the atomic volume $V_{tot,i}$ inside a "detecting cursor" of width Δz. We have used $\Delta z = d_{111}$. We assign a volume $V_0 = 4\pi r_0^3/3$ to each atom and, therefore, the quantity $S_i = V_{tot,i}/V_0$ corresponds to the nanowire section (in number of atoms) at the z_i position. In our case, we define the atomic radius r_0 to be equal to half the FCC (111) interplanar distance ($r_0 = d_{111}/2$). In figure 6.5a is sketched the method used to measure S_i from a [110] Ni nanowire simulation at 4K. The detecting cursor moves along the z axis between the two frozen bilayers, using a step equal to $0.1 \times d_{111}$. This allows to calculate with high spatial accuracy the cross-section S_i along the nanowire. Finally, from the set of collected S_i values, we determine the minimum cross-section value S_m. Note that the cursor size Δz is kept fixed independently on the nanowire crystalline direction along the z axis. This allows a true comparison between histograms obtained for different orientations, especially at the last breaking stages. In our study S_m is calculated every 10 MD steps, obtaining the $S_m(t)$. Figure 6.5a shows a S_i profile, as well as the Δz slab where the minimum cross section S_m is detected.

The evolution of S_m with time shows a typical staircase trace, similar to the conductance traces of experiments (see figure 6.2). In figure 6.5b some examples of

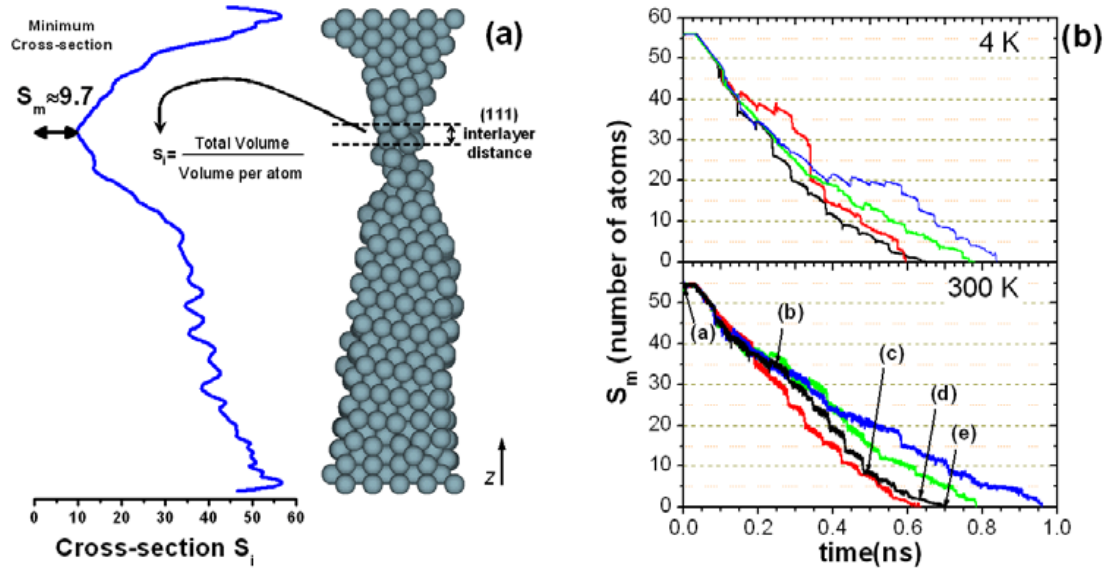

Figure 6.5: a) Example of how cross-section S is calculated along a [110] nanowire and its minimum value S_m. b) Evolution of the minimum cross-section S_m (measured in units of the number of atoms) as a function of time for four [111] Ni nanowires during their breaking process at two temperatures $T = 4$K and $T = 300$K. Labels (a)–(e) pointing at the black line correspond to the five different snapshots depicted in figure 6.4. (Illustration taken from [Peláez2010]).

$S_m(t)$ illustrate this behaviour. $S_m(t)$ traces show a stepped profile with well-marked jumps associated to atomic rearrangements that take place within the nanowire. As it is expected, the quantity S_m presents larger fluctuations when temperature increases, as it is shown when comparing the traces obtained at 4 and 300 K. This behaviour has been observed for the three stretching orientations.

Following the same methodology used in experiments, we summarize the information of many breaking events in histograms. In particular, the minimum cross-section histograms $H(S_m)$ are built by accumulating $S_m(t)$ traces acquired during the simulation of hundreds of nanowire stretching processes. We have shown that 100 independent nanowire breakages can be enough to build a reliable cross-section histogram, but more samples could be necessary for performing the statistical analysis of other quantities [GM2005a, GM2005b].

6.2.3 Merging different stretching orientations

As we have already mentioned, statistical analysis play a key role in order to extract valuable information from computer simulations of the breaking of metallic nanocontacts. However, an even more reliable comparison of our simulations with experimen-

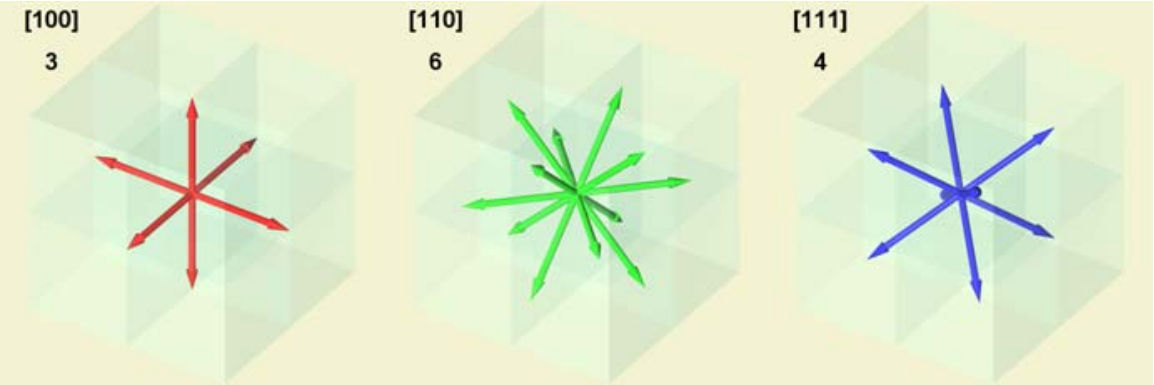

Figure 6.6: FCC main crystalline directions ([100], [110], [111]) and their multiplicities (3, 6 and 4 respectively).

tal results requires an additional element. Experimental data usually corresponds to the statistical average of nanowire breaking events involving random stretching directions. In a standard STM or MCBJ experiment there is no reason that indicates that any particular orientation would be preferred during the nanowire formation and breakage. Therefore, to accomplish a complete statistical analysis equivalent to the experimental one, computational calculations must simulate breaking events on random stretching directions. This could be a potential problem since it is not easy to perform simulations with arbitrary (random) initial stretching directions. Fortunately, it is not necessary to compute "every" stretching orientation to get the statistical behaviour of the breaking nanowires.

In an experiment, the final stages and behaviour of a breaking nanowire are leaded by the type of crystalline structure closest to its elongation direction. So should it be in simulations. Therefore, we need only to analyse main crystalline orientations (those that show different structural type) and average their results according to their occurrences. In other words, to achieve orientation statistics in computational simulations, results from the main crystalline directions have to be *merged* with the appropriate weights. These weights will be proportional to the zone axis multiplicity [Gonzál2004]. Of course, each main direction must have an accurate statistics to guarantee the correctness of the global results.

Nickel has a FCC crystalline structure. In figure 6.6 we show FCC main crystalline directions ([100], [110] and [111]) and their multiplicities (3, 6 and 4 respectively). Their relative occurrence at random stretching orientation should be 3/13, 6/13 and 4/13. These are the weights we have used in this thesis to *merge* the statistical results from the three main directions and obtain average results that can be compared with the experimental ones.

In this chapter, in our estimation of the probability of finding monomer and dimer structures, we provide (additionally to the results for every orientation) *merged* results, which correspond to this weighted average over the three crystallographic orientations considered.

6.2.4 Identification of monomers and dimers: the 'burning' algorithm

We have found that the final stages of a nanowire breaking can be classified according to three different categories: monomers, dimers and "others" (as illustrated in figure 6.3). The monomer structure is characterized by a central atom standing between two "pyramids". In the dimer structure, the apex atoms of two opposite pyramidal configurations form a two-atoms chain. Final configurations that do not match these two categories, presenting more complex structures, have been labelled as "others".

Complex structures (those labelled as "others") generally show an abrupt jump from $S_m \geq 2$ (i.e., structures formed by two or more atoms) to $S_m = 0$. This feature could be used as a signature of such type of breaking pattern. On the other hand, monomers and dimers are characterized by similar S_m values ($S_m \sim 1$), being difficult to distinguish among them if we only take into account the minimum cross-section value. So, an additional methodology is required to discriminate between monomer and dimer structures.

The procedure we have used is based on the "burning" algorithm introduced by Herrmann & Stanley [Herrmann1984a, Herrmann1984b]. This algorithm was originally designed to study the internal structure of percolating clusters at the percolation threshold. We have made a simple generalization of this algorithm to disordered lattices in order to solve the problem of identifying monomers, dimers and other structures at the last stages of the nanowire breaking process. In the spirit of the burning algorithm, if an atom belonging to a monomer or dimer structure is suppressed from the nanocontact, no connection will exist between both sides of the wire. This type of atoms (also called 'red bonds') represent the *links* in percolation theory. In a nanowire configuration, two atoms are identified as *linked* (i.e., they are neighbours) if its separation is smaller than a predefined distance d_{Cond}. This distance was chosen between the first and second nearest neighbours distance of the Ni FCC structure.

The steps of the actual algorithm are described in the next paragraphs with the support of figure 6.7:

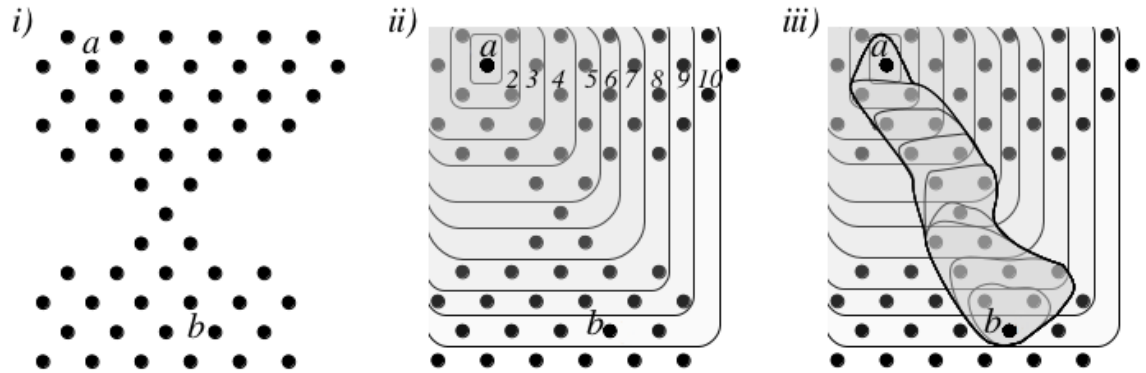

Figure 6.7: Bidimensional representation of the *burning* procedure designed by Herrmann *et al.* [Herrmann1984a] in a nanocontact. *i*) Step 1 of the Herrmann algorithm: An atom of each side of the contact is chosen. They are labelled as a and b. *ii*) Step 2 of the algorithm: The structure is *burned* starting from atom a until atom b is reached. *iii*) Step 3 of the algorithm: Another burning procedure is started from atom b until atom a is reached. The thick line indicates the subset of atoms of the *elastic backbone*, which contains the shortest possible paths between a and b.

1. Two atoms from both frozen sides of the wire are arbitrarily chosen. This atoms are called a and b, as schemed in figure 6.7 *i)*. This figure shows a bidimensional representation of the burning procedure.

2. From atom a the structure is "burned" for the first time. This means that atom a is labelled 1. All the neighbours of this atom are labelled 2. Next, all the neighbours of atoms of type 2 are labelled 3 except atoms that were already labelled. This procedure is repeated until the atom b is labelled as n. This can be seen in figure 6.7 ii). In this example, atom b is labelled as $n = 10$.

3. From atom b the structure is "burned" again. Atom b with label n and all its neighbours whose label is strictly lower than the label of atom b are separated in a new object. The neighbours with label $n-2$ from these atoms with labels $n-1$ are added to the new object, and so on. The procedure finishes when atom a is added to the object. In figure 6.7 *iii)* this is represented by a growing subset of atoms. The final subset of atoms is called *elastic backbone*. It is the union of all the minimal paths between atoms a and b. This includes atoms in monomer or dimer configurations.

4. Atoms in monomer or dimmer configuration are those responsible for the ultimate connection between two sides of the structure. In order to identify them, we iterate over every atom on the elastic backbone, temporally separating it

and burning the structure again. If no connection is observed, then we may safely say that this atom belongs to a monomer or a dimmer.

5. If only one connection atom is found, we can conclude that the structure is a monomer. If there are two connection atoms, then the structre corresponds to a dimer. If no connection atoms are obtained, this means that the breaking configuration corresponds to the "other structres" type, as depicted in figure 6.3.

We consider that two atoms are connected when the distance between their centres is lower than the distance $d_{Cond} = 3$ Å. Results using distances closer to the Ni nearest neighbours distance do not show relevant differences. Using this d_{Cond} value, we have determined the probability of appearence of monomers, dimers and other structures, for all of our simulations.

6.3 Simulations on the breaking of Ni nanowires

6.3.1 Minimum cross-section histograms $H(S_m)$

Minimum cross-section histograms $H(S_m)$ have been built by accumulating $S_m(t)$ traces acquired during the simulation of 300 nanowire breaking processes per histogram. In figures 6.8, 6.9 and 6.10 we show $H(S_m)$, at 4 and 300K, for the [111], [100] and [110] stretching directions, respectively. The geometric parameters characterizing the different initial bulk-like nanowires are shown at the right-hand side (cross-section×length). These histograms clearly show the effect of temperature, initial nanowire size, and crystallographic stretching directions on the average structural evolution of breaking Ni nanowires.

A first inspection reveals the existence of well-defined peaks associated to preferred nanowire configurations [Hasmy2001, Hasmy2005, GM2005a]. The peaked structures are rather sharp at $T = 4$ K. By increasing T, the general shape of the $H(S_m)$ is basically preserved, although the peaks show more rounded shapes with a better definition. Small peaks at $T = 4$ K correspond to metastable configurations with local minimum energy; the increase of temperature allows the exploration of more configurations, leading to a better peak definition. These thermal effects are more remarkable for [100] and [110] stretching directions. For both orientations, the histograms present a protruding $S_m = 5$ peak at $T = 300$ K that we will discuss in the next sections.

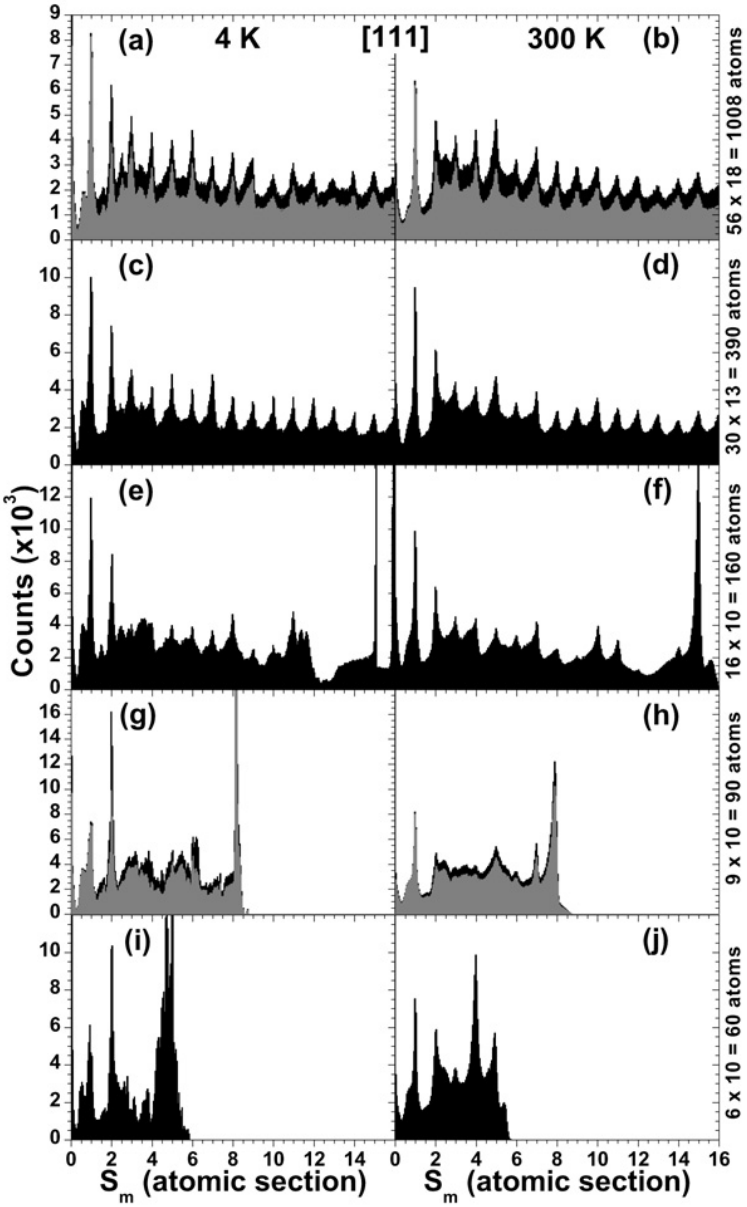

Figure 6.8: Minimum cross-section histograms $H(S_m)$ (black filled curves) built with 300 independent Ni nanowire ruptures under stretching along the [111] direction at $T = 4$K ((a), (c), (e), (g), (i)) and 300K ((b), (d), (f), (h), (j)). Different rows correspond to different initial parallelepiped sizes as indicated by the right-hand side labels (atoms per layer $\times$ number of layers). For two nanowire sizes [((a), (b)) and ((g), (h))] we show an $H^*(S_m)$ constructed taking into account only those samples that showed monomers or dimers in the interval $0.25 < S_m < 1.75$ (grey filled curves) as explained in subsection 6.3.2.

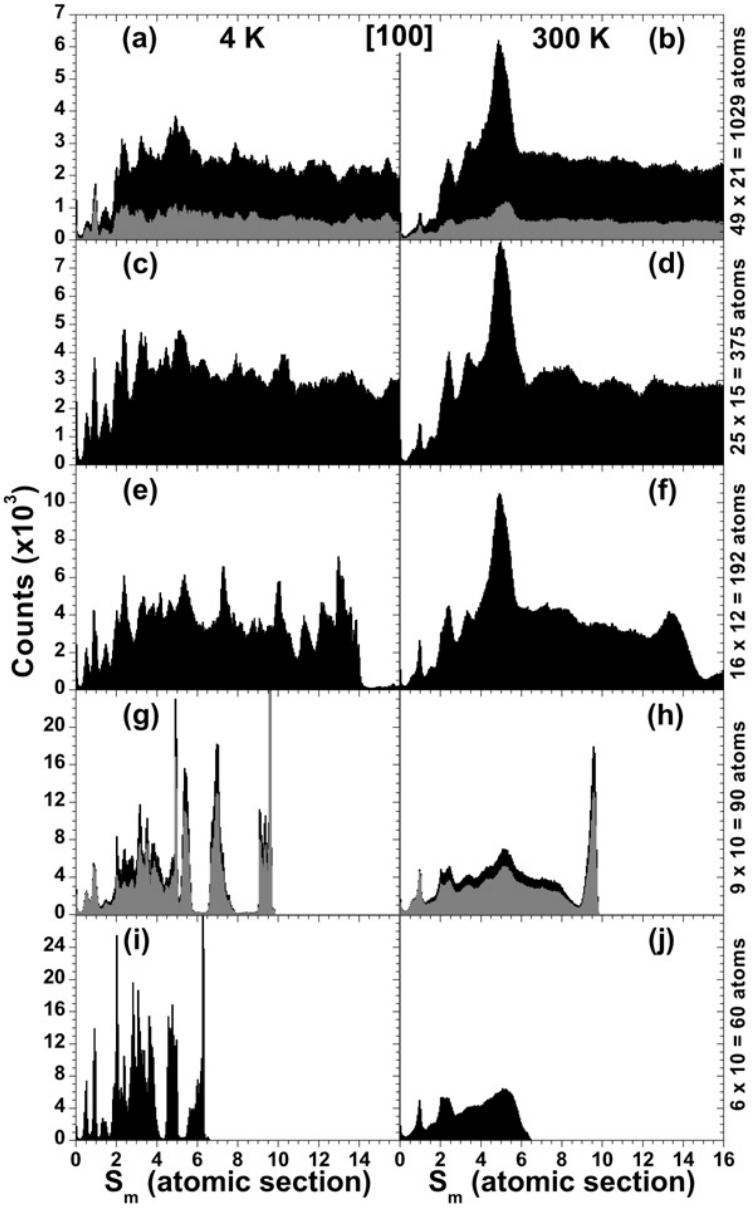

Figure 6.9: Minimum cross-section histograms $H(S_m)$ (black filled curves) built with 300 independent Ni nanowire ruptures under stretching along the [100] direction at $T = 4$K ((a), (c), (e), (g), (i)) and 300K ((b), (d), (f), (h), (j)). Different rows correspond to different initial parallelepiped sizes as indicated by the right-hand side labels (atoms per layer $\times$ number of layers). For two nanowire sizes [((a), (b)) and ((g), (h))] we show an $H^*(S_m)$ constructed taking into account only those samples that showed monomers or dimers (grey filled curves) as explained in subsection 6.3.2.

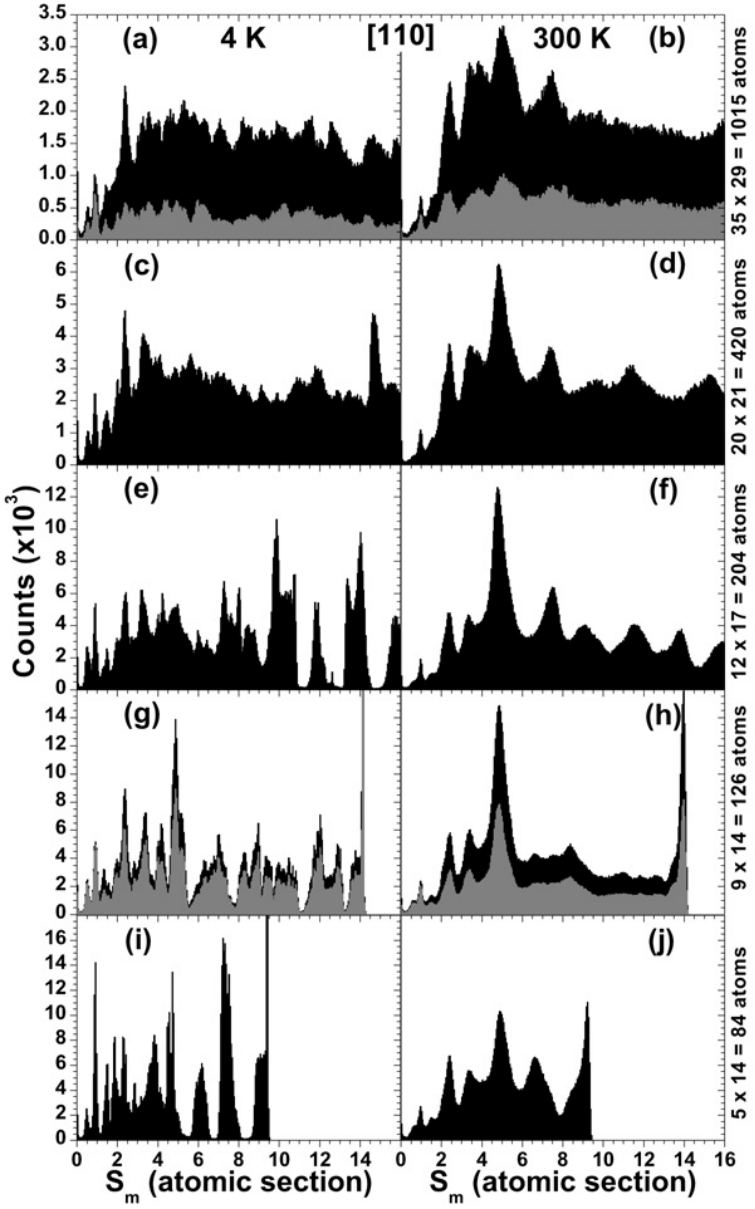

Figure 6.10: Minimum cross-section histograms $H(S_m)$ (black filled curves) built with 300 independent Ni nanowire ruptures under stretching along the [110] direction at $T = 4$K ((a), (c), (e), (g), (i)) and 300K ((b), (d), (f), (h), (j)). Different rows correspond to different initial parallelepiped sizes as indicated by the right-hand side labels (atoms per layer $\times$ number of layers). For two nanowire sizes [((a), (b)) and ((g), (h))] we show an $H^*(S_m)$ constructed taking into account only those samples that showed monomers or dimers (grey filled curves) as explained in subsection 6.3.2.

It is clear from figures 6.8, 6.9 and 6.10 that $H(S_m)$ is very dependent on the stretching direction. The [111] direction provides $H(S_m)$ with well-defined decreasing peaked structure in the low S_m region, whereas for [100] and [110] directions $H(S_m)$ presents a clear 'depletion' in the $S_m < 2$ region. Another noticeable feature is that the overall histogram shape is modified when the initial nanowire cross-section decreases. For the [111] case at $T = 4$K, those histograms from nanowires with an initial cross-section $N_s > 16$ are characterized by a decreasing peaked structure ($H(S_m = 1) > H(S_m = 2)$) that it is reversed ($H(S_m = 1) < H(S_m = 2)$) when $N_s < 9$. At room temperature and [111] orientation, $H(S_m)$ slightly changes when N_s decreases, keeping the trend $H(S_m = 1) > H(S_m = 2)$ for all the nanowire initial sizes. A similar situation happens for [100] and [110] histograms: the effects due to the initial nanowire section size are more evident at low temperatures.

The dependence of $H(S_m)$ on the nanowire size and orientation is a very important issue since theoretical conductance histograms $H(G)$ will also reflect such dependence. In the case of nickel, the use of the [100] stretching direction as well as narrow initial nanowires will determine a conductance histogram with small contributions from the low S_m region ($0.25 < S_m < 1.75$), mainly formed by monomers and dimers, as we will discuss in the following subsection. In contrast, the combination of the [111] stretching direction and a thick initial section provides a different conductance regime with large contributions from the region $0.25 < S_m < 1.75$. These differences explain the apparently conflicting histograms $H(S_m)$ found in the literature [Jacob2006, Pauly2006, GM2005a]. Therefore, those histograms obtained from small initial cross-section simulations should be treated cautiously since they do not capture the behaviour of actual thick breaking nanonecks formed in many experimental procedures.

6.3.2 Monomers and dimers

As we mentioned above, the lowest conductance peaks observed in conductance histograms are associated with those configurations appearing during the last stages of the breaking process of nanowires. For polyvalent metallic species (like Al or Ni) the electron transport is very different if the nanocontact is formed by one atom (monomer) or two atoms (dimer) [Sirvent1996, Dreher2005, Hasmy2005]. In order to complete the information depicted in the computational histograms, we have analysed the types of structures appearing when the nanocontact has one atom cross-section size. This allows us to determine the relative abundance of monomer-like and dimer-like structures and their surrounding environment.

It must be noted that we have not found any linear atomic chain (LAC) formed by three or more atoms for the three studied stretching directions. This result is in agreement with the absence of reports of Ni LACs in the literature. Notwithstanding, it is well known that the formation of LACs is a common feature of the breaking process of Au nanocontacts [Agraït2003]. Besides, other metallic species have also shown the formation of LACs in HRTEM experiments. Such is the case, for instance, of Ag [Rodrigue2002] and Cu [Sato2006]. Regarding computer simulations, results are somewhat controversial: A work by Bahn [Bahn2001] has reported the formation of LACs in Au and Pt, and the absence of these chains in Ni, Pd, Cu and Ag . However, other works have observed the formation of LACs in Cu [Sato2006]. This controversy has been attribuited to the influence of current induced forces in the nanocontact due to the bias voltage [Mizobata2003]. Another possible explanation for the low probability of LAC formation is the lack of proper thermal dissipation to the electrodes, which leads to a rapid heating and further melting of the atomic chain precursor atoms [Yang2005].

By means of the *burning* algorithm described in section 6.2.4 we have determined for every breaking nanowire the statistical weights of monomers, dimers and complex structures appearing around the $S_m \sim 1$ histogram peak for different simulation parameters (temperature, stretching direction, and initial size). In figure 6.11 the fractions of monomers, dimers and complex structures found in the range $0.25 < S_m < 1.75$ are depicted as function of the temperature for the two initial sizes of Ni nanowires.

From this figure it can be seen that the temperature has little influence on the production ratio of final structures. The main change is a slight decrease of other structures fraction with the temperature, especially for large size nanowires. This leads to a first conclusion: the decrease of height of the $S_m \approx 1$ and $S_m \approx 0.5$ peaks observed in figures 6.8, 6.9 and 6.10 between low and high temperature is not due to a lower proportion of monomer or dimer structures. Instead, it must be related to a decrease of the mean lifetime of these structures due to instabilities at high temperatures. This lifetime shortening is more remarkable for the dimer structure.

For the [111] stretching direction the joined proportion of monomer and dimers ($\sim 80\%$) is much larger than the fraction of other structures ($\sim 20\%$). This fraction seems to be rather independent of the temperature as well as the nanowire size, except for small ones near the nanowire melting temperature, where the monomers fraction increases and dimers fraction decreases. For the [100] and [110] cases, there is a large fraction of complex structures ($30-40\%$). The temperature behaviour of this fraction

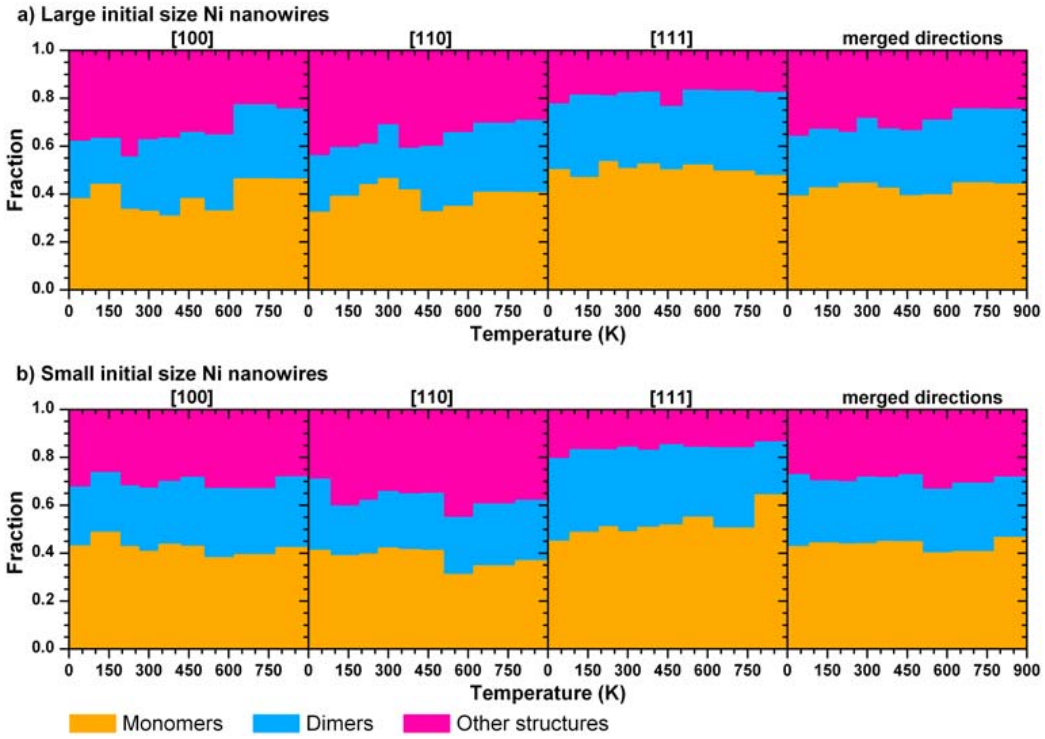

Figure 6.11: Fraction of monomers, dimers and more complex structures appearing during the Ni nanowire breaking process as functions of the temperature for Ni nanowires of large (a) and small (b) initial size. Different columns correspond to nanowires stretched along [100], [110], [111] and random (merged) crystallographic directions.

shows a dependence on the nanowire size: it keeps constant for small size nanowires but decreases with increasing temperature for the large size ones. The fraction of monomers is of the same order but slightly lower than that found for the [111] case. The fraction of dimers, on the other hand, takes values below those corresponding to the [111] case. On the contrary to the [111] case, dimers fraction increases with temperature for the large size nanowires set, especially if the stretching occurs along the [110] direction.

Figure 6.11 also shows the *merged* values of monomer and dimer proportions. These merged results show that for small sizes the proportion of monomers ($\sim 45\%$), dimers ($\sim 25\%$) and more complex structures ($\sim 30\%$) is constant with the temperature; for large systems, monomer ratio keeps constant ($\sim 45\%$) but that of dimers increases ($\sim 25- \sim 30\%$) slightly with temperature.

6.3.2.1 Partial histograms

We have taken advantage of the posibility of identifying monomers and dimers to further investigate on their influence on the shape of the cross section histograms $H(S_m)$. We have bulit *partial histograms* (labelled as $H^*(S_m)$) from those S_m traces that end up in a monomer or dimer configuration. We have obtained these $H^*(S_m)$ from nanowires stretched along the three crystallographic directions at 4 and 300 K and with two different (small and large) sizes. These partial histograms are depicted in figures 6.8, 6.9 and 6.10 for the [111], [100] and [110] crystallographic orientations respectively.

For the [111] stretching direction, we observe in figure 6.8 that these monomer and dimer based partial histograms are similar to the full histogram, indicating that the nanowire generally evolves to a monomer and/or dimer configuration before the breakage. This breaking scheme seems to be independent on the initial nanowire size and temperature.

However, the behaviour of partial histograms for the [100] and [110] stretching directions does depend on the initial nanowire size and temperature. This can be seen in figures 6.9 and 6.10. For small nanowires with [100] and [110] orientation and at low temperatures the partial and total histograms are very similar, as in the case of [111] naowires. However, as the temperature increases, the histograms start to differ although the general shape is conserved. Nanowires forming monomers and dimers are responsible of the $0.25 < S_m < 1.75$ region of $H(S_m)$, but for larger sections they show a significantly lower contribution. For the largest nanowire case for [100] and [110] orientations, independently of the temperature, nanowires with monomer and dimer

structures at the final breaking stage are solely responsible of those smaller peaks at the low S_m region, but do not recover the full peaked structure appearing in $H(S_m)$. These divergences of the partial histogram $H^*(S_m)$ from the full histogram $H(S_m)$ in the [100] and the [110] orientations (at high temperature for small nanowires, and at any temperature for large ones) indicates that those nanowires that end up breaking in a monomer or dimer configuration spend less time in $S_m > 1.75$ situations.

6.3.3 Local and non-local environment of monomers and dimers

Electron transport through a given nanocontact mainly depends on the size of its narrowest cross-section. However, the atomic structure of neighbouring regions also plays a key role in the electronic conductance [Pauly2006, Hasmy2005]. The study of the electronic transport through monomer-like or dimer-like Ni nanocontacts has been centred only on static structures with surrounding configurations obtained from crystalline structures [Sirvent1996, Jacob2005], proposing 3-1-3 and 4-1-4 as the most likely monomer configurations. However, a visual inspection of monomers and dimers from our MD simulations confirms that their environment does not follow such crystalline-like pattern. The MD calculations allow us the accurate determination of the actual type of neighbourhood formed around monomers and dimers and their relative probability of appearance. In addition, this information could provide an estimation of the probability of conductance associated to the lower peaks of the S_m histograms.

The electron transport through the nanowire also depends on more factors, including the presence of disorder (defects, vacancies, impurities, dislocations, etc.) along the nanowire. Actually the effect of disorder on the electrical conductance can be very important at the latest stages of the breaking process: if the scattering due to the disorder becomes very large, the electron transport could leave the ballistic regime and quantum diffusive transport features should appear.

6.3.3.1 Local environment

In our simulations, once the atom that forms the monomer is identified, it is trivial to determine its neighbour atoms (those closer than the distance d_{Cond}) and classify them with respect to the z coordinate. This gives us a configuration of type "n-1-m", meaning that there are n atoms at one side of the monomer and m atoms at the other side. For dimer structures the procedure is similar, providing configurations of type "n-1-1-m".

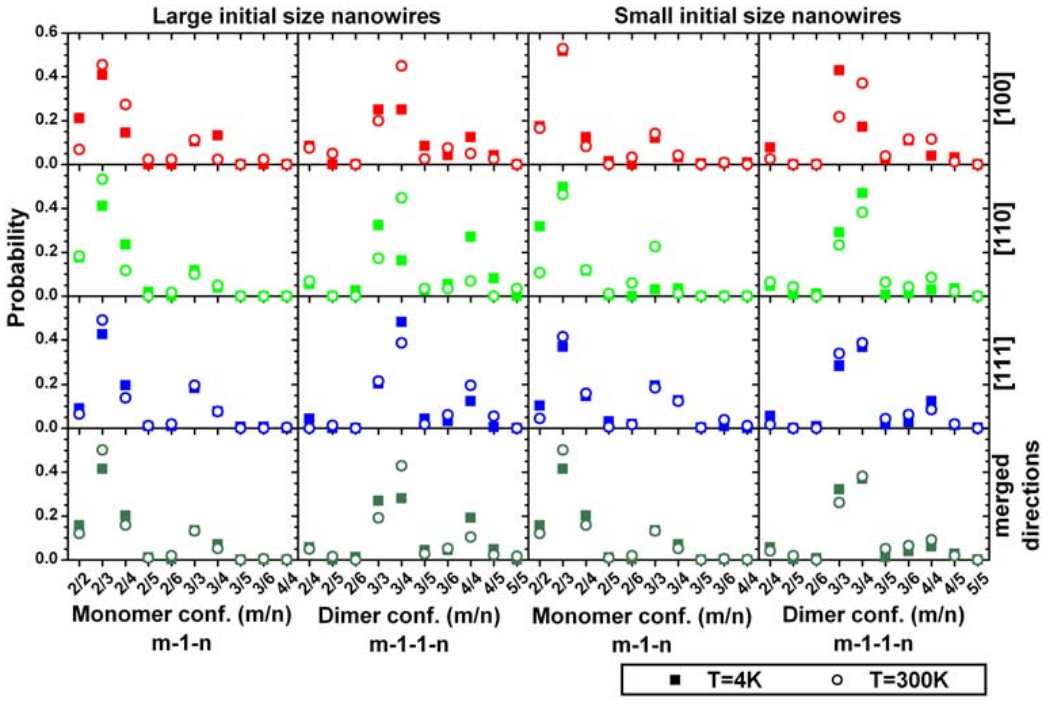

Figure 6.12: Probability of the occurrence of different atomic environments around Ni monomers and dimers. Data is shown for different stretching directions and temperatures. A "n/m" configuration means that the monomer (dimer) configuration is of the type "n-1-m" or "m-1-n" (type "n-1-1-m" or "m-1-1-n").

In figure 6.12 we present the occurrence probability of different atomic configurations around monomers and dimers. This graphic shows that the atomic structures around monomers and dimers (and its probability of occurrence) are roughly the same regardless of the size of the initial nanowire, the stretching direction or the temperature (although only T =4 and 300 K are showed). We notice that the most likely monomer structure presents the configuration 2-1-3. Around 40% of the monomers exhibit this configuration. Besides, we found that 2-1-4, 3-1-3, 3-1-4 and 2-1-2 configurations appear with a probability ranging between $\sim$ 20% and $\sim$ 10%. Some small deviations from this rule can be found for the [110] and small size nanowires: at low temperature the 2-1-2 configuration presents a probability larger than 30% but the 3-1-3 structure has less than a 5%, whereas at room temperature the probability of the 3-1-3 configuration is higher than the 20% (growing at the expense of the 2-1-3 structure). Comparing the actual monomer surrounding structures with those proposed on previous works [Sirvent1996, Jacob2005], the non-trivial 2-1-3 structure (the most probable, as we found) was not even considered. Moreover, we have not found evidences of the 4-1-4 crystalline-like configuration in our simulations.

Regarding dimer configurations, it can be seen in figure 6.12 that the most common structures are 3-1-1-4, 3-1-1-3 with occurrence probability between $\sim$ 20% and $\sim$ 50%. The most likely configuration varies slightly with the temperature, size and stretching direction of the nanowire. The 4-1-1-4 configuration has also a relative high probability ($\sim$ 10%$-$ $\sim$ 20%), being for the [110] stretching direction, low temperature and large initial size nanowire more probable ($\sim$ 30%) than the 3-1-1-4 configuration (that decreases below 20%). Other configurations show probabilities lower than 5%, reflecting that each dimer atom has to be connected with a stable base formed by 3 or 4 atoms.

The bottom panel in figure 6.12 shows the *merged* values of the probability distribution. These values show the main characteristics already described. For monomers, the 2-1-3 structure is the most probable ($\sim$ 50%) followed by 2-1-4, 2-1-2, 3-1-3 and 3-1-4, independently of the temperature. No signal is found of a 4-1-4 structure. For the dimer structure, the 3-1-1-4 configuration is the most probable one followed by the 3-1-1-3 and 4-1-1-4; their relative probabilities depend on the nanowire size and the temperature.

6.3.3.2 Non-local environment

As previously mentioned, the electron transport through the nanowire is also dependent on the existence of disorder along the nanowire. To determine the existence of a

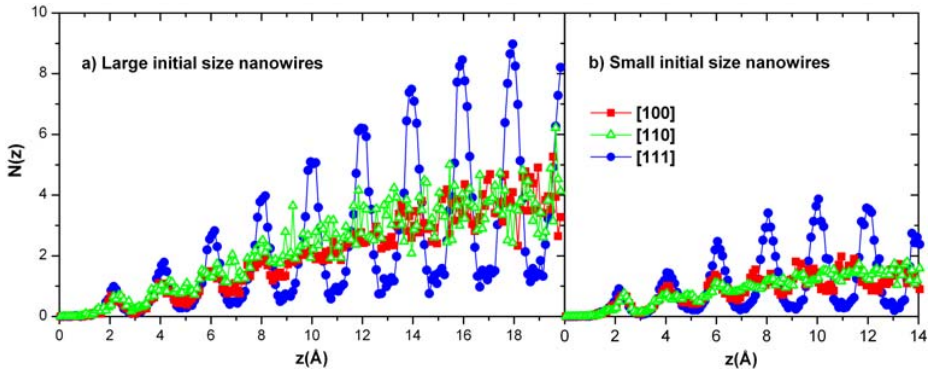

Figure 6.13: Average number of atoms $\langle N(z)\rangle$ at a distance z from the monomer atom for the [100], [110] and [111] directions at T =4 K for large (a) and small (b) initial size nanowires.

long-range structure (order) on the monomer configuration at T =4 K, in figure 6.13 we plot the average number of atoms $\langle N(z)\rangle$ located at a distance z from its position. This approximation will detect if the atomic structure keeps its crystalline character as the z distance from the monomer (or dimer) increases. We have calculated $\langle N(z)\rangle$ for the three stretching directions and two initial sizes. We have not observed significant differences between the two sizes. Both small and large nanowires show a similar behaviour of the $\langle N(z)\rangle$ curves.

On one hand, for the nanowires oriented along the [111] direction, we note clear peaks separated a distance close to the typical separation of the [111] planes d_{111} = 2.03 Å, indicating that the system tries to keep the same crystallographic structure through all the nanowire. On the other hand, for the [100] and [110] stretching directions, the situation is quite different, since for increasing z over $\sim$ 6 Å we could not distinguish a well defined peaked structure. For these orientations, the nanowire structure exhibits regions with a high degree of disorder (even at 4 K). A similar behaviour has been previously noticed for infinite nanowires under high strain rates [Braníc2000, Ikeda1999].

As pointed previously, the amorphization of the structure can be important in the electronic transport during latest stages of the nanowire breakage. The presence of disorder on a large region of the nanowire will lead to a conductance decrease. In our case, we have that for [111]-oriented nanocontacts the electron moves inside a well ordered system (keeping the ballistic transport features). However, for the [100] and [110] orientations an electron traveling through the nanocontact is expected to suffer many scattering events due to the disorder, which may lead to a diffusive transport regime.

6.4 Conclusions

We have run MD simulations of the breaking process of Ni nanowires. These simulations resemble experimental works of breaking suspended nanowires. In analogy to experimental conductance histograms $H(G)$, we have elaborated minimum cross section histograms $H(S_m)$. We have studied how these $H(S_m)$ histograms depend on three factors: temperature, nanowire size and crystalline orientation of the nanowire.

In order to obtain results comparable to experiments we have implemented a weighted average over crystallographic orientations, which yields orientation-independent or randomly-oriented results. Nevertheless, most of the results shown in this chapter need to be verified experimentally. This verification would require a better control over the technique of breaking nanowires, allowing to control the crystallographic orientation of the nanowire before its breaking.

Our results show that simulations with small nanowires render different $H(S_m)$ histograms than those with larger nanowires. These differences explain the apparenly conflicting histograms found in the literature [Jacob2006, Pauly2006, GM2005a]. Simulations using small nanowires -like those typically performed with *ab initio* methods- do not capture the behaviour of breaking experiments, where nanocontacts of bigger sizes are indeed used. So results from these first principles studies must be considered with caution.

We have also analyzed the atomic configurations at the narrowest section of the nanowire just before breaking. We have observed that the vast majority of nanowires end up in a monomer or dimer configuration. By means of an algorithm that allows to find the minimum connecting path between two atoms, we have been able to identify atoms in monomers and dimers structures. We have found that the fraction of all the breaking events ending up in a monomer (dimer) configuration is about $\sim 50\%(\sim 20\%)$.

By analyzing their local environments we have established the probability of formation of n-1-m and n-1-1-m structures at the monomers and dimers configurations respectively. The result of this analysis indicates that about 40% of monomers end up in a 2-1-3 configuration. Other less probable structures observed are the 2-1-2, 2-1-4 and 3-1-3 configurations. In the case of dimers, the most probable structures are the 3-1-1-4 one, followed closely by the 3-1-1-3. However the proportions of each structure change with the nanowire size, temperature and orientation. The *merged* results show that the probability occurrence for the 3-1-1-4 structure is higher than

that of the 3-1-1-3 structure for both sizes. However, this difference is more noticeable at 300 K, whereas at 4 K they show almost the same probabilities.

We have also studied the long-range order of the nanowires at the last stages of its rupture. This was done by calculating the spatial distribution of atoms, counting their distance to the monomer or dimer linker atom. The results of these calculations show a strong orientation dependence. Nanowires oriented along the [111] direction exhibit a long range order. On the other hand, those nanowires along the [100] and [110] directions, show long-range disorder. This disorder may be crucial in the conduction regime of these structures, since a high degree of disorder could induce a quantum diffusive transport.

Another interesting feature observed in the $H(S_m)$ histograms was the appearence of a remarkable peak in many histograms at 300 K at values of the cross section $S_m \approx 5$. This has lead us to analyze the origin of this peak. Our findings are explained in the following chapter.

Chapter 7

Formation of pentagonal chains

7.1 Introduction: Observation of pentagonal structures

In the previous chapter we showed histograms of the minimum cross-section $H(S_m)$ obtained from simulations of the breaking process of Ni nanowires. We have observed that these histograms exhibit a huge peak around $S_m \sim 5$ for the [100] and [110] cases (see figures 6.9 and 6.10). A similar peak in conductance histograms $H(G)$ has been reported by experimental groups in the breaking of Cu nanowires [Gonzál2004]. In that work a big peak is observed around $G = 4.5\,G_0$, which is attribuited to the possible formation of pentagonal chains in the narrowest section of the nanocontact.

Pentagonal chains do not correspond to any crystallographic FCC or BCC structure. Instead, these wires are formed by subsequent staggered parallel pentagonal rings (with a relative rotation of $\pi/5$) connected with single atoms. The unit cell of this structure is depicted in figure 7.1. The atomic sequence -5-1-5-1- presents a fivefold symmetry with respect to the nanowire axis. This staggered pentagonal configuration may also be understood as a sequence of interpenetrated icosahedra.

Icosahedral symmetry is quite common in very small systems due to the large stability and high coordination characterizing such geometry [Bulienko2001]. Contrary to monoatomic chains, pentagonal nanowires are rather robust structures at relatively high temperatures and, therefore, they may be considered as a promising candidate for being used as a component in nanodevices. Icosahedral structures have been reported for Cu [Mehrez1997] and Na [Barnett1997] breaking nanowires using MD simulations. The stability of such staggered pentagonal Cu nanowires was later confirmed by ab initio calculations [Sen2002]. More recently, MD tight-binding calculations have shown the presence of such pentagonal structures during the breaking

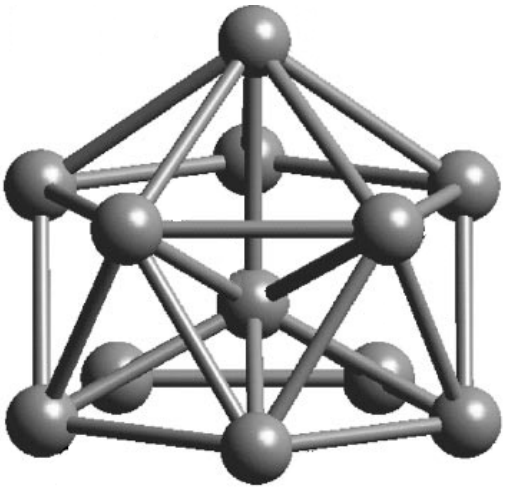

Figure 7.1: Unit cell of an infinite pentagonal nanowire. Notice that if we periodically repeat this structure in the vertical direction, the resulting nanowire becomes a set of interpenetrated icosahedra.

process of [110] Cu nanowires [Gonzál2004]. Stable pentagonal motives also appear in infinite Al nanowires [Gülser1998]. However, no statistical analysis has been performed to determine the probability of formation of these pentagonal chains in the breaking of metallic nanowires.

7.1.1 About this chapter

In this chapter we perform such statistical analysis. We have simulated the breaking process of Al, Ni and Cu nanowires by MD simulations. Following a similar approach as in the previous chapter, we have simulated nanowires oriented along the [100], [110] and [111] crystallographic orientations. As another variable in this study we have considered two nanowire sizes: *large* and *small*. What we call *large* nanowires have the following dimensions (atoms per layer $\times$ number of layers): $56 \times 18 = 1008$ atoms, $49 \times 21 = 1029$ atoms and $35 \times 29 = 1015$ atoms, for the [111], [110] and [110] orientations respectively. The sizes of *small* nanowires are: $16 \times 10 = 160$ atoms, $16 \times 12 = 192$ atoms and $12 \times 17 = 204$ atoms, again for the [111], [110] and [110] orientations respectively. For every one of these configurations we have run 300 constant temperature MD simulations of the nanowire breaking process. The temperature range has been between 4K and half the bulk melting temperature ($0.5\,T_{m,bulk}$) for each atomic species ($T_{m,bulk}$ =933 K, 1728 K and 1357 K for Al, Ni and Cu respectively [Lide2004]).

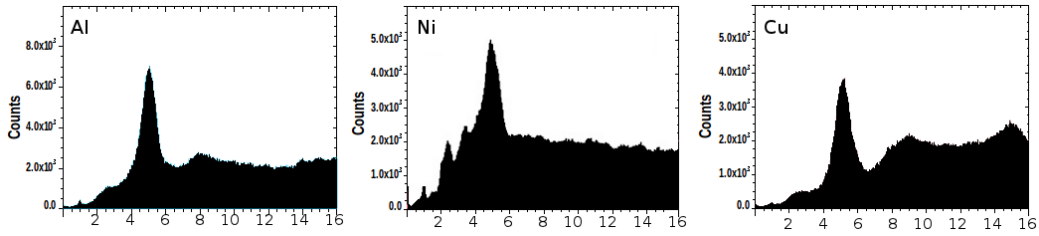

Figure 7.2: Minimum cross section histograms for Al, Ni and Cu nanowires of 1029 atoms oriented along the [100] direction at 300 K. These histograms show a clear peak at $S_m = 5$.

This chapter is organized as follows. In the following section we show the methodologies we have used to identify the presence of an icosahedral chain during the breaking of a nanowire. A first order approach to do so is to look at the $S_m(t)$ traces and measure the amount of time the nanowire spends around the $S_m = 5$ region. However we have further developed a more detailed algorithm that provides a precise identification of pentagonal rings along the nanowire. Using this algorithm we have been able to monitor the time evolution of every pentagonal chain, even identifying the aparison of each new pentagonal ring into the chain. The following section shows the statistical analysis we have performed. This includes an estimation of the probability $P(n_p^m)$ of finding a pentagonal chain with a given maximum number n_p^m of pentagonal rings. Furthermore, we have determined the influence of the temperature on this probability $P(n_p^m)$. We have observed that there is an optimal temperature at which the probability of getting larger pentagonal chains takes the highest values.

7.2 Characterizing the observed pentagonal chains

After observing the high peak around $S_m = 5$ in Ni nanowires (shown in section 6.3), we have run MD simulations on the breaking of Al and Cu nanowires. The aim of these simulations was to confirm wether or not a similar peak around $S_m = 5$ appeared in these materials. Figure 7.2 shows the $H(S_m)$ curves for Al, Ni and Cu nanowires oriented along the [100] direction at 300 K. From this figure it is evident that Al and Cu also exhibit a remarkable peak around $S_m = 5$.

Once the appearence of this high peak around $S_m = 5$ was confirmed for the three materials, we have visually inspected the time evolution of several breaking nanowires in our MD simulations. This inspection showed a great amount of pentagonal chains being formed from independent breaking processes. We have depicted in figure 7.3 different time snapshots of one of those breaking events, for a [110] Ni nanowire at

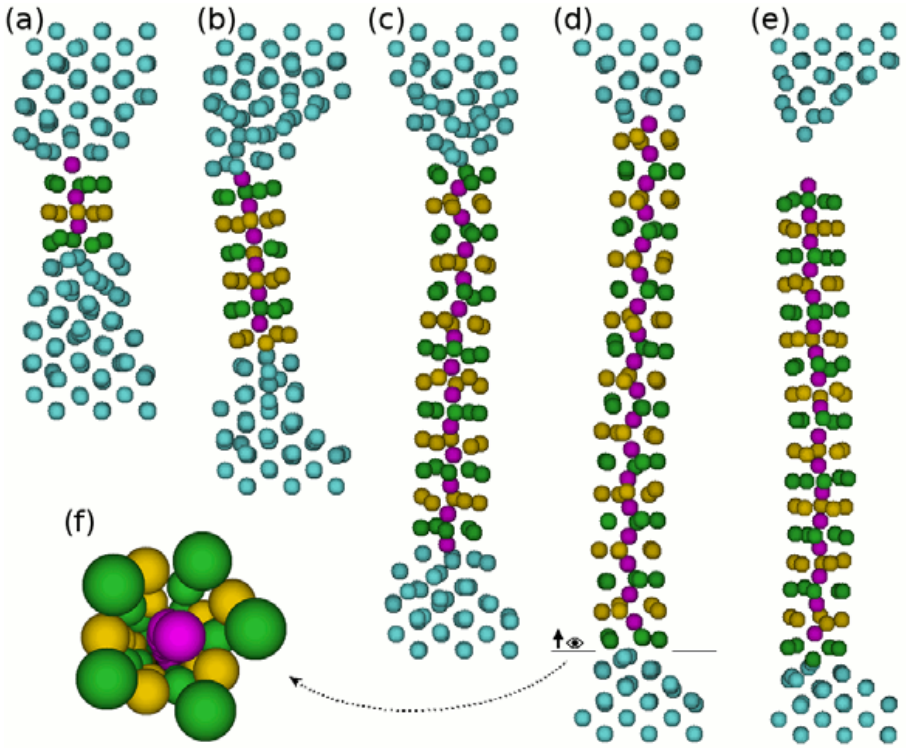

Figure 7.3: Visual inspection of the formation of a long pentagonal chain during the breaking of a small [110] Ni nanowire at T=550K; (f) shows the cross-sectional perspective view as seen from the position indicate on (d). Colours are used to identify the -5-1-5-1- structure.

$T = 550$ K. This figure shows the formation, growth and breakage of a long pentagonal chain. This structure shows the typical pentagonal rings along its length. We found that these structures are very common for the [100] and [110] stretching directions, whereas they rarely occur for the [111] case.

In order to get a better understanding of this structure, we have run CG optimizations of the atomic coordinates of an infinite pentagonal chain. This gives the geometrical description of the structure at 0 K. Table 7.1 shows these results, obtained both with the MFMP EAM potential used in our MD simulations [Mishin1999, Mishin2001] and an *ab initio* approach (with the SIESTA package [Soler2002]). This table shows that both approaches provide similar values for the two parameters defining the geometry of the pentagonal chain: the distance d_{5-5} between two consecutive pentagonal rings and the length l_5 of the pentagonal ring's side. Except for the value of d_{5-5} for the Al structure, the MFMP EAM parameterization provides values that are different from the DFT in less than 0.1 Å.

Furthermore, we have also performed calculations in order to estimate the melt-

	d_{5-5}(Å)	l_5(Å)
Al	2.84 (2.48)	2.95 (2.97)
Ni	2.22 (2.16)	2.55 (2.52)
Cu	2.22 (2.24)	2.58 (2.66)

Table 7.1: Geometrical description of an infinite pentagonal chain. d_{5-5} accounts for the distance between two consecutive pentagonal rings and l_5 is the length of a pentagonal ring's side. Values shown here were obtained from optimization of the pentagonal structure with EAM potentials. The numbers enclosed in parentheses correspond to an *ab initio* optimization using the SIESTA package [Soler2002].

	$T_{m,icos}$(K)	$T_{m,bulk}$(K)	E_{pent}(GPa)	E_{bulk}(GPa)
Al	688±74	933	108.1	69
Ni	1275±103	1728	287.1	213
Cu	357±58	1357	279.9	117

Table 7.2: Thermal and mechanical properties of the pentagonal chain. $T_{m,icos}$ and $T_{m,bulk}$ denote the melting temperatures of the infinite pentagonal nanowires and the bulk system, respectively. Notice that the melting temperature of the icosahedral nanowires presents a certain degree of dispersion. E_{pent} and E_{bulk} stand for the Young's modulus of an infinite pentagonal nanowire (as obtained from MD simulations at $T = 20$ K) and the FCC bulk structure respectively (values extracted from [Lide2004] (Al). [Smith1976] (Ni and Cu).

ing temperature $T_{m,icos}$ of an infinite icosahedral nanowire. This $T_{m,icos}$ was obtained from MD simulations of an infinite pentagonal chain at a slowly growing temperature. For each one of the materials under study (Al, Ni and Cu) we have run 50 independent simulations, in order to obtain a statistical estimation of the temperature $T_{m,icos}$ at which the pentagonal chain melts. Table 7.2 shows the results of these MD simulations. These results indicate that pentagonal chains will be melted at $T_{m,icos}/T_{m,bulk} = 0.95$, 0.90 and 0.40, for Al, Ni y Cu respectively.

7.2.1 Estimating how much time does the nanowire spend at $S_m \sim 5$

The aim of our work was to estimate the length of these chains. The first approach to do so was to compute the amount of time that a breaking process spends at a cross section value $S_m \sim 5$. This can be easily obtained by exaamining the $S_m(t)$ trace. To get this first order approach we have calculated the probability distribution function $P_{4.5-5.5}(\Delta t)$ of the time Δt spent by the nanowire between $S_m = 4.5$ and 5.5. Figure 7.4 shows this distribution function for Ni nanowires breaking along the

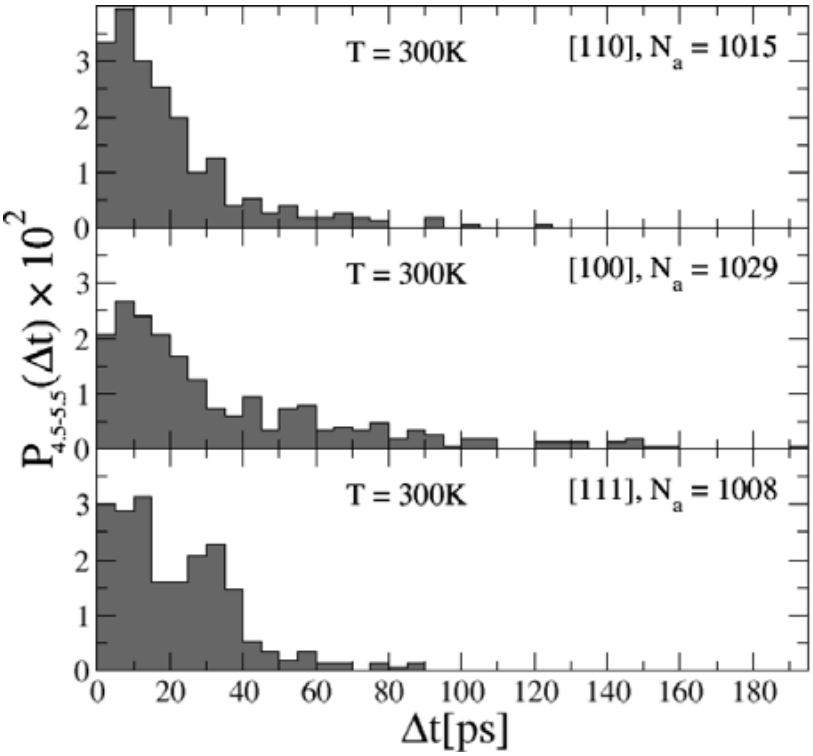

Figure 7.4: Distribution function $P_{4.5-5.5}(\Delta t)$ of the time Δt a Ni nanowire spends at a cross section value $4.5 < S_m < 5.5$. Top, middle and bottom boxes correspond to [110], [100] and [111] stretching directions, respectively. This figure shows results obtained from simulations with large nanowires (~ 1000 atoms).

three stretching directions at $T = 300\,\mathrm{K}$. The distribution is wider for the [100] case, in correspondence with the information provided by the $H(S_m)$ histograms shown in section 6.3. Notice that for the [100] case we have found some $S_m(t)$ traces where the nanowire stays in the $4.5 < S_m < 5.5$ region for up to $t \sim 200\,\mathrm{ps}$.

We have depicted in figure 7.5 some examples of those nanowires with a relatively long staying-power time in the $4.5 < S_m < 5.5$ region, for the [100], [110] and [111] cases. The huge peak at $S_m \sim 5$ shows the tendency of the system to form long wires. We found that these structures are very common for the [100] and [110] stretching directions, whereas they rarely occur for the [111] case. This trend is also noticed for all the range of initial nanowire cross-sections. We have found that long $S_m \sim 5$ nanowires break following the breaking pattern we have described as 'others' (see figure 6.3).

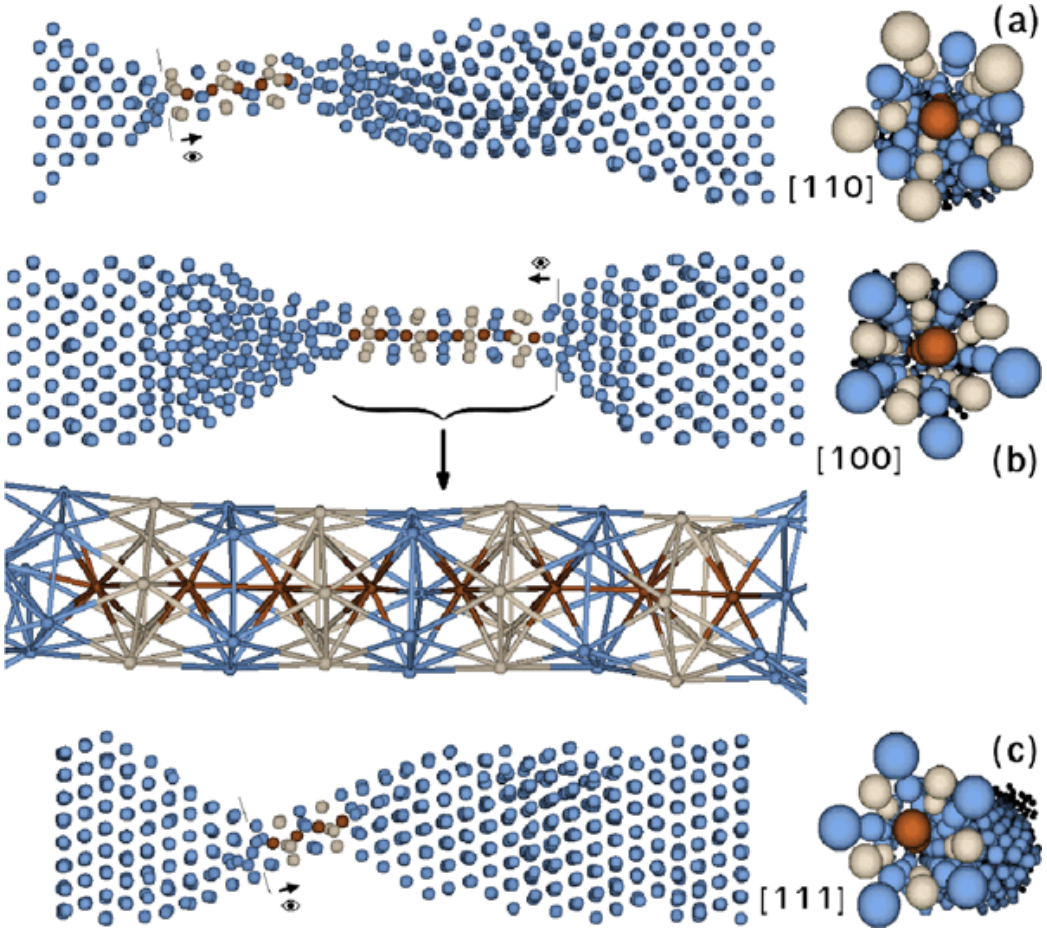

Figure 7.5: Snapshots of three configurations illustrating the appearance of long wire structures with atomic sections close to $S_m \sim 5$ for the [110] (a), [100] (b), and [111] (c) stretching directions of Ni nanowires. The right column shows cross-sectional perspective views as seen from the position indicated on the figures on the left.

7.2.2 An algorithm for proper identification of pentagonal structures

Even though $P_{4.5-5.5}(\Delta t)$ provides evidences of the formation of pentagonal structures and gives an idea of their life-time, it definetly does not provide a complete description of their length or the number of pentagonal rings they have. For this reason we have developed an algorithm that identifies the pentagonal structures that form the icosahedral nanowire [Peláez2009]. This algorithm also allows us to define the length L_p of the pentagonal chain as the distance between the outermost pentagonal rings. The algorithm also provides an exact count of the number of pentagonal rings n_p that form it.

Our algorithm is based on the determination of an angular distribution of the nearest neighbour atoms. It provides a parameter ($\alpha(z)$) which compares the angular distribution of the projected nanowire atomic coordinates with that corresponding to a perfect pentagonal nanowire. For a given z coordinate we consider a slice perpendicular to the z (stretching) direction with a thickness of 2 Å and centred on the z value. The N_t atoms inside such slice are projected onto the xy plane, each one getting new 2D coordinates $\vec{\eta_i}$; then the centroid of this structure $\vec{\eta_0} = \sum_i \vec{\eta_i}/N_t$ is calculated. The angular distribution is calculated from the angles $\theta_{i,j}$ between the pairs of vectors $\vec{\eta_i'}$ and $\vec{\eta_j'}$ defining the projected atomic coordinates with respect to the centroid ($\vec{\eta_i'} = \vec{\eta_i} - \vec{\eta_0}$)

$$cos(\theta_{i,j}) = \frac{\vec{\eta_i'} \cdot \vec{\eta_i'}}{|\vec{\eta_i'}|\ |\vec{\eta_i'}|}. \tag{7.1}$$

The parameter α is calculated as

$$\alpha = \frac{2}{N_a} \sum_{i,j}^{N_a} \frac{|\theta_{i,j} - m\theta_0|}{\theta_0} \tag{7.2}$$

where N_a is the number of pair of atoms considered, $\theta_0 = \pi/5$ is the reference angle of a perfect staggered pentagonal structure and m is the integer that minimizes the expression $|\theta_{i,j} - m\theta_0|$. To avoid spurious contributions from atoms near the centroid, only vectors satisfying $|\vec{\eta_j'}| > a/4$ are considered (a being the FCC lattice constant), i.e., centre atoms are excluded from the calculation of α. This algorithm is applied along the z-coordinate of the nanowire, displacing the imaginary slab $\delta z = 0.1$ Å at a time. This results in a $\alpha(z)$ profile of the nanowire, showing where pentagonal structures appear.

In order to minimize artifacts, the $\alpha(z)$ curve is softened over a Δz interval. This softened curve $\langle\alpha\rangle(z)$ is defined as

$$\langle\alpha\rangle(z) = \frac{1}{\Delta z}\int_{z-\Delta z/2}^{z+\Delta z/2} \alpha(z')dz' \tag{7.3}$$

where a value of $\Delta z = 1\,\text{Å}$ has been found appropriate. This average of α ($\langle\alpha\rangle$) over a 1 Å interval provides a quantity that distinguishes between pentagonal and non-pentagonal structures along the nanowire's z-axis. We have observed that when the parameter $\langle\alpha\rangle(z) < 0.5$, the set of atoms around z forms a structure similar to that of a pentagonal ring. On the contrary, if $\langle\alpha\rangle(z) > 0.5$ the set of atoms presents another structure (bulk-like, helical or disordered).

To check the ability of the algorithm to discriminate between different structures in figure 7.6 we show the average α values obtained using the algorithm along different nanowires with increasing amount of disorder. The test structures for the algorithm were: square nanowires with an atomic sequence 5-4-5-4 taken from a FCC structure along the [100] direction; staggered pentagonal nanowires with atoms sequence 5-1-5-1; staggered hexagonal 6-1-6-1 nanowires; and staggered heptagonal nanowires with a 7-1-7-1 sequence. The degree of disorder was measured with the mean displacement σ of the atoms from their position in the perfect structure: $\sigma = \sum_i |\vec{\rho_i} - \vec{\rho_{i,0}}|/RN_t$ where $\vec{\rho_{i,0}}$ corresponds to the atom's position in the original (ordered) structure, and R is the effective radius associated to the cross section of the ordered test configuration. The initial ordered structures ($\sigma = 0$) are depicted as insets in figure 7.6, and only in the case of the pentagonal nanowire the parameter α takes a value 0, being ~ 1 for the other structures. As the disorder increases, the α average ($\bar{\alpha}$) varies: it increases for pentagonal nanowires and slightly decreases for the other nanowires. If the disorder with respect to the initial structure is strong enough, the average of α for all the test nanowires converges to a value ~ 0.9.

In order to further check the ability of the algorithm to identify pentagonal regions within a MD simulation of a breaking process, we tested its performance over simulated nanowires showing icosahedral structure. As we mentioned before, figure 7.3 shows several snapshots of a nanowire breaking process where an icosahedral structure is observed. For these snapshots, figure 7.7 shows the $\langle\alpha\rangle(z)$ profile curves, as well as the radial and angular distribution functions $g(r)$ and $g(\theta)$ through different sections of the nanowire (b) (see figure). As illustrated in the figure, the algorithm returns a value near to 1 when is applied to the ordered FCC regions of the nanowire, and

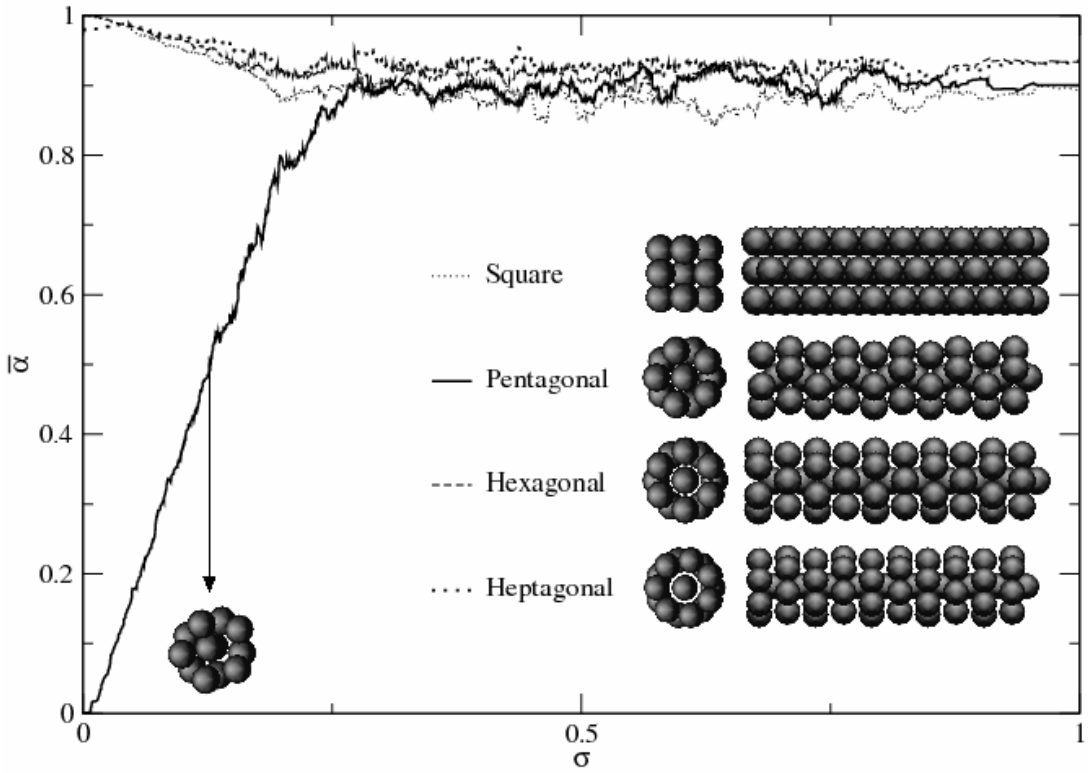

Figure 7.6: The average of the α-parameter ($\bar{\alpha}$) versus different strengths of the disorder parameter σ (see text) for four test configurations: square 5-4-5-4, staggered pentagonal 5-1-5-1, staggered hexagonal 6-1-6-1 and staggered heptagonal 7-1-7-1 nanowires (the inset shows the perfect ordered configurations of the four test nanowires). σ is the mean atomic displacement of atoms with respect to the perfect position of the ordered configuration. The average value of α for disordered nanowires was obtained averaging over 50 configurations.

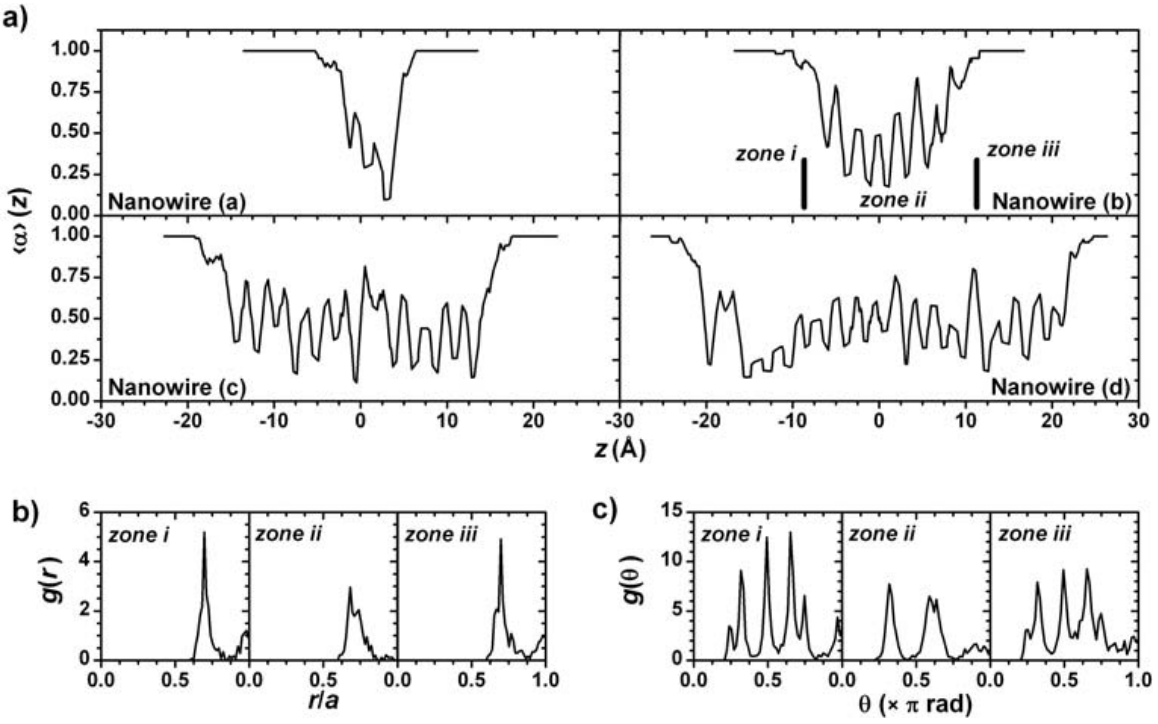

Figure 7.7: a) Average α-parameter $\langle\alpha\rangle(z)$ along the Ni [110] simulated nanowire shown in figure 7.3. Each box corresponds to a given nanowire snapshot as shown in that figure, which are labelled as (a), (b), (c) and (d). Minimum values of $\langle\alpha\rangle$ below 0.5 correspond to the position of pentagonal rings forming the icosahedral nanowire. b-c) Radial $g(r)$ and angular $g(\theta)$ distributions for the three marked region of the nanowire labelled as (b).

values below 1 for the pentagonal region. Minima of $\langle\alpha\rangle$ correspond to the position of the pentagonal rings; as they are not perfect ordered structures (though still can be recognized as pentagons) their $\langle\alpha\rangle$ values are a bit greater than zero. We have chosen the value of $\langle\alpha\rangle = 0.5$ as the limit value to recognize a pentagonal structure. This value $\langle\alpha\rangle = 0.5$ discriminates between pentagonal and non- pentagonal structures. We define the pentagonal nanotube length $L_p(t)$, observed during stretching at a given time t, as the distance between the maximum and minimum z coordinates with $\langle\alpha\rangle = 0.5$. We also define n_p as the number of pentagonal rings forming the icosahedral nanowire at its late stage (equivalent to the number of $\langle\alpha\rangle$ local minima below 0.5).

In figure 7.7b we have also divided one of the nanowire snapshots in three regions that seem to have different structures from visual inspection and from the $\langle\alpha\rangle(z)$ profile. For each one of these three regions we show the radial and angular distribution functions $g(r)$ and $g(\theta)$. We can see that the outermost regions exhibit a mostly FCC

structure, with the FCC typical interatomic distances and angles. The central region corresponds to the pentagonal structure according to both visual inspection and the $\langle\alpha\rangle(z)$ profile. Inspecting the angular distribution function in this region we can see how the central peak of the FCC structure has disappeared and the peak at the right has displaced a bit towards the left. This is the typical structure of the pentagonal angular distribution function. Regarding the interatomic distances, not a big change is appreciated in this region from the radial distribution function. As it can be seen, the parameter $\langle\alpha\rangle$ proves to be a very efficient parameter to identify the pentagonal regions in a breaking nanowire.

7.2.3 Time evolution of pentagonal chains formation

Once the presence and position of pentagonal rings in a nanowire can be determined, we have calculated the time evolution of both the number of pentagonal rings $n_p(t)$ and the actual length of the pentagonal chain $L_p(t)$ in a large set of breaking simulations. In this analysis we have included simulations of the breaking process of Al and Cu nanowires (as well as the previously discussed simulations for Ni).

Figure 7.8 shows an example of the latest stages of the evolution of a prismatic FCC Cu nanowire stretched along the [100] direction where the formation of an icosahedral chain can be clearly seen. Figure 7.8a shows different snapshots of the evolution of an icosahedral structure that grows from those atoms located in the non-crystalline regions formed at both ends of the nanowire.

For each breaking event we monitor the time evolution of the nanocontact minimum cross section $S_m(t)$. Figure 7.8b displays the $S_m(t)$ curve (measured in number of atoms) corresponding to the nanowire evolution. The formation of a staggered pentagonal nanowire is indicated by a long plateau around $S_m \sim 5$. This figure 7.8b also shows the evolution of the pentagonal chain length $L_p(t)$, the number of pentagonal rings $n_p(t)$ and the force F_z exerted on the nanowire while stretching. Corresponding to every jump in L_p there is a sharp decrease in the F_z curve, giving rise to a saw-tooth like shape of the F_z curve. This type of force versus time curve has been typically observed in experiments of the breaking process of metallic nanocontacts [RB1996], particularly in the formation of long monatomic Au chains [RB2001] and more recently on Pt chains [Valkerin2005]. This saw-tooth structure is the signature of subsequent elastic deformations (ramps) and inelastic atomic rearrangements (jumps). Some inelastic rearrangements can be associated with the appearance of a new 5+1 subunit: a pentagonal ring and a central atom that acts as connector to the already existing pentagonal ring. Once the icosahedral chain incorporates a new 5+1

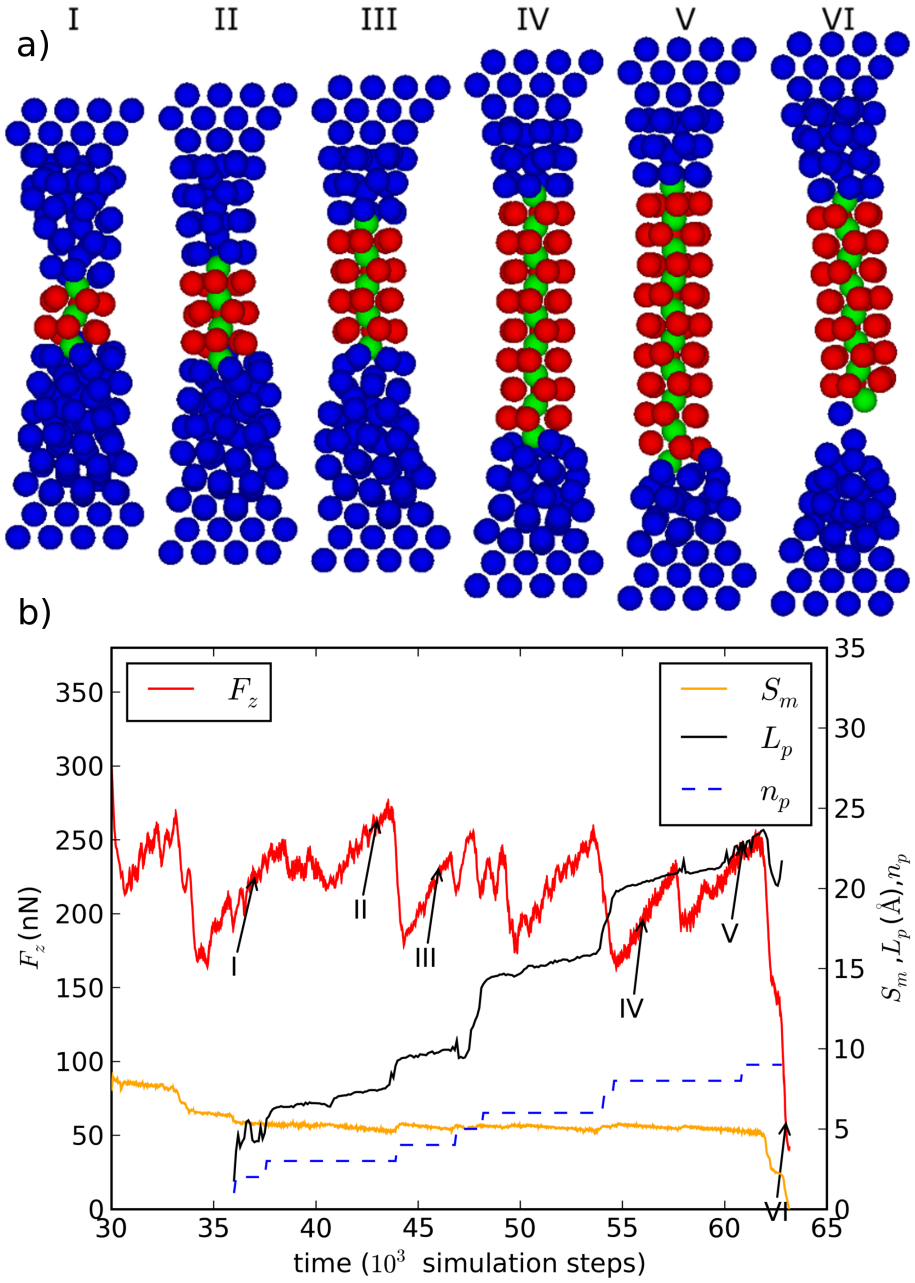

Figure 7.8: (a) Six snapshots of the atomic configurations at the lastest stages of a Cu nanowire stretched along the [100] direction until its breaking. Atoms forming a 5-1-5-1 structure are coloured in red (pentagonal rings) and green (core atoms). Notice the "disordered" region between the pentagonal chain and the bulk-like electrodes. For this particular simulation we show in (b) the time evolution of the force F_z exerted by the nanowire on the rigid top and bottom layers (red line), the minimum cross section S_m measured in number of atoms (orange line), the evolution of the pentagonal chain length L_p (black line) and the number of pentagonal rings n_p in it. Notice that L_p and n_p increase following a stepwise manner.

subunit, it deforms elastically under stretching, absorbing part of the deformation induced by the overall nanowire elongation. At a certain point the accumulated elastic energy is enough to induce the extraction of a new 5+1 subunit from the regions surrounding the icosahedral nanowire. This process is repeated several times until the icosahedral nanostructure reaches its maximum length. During the elastic-inelastic cycles, the minimum nanowire cross section S_m is approximately constant around 5, showing only very small fluctuations corresponding to the jumps noticed in the F_z and L_p curves.

We have detected that the breaking of icosahedral nanowires always occurs at one of its ends. This indicates that this structure is quite robust. It also can be inferred that the addition of new 5+1 subunits to the pentagonal chain is interrupted by some processes taking place at the region of connection between the icosahedral chain and the rest of the nanowire. We have checked that the connection region that "feeds" the pentagonal chain presents a certain level of disorder in comparison to the crystalline regions. The formation of such disordered regions during the breaking of Cu nanowires has been already reported in the past [Medina2003]. We have also noticed that the 5+1 subunits can be added at both ends irrespective of the end where the previous subunit was attached.

We have found that temperature plays a key role in the pentagonal chain growth mechanism. On one hand the mobility (diffusion) of the atoms increases when temperature does, allowing them to rearrange and become part of the pentagonal chain. On the other hand, higher temperatures may cause the melting of the contact region, leading to a spontaneous nanocontact breaking. Therefore it is easy to realize that for each metallic species there is an optimal temperature T_{opt} that balances both effects and favours the addition of pentagonal rings, leading to the formation of long icosahedral chains. The following section illustrates this behaviour.

7.3 Statistical analysis of the appearence of pentagonal chains

7.3.1 Length and number of rings

As we have mentioned before, every breaking event has a different time evolution, giving rise to different $S_m(t)$, $L_p(t)$ and $F_z(t)$ curves. As a consequence, the prediction of the general properties of pentagonal chains (the nanowire length and the number of pentagonal rings) from a single (or a few) breaking event is not feasible. Actually,

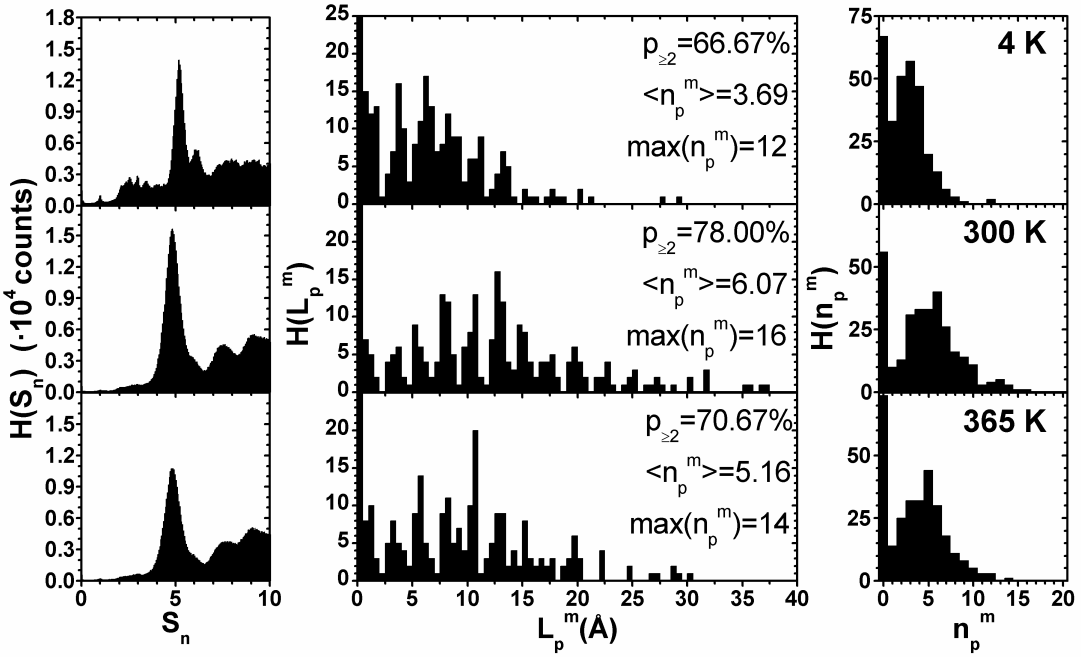

Figure 7.9: Histograms of the minimum cross section $H(S_m)$ (left column), the maximum length of the icosahedral nanowire $H(L_p^m)$ (middle column), and the maximum number of pentagonal rings $H(n_p^m)$ (right column) for Cu[100] nanowires containing 192 atoms at three different temperatures: 4 (top row), 300 (middle row) and 365 K (bottom row). The $H(L_p^m)$ distributions show a peaked structure, with peaks spaced approximately d_{5-5}, the calculated equilibrium separation between successive staggered pentagonal rings. The value $H(L_p^m = 0)$ (67, 56 and 74 for the three temperatures, respectively) corresponds to the number of nanowires out of the set of 300 that do not show any pentagonal ring in its structure. The data insets in the middle column include, for each temperature, the probability $p_{\geq 2}$ of creating an icosahedral nanowire with $n_p^m \geq 2$, the average of the maximum number of pentagonal rings $\langle n_p^m \rangle$ (averaged only over those nanowires presenting icosahedral features, i.e. that satisfy $n_p^m \geq 2$) and the number of pentagonal rings found for the longest observed icosahedral nanowire ($max(n_p^m)$).

as we already mentioned in section 6.2.2, previous works [GM2005a, GM2005b] have determined that the statistical analysis of breaking nanowires requires at least 100 independent breaking events in order to provide converged histograms and reliable averages. The statistical approach that we are using is widely implemented in experimental studies, where histograms of the conductance, histograms of linear atomic chains lengths, etc. are state of the art methods for the analysis of metallic nanowires. In our case we have constructed histograms of diverse parameters of interest for analyzing the formation of pentagonal chains. Figure 7.9 shows some of these histograms from Cu[100] nanowires with small initial cross-section at three temperatures. In the case of minimum cross section histograms $H(S_m)$ the high peak around $S_m \sim 5$ is an unmistakable sign of the high probability of formation of pentagonal chains. Moreover, we have defined the maximum pentagonal length L_p^m and maximum number of pentagonal rings n_p^m as the values taken by $L_p(t)$ and $n_p(t)$ at the breaking point of the icosahedral nanowire, respectively. From these quantities (L_p^m and n_p^m) we have built histograms ($H(L_p^m)$ and $H(n_p^m)$) that help to characterise the icosahedral nanowire formed during the stretching process. These histograms can also be seen in figure 7.9.

The $H(L_p^m)$ histogram presents a peaked structure, indicating that the formed pentagonal chains posses maximum lengths with well defined values. A quite similar peaked structure is observed in the experimental study of linear atomic chains (LACs) [Yanson1998]. In our case, the peaked shape indicates the formation of icosahedral structures with a well defined separation (d_{5-5}) between two consecutives pentagons. A Fourier analysis of these histograms let us determine the mean separation between pentagons, finding out $d_{5-5} = 2.6 \pm 0.2$, 2.3 ± 0.3 and 2.4 ± 0.2Å, for Al, Ni, and Cu respectively, independently of the stretching direction. These d_{5-5} values are slightly larger than those corresponding to optimized icosahedral nanowires (as shown in table 7.2) due to the fact that these histograms of $H(L_p^m)$ are obtained when the icosahedral nanowire is stretched and about to break.

7.3.2 Influence of the temperature on the chain length

As we have discussed above, temperature plays a key role in the pentagonal chain growth mechanism: low temperatures do not allow enough mobility of atoms to search lower energy configurations (like the icosahedral structure that gives rise to the pentagonal chain); on the other hand, too high temperatures may induce melting in the contact region, avoiding the formation of longer pentagonal chains. In this subsection

we analyze how the maximum number of pentagonal rings n_p^m changes at different temperatures.

Since we have collected results from thousands of simulations we present the statistical analysis using a compact format, drawing the probability $p_{\geq X}$ (with $X = 2, 3, 4, ...$) of finding chains with a number of pentagonal rings equal or larger than a given number X. This quantity facilitates the determination of those conditions that favour the creation of icosahedral nanowires. Figures 7.10 and 7.11 show the probability of finding chains with more than X =2, 3, 4, 5, etc... pentagonal rings for large and small initial nanowire sizes respectively. In our study we have found icosahedral nanostructures in the range $2 \leq n_p^m \leq 19$. Figures 7.10 and 7.11 clearly show that the probability of finding an icosahedral chain (with $n_p^m \geq 2$) takes a maximum value at a given temperature, which we identify as the optimum temperature T_{opt}. To simplify the huge amount of information we get from the statistical analysis, we only display the $\langle n_p^m \rangle$ and $max(n_p^m)$ parameters that characterise $H(n_p^m)$ at the T_{opt} temperature, denoting them as $\langle n_p^m \rangle^o$ and $max(n_p^m)^o$. These quantities obtained for each metallic species (Al, Ni, or Cu), crystalline directions and initial sizes appear in the different boxes of figures 7.10 and 7.11.

The inspection of figure 7.11 (small nanowires) reveals that for the [100] and [110] orientations long chains are produced with higher probability at $T_{opt} = 300$ K for Al and Cu. For the Ni case the optimal temperature is found at $T_{opt} = 500$ K. These temperatures slightly change for wires with large initial section (figure 7.10). Anyway, these figures illustrate that, at low temperature and for Al and Ni, it is difficult to find pentagonal chains while Cu nanowires present a non-negligible probability of forming icosahedral chains.

In general, for a given size and breaking orientation, we find that $T_{opt}(Ni) > T_{opt}(Al) > T_{opt}(Cu)$. This order is expected because it is related with the melting temperature of the icosahedral nanowire as shown in table 7.2. Furthermore, for a given species, the probability $p_{\geq 2}^o$ is much larger for the [100] and [110] stretching directions than for the [111] orientation. In particular we have detected that for small section wires (figure 7.11), the quantity $p_{\geq 2}^o$ is between 78% and 89% for the [100] and [110] orientations. In these cases the icosahedral chains must be easily observable at the optimal temperature. At these orientations we have found $\langle n_p^m \rangle^o$ values ranging between 5.37 and 6.72, and $max(n_p^m)^o$ values between 14 y 18 rings, pointing out that the probability of obtaining "long" pentagonal wires is relatively high. On the contrary, breakages along the [111] directions produce icosahedral chains with smaller probabilities ($19\% < p_{\geq 2}^o < 51\%$). Moreover, the resulting icosahedral chains are shorter

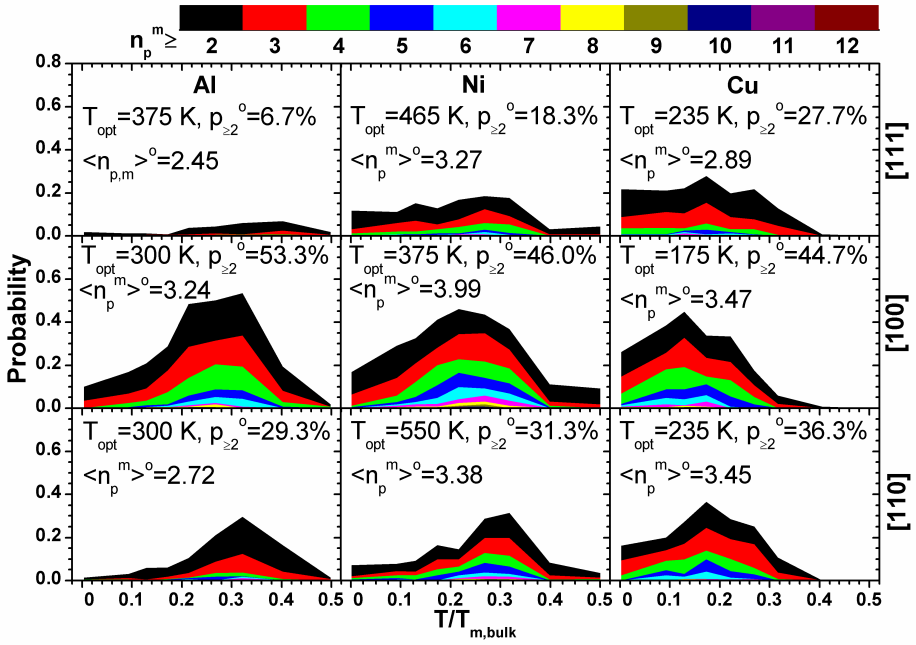

Figure 7.10: Temperature dependence of the probability of finding an icosahedral nanowire containing a maximum number of pentagonal rings equal or larger than a given reference value n_p^m for Al, Ni and Cu nanowires with large initial size (containing $\approx$1000 atoms). The colour bar (top) determines the reference value of n_p^m. The temperature is given in units of the bulk melting temperature $T_{m,bulk}$ for each material. Different rows correspond to different stretching directions. For each material and stretching direction, we include the optimal temperature T_{opt} at which the production of icosahedral nanowires takes a maximum, and the quantities $p_{\geq 2}$, $max(n_p^m)$, and $\langle n_p^m \rangle$ evaluated at T_{opt} (as indicated by the superindex 'o').

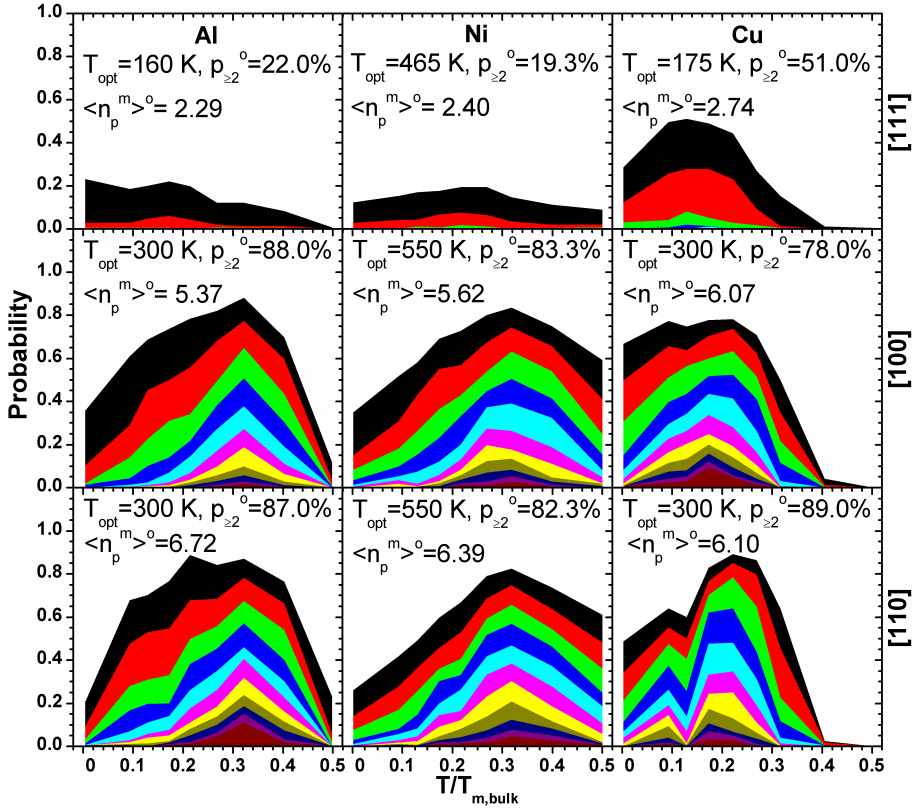

Figure 7.11: Temperature dependence of the probability of finding an icosahedral nanowire containing a maximum number of pentagonal rings equal or larger than a given reference value n_p^m for Al, Ni and Cu nanowires with small initial size (containing ≈200 atoms). The colour bar (top) determines the reference value of n_p^m. The temperature is given in units of the bulk melting temperature $T_{m,bulk}$ for each material. Different rows correspond to different stretching directions. For each material and stretching direction, we include the optimal temperature T_{opt} at which the production of icosahedral nanowires takes a maximum, and the quantities $p_{\geq 2}$, $max(n_p^m)$, and $\langle n_p^m \rangle$ evaluated at T_{opt} (as indicated by the superindex 'o').

than those seen for the other stretching directions. This behaviour is noteworthy for aluminium and nickel. Cooper nanowires stretched along the [111] direction represent a special case because at low temperatures they present a non-negligible probability of formation of relatively long icosahedral chains. This is probably due to the low cohesive energy of the Cu, and its high ductility, that facilitates the appearance of chains because of the mechanical energy supplied by the stretching. Anyway, these results graphically illustrate the higher possibility of finding icosahedral structures by stretching nanowires along [100] and [110] orientations. This observation is valid for the three metallic species studied here, but we believe it is likely to be extended to other FCC metals. This kind of orientational dependent behaviour has also been reported from experimental and theoretical observations of Au nanowires breaking [Coura2004], where [110] direction seems to favour the appearance of rod-like structures, whereas [100] and [111]-oriented nanowires tend to form one-atom contacts and LACs. Other theoretical approaches based in MD simulations within EAM have also found that the role of stretching direction is relevant for the formation of Cu LACs [Bahn2001, GM2008a, Liu2009].

As we have mentioned previously, the existence of an optimal temperature that favours the production of icosahedral nanowires is due to the competition of two mechanisms. The formation of the icosahedral chain, by extraction of atoms from regions with an initial geometry of FCC type, is initially favoured by the increase of the temperature. Such temperature increase allows the exploration of favourable configurations in the phase space as it occurs in the formation of nanowires with 'magic' sections [Medina2003, Yanson1999]. We must mention that, in addition, the formation of longer icosahedral chains is also favoured by the possibility of a slight rotation of the pentagonal nanowire around its axes. The figure 7.8 shows the twists of the pentagonal chain in several sequences/stages of its formation. This small twists favour a better coupling of the icosahedral chain with the contiguous disordered regions that feed the growing structure. However, as the temperature increases, large atomic fluctuations lead to the melting of the nanowire as well as the FCC zones, making difficult the extraction mechanism of atoms from the FCC region and their incorporation into the icosahedral wire.

It is worth noting that, as shown in figures 7.10 and 7.11, the production of Cu pentagonal chains has finished when $T/T_{m,bulk} \simeq 0.4$. By comparing with the melting temperature $T_{m,icos}$ of the infinite Cu pentagonal chain shown in table 7.2 , which is $T_{m,icos}/T_{m,bulk} = 0.4$, it seems evident that the production of Cu nanowires is limited in temperature by the melting of the icosahedral chains. For Al and Ni, we

notice a decrease of the production ratio of icosahedral nanowires as the temperature increases above the temperature T_{opt}, but the temperature at which their production would seem to cease completely due to melting is above the highest temperature we have considered in our simulations ($0.5 \times T_{m,bulk}$).

From the comparison of figures 7.10 and 7.11 it is also evident that there exists a dependence of the quantities $p^o_{\geq 2}$, $\langle n^m_p \rangle^o$, and $max(n^m_p)^o$ with the nanowire size. In particular, all these quantities decrease as the nanowire size increases. This is due to the fact that the pentagonal chain is easily formed from atoms that initially occupied surface positions in the FCC structure. These atoms need less energy to overcome the energy barrier between the FCC configuration and the icosahedral one. Therefore, thinner nanowires (with a large surface/volume ratio) can perform more easily the required transformation to form icosahedral chains.

7.4 Conclusions

We have performed massive computer simulations of the breaking of Al, Ni and Cu nanowires. These simulations have shown that under certain conditions long chains with pentagonal structure appear in the narrowest part of the nanowire. This type of structures had already been reported by other authors as one of those nanowire configurations with higher stability than the FCC structure of similar linear density. Their appearance has also been proposed in previous experimental works [Gonzál2004] as an explanation to the high peak around $G = 4.5\,G_0$ in conductance histograms of Cu. However, neither theoretical nor experimental works have addressed so far the probability of formation of these chains.

Our statistical analysis includes nanowires oriented along three different crystallographic directions ([100], [110] and [111]). Different simulation temperatures were tried between 4 K and half the melting temperature of the corresponding material. Another variable in our study is the size of the nanowire. We have considered, for every material, orientation and temperature, two nanowire sizes: a small one with about 200 atoms and a large one with 1000 atoms approximately.

The use of MD simulations provides a detailed control over the atomic coordinates during the whole breaking process. This has allowed us to developed a methodology to properly identify these pentagonal chains and monitor their time evolution. Using this methodology we have built histograms of the maximum lengths L^m_p and maximum number of pentagonal rings n^m_p of the pentagonal chains.

We have elaborated histograms of the maximum pentagonal chain length $H(L_p^m)$. These histograms exhibit a clearly peaked structure. These peaks are regularly spaced by about the distance d_{5-5} between pentagonal rings. For each study case we have also determined the formation probability of such chains, the average chain length and the maximum length we have detected. These analysis have identified chains of up to 16 pentagonal rings, with average maximum lengths of $n_p^m \sim 6$ for the small nanowires strained along the [100] or [110] directions. We have observed that the axial orientation of the nanowire plays a key role in the formation of pentagonal chains. In particular, nanowires stretched along the [111] direction show much lower probability of forming a pentagonal chain than those oriented along the [100] or [110] directions.

One of the most interesting results of this chapter is the role of temperature in the probability of formation of pentagonal chains. We have observed that there is an optimal temperature (which we call T^{opt}) at which the probability of formation of pentagonal chains is the highest. This probability gradually decreases if we break nanowires either at lower or at higher temperatures than T^{opt}. The existence of an optimal temperature is the consecuence of two competing mechanisms: On one hand, too low temperatures do not allow the exploration of new configurations in the phase space, like the pentagonal structure, that are more stable than crystalline FCC structures with ultra small cross-section. On the other hand, when the temperature increases too much, the thermal fluctuations prevent the efficient formation of such chains, promoting instead their melting.

A brief consideration should be made regarding the reliability of these results. If we look at the coordination number N_c of atoms in a pentagonal chain we find that central atoms have $N_c = 12$, whereas atoms in a pentagonal ring have $N_c = 8$. From this observation we can say that every -5-1- subunit has an average coordination

$$\bar{N_c} = \frac{1}{6}(5 \times 8 + 1 \times 12) \simeq 8.67. \tag{7.4}$$

In chapter 3 we have seen that the MFMP EAM parameterization describes reasonably well properties like E_c and d_{nn} in a system of $N_c = 8$, like the BCC structure. This makes us expect that this potential should account properly for the qualitative behaviour of these pentagonal chains and their formation during the breaking process of nanowires.

7.4.1 Could pentagonal nanowires be observed in 'real life' experiments?

A few experimental approaches may be proposed that could allow the detection of these long icosahedral nanowires that we have found in our computational simulations. First, the study of the conductance histogram as a function of the temperature can show evidences about the formation of icosahedral chains observing the conductance peak associated with sections $S_m \sim 5$. This procedure seems the easiest, extending former studies performed for Cu [Gonzál2004]. Furthermore, some techniques, as the Mechanically Controllable Break Junction (MCBJ) allow a relatively good control of the initial geometry of the nanowire, allowing to check the effect of the stretching directions and the initial nanocontact section size on the production of pentagonal nanowires.

A second experimental approach could be based on the inspection of individual conductance traces $G(t)$ as it has been done for studying the formation and properties of LACs. These studies would allow the construction of pentagonal nanowire length histograms similar to those obtained for studying the length of linear atomic chains of different metals [Untiedt2002].

A third method, closely related with the previous one, is based on the measurement of the stretching forces during the production of the icosahedral nanowire using an experimental configuration similar to that used to simultaneously measure the conductance and forces during a nanocontact breakage [RB2001, RB1996]. Under this approach, the appearance of a new pentagonal ring would be seen as an abrupt jump in the force followed by an elastic deformation stage; meanwhile the conductance should show approximately a constant value close to that expected for a pentagonal nanowire and possibly including some smaller fluctuations due to Fabry-Perot phenomena [Yanson1999]. These experiments, similar to those performed to analyse the formation mechanism of LACs, should be carried out at very low temperature to avoid fluctuations that could mask the force jumps predicted by our simulations.

The best candidate for these experiments of the metallic species analysed in this chapter is Cu, which shows the highest $p_{\geq 2}$ value at low temperature. A major challenge for our previous experimental proposals is the control over the initial crystalline orientation (and stretching direction) of the nanocontact. In the case that the orientation control would be not possible, the expected result should be an average of the results of the three orientations we have shown, taking into account the different weights associated with the probability of finding each crystalline orientation [Gonzál2004, Rodrigue2000].

7.4.2 Possible applications of pentagonal nanowires

Finally, some comments about the possible technological utility of these icosahedral nanowires should be addressed. It is worth say that chain-like nanometric structures (that are stable at room or higher temperatures) open the possibility of using them in electronic devices under real working conditions, adding a new candidate to take into account into the nanoelectronic scope. These stable pentagonal nanowires are also good candidates to ballistic spin filters, if they are made of a magnetic material, opening their use to incoming spintronics devices. The use of these pentagonal nanowires is conditioned to the availability of efficient production methods based in the procedures here described or by means of other synthesis techniques. One of the experimental possibilities to be explored (one that falls out of the reach of this thesis) is to significantly increase the length of the pentagonal chains by using controlled cycles of indentation and retraction, that could allow a controlled increase of the number of pentagonal rings that form the chain.

More immediate applications that do not require very long icosahedral wires can be found in others fields. As it was previously pointed out, long pentagonal chains formed always break near one of their ends. This means that one of the resulting fragments after the rupture is a large aspect ratio nanostructure formed by an icosahedral nanotube ended in one atom. These conducting nanotips obtained after an indentation process can be used in applications of electronic field emission (FE) [Fursey2005] or nanoantennas [Friedler2009, Podolski2005]. Therefore, the results of this thesis about the formation of icosahedral nanowires open a path to their production in a controllable way, providing nanostructures with a great deal of applications in electronics, magneto-resistivity, spintronics or field emission devices at room or higher temperatures.

References

[Adams1983] D. L. Adams, H. B. Nielsen, and J. N. Andersen. Oscillatory relaxation of the Cu(110) surface. *Surface Science*, 128(2-3):294–310, 1983.

[Adams1985] D. L. Adams, L. E. Petersen, and C. S. Sorensen. Oscillatory relaxation of the Ni(110) surface: a LEED study. *Journal of Physics C: Solid State Physics*, 18(8):1753–1766, March 1985.

[Agraït1995] N. Agraït, G. Rubio, and S. Vieira. Plastic Deformation of Nanometer-Scale Gold Connective Necks. *Physical Review Letters*, 74(20):3995–3998, May 1995.

[Agraït2003] N. Agraït, A. L. Yeyati, and J. M. van Ruitenbeek. Quantum properties of atomic-sized conductors. *Physics Reports*, 377:81 – 279, 2003.

[Alder1957] B. J. Alder and T. E. Wainwright. Phase Transition for a Hard Sphere System. *The Journal of Chemical Physics*, 27(5):1208, August 1957.

[Alder1959] B. J. Alder and T. E. Wainwright. Studies in Molecular Dynamics. I. General Method. *The Journal of Chemical Physics*, 31(2):459, 1959.

[Allen1999] M. P. Allen and D. J. Tildesley. *Computer simulation of liquids.* Oxford University Press, 1999.

[Alonso2005] J. A. Alonso. *Structure and properties of atomic nanoclusters.* Imperial College Press, 2005.

[Andersen1980] H. C. Andersen. Molecular dynamics simulations at constant pressure and/or temperature. *The Journal of Chemical Physics*, 72(4):2384, July 1980.

[Ao2008] Z. M. Ao, S. Li, and Q. Jiang. The determination of Young's modulus in noble metal nanowires. *Applied Physics Letters*, 93:81905, 2008.

[Arden2010] W. Arden, M. Brillouët, P. Cogez, M. Graef, B. Huizing, and R. Mahnkopf. "More-than-Moore" White paper. Technical Report 10, International Technology Roadmap for Semiconductors, October 2010.

[Artacho1999] E. Artacho, D. Sánchez-Portal, P. Ordejón, A. García, and J. M. Soler. Linear-Scaling ab-initio Calculations for Large and Complex Systems. *physica status solidi (b)*, 215(1):809–817, September 1999.

[Ashcroft1976] N. W. Ashcroft and N. D. Mermin. *Solid State Physics*. Saunders College, 1976.

[Bahn2001] S. Bahn and K. Jacobsen. Chain Formation of Metal Atoms. *Physical Review Letters*, 87(26):24–27, December 2001.

[Bakker2002] D. Bakker, Y. Noat, A. I. Yanson, and J. M. van Ruitenbeek. Effect of disorder on the conductance of a Cu atomic point contact. *Physical Review B*, 65(23):1–5, May 2002.

[Barnett1997] R. N. Barnett and U. Landman. Cluster-derived structures and conductance fluctuations in nanowires. *Nature*, 387(June):788, 1997.

[Basinski1971] Z. S. Basinski, M. S. Duesbery, and R. Taylor. Influence of Shear Stress on Screw Dislocations in a Model Sodium Lattice. *Canadian Journal of Physics*, 49(16):2160–2180, 1971.

[Berendse1984] H. J. C. Berendsen, J. P. M. Postma, W. F. Van Gunsteren, A. DiNola, and J. R. Haak. Molecular dynamics with coupling to an external bath. *The Journal of Chemical Physics*, 81(8):3684, 1984.

[Born1912] M. Born and T. von Karman. Über Schwingungen in Raumgittern. *Physik Z*, 13:297–309, 1912.

[Born1927] M. Born and R. Oppenheimer. Zur Quantentheorie der Molekeln. *Annalen der Physik*, 389(20):457–484, 1927.

[Braníc2000] P. S. Branício and J. P. Rino. Large deformation and amorphization of Ni nanowires under uniaxial strain: A molecular dynamics study. *Physical Review B*, 62(24):950–955, 2000.

[Bratkovs1995] A. M. Bratkovsky, A. P. Sutton, and T. N. Todorov. Conditions for conductance quantization in realistic models of atomic-scale metallic contacts. *Physical Review B*, 52:5036, 1995.

[Brooks1988] C. L. Brooks, M. Karplus, and B. Montgomery. *Proteins: A theoretical perspective of dynamics, sructure, and thermodynamics by Charles L. Brooks III, Martin Karplus and B. Montgomery Pettitt; Advances in Chemical Physics, Volume LXXI; edited by I. Prigogine and S.A. Rice, Wiley-Interscience, New York*, volume 71 of *Advances in Chemical Physics*. Wiley, New York, April 1988.

[Bulienko2001] N. A. Bulienkov and D. L. Tytik. Modular design of icosahedral metal clusters. *Russian Chemical Bulletin*, 50(1):1–19, 2001.

[Cao2010] A. Cao. Shape memory effects and pseudoelasticity in bcc metallic nanowires. *Journal of Applied Physics*, 108(11):113531, 2010.

[Car1985] R. Car and M. Parrinello. Unified Approach for Molecular Dynamics and Density-Functional Theory. *Physical Review Letters*, 55(22):2471–2474, November 1985.

[Chen2005] D. Chen and T. Chen. Mechanical properties of Au nanowires under uniaxial tension with high strain-rate by molecular dynamics. *Nanotechnology*, 16(12):2972–2981, 2005.

[CK1997] J. L. Costa-Krämer. Conductance quantization at room temperature in magnetic and nonmagnetic metallic nanowires. *Physical Review B*, 55(8):R4875–R4878, February 1997.

[Coskun2011] Sahin Coskun, Burcu Aksoy, and Husnu Emrah Unalan. Polyol Synthesis of Silver Nanowires: An Extensive parametric Study. *Crystal Growth & Design*, 11(11):4963–4969, August 2011.

[Coura2004] P. Z. Coura, S. B. Legoas, A. S. Moreira, F. Sato, V. Rodrigues, S. O. Dantas, D. Ugarte, and D. S. Galvão. On the Structural and Stability Features of Linear Atomic Suspended Chains Formed from Gold Nanowires Stretching. *Nano Letters*, 4(7):1187–1191, July 2004.

[Daw1983] M. S. Daw and M. I. Baskes. Semiempirical, quantum mechanical calculation of hydrogen embrittlement in metals. *Physical Review Letters*, 50:1285–1288, 1983.

[Daw1984] M. S. Daw and M. I. Baskes. Embedded-atom method: Derivation and application to impurities, surfaces, and other defects in metals. *Physical Review B*, 29(12):6443, 1984.

[Daw1993] M. S. Daw, S. M. Foiles, and M. I. Baskes. The embedded-atom method: a review of theory and applications. *Materials Science Reports*, 9(7-8):251, 1993.

[Diao2003] J. Diao, K. Gall, and M. L. Dunn. Surface-stress-induced phase transformation in metal nanowires. *Nature materials*, 2(10):656–60, October 2003.

[Díaz2006] M. Díaz, J. L. Costa-Krämer, and P. A. Serena. Partial versus total conductance histograms: A tool to identify magnetic effects in nanocontacs. *Journal of Magnetism and Magnetic Materials*, 305(2):497–503, October 2006.

[Dreher2005] M. Dreher, F. Pauly, J. Heurich, J. Cuevas, E. Scheer, and P. Nielaba. Structure and conductance histogram of atomic-sized Au contacts. *Physical Review B*, 72(7):1–11, August 2005.

[Drexler1981] K. E. Drexler. Molecular engineering: An approach to the development of general capabilities for molecular manipulation. *Proceedings of the National Academy of Sciences of the United States of America*, 78(9):5275–8, September 1981.

[Elhoussi2002] F. Elhoussine, S. Mátéfi-Tempfli, A. Encinas, and L. Piraux. Conductance quantization in magnetic nanowires electrodeposited in nanopores. *Applied Physics Letters*, 81(9):1681, 2002.

[Ercoless1988] F. Ercolessi, M. Parrinello, and E. Tosatti. Simulation of gold in the glue model. *Philosophical Magazine A*, 58(1):213–226, July 1988.

[Ercoless1994] F. Ercolessi and J. B. Adams. Interatomic Potentials from First-Principles Calculations: The Force-Matching Method. *Europhysics Letters (EPL)*, 26(8):583–588, June 1994.

[Ercoless1997] F. Ercolessi. A molecular dynamics primer. *Spring College in Computational Physics*, 1997.

[Evans1983] D Evans. The isothermal/isobaric molecular dynamics ensemble. *Physics Letters A*, 98(8-9):433–436, November 1983.

[Fazio2003] R. Fazio, V. F. Gantmakher, and Y. Imry. *New directions in mesoscopic physics (towards nanoscience)*, volume 125 of *NATO science series: Mathematics, physics, and chemistry*. Springer, 2003.

[Feynman1960] R. P. Feynman. There is plenty of room at the bottom. *Engineering and Science*, 23(5):22–36, 1960.

[Finnis1984] M. W. Finnis and J. E. Sinclair. A simple empirical N-body potential for transition metals. *Philosophical magazine. A. Physics of condensed matter. Defects and mechanical properties*, 50(1):45–55, July 1984.

[Fisher2009] D. J. Fisher, editor. *Surface reconstructions*, volume 287-288 of *Defect and Diffusion Forum*. Trans Tech Pubn, 2009.

[Fletcher1964] R. Fletcher. Function minimization by conjugate gradients. *The Computer Journal*, 7(2):149–154, February 1964.

[FP2002] L. Froufe-Pérez, P. García-Mochales, P. A. Serena, P. Mello, and J. Sáenz. Conductance Distributions in Quasi-One-Dimensional Disordered Wires. *Physical Review Letters*, 89(24):246403, November 2002.

[Franssil2010] S. Franssila. *Introduction to Microfabrication*. John Wiley and Sons, 2010.

[Friedler2009] I. Friedler, C. Sauvan, J. P. Hugonin, P. Lalanne, J. Claudon, and J. M. Gérard. Solid-state single photon sources: the nanowire antenna. *Optics express*, 17(4):2095–110, February 2009.

[Fursey2005] G. Fursey. *Field emission in vacuum microelectronics*. Springer, 2005.

[Garzón1998] I. Garzón, K. Michaelian, M. Beltrán, A. Posada-Amarillas, P. Ordejón, E. Artacho, D. Sánchez-Portal, and J. Soler. Lowest Energy Structures of Gold Nanoclusters. *Physical Review Letters*, 81(8):1600–1603, August 1998.

[Gear1966] C.W. Gear. The numerical integration of ordinary differential equations of various orders. Technical report, Argonne National Lab., Ill., 1966.

[Gear1971] C.W. Gear. Numerical initial value problems in ordinary differential equations. *Prentice-Hall Series in Automatic Computation, Englewood Cliffs: Prentice-Hall, 1971*, 1, 1971.

[Ghodssi2011] R. Ghodssi and P. Lin. *MEMS Materials and Processes Handbook*. Springer, 2011.

[Gillingh2002] D. M. Gillingham, I. Linington, and J. A. C. Bland. e2/h quantization of the conduction in Cu nanowires. *Journal of Physics: Condensed Matter*, 14(29):L567, July 2002.

[GM2005a] P. García-Mochales, S. Peláez, P. A. Serena, E. Medina, and A. Hasmy. Breaking processes in nickel nanocontacts: a statistical description. *Applied Physics A*, 81(8):1545–1549, September 2005.

[GM2005b] P. García-Mochales, P. A. Serena, C. Guerrero, E. Medina, and A. Hasmy. Atomic configurations of breaking nanocontacts of aluminium and nickel. *Materials Science - Poland*, 23(2):413–419, 2005.

[GM2008a] P. García-Mochales, R. Paredes, S. Peláez, and P. A. Serena. Statistical analysis of the breaking processes of Ni nanowires. *Nanotechnology*, 19(22):225704, June 2008.

[GM2008b] P. García-Mochales, R. Paredes, S. Peláez, and P. A. Serena. Statistical Molecular Dynamics Study of (111) and (100) Ni Nanocontacts: Evidences of Pentagonal Nanowires. *Journal of Nanomaterials*, 2008:1–10, 2008.

[GM2008c] P. García-Mochales, R. Paredes, S. Peláez, and P. a. Serena. Statistical Molecular Dynamics Study of (111) and (100) Ni Nanocontacts: Evidences of Pentagonal Nanowires. *Journal of Nanomaterials*, 2008:1–9, 2008.

[GM2008d] P. García-Mochales, R. Paredes, S. Peláez, and P. A. Serena. The formation of pentagonal Ni nanowires: dependence on the stretching direction and the temperature. *Physica Status Solidi (a)*, 205(6):1317–1323, June 2008.

[Goddard 2007] W. A. Goddard III, D. W. Brenner, S. E. Lyshevski, and G. J. Iafrate, editors. *Handbook of nanoscience, engineering and technology.* CRC Press, 2nd edition, 2007.

[Gonzál2004] J. González, V. Rodrigues, J. Bettini, L. Rego, A. Rocha, P. Z. Coura, S. O. Dantas, F. Sato, D. Galvão, and D. Ugarte. Indication of Unusual Pentagonal Structures in Atomic-Size Cu Nanowires. *Physical Review Letters*, 93(12):1–4, September 2004.

[Guerrero2010] C. Guerrero. *Estudio estadístico de la ruptura de nanocontactos metálicos: hacia la interpretación de los histogramas de conductancia.* Phd. thesis, Instituto Venezolano de Investigaciones Científicas, 2010.

[Gülser1998] O. Gülseren, F. Ercolessi, and E. Tosatti. Noncrystalline Structures of Ultrathin Unsupported Nanowires. *Physical Review Letters*, 80(17):3775–3778, April 1998.

[Hansen2006] J.-P. Hansen and I. R. McDonald. *Theory of simple liquids.* Academic Press, 2006.

[Hashim2011] A. Hashim, editor. *Nanowires - Implementations and Applications.* InTech, 1 edition, 2011.

[Hasmy2001] A. Hasmy, E. Medina, and P. A. Serena. From Favorable Atomic Configurations to Supershell Structures: A New Interpretation of Conductance Histograms. *Physical Review Letters*, 86(24):5574–5577, June 2001.

[Hasmy2005] A. Hasmy, A. Pérez-Jiménez, J. Palacios, P. García-Mochales, J. L. Costa-Krämer, M. Díaz, E. Medina, and P. A. Serena. Ballistic resistivity in aluminum nanocontacts. *Physical Review B*, 72(24):2–6, December 2005.

[Hermann2011] K. Hermann. *Crystallography and Surface Structure: An Introduction for Surface Scientists and Nanoscientists.* John Wiley and Sons, 2011.

[Herrmann1984a] H. J. Herrmann, D. C. Hong, and H. E. Stanley. Backbone and elastic backbone of percolation clusters obtained by the new method of

'burning'. *Journal of Physics A: Mathematical and General*, 17:L261, 1984.

[Herrmann1984b] H. J. Herrmann and H. E. Stanley. Building blocks of percolation clusters: volatile fractals. *Physical Review Letters*, 53(12):1121–1124, 1984.

[Hestenes1952] M. R. Hestenes and E. Stiefel. Methods of conjugate gradients for solving linear systems. *Journal of Research of the National Bureau of Standards*, 49(6):409–436, 1952.

[Hoover1985] W. Hoover. Canonical dynamics: Equilibrium phase-space distributions. *Physical Review A*, 31(3):1695–1697, March 1985.

[Huang2008] Q. Huang. *Size and surface effects on the electrical properties of metallic nanowires*. ProQuest, University of Illinois at Chicago, 2008.

[Huo2008] F. Huo, Z. Zheng, G. Zheng, L. R. Giam, H. Zhang, and C. A. Mirkin. Polymer pen lithography. *Science*, 321(5896):1658–60, September 2008.

[Hurst2006] S. J. Hurst, E. K. Payne, L. Qin, and C. A. Mirkin. Multisegmented one-dimensional nanorods prepared by hard-template synthetic methods. *Angewandte Chemie (International ed. in English)*, 45(17):2672–92, April 2006.

[Ikeda1999] H. Ikeda, Y. Qi, T. Çagin, K. Samwer, W. L. Johnson, and W. A. Goddard. Strain Rate Induced Amorphization in Metallic Nanowires. *Physical Review Letters*, 82(14):2900–2903, April 1999.

[Iniewski2010] K. Iniewski. *Nanoelectronics: Nanowires, Molecular Electronics, and Nanodevices*. McGraw-Hill Prof Med/Tech, 2010.

[Jacob2005] D. Jacob, J. Fernández-Rossier, and J. Palacios. Magnetic and orbital blocking in Ni nanocontacts. *Physical Review B*, 71(22):1–4, June 2005.

[Jacob2006] D. Jacob, M. J. Caturla, R. Calvo, C. Untiedt, and J. J. Palacios. Mechanical and electrical properties of Ni nanocontacts. In *2006 IEEE Nanotechnology Materials and Devices Conference*, pages 236–237. IEEE, October 2006.

[Jaffe2000] J. Jaffe. Comparison of embedded-atom models and first-principles calculations for Al phase equilibrium. *Computational Materials Science*, 18(2):199–204, August 2000.

[Jiang2009] S. Jiang, H. Zhang, Y. Zheng, and Z Chen. Atomistic study of the mechanical response of copper nanowires under torsion. *Journal of Physics D: Applied Physics*, 42(13):135408, July 2009.

[Joachim2009] C. Joachim and L. Plévert. *Nanosciences: the invisible revolution*. World Scientific, 2009.

[Junquera2001] J. Junquera, Ó. Paz, D. Sánchez-Portal, and E. Artacho. Numerical atomic orbitals for linear-scaling calculations. *Physical Review B*, 64(23), November 2001.

[Kimura1998] Y. Kimura, Y. Qi, and C. Tahir. The Quantum Sutton-Chen Many Body Potential for Properties of fcc Metals. *Unpublished*, http://wag, 1998.

[Kirkpatr1983] S. Kirkpatrick, C. D. Gelatt, and M. P. Vecchi. Optimization by Simulated Annealing. *Science*, 220(4598):671–680, May 1983.

[Kittel1995] C. Kittel. *Introduction to Solid State Physics*. John Wiley & Sons Canada, Limited, 1995.

[Kline2006] T. R. Kline, M. Tian, J. Wang, A. Sen, M. W. H. Chan, and T. E. Mallouk. Template-grown metal nanowires. *Inorganic chemistry*, 45(19):7555–65, September 2006.

[Kohanoff2006] J. Kohanoff. *Electronic structure calculations for solids and molecules: theory and computational methods*. Cambridge University Press, 2006.

[Kondo1997] Y. Kondo and K. Takayanagi. Gold Nanobridge Stabilized by Surface Structure. *Physical Review Letters*, 79(18):3455–3458, November 1997.

[Kondo2000] Y. Kondo and K. Takayanagi. Synthesis and characterization of helical multi-shell gold nanowires. *Science*, 289(5479):606–8, July 2000.

[Krans1995] J. M. Krans, J. M. van Ruitenbeek, V. V. Fisun, I. K. Yanson, and L. J. de Jongh. The signature of conductance quantization in metallic point contacts. *Nature*, 375(6534):767–769, June 1995.

[Landauer1968] R. Landauer and J. J. Hall. Solid State Physics as a Source of Modern Electronics. *Science*, 160(3829):736–41, May 1968.

[Landauer1970] R. Landauer. Electrical resistance of disordered one-dimensional lattices. *Philosophical Magazine*, 21:863–867, April 1970.

[Landman1990] U. Landman, W. D. Luedtke, N. A. Burnham, and R. J. Colton. Atomistic mechanisms and dynamics of adhesion, nanoindentation, and fracture. *Science*, 248(4954):454–61, April 1990.

[Landman1996] U. Landman, W. Luedtke, B. Salisbury, and R. Whetten. Reversible Manipulations of Room Temperature Mechanical and Quantum Transport Properties in Nanowire Junctions. *Physical Review Letters*, 77(7):1362–1365, August 1996.

[Liang2005a] H. Liang, M. Upmanyu, and H. Huang. Size-dependent elasticity of nanowires: Nonlinear effects. *Physical Review B*, 71(24):1–4, June 2005.

[Liang2005b] W. Liang, M. Zhou, and F. Ke. Shape memory effect in Cu nanowires. *Nano Letters*, 5(10):2039–43, October 2005.

[Liang2006] W. Liang and M. Zhou. Atomistic simulations reveal shape memory of fcc metal nanowires. *Physical Review B*, 73(11):1–11, March 2006.

[Lide2004] D. R. Lide, editor. *CRC handbook of chemistry and physics: a ready-reference book of chemical and physical data*. CRC Press, 87 edition, 2004.

[Lind1987] D. Lind, F. Dunning, G. Walters, and H. Davis. Surface-structural analysis by use of spin-polarized low-energy electron diffraction: An investigation of the Cu(100) surface. *Physical Review B*, 35(17):9037–9044, June 1987.

[Liu2009] Y. Liu, F. Wang, J. Zhao, L. Jiang, M. Kiguchi, and K. Murakoshi. Theoretical investigation on the influence of temperature and crystallographic orientation on the breaking behavior of copper nanowire.

Physical chemistry chemical physics : PCCP, 11(30):6514–9, August 2009.

[Liu2011] Y. Liu and J. Zhao. The size dependence of the mechanical properties and breaking behavior of metallic nanowires: A statistical description. *Computational Materials Science*, 50(4):1418–1424, February 2011.

[LJ1924] J. E. Lennard-Jones. On the Determination of Molecular Fields. II. From the Equation of State of a Gas. *Proceedings of the Royal Society A: Mathematical, Physical and Engineering Sciences*, 106(738):463–477, October 1924.

[Lu2010] Y. Lu, J. Y. Huang, C. Wang, S. Sun, and J. Lou. Cold welding of ultrathin gold nanowires. *Nature nanotechnology*, 5(3):218–24, March 2010.

[Lüth2001] H. Lüth. *Solid surfaces, interfaces and thin films*. Springer, 2001.

[Lyshevsk2002] S. E. Lyshevski. *MEMS and NEMS: systems, devices, and structures*. CRC Press, 2002.

[Medina2003] E. Medina, M. Díaz, N. León, C. Guerrero, A. Hasmy, P. A. Serena, and J. L. Costa-Krämer. Ionic Shell and Subshell Structures in Aluminum and Gold Nanocontacts. *Physical Review Letters*, 91(2):1–4, July 2003.

[Mehrez1997] H. Mehrez and S. Ciraci. Yielding and fracture mechanisms of nanowires. *Physical Review B*, 56(19):12632–12642, November 1997.

[Melchion1993] S. Melchionna, G. Ciccotti, and B. Lee Holian. Hoover NPT dynamics for systems varying in shape and size. *Molecular Physics*, 78(3):533–544, February 1993.

[Mishin1999] Y. Mishin, D. Farkas, M. Mehl, and D. Papaconstantopoulos. Interatomic potentials for monoatomic metals from experimental data and ab initio calculations. *Physical Review B*, 59(5):3393–3407, February 1999.

[Mishin2001] Y. Mishin, M. Mehl, D. Papaconstantopoulos, A. Voter, and J. Kress. Structural stability and lattice defects in copper: Ab initio, tight-binding, and embedded-atom calculations. *Physical Review B*, 63(22):1–16, May 2001.

[Mizobata2003] J. Mizobata, A. Fujii, S. Kurokawa, and A. Sakai. High-bias conductance of atom-sized Al contacts. *Physical Review B*, 68(15):1–7, October 2003.

[Monnier1978] R. Monnier. Surfaces of real metals by the variational self-consistent method. *Physical Review B*, 17(6):2595–2611, March 1978.

[Moore1998] G. E. Moore. Cramming more components onto integrated circuits. *Proceedings of the IEEE*, 86(1):82–85, 1998.

[Muller1992] C. J. Muller, J. M. van Ruitenbeek, and L. J. de Jongh. Experimental observation of the transition from weak link to tunnel junction. *Physica C: Superconductivity*, 191(3-4):485–504, February 1992.

[Muller1996] C. Muller, J. Krans, T. N. Todorov, and M. Reed. Quantization effects in the conductance of metallic contacts at room temperature. *Physical Review B*, 53(3):1022–1025, January 1996.

[Murr1975] L. E. Murr. *Interfacial phenomena in metals and alloys.* Addison-Wesley Pub. Co., Advanced Book Program, London, 2nd edition, 1975.

[Nosé1984] S. Nosé. A molecular dynamics method for simulations in the canonical ensemble. *Molecular Physics*, 52(2):255–268, June 1984.

[Olesen1994] L. Olesen, E. Laegsgaard, I. Stensgaard, F. Besenbacher, J. Schiotz, P. Stoltze, K. Jacobsen, and J. K. Norskov. Quantized conductance in an atom-sized point contact. *Physical Review*, 72(14):2251–2254, 1994.

[Olesen1995] L. Olesen, E. Laegsgaard, I. Stensgaard, F. Besenbacher, J. Schiotz, P. Stoltze, K. Jacobsen, and J. K. Norskov. Reply. *Physical Review*, 74(11):2147–2147, 1995.

[Ono1999] T. Ono, Y. Ooka, H. Miyajima, and Y. Otani. 2e/h to e/h switching of quantum conductance associated with a change in nanoscale ferromagnetic domain structure. *Applied Physics Letters*, 75(11):1622, 1999.

[Ooka2001] Y. Ooka, T. Ono, and H. Miyajima. Conductance quantization in ferromagnetic Ni nanowire. *Journal of Magnetism and Magnetic Materials*, 226-230:1848–1849, May 2001.

[Oshima1998] H. Oshima and K. Miyano. Spin-dependent conductance quantization in nickel point contacts. *Applied Physics Letters*, 73(15):2203, 1998.

[Oshima2006] Y. Oshima, K. Mouri, H. Hirayama, and K. Takayanagi. Quantized Electrical Conductance of Gold Helical Multishell Nanowires. *Journal of the Physics Society Japan*, 75(5):053705, May 2006.

[Ott1998] F. Ott, S. Barberan, J. Lunney, J. Coey, P. Berthet, A. de Leon-Guevara, and A. Revcolevschi. Quantized conductance in a contact between metallic oxide crystals. *Physical Review B*, 58(8):4656–4659, August 1998.

[Oura2010] K. Oura, V. G. Lifshits, A. A. Saranin, A. V. Zotov, and M. Katayama. *Surface Science: An Introduction*. Springer, 2010.

[Park2005a] H. Park, K. Gall, and J. A. Zimmerman. Shape Memory and Pseudoelasticity in Metal Nanowires. *Physical Review Letters*, 95(25):1–4, December 2005.

[Park2005b] H. Park and J. A. Zimmerman. Modeling inelasticity and failure in gold nanowires. *Physical Review B*, 72(5):54106, August 2005.

[Park2006a] H. S. Park, K. Gall, and J. A. Zimmerman. Deformation of FCC nanowires by twinning and slip. *Journal of the Mechanics and Physics of Solids*, 54(9):1862–1881, September 2006.

[Park2006b] H. S. Park and J. A. Zimmerman. Stable nanobridge formation in [110] gold nanowires under tensile deformation. *Scripta Materialia*, 54(6):1127–1132, March 2006.

[Pascual1993] J. I. Pascual, J. Mendez, J. Gómez-Herrero, A. M. Baró, and N. García. Quantum contact in gold nanostructures by scanning tunneling microscopy. *Physical Review Letters*, 71(12):1852–1855, 1993.

[Pascual1995] J. I. Pascual, J. Méndez, J. Gómez-Herrero, A. M. Baró, N. García, U. Landman, W. D. Luedtke, E. N. Bogachek, and H. P. Cheng. Properties of metallic nanowires: from conductance quantization to localization. *Science*, 267(5205):1793–5, March 1995.

[Pauly2006] F. Pauly, M. Dreher, J. Viljas, M. Häfner, J. Cuevas, and P. Nielaba. Theoretical analysis of the conductance histograms and structural properties of Ag, Pt, and Ni nanocontacts. *Physical Review B*, 74(23):1–21, December 2006.

[Peercy2000] P. S. Peercy. The drive to miniaturization. *Nature*, 406(6799):1023–6, August 2000.

[Peláez2006] S. Peláez, P. García-Mochales, and P. a. Serena. A comparison between EAM interatomic potentials for Al and Ni: from bulk systems to nanowires. *Physica Status Solidi (a)*, 203(6):1248–1253, May 2006.

[Peláez2007] S. Peláez and P. A. Serena. Equation of state of ultra-narrow metallic nanowires. *Surface Science*, 601(18):4163–4168, September 2007.

[Peláez2009] S. Peláez, C. Guerrero, R. Paredes, P. A. Serena, and P. García-Mochales. Identification and characterization of icosahedral metallic nanowires. *Physica Status Solidi (c))*, 6(10):2133–2138, October 2009.

[Peláez2010] S. Peláez, C. Guerrero, R. Paredes, P. A. Serena, and P. García-mochales. Modelling Metallic Nanowires Breakage for Statistical Studies: Ni Case as Example. In Nicoleta Lupu, editor, *Electrodeposited nanowires and their applications*, chapter 2, pages 35–60. InTech, 1st edition, 2010.

[Peng2009] Y. Peng, T. Cullis, and B. Inkson. Bottom-up nanoconstruction by the welding of individual metallic nanoobjects using nanoscale solder. *Nano Letters*, 9(1):91–6, January 2009.

[Podolski2005] V. A. Podolskiy, A. K. Sarychev, E. E. Narimanov, and V. M. Shalaev. Resonant light interaction with plasmonic nanowire systems. *Journal of Optics A: Pure and Applied Optics*, 7(2):S32–S37, February 2005.

[Polak1969] E. Polak and G. Ribière. Note sur la convergence de méthodes de directions conjuguées. *Revue francaise d'informatique et de recherche opérationnelle, série rouge*, 3(1):35–43, 1969.

[Press2007] W. H. Press. *Numerical recipes: the art of scientific computing.* Cambridge University Press, 2007.

[Qiao2008] L. Qiao and X. Zheng. Elastic property of fcc metal nanowires via an atomic-scale analysis. *Applied Physics Letters*, 92:231908, 2008.

[Rahman1964] A. Rahman. Correlations in the Motion of Atoms in Liquid Argon. *Physical Review*, 136(2A):A405–A411, October 1964.

[Rahman1974] A. Rahman and F. Stillinger. Propagation of sound in water. A molecular-dynamics study. *Physical Review A*, 10(1):368–378, July 1974.

[Ramsden2009] J. Ramsden. *Essentials of Nanotechnology.* Ventus Publishing ApS, 2009.

[Rapaport1997] D. C. Rapaport. *The art of molecular dynamics simulation.* Cambridge University Press, 1997.

[RB1996] G. Rubio-Bollinger, N. Agraït, and S. Vieira. Atomic-sized metallic contacts: mechanical properties and electronic transport. *Physical Review Letters*, 76(13):2302, 1996.

[RB2001] G. Rubio-Bollinger, S. Bahn, N. Agraït, K. Jacobsen, and S. Vieira. Mechanical Properties and Formation Mechanisms of a Wire of Single Gold Atoms. *Physical Review Letters*, 87(2):1–4, June 2001.

[Robert2004] C. P. Robert and G. Casella. *Monte Carlo statistical methods.* Springer, 2004.

[Rodrigue2000] V. Rodrigues, T. Fuhrer, and D. Ugarte. Signature of atomic structure in the quantum conductance of gold nanowires. *Physical Review Letters*, 85(19):4124–7, November 2000.

[Rodrigue2002] V. Rodrigues, J. Bettini, a. Rocha, L. Rego, and D. Ugarte. Quantum conductance in silver nanowires: Correlation between atomic structure and transport properties. *Physical Review B*, 65(15):2–5, March 2002.

[Rodrigue2003] V. Rodrigues, J. Bettini, P. Silva, and D. Ugarte. Evidence for Spontaneous Spin-Polarized Transport in Magnetic Nanowires. *Physical Review Letters*, 91(9):1–4, August 2003.

[Sato2006] F. Sato, A. S. Moreira, J. Bettini, and P. Z. Coura. On the Formation of Copper Linear Atomic Suspended Chains. *Arxiv preprint cond-mat*, (0602092):1–4, 2006.

[Schaefer2010] H.-E. Schaefer. *Nanoscience: The Science of the Small in Physics, Engineering, Chemistry, Biology and Medicine*. Springer, 2010.

[Scheer1997] E. Scheer, P. Joyez, D. Esteve, and C. Urbina. Conduction channel transmissions of atomic-size aluminum contacts. *Physical Review Letters*, 78(18):3535–3538, May 1997.

[Sekiguch2005] K. Sekiguchi, E. Saitoh, and H. Miyajima. Conductance quantization by the application of magnetic fields in ballistic Ni nanocontacts. *Journal of Applied Physics*, 97(10):10B312, 2005.

[Sen2002] P. Sen, O. Gülseren, T. Yildirim, I. Batra, and S. Ciraci. Pentagonal nanowires: A first-principles study of the atomic and electronic structure. *Physical Review B*, 65(23):1–7, June 2002.

[Serena1996] P. A. Serena and N. García. *Nanowires*. Springer, 1997 edition, 1996.

[Serena1997] P. A. Serena and N. García. *Nanowires*. Springer, 1997.

[Serena2010] P. A. Serena. *La nanotecnología*. Â¿Qué sabemos de? CSIC, Madrid, 2010.

[Sharvin1965] Y. V. Sharvin. A possible method for studying fermi surfaces. *Zhurnal Eksperimental'noi i Teoreticheskoi Fiziki*, 48:984, 1965.

[Shchukin2004] V. A. Shchukin, N. N. Ledentsov, and D. Bimberg. *Epitaxy of nanostructures*. Springer, Berlin, 2004.

[Shimizu2002] M Shimizu. Conductance quantization in ferromagnetic Ni nanoconstriction. *Journal of Magnetism and Magnetic Materials*, 239(1-3):243–245, February 2002.

[Simmons1971] G. Simmons and H. Wang. *Single crystal elastic constants and calculated aggregate properties: a handbook*. M.I.T. Press, 1971.

[Sirvent1996] C. Sirvent, J. G. Rodrigo, S. Vieira, L. Jurczyszyn, N. Mingo, and F. Flores. Conductance step for a single-atom contact in the scanning tunneling microscope: Noble and transition metals. *Physical Review B*, 53(23):16086–16090, June 1996.

[Smith1976] C. J. Smith, editor. *Metal Reference Book*. Butterworths, London, 5 edition, 1976.

[Smogunov2006] A. Smogunov, A. Dal Corso, and E. Tosatti. Ballistic conductance and magnetism in short tip suspended Ni nanowires. *Physical Review B*, 73(7):1–8, February 2006.

[Soler2002] J. M. Soler, E. Artacho, J. D. Gale, A. García, J. Junquera, P. Ordejón, and D. Sánchez-Portal. The SIESTA method for ab initio order-N materials simulation. *Journal of Physics: Condensed Matter*, 14:2745, 2002.

[Sorensen1998] M. Sorensen, M. Brandbyge, and K. Jacobsen. Mechanical deformation of atomic-scale metallic contacts: Structure and mechanisms. *Physical Review B*, 57(6):3283–3294, February 1998.

[SP1997] D. Sánchez-Portal, P. Ordejón, E. Artacho, and J. M. Soler. Density-functional method for very large systems with LCAO basis sets. *International Journal of Quantum Chemistry*, 65(5):453–461, 1997.

[Stalder1996] A. Stalder. Study of plastic flow in ultrasmall Au contacts. *Journal of Vacuum Science & Technology B: Microelectronics and Nanometer Structures*, 14(2):1259, March 1996.

[Steiner2004] T. D. Steiner. *Semiconductor nanostructures for optoelectronic applications*. Artech House, 2004.

[Stern2004] H. A. Stern. Simple algorithm for isothermal-isobaric molecular dynamics. *Journal of computational chemistry*, 25(5):749–61, April 2004.

[Stilling1985] F. H. Stillinger and T. A. Weber. Computer simulation of local order in condensed phases of silicon. *Physical Review B*, 31(8):5262–5271, April 1985.

[Sun2003] Y. Sun, B. Mayers, T. Herricks, and Y. Xia. Polyol Synthesis of Uniform Silver Nanowires: A Plausible Growth Mechanism and the Supporting Evidence. *Nano Letters*, 3(7):955–960, July 2003.

[Sutrakar2009] V. K. Sutrakar and D. R. Mahapatra. Stress-induced phase transformation and pseudo-elastic/pseudo-plastic recovery in intermetallic Ni-Al nanowires. *Nanotechnology*, 20(29):295705, July 2009.

[Sutton1990] A. P. Sutton and J. Chen. Long-Range Finnis-Sinclair Potentials. *Philos. Mag. Lett.*, 61(3):139–146, 1990.

[Taniguch1974] N. Taniguchi. On the basic concept of nanotechnology. *Proceedings of the International Conference of Products Engineering Tokio, Part II*, 1974.

[Tersoff1988] J. Tersoff. New empirical approach for the structure and energy of covalent systems. *Physical Review B*, 37(12):6991–7000, April 1988.

[Tian2003] M. Tian, J. Wang, J. Kurtz, T. E. Mallouk, and M. H. W. Chan. Electrochemical Growth of Single-Crystal Metal Nanowires via a Two-Dimensional Nucleation and Growth Mechanism. *Nano Letters*, 3(7):919–923, July 2003.

[Tinga1973] W. R. Tinga. Generalized approach to multiphase dielectric mixture theory. *Journal of Applied Physics*, 44(9):3897, 1973.

[Tyson1977] W. Tyson and W. Miller. Surface free energies of solid metals: Estimation from liquid surface tension measurements. *Surface Science*, 62(1):267–276, January 1977.

[Untiedt1997] C. Untiedt, G. Rubio, S. Vieira, and N. Agraït. Fabrication and characterization of metallic nanowires. *Physical Review B*, 56(4):2154–2160, July 1997.

[Untiedt2002] C. Untiedt, A. I. Yanson, R. Grande, G. Rubio-Bollinger, N. Agraït, S. Vieira, and J. M. van Ruitenbeek. Calibration of the length of a chain of single gold atoms. *Physical Review B*, 66(8):1–6, August 2002.

[Untiedt2004] C. Untiedt, D. Dekker, D. Djukic, and J. M. van Ruitenbeek. Absence of magnetically induced fractional quantization in atomic contacts. *Physical Review B*, 69(8):1–4, February 2004.

[Valkerin2005] A. M. Valkering, A. I. Mares, C. Untiedt, K. Babei Gavan, T. H. Oosterkamp, and J. M. van Ruitenbeek. A force sensor for atomic point contacts. *Review of Scientific Instruments*, 76(10):103903, 2005.

[Verlet1967] L. Verlet. Computer "Experiments" on Classical Fluids. I. Thermodynamical Properties of Lennard-Jones Molecules. *Physical Review*, 159(1):98–103, July 1967.

[Verlet1968] L. Verlet. Computer "Experiments" on Classical Fluids. II. Equilibrium Correlation Functions. *Physical Review*, 165(1):201–214, January 1968.

[Vitos1998] L. Vitos, A. V. Ruban, H. L. Skriver, and J. Kollar. The surface energy of metals. *Surface Science*, 411(1-2):186–202, August 1998.

[Wang2002] J. Wang, Guanghou Wang, and Jijun Zhao. Density-functional study of Au_n (n=2-20) clusters: Lowest-energy structures and electronic properties. *Physical Review B*, 66(3):035418, 2002.

[Weisbuch1991] C. Weisbuch and B. Vinter. *Quantum semiconductor structures: fundamentals and applications*, volume 5. Elsevier, Boston, 1991.

[Wen2007] Y. Wen, Y. Zhang, and Z. Zhu. Size-dependent effects on equilibrium stress and strain in nickel nanowires. *Physical Review B*, 76(12):1–6, September 2007.

[Wen2008] Y. Wen, S. Wu, J. Zhang, and Z. Zhu. The elastic behavior in Ni monocrystal: Nonlinear effects. *Solid State Communications*, 146:253–257, February 2008.

[Wen2010] Y.-H. Wen, Y. Zhang, Q Wang, J.-C. Zheng, and Z.-Z. Zhu. Orientation-dependent mechanical properties of Au nanowires under uniaxial loading. *Computational Materials Science*, 48(3):513–519, May 2010.

[Yang2005] Z. Yang, M. Chshiev, M. Zwolak, Y.-C. Chen, and M. Di Ventra. Role of heating and current-induced forces in the stability of atomic wires. *Physical Review B*, 71(4):1–4, January 2005.

[Yanson1997] A. I. Yanson and J. M. Van Ruitenbeek. Do histograms constitute a proof for conductance quantization? *Physical Review Letters*, 79(11):2157–2157, 1997.

[Yanson1998] A. I. Yanson, G. R. Bollinger, H. E. van Den Brom, N. Agraït, and J. M. van Ruitenbeek. Formation and manipulation of a metallic wire of single gold atoms. *Nature*, 395:783–785, 1998.

[Yanson1999] A. I. Yanson, I. K. Yanson, and J. M. van Ruitenbeek. Observation of shell structure in sodium nanowires. *Nature*, 400:144–146, 1999.

[Yu2007] M. Yu, R. Ramprasad, G. W. Fernando, and R. M. Martin. Efficient method to calculate total energies of large nanoclusters. *Bulletin of the American Physical Society*, Volume 52,, March 2007.

[Zhong2003] Zhaohui Zhong, Deli Wang, Yi Cui, Marc W Bockrath, and Charles M Lieber. Nanowire crossbar arrays as address decoders for integrated nanosystems. *Science (New York, N.Y.)*, 302(5649):1377–9, November 2003.

[Zimmerma2000] J. A. Zimmerman, H. Gao, and F. F. Abraham. Generalized stacking fault energies for embedded atom FCC metals. *Modelling and Simulation in Materials Science and Engineering*, 8:103–115, 2000.

Appendix A

Future work

In this thesis we have shown results obtained from computer simulations on several different properties of metallic nanowires. In such a wide work there are always pending tasks. Here we list some of the features we would like to explore in the near future, in order to gain further insight on the topics we dealt with in this thesis.

A.1 Structure of FCC nanowires

In section 4.5 we observed that in nanowires, sometimes surfaces exhibit relaxations different than those in free surfaces (slabs). This is the case of the outwards relaxation of the [110] surface observed in $rec-110$ Ni nanowires. It woulld be interesting to check how strong is the edge influence in this behaviour. Simulations with thicker nanowires should be run until surfaces recover their relaxation pattern as in free slabs. Actually, it is not clear wether or not this unexpected relaxation pattern is somehow related to the axial expansion exhibited by Ni $rec-110$ nanowires, contrary to the compression observed for all the other nanowires. The origin of this weird behaviour should be studied carefully.

Furthermore, we have not estimated the relaxation of the exposed facets of all nanowires under study. Such study should be carried out in order to verify if other nanowire facets exhibit different relaxations that their corresponding free surfaces. If this is the case, we may be facing a new relaxation mechanism, which can be influenced by the presence of edges.

It is evident from our simulations that edge relaxations involve more than just corner atoms. We expect that also atoms in the neighborhood of corners contribute to the edge energy. A more detailed calculation should include a wider concept of edge: corner atoms and their nearest neighbors should be considered as the components of an edge.

A.2 Elastic properties of nanowires

In chapter 5 we have restricted ourselves to studying the response of nanowires upon stress within the elastic range. We have not studied the yielding stress and strain of these nanowires. Our restriction of up to 8% expansion is too small to observe the breaking of these nanowires. Further studies should be run with larger expansions, in order to find out how do both the yielding stress and strain depend on the axial orientation, shape and thickness of the nanowires.

We have observed a strong non-linearity of the stress strain curves in Al and Ni. We have observed a correlation of this non-linearity with the nature of the density function in the EAM parameterization that we used. Wether this behaviour is to be expected in real crystalline systems or it is just an artifact of the potential, is a question that future studies should address. In particular, we expect that simulations using first principles methodologies may shed light on this subject.

A.3 Breaking nanowires

In our simulations on the breaking process of metallic nanowires we have used a velocity rescaling method to keep the average temperature constant. However, other thermostat schemes could be more appropriate to mimic the experimental conditions, in which only the temperature of the electrodes is monitored. A possible approach is to thermalize only those atoms at the two end bilayers; then the rest of the system will be thermalized naturally and the distribution of the temperature will be more similar to the experimental conditions. It is important to check wether a different thermostat approach influences the temperature spatial distribution and particularly the behaviour of atoms in the narrowest section of the nanowire.

We have demonstrated that several features of the minimum section histograms $H(S_m)$ change between simulations with small and larger nanowires. This is a relevant result, since it raises concerns about *ab initio* simulations in which small nanowires are simulated due to the size limitations of this approach. We believe that it should be important to run simulations on much thicker nanowires, until the shape of H(Sm) histograms converges with respect to the nanowire size and we are closer to the size dimensions of actual experimental setups.

A.4 Pentgonal nanowires

From our simulations it is not clear at all which is the mechanism that determines when the growth of a pentagonal chain stops for Al and Ni nanowires. However, we have observed that after breaking, the long pentagonal chain remains attached to one of the electrodes. We wonder wether re-indenting and pulling again could produce longer pentagonal chains. These simulations shall be run in the near future.

Appendix B

Short CV

B.1 Publications

In the following pages there is a list of the scientific publications derived from the work carried out in this thesis.

Appl. Phys. A 81, 1545–1549 (2005)
DOI: 10.1007/s00339-005-3393-z

Applied Physics A
Materials Science & Processing

P. GARCÍA-MOCHALES[1,*]
S. PELÁEZ[1]
P.A. SERENA[1,✉]
E. MEDINA[2]
A. HASMY[2]

Breaking processes in nickel nanocontacts: a statistical description

[1] Instituto de Ciencia de Materiales de Madrid, Consejo Superior de Investigaciones Científicas, Cantoblanco, 28049 Madrid, Spain
[2] Centro de Física, Instituto Venezolano de Investigaciones Científicas, Apdo. 21827, Caracas 1020A, Venezuela

Received: 11 March 2005/Accepted: 23 August 2005
Published online: 28 September 2005 •

ABSTRACT In this work we perform a statistical study of favorable atomic configurations of nickel nanocontacts during their stretching at 4 K and 300 K. Nanowire breaking events are simulated using molecular dynamics (MD) where atomic interactions are represented with state-of-the-art embedded atom (EAM) interatomic potentials. The full determination of atomic positions during the contact evolution allows determination of the evolution of the minimum-cross section S_m during stretching. By accumulating many breaking traces, we built minimum cross-section histograms $H(S_m)$. These simulated histograms reveal the presence of preferential geometrical arrangements during the nanocontact breaking, showing that no remarkable differences should appear between the low (4 K) and room temperature (300 K) situations. These results show that differences observed between low and room temperature experimental Ni conductance histograms, are not caused by the different structural evolution and, that therefore, other phenomena are involved.

PACS 81.07.Lk; 68.65.-k; 73.63.Rt; 31.15.Qg

1 Introduction

Metallic wires with diameters of the order of a few nanometers (nanowires) are key systems for both basic science and future development of nanoelectronic devices [1]. Electron transport through metallic nanowires presents ballistic features below room temperature since the electron elastic mean free path is larger than the characteristic nanocontact dimensions. Furthermore, well defined quantized propagating modes appear in nanowires with diameters of the order of few Fermi wavelengths (λ_F), due to the quantization of the electron motion associated with transversal confinement. In such limits, the electric conductance G is well described within the scattering matrix formalism through the Landauer formula $G = G_0 \sum_{n=1}^{N} T_n$, where $G_0 = 2e^2/h$ is the conductance quantum (where e and h are the electron charge and Planck's constant, respectively), T_n is the transmission probability associated with the n-th channel or mode, and N is the number of propagating or opened modes (those with energies below the Fermi energy, E_F) [2].

There are several experimental approaches for obtaining metallic nanowires [1], although methods based on scanning tunneling microscopy (STM) [3–6] and mechanically controllable break junctions (MCBJ) [7–9] have been widely used due to their sub nanometric accuracy. Furthermore, methods based on "table-top" experiments (by separating macroscopic wires) [10], using electron-beam irradiation inside a transmission electron microscope (TEM) [11, 12], or applying electrochemical methods [13, 14] have been proposed as candidates to fabricate metallic nanowires.

The electrical characterization of a metallic nanowire is generally done by measuring its conductance G as a function of the nanowire elongation during its rupture process. In this way, a standard experiment acquires a conductance trace formed by those conductance values associated with a sequence of different nanowire configurations. Since each conductance trace presents its own features, it is difficult to extract representative information from it. A deeper understanding is obtained by means of the so-called conductance histogram $H(G)$ [6] which is built by adding hundreds of independent conductance traces. In general, these conductance histograms present well defined peaks associated with preferred conductance values which reflect the presence of conductance quantization [9], or the existence of energetically favorable atomic arrangements [15–18]. Conductance histograms constitute a standard tool to analyze metallic nanowires, although it is very difficult to interpret them, since they simultaneously include mechanical as well as information of ionic and electronic origin. This complexity increases for polyvalent metals since several electronic transport channels per atom are involved [19, 20]. For instance, aluminum conductance histograms obtained at 4 K [15] and room temperature [17] show well defined peaks at conductance values close to integer values of G_0, although three channels per atom are involved in electron transport.

The analysis of $H(G)$ becomes even more intricate in magnetic nanowires due to the presence of a new degree of freedom, the electron spin. In particular, nickel nanowires have been studied for a long time [5, 6, 21–29] due to their promising applications. The first study where a conductance histogram was shown [6] also reported the existence of a Ni

✉ Fax: +34 91 372 0623, E-mail: pedro.serena@icmm.csic.es
Present address: Depto. de Física de la Materia Condensada, C–III, Universidad Autónoma de Madrid, Cantoblanco 28049 Madrid, Spain

Breaking processes in nickel nanocontacts: a statistical description. P. García-Mochales, S. Peláez, P. Serena. Applied Physics A. (81) 1545 (2005)

phys. stat. sol. (a) **203**, No. 6, 1248–1253 (2006) / **DOI** 10.1002/pssa.200566144

A comparison between EAM interatomic potentials for Al and Ni: from bulk systems to nanowires

S. Peláez[1], **P. García-Mochales**[2], and **P. A. Serena**[*, 1]

[1] Instituto de Ciencia de Materiales de Madrid, Consejo Superior de Investigaciones Científicas, Cantoblanco, 28049 Madrid, Spain
[2] Depto. de Física de la Materia Condensada, Universidad Autónoma de Madrid, Cantoblanco, 28049 Madrid, Spain

Received 3 October 2005, revised 20 December 2005, accepted 28 December 2005
Published online 24 March 2006

PACS 61.46.–w, 68.65.La

Two different kinds of interatomic potentials within the Embedded Atom Method (EAM) have been used to study several properties of selected crystalline structures and nanowire configurations (ordered and helical) for Al and Ni based systems. Reliability of these potentials has been explored when describing cohesive energy and geometrical properties of the systems under consideration as the atomic coordination number decreases. Results provide a criteria for stablishing the limits of validity of EAM potentials when applied to such systems as metallic ultra-narrow or single atom nanowires.

1 Introduction

Nanotechnology is based on the combination of known and new methodologies of synthesis, fabrication and characterization of materials, systems or devices at the nanometer scale, designed to exploit the broad spectrum of properties derived from their nanometric typical dimensions. These properties are intimately associated to the bonding and electronic features of the involved atomic species in a particular system as well as to its specific shape and size [1]. Within this context, the computational determination of favourable nanometric systems configurations is of capital interest to predict their intrinsic properties as well as their evolution under modification of external parameters. Ab-initio based computational techniques constitute a standard approach [2] able to accurately determine the most stable structures of a given set of atoms, taking into account the electronic wavefunctions and, then, suitably describing the electronic structure, chemical bonding and internal forces. Nevertheless, shortcomings in both conventional computing resources and programming methods determine that standard ab-initio calculations be usually restricted to systems containing few hundreds atoms. Since a cube with 10^3 nm^3 typically contains of the order of 10^5 atoms it is clear that its computational description at this scale requires alternative methods to the ab-initio approaches in order to effectively describe the atomic interactions. Following this strategy, the Embedded Atom Method (EAM) [3] represents an effective approach that is designed to efficiently optimise systems formed with millions of atoms and determine their time evolution upon modification of external parameters using classical Molecular Dynamics simulations (MD) or Monte Carlo methods [2].

As a general rule, different versions of EAM interatomic potentials [3–7] are designed to accurately describe a set of bulk system properties (i.e. configurations with large coordination number, N_c). There-

* Corresponding author: e-mail: pedro.serena@icmm.csic.es, Phone: +34 91 334 9000, Fax: +34 91 372 0623

A comparison between EAM interatomic potentials for Al and Ni: from bulk systems to nanowires. S. Peláez, P. García-Mochales, P. Serena. Physica Status Solidi (a) (203) 1248 (2006)

Available online at www.sciencedirect.com
ScienceDirect
Surface Science 601 (2007) 4163–4168
SURFACE SCIENCE
www.elsevier.com/locate/susc

Equation of state of ultra-narrow metallic nanowires

S. Peláez *, P.A. Serena

Instituto de Ciencia de Materiales de Madrid, Consejo Superior de Investigaciones Científicas, C/Sor Juana Inés de la Cruz 3, Cantoblanco, E-28049-Madrid, Spain

Available online 4 May 2007

Abstract

Equilibrium configurations of aluminum and nickel ordered nanowires are studied by means of a conjugate gradients minimization of the cohesive energy. The cohesive energy is computed using embedded atom method (EAM) semi-empirical potentials under two different parameterizations, in order to identify the influence of these approximations on the obtained results. We have tested, for several nanowire families, the concept of the nanowire equation of state which describes the nanowire cohesive energy as a function of its effective radius (reflecting the changes in the cohesive energy due to the presence of surfaces and edges). Using the equation of state we are able to determine the edge energies for different edge geometries. Our results show remarkable differences for these edge energies between both EAM approaches, as expected in low atomic coordination systems.

Keywords: Computer simulations; Semi-empirical models and model calculations; Aluminum; Nickel; Surface energy; Nanostructures

1. Introduction

Nanotechnology involves the design, characterization, production and application of structures, devices and systems by controlling their shapes and sizes at the nanometer scale [1]. One of the topics of increasing interest in the last two decades has been the study of the electronic transport through nanometric sized systems. In particular, metallic nanowires have raised considerable interest during the last years [2], since, on one hand, their electronic transport presents ballistic features, and, on the other hand, they show a rich quantum phenomenology associated with the traverse confinement of electrons. This rich phenomenology is reproduced in the laboratory in a controlled way, using experimental setups based on scanning tunneling microscopy (STM) or mechanically controllable break junction (MCBJ) approaches [2]. These techniques bring the possibility of performing statistical analysis, providing information on very interesting properties of the nanowires as, for instance, the formation of 'magic' nanowire configurations [3–5].

Within this context, the computational determination of those favorable nanowire configurations is of capital interest to understand their static and dynamic properties, as well as their evolution under modification of external parameters. Ab-initio based computational techniques constitute a standard approach [6] to accurately determine the optimal configuration of a given set of atoms taking into account the electronic structure of the system. Nevertheless, shortcomings in both conventional computing resources and programming methods determine that standard ab-initio calculations be usually restricted to systems containing few hundreds atoms. It is for this reason that molecular dynamics (MD), optimization algorithms or Monte Carlo methods, based on the use of *semi-classical potentials* [7–10] are still necessary to describe nanoscale systems containing thousands of atoms, long timescales phenomena or perform statistical analysis of a given phenomena. This kind of approximation has been widely used to describe the structure and mechanical properties of nanowires and nanocontacts [5,11–22].

One of the most interesting properties of metallic nanowires is observed as their cross section is reduced to a few atoms. For a given radius, the nanowires experiment a

* Corresponding author. Tel.: +34 913349000; fax: +34 913720623.
E-mail address: spelaez@icmm.csic.es (S. Peláez).

0039-6028/$ - see front matter © 2007 Elsevier B.V. All rights reserved.
doi:10.1016/j.susc.2007.04.184

Equation of state of ultra-narrow metallic nanowires. S. Peláez, P. Serena. Surface Science (601) 4163 (2007).

IOP PUBLISHING NANOTECHNOLOGY

Nanotechnology **19** (2008) 225704 (9pp) doi:10.1088/0957-4484/19/22/225704

Statistical analysis of the breaking processes of Ni nanowires

P García-Mochales[1], R Paredes[2,3], S Peláez[3] and P A Serena[3]

[1] Departamento de Física de la Materia Condensada, Facultad de Ciencias, Universidad Autónoma de Madrid, c/ Francisco Tomás y Valiente 7, Campus de Cantoblanco, E-28049-Madrid, Spain

[2] Centro de Física, Instituto Venezolano de Investigaciones Científicas, Apartado 20632, Caracas 1020A, Venezuela

[3] Instituto de Ciencia de Materiales de Madrid, Consejo Superior de Investigaciones Científicas, c/ Sor Juana Inés de la Cruz 3, Campus de Cantoblanco, E-28049-Madrid, Spain

E-mail: pedro.garciamochales@uam.es

Received 5 November 2007, in final form 16 March 2008
Published 28 April 2008
Online at stacks.iop.org/Nano/19/225704

Abstract

We have performed a massive statistical analysis on the breaking behaviour of Ni nanowires using molecular dynamic simulations. Three stretching directions, five initial nanowire sizes and two temperatures have been studied. We have constructed minimum cross-section histograms and analysed for the first time the role played by monomers and dimers. The shape of such histograms and the absolute number of monomers and dimers strongly depend on the stretching direction and the initial size of the nanowire. In particular, the statistical behaviour of the breakage final stages of narrow nanowires strongly differs from the behaviour obtained for large nanowires. We have analysed the structure around monomers and dimers. Their most probable local configurations differ from those usually appearing in static electron transport calculations. Their non-local environments show disordered regions along the nanowire if the stretching direction is [100] or [110]. Additionally, we have found that, at room temperature, [100] and [110] stretching directions favour the appearance of non-crystalline staggered pentagonal structures. These pentagonal Ni nanowires are reported in this work for the first time. This set of results suggests that experimental Ni conducting histograms could show a strong dependence on the orientation and temperature.

1. Introduction

The interest in metallic nanowires and nanocontacts arises from their very rich phenomenology. Electron transport through metallic nanowires presents ballistic features at and below room temperature (RT) since, in general, the electron mean free path is larger than the characteristic nanowire dimensions. Furthermore, well-defined electron transport modes appear, associated to the transversal confinement of electrons and the conductance G (inverse of the nanowire resistance R, $G = 1/R$) can be described in terms of the Landauer formula [1] which relates the conductance with the transmission probabilities associated with electron scattering processes taking place at the nanocontact region.

Metallic nanowires are usually fabricated using methods based in scanning tunnelling microscopy (STM), mechanically controllable break junctions (MCBJs), electron-beam irradiation, electrochemistry or 'table-top' set-ups [2]. In many cases, these methods allow one to monitor the so-called conductance trace, $G(t)$, i.e. the conductance time evolution measured during the nanowire breaking process. Each conductance trace shows its own features since it is very difficult to accurately control the nanowire geometry during its mechanical deformation.

Conductance histograms $H(G)$ are constructed by accumulating hundreds of $G(t)$ curves obtained under the same experimental conditions. These histograms provide valuable statistical information on the transport and structural nanocontacts properties. In many cases, conductance histograms present well-defined peaked structures close to integer multiples of the conductance quantum $G_0 = 2e^2/h$ (e is the electron charge and h the Planck constant). Such preferred conductance values have been interpreted in terms of conductance quantization [3] or favourable

Statistical analysis of breaking processes of Ni nanowires. P. García-Mochales, R. Paredes, S. Peláez, P. Serena. Nanotechnology 19 (2008) 225704.

Hindawi Publishing Corporation
Journal of Nanomaterials
Volume 2008, Article ID 361464, 9 pages
doi:10.1155/2008/361464

Research Article

Statistical Molecular Dynamics Study of (111) and (100) Ni Nanocontacts: Evidences of Pentagonal Nanowires

P. García-Mochales,[1] R. Paredes,[2,3] S. Peláez,[3] and P. A. Serena[3]

[1] *Departamento de Física de la Materia Condensada, Universidad Autónoma de Madrid, Cantoblanco, 28049 Madrid, Spain*
[2] *Centro de Física, Instituto Venezolano de Investigaciones Científicas Altos de Pipe, 1020-A Caracas, Venezuela*
[3] *Instituto de Ciencia de Materiales de Madrid, Consejo Superior de Investigaciones Científicas, c/ Sor Juana Inés de la Cruz 3, Cantoblanco, 28049 Madrid, Spain*

Correspondence should be addressed to P. A. Serena, pedro.serena@icmm.csic.es

Received 21 September 2007; Accepted 11 January 2008

Recommended by Jun Lou

We present molecular dynamics calculations on the evolution of Ni nanowires stretched along the (111) and (100) directions, and at two different temperatures. Using a methodology similar to that required to build experimental conductance histograms, we construct minimum crosssection histograms $H(S_m)$. These histograms are useful to understand the type of favorable atomic configurations appearing during the nanowire breakage. We have found that minimum crosssection histograms obtained for (111) and (100) stretching directions are rather different. When the nanowire is stretched along the (111) direction, monomer and dimer-like configurations appear, giving rise to well-defined peaks in $H(S_m)$. On the contrary, (100) nanowire stretching presents a different breaking pattern. In particular, we have found, with high probability, the formation of staggered pentagonal nanowires, as it has been reported for other metallic species.

1. INTRODUCTION

Nanotechnology involves the design, fabrication, and application of structures by controlling their composition, shape, and size at the nanometer scale [1]. In particular, the control of these properties will allow to exploit a whole set of novel physical and chemical features in future nanoelectronics development. Such development includes the study of the electron transport through different candidates to be used as nanoelectronics building blocks. Among these candidates, metallic nanowires or nanocontacts will play a relevant role [2].

The interest on metallic nanowires and nanocontacts rises from their rich phenomenology. Electron transport through metallic nanowires present ballistic features and, in addition, well-defined electron transport modes or channels appear associated to the transversal confinement of electrons for those nanowires with diameters of the order of few Fermi wavelengths λ_F. In the ballistic limit, the conductance G (inverse of the nanowire resistance R, $G = 1/R$) is described in terms of the transmission probabilities associated to these transport channels [3, 4].

Several experimental techniques have been used to form metallic nanocontacts and nanowires. Scanning tunneling microscopy (STM) [5–7] and mechanically controllable break junction (MCBJ) [8] methods are standard approaches to study the formation and rupture of nanocontacts under different experimental conditions. Metallic nanowires are also obtained using electron-beam irradiation inside ultra-high vacuum (UHV) transmission electron microscopes (TEM) [9] or using electrochemical methods [10].

The electric characterization of a metallic nanowire is usually done during its rupture. This rupture is achieved using SPM or MCBJ methods, leading to the acquisition of a nanowire conductance trace $G(t)$. In order to obtain relevant information concerning the electronic transport through nanowires of a given metallic species, conductance histograms $H(G)$ are constructed by accumulating many different conductance traces. Usually, conductance histograms present well-defined peaked structures, reflecting

Statisitical molecular dynamics study of (111) and (100) Ni nanocontacts: Evidences of pentagonal nanowires. P. García-Mochales, R. Paredes, S. Peláez, P. Serena. J. Nanomaterials 2008 361464 (2008).

phys. stat. sol. (a) **205**, No. 6, 1317–1323 (2008) / **DOI** 10.1002/pssa.200778170

physica status solidi a
www.pss-a.com
applications and materials science

The formation of pentagonal Ni nanowires: dependence on the stretching direction and the temperature

P. García-Mochales[*,1], **R. Paredes**[2,3], **S. Peláez**[3], **and P. A. Serena**[3]

[1] Departamento de Física de la Materia Condensada, Facultad de Ciencias, Universidad Autónoma de Madrid, c/Francisco Tomás y Valiente 7, Cantoblanco, 28049 Madrid, Spain
[2] Centro de Física, Instituto Venezolano de Investigaciones Científicas, Apto. 20632, Caracas 1020A, Venezuela
[3] Instituto de Ciencia de Materiales de Madrid, Consejo Superior de Investigaciones Científicas, c/Sor Juana Inés de la Cruz 3, Cantoblanco, 28049 Madrid, Spain

Received 8 October 2007, revised 1 February 2008, accepted 1 February 2008
Published online 9 May 2008

PACS 02.70.Ns, 61.46.Km, 62.25.–g, 73.40.Jn, 73.63.Rt

[*] Corresponding author: e-mail pedro.garciamochales@uam.es, Phone: (+34) 91 497 4757, Fax: (+34) 91 497 3961

We have constructed computational minimum cross-section histograms that statistically unveil the presence of preferred configuration during the breakage of Ni nanowires. The computed histograms showed strong dependence on the nanowire stretching direction. For the [100] and [110] stretching directions we have observed a very large peak associated to a minimum cross-section of 5 atoms. We have confirmed the configurations that contribute to this peak are staggered pentagonal nanowires. We have found that the formation of these nanowires is enhanced by increasing the temperature up to 550 K. At higher temperatures, the formation of pentagonal nanowires declines due to the competence against the nanowire melting processes.

1 Introduction Different candidates have been proposed as conducting or semiconducting elements for future nanoelectronics. Among them, metallic nanowires are considered promising nanoelectronic devices as well as an exigent benchmark to test basic phenomena [1]. Metallic nanowires show a very rich phenomenology: (i) their electrical properties present ballistic features at and below room temperature (RT), and (ii) well defined electron transport channels associated to the transversal confinement of electrons give rise to remarkable quantum features.

Several experimental techniques have been used to form metallic nanocontacts and nanowires [1]. Scanning tunnelling microscopy (STM) [2, 3] and mechanically controllable break junction (MCBJ) [4, 5] methods are standard approaches to study the formation and rupture of nanocontacts under different experimental conditions. Metallic nanowires are also obtained using electron-beam irradiation inside ultra high vacuum (UHV) transmission electron microscopes (TEM) [6]. This technique has revealed that ultra-narrow nanowires present helical and non crystalline weird configurations [7]. Metallic nanowires are also formed through electrochemical methods [8] or 'table-top' experiments [9].

The electric characterization of a metallic nanowire is usually done by measuring the conductance time evolution (i.e. the conductance trace) during its formation or rupture. Each conductance trace presents its own features since it is very difficult to control the nanowire geometry. In order to obtain collective information on the electronic transport, conductance histograms $H(G)$ are constructed by accumulating hundreds of conductance traces. In many cases, conductance histograms present a well defined peaked structure, reflecting the existence of high probability conductance values. For some specific cases, s-metals for instance, such peaks appear at integer multiples of the conductance quantum $G_0 = 2e^2/h$ (being e the electron charge and h Planck's constant). Such preferential integer values are usually interpreted in terms of conductance quantization [10] or favourable atomic arrangements [11, 12].

The formation of pentagonal Ni nanowires; dependence on the stretching direction and the temperature. P. García-Mochales, R. Paredes, S. Peláez and P. Serena. Phys. Stat. Sol. (a) 205(6), 1317-1323 (2008).

Phys. Status Solidi C 6, No. 10, 2133–2138 (2009) / DOI 10.1002/pssc.200881739

physica status solidi c
www.pss-c.com
current topics in solid state physics

Identification and characterization of icosahedral metallic nanowires

Samuel Peláez[1], Carlo Guerrero[2], Ricardo Paredes[3], Pedro A. Serena[*,1], and Pedro García-Mochales[,4]**

[1] Instituto de Ciencia de Materiales de Madrid, Consejo Superior de Investigaciones Científicas, c/Sor Juana Inés de la Cruz 3, Cantoblanco, 28049-Madrid, Spain
[2] Departamento de Física, Facultad Experimental de Ciencias, La Universidad del Zulia, Maracaibo, Venezuela
[3] Centro de Física, Instituto Venezolano de Investigaciones Científicas, Apto. 20632, Caracas 1020A, Venezuela
[4] Departamento de Física de la Materia Condensada, Facultad de Ciencias, Universidad Autónoma de Madrid, c/Tomas y Valiente 7, Cantoblanco, 28049-Madrid, Spain

Received 25 October 2008, accepted 31 January 2009
Published online 24 June 2009

PACS 02.70.Ns, 61.46.Km, 62.23.Hj, 62.25.–g

[*] Corresponding author: e-mail pedro.serena@icmm.csic.es, Phone: (+34) 913 348 999, Fax: (+34) 913 720 623
[**] Corresponding author: e-mail pedro.garciamochales@uam.es, Phone: (+34) 914 974 757, Fax: (+34) 914 973 961

We present and discuss an algorithm to identify ans characterize the long icosahedral structures (staggered pentagonal nanowires with 1-5-1-5 atomic structure) that appear in Molecular Dynamics simulations of metallic nanowires of different species subjected to stretching. The use of the algorithm allows the identification of pentagonal rings forming the icosahedral structure as well as the determination of its number n_p, and the maximum length of the pentagonal nanowire L_p^m. The algorithm is tested with some ideal structures to show its ability to discriminate between pentagonal rings and other ring structures. We applied the algorithm to Ni nanowires with temperatures ranging between 4 K and 865 K, stretched along the [100] direction. We studied statistically the formation of pentagonal nanowires obtaining the distributions of length L_p^m and number of rings n_p as function of the temperature. The L_p^m distribution presents a peaked shape, with peaks locate at fixes distances whose separation corresponds to the distance between two consecutive pentagonal rings.

1 Introduction Icosahedral or pentagonal nanowires are formed by subsequent staggered parallel pentagonal rings (with a relative rotation of $\pi/5$) connected with single atoms, showing a characteristic -5-1-5-1- ordering (see an example in Fig. 1a). Metallic nanowires are of great technological importance due to their properties and potential applications [1, 2]. Contrary to monoatomic chains, pentagonal nanowires are rather robust structures at relatively high temperatures and, therefore, they may consider as a promising candidate for being used as nanodevice components.

Different computational works during the last decade have showed the formation of staggered pentagonal configurations on breaking nanowires of different species [3-13]. The atomic sequence -1-5-1-5- presents a fivefold symmetry with respect the nanowire axis. This symmetry does not correspond to any crystallographic FCC nor BCC structures. The -1-5-1-5- staggered nanowire configuration may be understood in terms of a sequence of interpenetrated icosahedra. This icosahedral symmetry is very common in very small systems due to the large stability and high coordination characterizing such geometry [14].

The formation of staggered pentagonal configurations during the stretching process has been already reported for Na [3] using first principles methods, and for Cu [4-7] and Au [8] nanowires with different Molecular Dynamic (MD) approaches. In particular the high stability of the Cu nanowire was confirmed with *ab-initio* calculations [9]. Pentagonal motives also appear in infinite Al and Pb nanowires obtained from MD simulated annealing methods [10]. More recently such structures have been reported for stretched Ni nanowires with different crystallographic orientations [11-13], and confirmed their stability by *ab-initio* simulations [12, 13]. These pentagonal structures are very stable, with lengths larger than 20 Å and presenting a high plastic deformation under strain.

In general, the reported pentagonal nanowires have been found for single stretching evens. However, it is well

Identification and characterization of icosahedral metallic nanowires. S. Peláez, C. Guerrero, R. Paredes, P. A. Serena, P. García-Mochales. Physica Status Solidi (c) 6 (10) 2133-2138 (2009).

Current Nanoscience, 2011, *7*, 219-226

Icosahedral Ni Nanowires Formed from Nanocontacts Breaking: Identification and Characterization by Molecular Dynamics

Samuel Peláez[1,*], Pedro A. Serena[1], Carlo Guerrero[2], Ricardo Paredes[3] and Pedro García-Mochales[4]

[1]*Instituto de Ciencia de Materiales de Madrid, Consejo Superior de Investigaciones Científicas, c/Sor Juana Inés de la Cruz 3,Cantoblanco. Madrid - 28049, Spain,* [2]*Centro de Física. Instituto Venezolano de, Investigaciones Científicas. Km. 11 Ctra. Panamericana, Altos de Pipe, Estado Miranda, Venezuela and Departamento de Física, Facultad Experimental de Ciencias, La Universidad del Zulia, Maracaibo, Venezuela,* [3]*Laboratorio de Simulación. Instituto de Matemáticas, Unidad Cuernavaca, Universidad, Nacional Autónoma de México. A. P.273-3 Admon 3. Cuernavaca, Morelos, 62251, México, Departamento de Física y Matemáticas,Universidad Iberoamericana Ciudad de México. Prolongación Paseo de la Reforma 880, Colonia and Centro de Física. Instituto Venezolano de Investigaciones Científicas. Km. 11 Ctra. Panamericana, Altos de Pipe, Estado Miranda, Venezuela. Lomas de Santa Fe, México, D.F. 01219, México,* [4]*Departamento de Física de la Materia Condensada. Facultad de Ciencias, Universidad Autónoma de Madrid. c/Tomás y Valiente 7, Cantoblanco. Madrid - 28049, Spain*

Abstract: We present and discuss an algorithm to identify and characterize the long icosahedral structures (staggered pentagonal nanowires with 1-5-1-5 atomic structure) that appear in Molecular Dynamics simulations of metallic nanowires of different species subjected to stretching. The use of this algorithm allows the identification of pentagonal rings forming the icosahedral structure as well as the determination of its number n_p, and the maximum length of the pentagonal nanowire L_p^m. The algorithm is tested with some ideal structures to show its ability to discriminate between pentagonal rings and other ring structures. We applied the algorithm to Ni nanowires with temperatures ranging between 4K and 865K, stretched along the [111], [100] and [110] directions. We studied statistically the formation of pentagonal nanowires obtaining the distributions of length L_p^m and number of rings n_p as function of the temperature. The L_p^m distribution presents a peaked shape, with peaks located at fixed distances whose separation corresponds to the distance between two consecutive pentagonal rings.

Keywords: Molecular dynamics, metallic nanocontacts, icosahedral nanowires, embedded atom method.

1. INTRODUCTION

Icosahedral (also known as pentagonal) nanowires are formed by subsequent staggered parallel pentagonal rings (with a relative rotation of $\pi/5$) connected with single atoms, showing a characteristic -1-5-1-5- ordering (see an example in Fig. **1a**). The atomic sequence -1-5-1-5- presents a fivefold symmetry with respect to the nanowire axis. This symmetry does not correspond to any crystallographic FCC nor BCC structures. The -1-5-1-5- staggered nanowire configuration may be understood in terms of a sequence of interpenetrated icosahedra. This icosahedral symmetry is quite common in very small systems due to its large stability and high coordination [1]. Metallic nanowires are of great technological importance due to their properties and potential applications as nanoelectronics interconnectors or sensing elements [2,3]. Contrary to monoatomic chains, pentagonal nanowires are rather robust structures at relatively high temperatures and, therefore, they may be considered as a promising candidate for being used as nanodevice components working at realistic conditions. Different computational works during the last decade have shown the formation of staggered pentagonal configurations on breaking nanowires of different species [4-13]. The formation of staggered pentagonal configurations during the stretching process has been already reported for Na [4] using first principles methods, and for Cu [5-8] and Au [9] nanowires with different Molecular Dynamics (MD) approaches. In particular the high stability of the Cu nanowire was confirmed with ab-initio calculations [10]. Pentagonal motives also appear in infinite Al and Pb nanowires obtained from MD simulated annealing methods [11]. More recently such structures have been reported for stretched Ni nanowires with different crystallographic orientations [10,12,13], and confirmed their stability by ab-initio simulations [10,13]. These pentagonal structures are very stable, with lengths larger than 20Å and presenting a high plastic deformation under strain. In general, the reported pentagonal nanowires have been found for simulated single stretching events. However, it is well known that the analysis of nanoscale processes requires the use of statistical approaches since there exist many breaking paths in the nanowire configuration space. Such statistical studies addressing the formation of Ni pentagonal nanowires have been only addressed for Ni up to date [10,12,13]. It has been shown that [100] and [110] stretching directions favor the appearance of long pentagonal nanowires [10-12], and that there exists an optimal temperature at which the pentagonal nanowire yield is maximized [13]. In Refs. [10,12,13] the formation of -1-5-1-5- structures was detected by using a method based on the time Δt_s that the breaking nanowire lasts with a minimum cross section $S_m \sim 5$ (in units of atoms). The quantity $S_m \sim 5$ is close to the minimum cross-section of a pentagonal ring. As it is shown in Fig. (**1b**), the formation of the pentagonal nanowire (shown in Fig. **1a**) is reflected in the curve of the nanowire minimum cross-section versus time, presenting a long plateau around $S_m \sim 5$ during the pentagonal nanowire formation. A large statistical occurrence of pentagonal nanowires (for a given initial size, orientation and temperature) is reflected in its histogram of minimum cross-section H(S_m) as a huge peak centered at $S_m \sim 5$ (as it is shown in Fig. **1c**). In those previous works, the relative height of that peak or its area has been used to classify the conditions and probability of formation of icosahedral

*Address correspondence to this author at the Instituto de Ciencia de Materiales de Madrid. Consejo Superior, de Investigaciones Científicas, c/Sor Juana Inés de la Cruz 3, Cantoblanco. Madrid - 28049, Spain;
Tel: +34 913349000; Fax: +34 91 3720623;
E-mail: samuel.pelaez@icmm.csic.es

1573-4137/11 $58.00+.00

Icosahedral Ni Nanowires Formed from Nanocontacts Breaking: Identification and Characterization by Molecular Dynamics. S. Pelaez, P. Serena, C. Guerrero, R. Paredes, P. Garcia-Mochales. Current Nanoscience 7(2) 219-226 (2011).

IOP Publishing Nanotechnology

Nanotechnology **21** (2010) 305703 (7pp) doi:10.1088/0957-4484/21/30/305703

Metal-organic extended 2D structures: Fe-PTCDA on Au(111)

Lucía Álvarez[1], Samuel Peláez[2], Renaud Caillard[1], Pedro A Serena[2], José A Martín-Gago[1] and Javier Méndez[1]

[1] Grupo ESISNA, Instituto de Ciencia de Materiales de Madrid, Consejo Superior de Investigaciones Científicas (CSIC), c/ Sor Juana Inés de la Cruz 3, Campus de Cantoblanco, E-28049 Madrid, Spain

[2] Grupo de Teoría y Simulación de Materiales, Instituto de Ciencia de Materiales de Madrid, Consejo Superior de Investigaciones Científicas (CSIC), c/ Sor Juana Inés de la Cruz 3, Campus de Cantoblanco, E-28049 Madrid, Spain

E-mail: jmendez@icmm.csic.es

Received 23 March 2010, in final form 31 May 2010
Published 6 July 2010
Online at stacks.iop.org/Nano/21/305703

Abstract

In this work we combine organic molecules of 3,4,9,10-perylenetetracarboxylic dianhydride (PTCDA) with iron atoms on an Au (111) substrate in ultra-high vacuum conditions at different temperatures. By means of scanning tunnelling microscopy (STM) we study the formation of stable 2D metal-organic structures. We show that at certain growth conditions (temperature, time and coverage) stable 'ladder-like' nanostructures are obtained. These are the result of connecting together two metal-organic chains through PTCDA molecules placed perpendicularly, as rungs of a ladder. These structures, stable up to 450 K, can be extended in a 2D layer covering the entire surface and presenting different rotation domains. STM images at both polarities show a contrast reversal between the two molecules at the unit cell. By means of density functional theory (DFT) calculations, we confirm the stability of these structures and that their molecular orbitals are placed separately at the different molecules.

(Some figures in this article are in colour only in the electronic version)

1. Introduction

Supramolecular assembly of complexes [1] has become a relevant issue in the scientific community [2, 3] since several investigations have successfully shown the potential applications of molecular assemblies in the fields of magnetism, optical applications and catalysis [4–7]. A possible strategy to obtain these assemblies is to combine different organic molecules leading to ordered domains with different stoichiometries [8–10]. Other efforts focus on the combination of organic molecules with metals, in order to form metal-organic complexes [11]. In most cases these complexes are formed by a dehydrogenation process [12–15]. In this work we will address the study on the formation conditions and stability of extended 2D molecular layers covering large surface regions. The molecular species we have used is 3,4,9,10-perylene-tetracarboxylic-dianhydride (PTCDA), a planar molecule well known in the literature as an archetypal organic semiconducting molecule used for growth studies of organic molecules on various substrates [16–18]. PTCDA molecules grow on the Au(111) substrate forming well-ordered monolayers with a 'herring-bone' structure [19] that is stabilized through hydrogen bonds between the molecules. The PTCDA molecular layer exhibits a weak substrate interaction [20] with molecules separated from the substrate by about 0.33 nm [21, 22]. Previously, we have reported the formation of stable coordination compounds made of PTCDA molecules coordinated with iron atoms to form higher order molecular structures as nanodots or metal-organic chains [23, 24]. In this paper we investigate the experimental conditions to form ordered 2D metal-organic structures based on the combination of PTCDA molecules and iron on a Au(111) surface. Also, we observe changes in the contrast of the STM images when measuring them at both bias polarities. By density functional theory (DFT) calculations we confirm the stability of these 2D structures, and we correlate the changes in the contrast with the charge transfer processes between the molecules forming the structure.

0957-4484/10/305703+07$30.00

Metal-organic extended 2D structures: Fe-PTCDA on Au(111). L. Alvarez, S. Peláez, R. Caillard, P. A. Serena, J. A. Martín-Gago, J. Méndez. Nanotechnology 21 (30) 305703 (2010). Note: this paper corresponds to a collaborative work with the ESISNA group of the Instituto de Ciencia de Materiales de Madrid (ICMM-CSIC). In this work we have analysed the stability of bidimensional structures of PTCDA organic molecules on a Au substrate.

B.2 Participation in scientific conferences

The following is a list of the scientific conferences and workshops in which the candidate has participated, either with an oral or a poster presentation.

- December 2003. IV Conference of the Venezuelan Physics Society. Venezuelan Physics Society. Poster presentation. Margarita, Venezuela.
- October 2004. Trends in Nanotechnology (TNT2004). Phantoms Foundation. Attendance. Segovia, Spain.
- July 2005. Summer School. Photonics: From macrostructure to nanostructure. University of Cantabria. Attendance. Castro-Urdiales, Spain.
- August 2005. Trends in Nanotechnology (TNT2005). Phantoms Foundation. Poster presentation. Oviedo, Spain.
- September 2005. XXX Meeting of the Spanish Royal Society of Physics. Spanish Royal Society of Physics. Oral dissertation. Ourense, Spain.
- November 2005. V Conference of the Venezuelan Physics Society. Venezuelan Physics Society. Oral dissertation. Punto Fijo, Venezuela.
- March 2006. NanoSpain Network Meeting. Poster presentation. Pamplona, Spain.
- May 2006. International Conference in Nanotechnology ICON2006. Oral dissertation. Choroní, Venezuela.
- September 2006. European Conference on Surface Science ECOSS. Poster presentation. París, France.
- September 2006. Workshop: Introduction to Atomic Force Microscopy. Attendance. Murcia, Spain.
- September 2006. V Spanish Conference on Forces and Tunneling Microscopy. Poster presentation. Murcia, Spain.
- March 2007. NanoSpain Network Meeting. Poster presentation. Sevilla, Spain.
- March 2007. Workshop: Graduate School on electronic structure methods. Attendance. Bristol, United Kingdom.

- September 2007. IX European Conference on Surface Crystallography and Dynamics ECSCD-9. Poster presentation. Viena, Austria.
- September 2007. XXXI Reunión Bienal de la Real Sociedad Española de Física. Real Sociedad Española de Física. Oral dissertation. Granada, Spain.
- April 2008. Reunión de la Red Nanospain. Poster presentation. Braga, Portugal.
- September 2008. VI Spanish Conference on Forces and Tunneling Microscopy. Poster presentation. Sevilla, Spain.
- September 2008. Granada Seminar on Computational and Statistical Physics. Poster presentation. Granada, Spain.
- March-april 2009. Nanotech Insight. Poster presentation. Barcelona, Spain.
- July 2009. International Conference on Experiments/Process/Synthesis Modelling/Simulation/Optimization (IC-EpsMsO). Oral dissertation. Athens, Greece.
- September 2009. Trends in Nanotechnology (TNT2009). Phantoms Foundation. Poster presentation. Barcelona, Spain.
- November 2010. Workshop: Transport of Electrons and Phonons through nanoscale sized systems (TEP2010). Oral dissertation. Pamplona, Spain.
- April 2011. ImagineNano. Poster presentation. Bilbao, Spain.

Apéndice C

Resumen de resultados

A lo largo de esta tesis hemos ido presentando las conclusiones correspondientes a cada capítulo al final del mismo. No obstante, a continuación presentamos una breve síntesis de los resultados más relevantes que hemos conseguido.

C.1 Estructura de nanohilos con estructura FCC

En esta tesis hemos encontrado las configuraciones de equilibrio de nanohilos metálicos de Al, Ni y Cu con estructura cristalina FCC. Hemos estudiado la influencia de la orientación cristalina y de la forma de la sección transversal de estos nanohilos en diversas propiedades. En particular, hemos estudiado la dependencia de la energía de cohesión, compresión axial y energía de arista promedio con el grosor del nanohilo. Hemos observado que los nanohilos estudiados muestran una compresión axial al compararlos con su estructura sin relajar. Tal y como hemos discutido, este comportamiento es una manera de maximizar la cohesión y compensar la baja coordinación de los átomos de superficie, cuya cantidad frente a los de volumen se hace mayor a medida que observamos nanohilos más delgados.

Tal y como era de esperar en sistemas de coordinación atómica baja, hemos observado que los átomos situados en los bordes de los nanohilos muestran una fuerte relajación. Además, como hemos señalado, esta relajación de los átomos de arista afecta a la de los átomos de superficie, que no presenta el mismo comportamiento que las superficies infinitas estudiadas en el capítulo 3. Esto implica que las propiedades de las superficies en nanohilos muy delgados se ven afectadas por la presencia de aristas.

Hemos usado una Ecuación de Estado (EOS) para relacionar la energía de cohesión de nanohilos con su grosor. El uso de esta EOS permite estimar la energía de arista promedio de los nanohilos estudiados. Por primera vez en la literatura (hasta

donde sabemos) hemos realizado una estimación de las energías de arista asociadas a varias configuraciones de arista específicas. No obstante, no hemos podido correlacionar completamente estos valores con el aspecto geométrico o la cordinación de estas aristas.

C.2 Propiedades elástias de nanohilos FCC

Hemos realizado cálculos del módulo de Young E de los nanohilos estudiados. Este estudio nos ha permitido entender la relación de esta magnitud con el grosor de los hilos teniendo en cuenta diferentes orientaciones y formas de su sección transversal. Nuestros resultados muestran que la orientación del hilo juega el papel primordial en la dependencia de E con el grosor del mismo. A medida que consideramos nanohilos más delgados, el valor de E aumenta o disminuye dependiendo de la orientación crystalina del sistema. Sin embargo, a medida que el radio R del hilo es mayor, E tiende lentamente a su valor correspondiente a la estructura de volumen.

Sin embargo hemos observado un comportamiento atípico en la curva de E vs R para los nanohilos de Ni orientados a lo largo de la dirección [100]. En lugar de tener un comportamiento asintótico hacia el valor de volumen para hilos infinitamente gruesos, estas curvas muestran un valle en torno a $R = 11$ Å. Hemos encontrado que el origen de estos resultados está en el hecho de que el estrés σ_{zz} tiene un comportamiento no lineal en relación al estiramiento ϵ. Este comportamiento se presenta en varios hilos, pero es más marcado en los de Ni en la dirección [100].

Indagando en el origen de este fenómeno, hemos encontrado que esta no linealidad está relacionada con un pico en la función de densidad $\rho(r_{ij})$ de la parametrización EAM utilizada. Hemos concluido que son necesarios cálculos más precisos, utilizando alguna metodología de primeros principios, para definir si este comportamiento no lineal es esperable en sistemas reales, o si por el contrario es un artefacto del potencial EAM utilizado aquí.

C.3 Ruptura de nanohilos metálicos y observación de cadenas pentagonales

Continuando con el trabajo realizado históricamente en nuestro grupo, en esta tesis hemos simulado mediante MD la ruptura de nanohilos de Ni con forma rectangular y con diferentes orientaciones cristalográficas, a diferentes temperaturas y con diferentes

tamaños. Estos cálculos nos han permitido elaborar histogramas de la sección mínima $H(S_m)$, en analogía con los de conductancia $H(G)$ que se obtienen experimentalmente.

Nuestros resultados muestran que la forma de los histogramas $H(S_m)$ obtenidos a partir de rupturas de nanohilos de tamaño grande es distinta de la de los obtenidos de rupturas de nanohilos pequeños. Esto significa que para recuperar el comportamiento de nanocontactos en condiciones experimentales se necesitan simulaciones con nanohilos muy grandes, que incluyan miles de átomos. Entre las implicaciones de este resultado está el hecho de que los histogramas obtenidos por otros autores, usando simulaciones *ab initio* con pocos átomos, deberían ser revisados cuidadosamente.

Por otra parte hemos estudiado las configuraciones atómicas en la parte más estrecha del nanocontacto justo cuando está a punto de romperse. Nuestros resultados muestran que un alto porcentaje de las rupturas terminan en una configuración de monómero o dímero antes de romperse. En este trabajo calculamos también el entorno (distribución de los primeros vecinos) de los monómeros y dímeros. El resultado muestra que las configuración 2-1-3 se observa con mayor frecuencia en los monómeros. En dímeros, por otro lado, las configuraciones 3-1-1-4 y 3-1-1-3 son las que se observan con mayor probabilidad.

Adicionalmente, hemos estudiado el grado de crystalinidad en las regiones entre los átomos que forman monómeros o dímeros y las bicapas de los extremos del nanohilo. Este estudio demuestra que para las orientaciones [100] y [110], esta región presenta un alto grado de desorden, mientras que para la orientación [111], la estructura es ordenada. Estos resultados son un indicio de que, en determinadas condiciones, nanohilos orientados en las direcciones [110] ó [100] podrían favorecer un régimen de transporte cuántico difusivo, debido al alto grado de desorden en su estructura.

Hemos observado que los histogramas de sección mínima $H(S_m)$ muestran un pico alto alrededor de $S_m = 5$. Al inspeccionar visualmente las coordenadas atómicas hemos constatado que se trata de cadenas pentagonales largas que se forman espontáneamente durante la ruptura, de manera similar a la formación de LACs reportadas en diversos metales. Hemos desarrollado herramientas computacionales que nos permiten identificar con precisión la presencia de una cadena pentagonal durante el proceso de ruptura y, además, determinar el número de anillos pentagonales y longitud de la cadena. Usando esta herramienta hemos conseguido hacer un análisis estadístico de la probabilidad de aparición de cadenas con un número máximo n_p^m de anillos pentagonales. Estos resultados muestran que estas estructuras aparecen con mucha más probabilidad en hilos orientados a lo largo de las direcciones [100] y [110]. Además hemos encontrado que su aparición se ve favorecida por la temperatura. A

temperaturas muy bajas, la poca movilidad de los átomos dificulta la exploración de configuraciones alternativas a la FCC. No obstante, temperaturas muy altas pueden dificultar que los átomos se fijen a la estructura pentagonal durante el estiramiento, propiciando la ruptura de la cadena. De manera que existe una temperatura óptima T_{opt} a la cual se obtienen cadenas más largas según el material, orientación y tamaño del nanohilo.

La mayoría de estos y otros resultados obtenidos a lo largo de esta tesis traen consigo nuevas preguntas y/o sugieren trabajos adicionales que deberán ser abordados en el futuro. En el apéndice A se mencionan las principales líneas de trabajo que surgen de esta tesis, con el fin de alcanzar un conocimiento más profundo de las propiedades de los nanohilos metálicos estudiadas en esta tesis.

Apéndice D

Agradecimientos

Siempre que uno finaliza una etapa importante en la vida personal o profesional, es inevitable echar la vista atrás y hacer recuento. Entonces recuerdas situaciones o personas que de alguna manera han contribuido positivamente para que esa etapa fuera más agradable y productiva. Afortunadamente, en las tesis doctorales existe la costumbre de dedicar un apartado a expresar públicamente nuestra gratitud hacia esas personas.

También es costumbre dedicar las primeras líneas de este apartado a agradecer a los directores de tesis y a los actores institucionales. Pero yo quiero comenzar por recordar que, en un principio recibí la beca para venir a España a doctorarme gracias a que Rafael Angulo le habló bien de mí a Anwar. Y a que luego éste transmitió esas buenas referencias a Pedro. Así que muchas gracias a Angulo y a Anwar en primera instancia.

Total, que de todos los sitios donde pude haber ido a parar, tuve la suerte de dar con Pedro Serena. Siempre pensé que era el mejor jefe que podía haberme tocado. Y lo mejor de todo es que ahora al acabar la tesis lo sigo pensando. Con sus virtudes y defectos, ha sido el jefe perfecto para mí. Siempre está disponible. Siempre se le ocurre una buena idea. Y además de física me ha dado buenas y abundantes lecciones de historia, geografía, política, economía, administración, etc. en las largas y provechosas sesiones en la cafetería. La verdad es que a veces incluso me reprocho no haber sido el becario que él se merecía. Y ya sé que todo esto suena muy pelota, pero no tengo ninguna necesidad de serlo ahora y en verdad es lo que pienso. Por su parte, Pedro García-Mochales también ha sido de una gran ayuda. Desde el primer día que llegué a España, siempre ha tenido una actitud de 10. Siempre ha estado disponible y dispuesto a ayudar. Ha sido un gran colaborador, muy responsable y confiable. Y en su faceta de director de tesis también ha hecho un gran trabajo y además me ha facilitado mucho la interacción con la UAM.

Federico Soria, además de su labor administrativa como Director del ICMM, se ha mostrado siempre cercano, amable y colaborador conmigo. Sin su valiosa ayuda habría sido difícil montar sendos guateques y actividades culturales extra-académicas en el Instituto. Él entiende bien la importancia de estas actividades en un centro como este. Y por si fuera poco, me llevó a cantar Carmina Burana en el Auditorio Nacional, una experiencia inolvidable.

También quiero agradecer a Rosa Rufo. Una secretaria modelo. Siempre puedes contar con ella. Siempre he pensado que si la quinta parte del personal administrativo en general tuviera la mitad de la vocación de trabajo y servicio, así como su entrega y profesionalidad, las otras cuatro partes ya podrían quedarse en casa. Y el sistema funcionaría muchísimo más eficientemente.

El trabajo de esta tesis se ha visto favorecido en buena medida por las estancias cortas de investigación que he realizado en el Instituto Venezolano de Investigaciones Científicas (IVIC-Venezuela) y el Centre d'Investigació en Nanociència y Nanotecnologia (CIN2-CSIC). Les estoy muy agradecido a R. Paredes, M. Díaz y a P. Ordejón por su cooperación, amabilidad, tiempo y hospitalidad durante estas estancias.

En lo concerniente al trabajo de investigación de esta tesis, les debo mucho a Ricardo Paredes, Carlo Guerrero y a Pedro García-Mochales, quienes han participado activamente en las simulaciones, análisis de datos y discusión de los resultados de los capítulos 6 y 7, referentes a rupturas de nanohilos. De hecho, fue Ricardo quien nos propuso el uso del algoritmo de "burning" de Hermann para identificar monómeros y dímeros en Ni. Carlo además ha sido un gran anfitrión en La Universidad del Zulia durante discusiones científicas y piscinadas familiares. Y Pedro ha corrido muchas simulaciones y se ha currado infinitos histogramas.

Continuando con el ICMM, quiero agradecer a Primitivo, quien además de ser un ejemplo de profesionalidad, me permitió trabajar en el Instituto a horas intempestivas y fines de semana. A Sonia le agradezco las chuches diarias y sus palabras siempre positivas.

Juanma se merece una mención aparte. Es un tío verdaderamente especial. Con una vocación infinita de ayudar a los demás. No en vano es el hombre de referencia en el ICMM cuando alguien necesita auxilio informático. A mí particularmente me ha dedicado muchas horas, resolviéndome problemas informáticos y sobre todo enseñándome a resolverlos.

En el ICMM era un gusto ir a trabajar cada día. Y eso es de agradecer. Sobre todo cuando llegas a tu despacho y tienes a tu lado compañeros como Rafa, Rocío,

Fernando o Álvaro. Nunca pensé que se podía trabajar escuchando Radio 3 todo el día. Pero el caso es que no sólo se puede, sino que mola.

Durante los primeros meses de mi tesis comía con "los teóricos", gente muy real con la que era un gusto compartir, como Alberto, Juan Luis, Débora, Ramón Aguado, Geli, Rafa Roldán o Javi Sabio.

Luego cambiamos a comer en la Facultad de Psicología, donde el personal era una pasada. Edu, Tomás, Plácido, Pablo, Rosa, Natalia y el "Jefe", siempre están de buen humor y son muy atentos y simpáticos. Y junto con el menú diario, estaba la mejor compañía a la mesa: Lucía Vergara, Fernando, Diego, Ricardo, Jángel, Nacho, Carlos, Rafa, Ramón Escobar, María, Míriam, Covadonga, Sigmund, Mathias y el visitante de turno. Cada uno de su padre y de su madre, pero en conjunto hacíamos un buen grupo y las comidas eran una gozada.

Durante un tiempo tuve la suerte de coincidir con Jesús Araiza, Ricardo Paredes, su hermano y Don Julio. Un gran tándem, al que recuerdo con mucho cariño.

De vez en cuando por la tarde, al salir del Instituto, echábamos una pachanga de fútbol once o de fútbol sala. Ahí y siempre Javi Méndez, Jorge, Raúl, Sacha, Gonzalo, Quique, Mariano, Chicho, Javi Sánchez, Enrique Chacón, Jángel y Víctor Velasco, fueron grandes compañeros. Unos más generosos, otros más chupones. Pero entre todos hacíamos buenos equipos. En el penúltimo torneo, una nariz rota fue el (bajo) precio que tuve que pagar a cambio tantas jornadas goleadoras. Y después del fútbol, al chiringuito. Allí cayeron unas cuantas birras en entrañables atardeceres, mientras reclutábamos a los que iban saliendo del Instituto.

En fin, que el trabajo y la vida en el ICMM eran una maravilla. Me gusta pensar que por eso seguramente tardé tanto en acabar la tesis.

Por último quiero agradecer a mi familia. Tanto a la que me tocó al nacer como a la que me he hecho aquí durante estos años. Por ejemplo, desde que llegué al ICMM he tenido la suerte de entablar una entrañable amistad (por orden cronológico aproximado) con Rafa, Jángel, Nacho, María, Quique y Jorge. Por ellos siento un profundo cariño, difícil de explicar con palabras. Con ellos he vivido infinidad de aventuras. De alguna manera han sido mi familia durante mucho tiempo. Y ¡tengo tanto que agradecerles...! Y me gusta saber que siempre estarán ahí, a pesar del tiempo y la distancia.

Luego está la familia en la que me tocó nacer. Fue la primera vez que me tocó la lotería. Hilda y Abdul me dieron la mejor educación y crianza que se le puede dar a un hijo. E infinito amor. Tanto, que seguramente será por eso que, aún estando lejos de ellos, no noto tanto su ausencia física. Aún hoy no deja de sorprenderme cuánto de

ellos hay en mí. De lo bueno y de lo demás. Y para completar un núcleo familiar de lujo, me salió un hermano que es un auténtico regalo. Un gran amigo y un tipo al que admiro muchísimo. Cuya entrega, responsabilidad y capacidad para asumir el timón en los momentos difíciles nunca podré agradecerle lo suficiente. Si sólo hubiese una cosa que echara de menos de mi país, sería Guillermo. Pero afortunadamente también hay mucho de él en mí y lo veo a diario.

Y por último menciono a la familia que he decidido formar, en el sentido más convencional de la palabra. Con el matrimonio he ganado, además de una gran mujer, una suegra, una cuñada y unas tías fantásticas que me han adoptado de una manera increíble. Hasta el punto de preocuparse genuinamente por mí más que yo mismo, lo cual les convierte, conceptual además de emocionalmente, en parte de mi familia.

Y si quisiera hacer aquí una lista de todas las cosas que tengo que agradecerle a Adri, no acabaría. Pero éste no es el sitio para ello. Baste decir, en líneas muy generales, que me ha cambiado la vida (para mucho mejor, claro). Y no me refiero sólo a los cambios más evidentes (ciudad, estado civil, entorno y esas cosas) sino a mi evolución personal, interna. A esos cambios que sólo yo veo y que son el resultado de su amor, su disposición a ayudarme y su manera tan racional de ver las cosas y tan cuidadosa de hacérmelas ver. Vamos, que cada día me hace ser mejor persona. Y en lo que respecta a esta tesis, sobra decir que me ha apoyado en los momentos difíciles y ha hecho que, sorprendente y mágicamente, su escritura fuese casi coser y cantar. Porque con su amor ella sabe acompañarme mejor que yo mismo.